



U.S. DEPARTMENT OF  
**ENERGY**

PNNL-21040

Prepared for the U.S. Department of Energy  
under Contract DE-AC05-76RL01830

# A Novel Passive Millimeter Imager for Broad-Area Search

**Final Report on Project PL09-NPMI-PD07 (PNNL-55180)**

JR Tedeschi  
BE Bernacki  
JF Kelly  
DM Sheen  
RV Harris  
TE Hall  
BK Hatchell

CD Knopik  
WM Lechelt  
DL McMakin  
A Mendoza  
RH Severtsen  
PLJ Valdez

December 2011



**Pacific Northwest**  
NATIONAL LABORATORY

*Proudly Operated by **Battelle** Since 1965*

## DISCLAIMER

This report was prepared as an account of work sponsored by an agency of the United States Government. Neither the United States Government nor any agency thereof, nor Battelle Memorial Institute, nor any of their employees, makes **any warranty, express or implied, or assumes any legal liability or responsibility for the accuracy, completeness, or usefulness of any information, apparatus, product, or process disclosed, or represents that its use would not infringe privately owned rights.** Reference herein to any specific commercial product, process, or service by trade name, trademark, manufacturer, or otherwise does not necessarily constitute or imply its endorsement, recommendation, or favoring by the United States Government or any agency thereof, or Battelle Memorial Institute. The views and opinions of authors expressed herein do not necessarily state or reflect those of the United States Government or any agency thereof.

PACIFIC NORTHWEST NATIONAL LABORATORY  
*operated by*  
BATTELLE  
*for the*  
UNITED STATES DEPARTMENT OF ENERGY  
*under Contract DE-AC05-76RL01830*

Printed in the United States of America

Available to DOE and DOE contractors from the  
Office of Scientific and Technical Information,  
P.O. Box 62, Oak Ridge, TN 37831-0062;  
ph: (865) 576-8401  
fax: (865) 576-5728  
email: [reports@adonis.osti.gov](mailto:reports@adonis.osti.gov)

Available to the public from the National Technical Information Service  
5301 Shawnee Rd., Alexandria, VA 22312  
ph: (800) 553-NTIS (6847)  
email: [orders@ntis.gov](mailto:orders@ntis.gov) <<http://www.ntis.gov/about/form.aspx>>  
Online ordering: <http://www.ntis.gov>



This document was printed on recycled paper.

(8/2010)

# **A Novel Passive Millimeter Imager for Broad-Area Search**

## **Final Report on Project PL09-NPMI-PD07 (PNNL-55180)**

JR Tedeschi	CD Knopik
BE Bernacki	WM Lechelt
JF Kelly	DL McMakin
DM Sheen	A Mendoza
RV Harris	RH Severtsen
TE Hall	PLJ Valdez
BK Hatchell	

December 2011

Prepared for  
the U.S. Department of Energy  
under Contract DE-AC05-76RL01830

Pacific Northwest National Laboratory  
Richland, Washington 99352



# Summary

This report describes research and development efforts toward a novel passive millimeter-wave (mm-wave) electromagnetic imaging device for broad-area search. It addresses the technical challenge of detecting anomalies that occupy a small fraction of a pixel. The purpose of the imager is to pinpoint suspicious locations for cuing subsequent higher-resolution imaging. The technical basis for the approach is to exploit thermal and polarization anomalies that distinguish man-made features from natural features. The scale of applicability ranges from several meters to hundreds of kilometers.

This project began by building two research-grade passive mm-wave polarimeters for studying anomalies in ambient scene thermal emissions. The first system consisted of a full polarimeter to take single-channel imaging data using a 2D elevation and azimuthal steerable scanner. It was conservatively designed as a balanced Dicke switching radiometer to obtain reliable phenomenological data from the field. It was later adapted into a differential unbalanced Dicke radiometer that performed comparative radiance and polarimetry measurements between two closely aligned but slightly different views of a common scene. This differential radiometer afforded new insights into the small but real polarimetric changes that complex scenes can display as a result of man-made disturbances or, from reflective or angular materials that reflect/scatter efficiently the cold overhead skyshine into the field-of-view (FOV) of a down-looking imaging radiometer. The results were surprisingly devoid of scene clutter from natural scattering and reflective surfaces, presumably because of the random raking, fractal-like textures of natural surfaces. In contrast, surfaces or materials disturbed by non-random actions, such as human foot traffic over grass, produced notable radiometric anomalies. Subsequently, we designed and built a larger differential imager using a two-aperture binocular system to give better angular resolution. This system worked remarkably well and has provided surprisingly crisp differential scene data that appears to substantiate an important thesis of this proposed work: that differential thermal imagery using a large baseline offset between two imaging telescopes could generate sub-Rayleigh limit spatial resolution of small anisotropies induced into their emitted or scattered radiation.

Demonstrated capabilities during the project include:

- We were able to provide a complete and sensitive Stokes analysis of the mm-wave radiation. All radiation has two vector quantities that completely describe the amplitude and phase of the E- and B-fields, and the changes of these field quantities can be quantified as a four-component vector known as the Stokes vector. Rapid analysis of this vector (I, Q, U, V) can be made with full polarimeters, and we carried out this work near to the theoretical radiometric sensitivities predicted by classical formulae.
- From an analysis of the Stokes vectors for sundry different materials and scenarios of observation, we identified several important signatures of artificial change in large scenes due to man-made effects. The signatures were caused by texture changes, rake-inclination or twist changes, or due to reduced emissivity-temperature changes of natural radiance by objects that blocked or altered emission and thermal scatter from natural underlying (or even in some cases overlaying layers of) soils or by modifying the reflected thermal emission patterns from nearby surfaces such as vegetation or berms.
- We evaluated system improvements to measure smaller or slight disturbances to scenes, and have identified a means to highlight these changes rapidly. In the case of the simple full polarimetry data, we use a commercial multispectral analysis program to perform correlated reductions of the Stokes

parameters, while data obtained with differential imagers produces novel derivative signatures of edge or shadowing effects. From the field studies we learned some surprising insights:

1. Unlike coherent change detection with synthetic aperture radar, passive mm-wave (PMMW) imagery with full polarimetry has shown surprising sensitivity to disturbances of surface textures, such as grasses – even after a small amount of walk overs.
2. While looking for other unique or rare cues of polarization change to recommend a down select, we demonstrated that the polarimetric signatures could be treated as multi-spectral data and effectively mapped to new vectors using principle components analyses (PCAs) or via other spectral angle mapping techniques to create highly informative red, green, and blue colorized scenic graphs for effective human factors enhanced identifications.

At the outset of this work, we had expected that three of the four Stokes parameters Q and U along with total intensity I would be the most dominant in identifying man-made disturbances, while V, a measure of rarer circular dichroism or chirality changes, might be useful for tracking subtler effects, such as rotated field ellipticity resulting from twisted or curved objects. Indeed, such effects were seen and could perhaps become the means to detect and track shielded coax, and/or twisted wire remnants or braided cable into underground facilities, or as partially exposed frayed ends near former weapons testing sites that point the way to low yield tests that do not leave any noticeable subsidence or spallation changes. While we expected Q, U, and I to undergo the dominant changes, and V to be slight, it may behoove future designers to consider retaining full polarimetry. A priori attempts to predict or ‘guesstimate’ the polarization signatures proved less than systematic, at least at our current state of understanding. Indeed literature searches appear to be relatively devoid of high-quality images of useful and relevant phenomena of interest to the U.S. Department of Energy (DOE) or Defense Threat Reduction Agency. In fact, the Schubert review committee consisting of world renown mm-wave radar-experts urged early publication of our imagery data and Stokes remapping algorithms that highlight the often non-intuitive scene changes.

One result of this work is a partial development of more interesting phenomenological studies that might aid future field experts in locating odd ground disturbances or partially buried metals in dry soils. It seems nature is more subtle than we first appreciated. There are often circumstances when specific correlations of two or three subsets of the Stokes components give surprisingly good novelty filtering for specific conditions of disruption to otherwise unobtrusive scenes viewed as intensity maps I or as reduced maps of linear polarization ( $T_V$  and  $T_H$  or their correlated difference Q).

One of the most important consequences of our work may be the methods of ‘polar-to-spectral’ angle mapping or PCA analyses and our formative attempts to systematically cull correlated histograms of novel features. This effort, led by Dr. Bernacki and Mr. Tedeschi, has proved quite fruitful for concerted scene reductions in a manner that aids rapid focus on novel features of interest. We would like to study more DOE NNSA relevant situations where natural emissions and skyshine scatter can be viewed at lower (steeper) depression angles less than approximately  $-20$  degrees from horizontal. We began looking at means to do a tipping angle study of emission-temperature changes of complex scenes to assess perspective changes that would occur in realistic fly-overs. While we do not expect that our four-vector methods will rival the higher channel data reductions afforded by mutli-thermal imagery or hyperspectral imagery, we do think that the polar-to-spectral analyses do remarkably well at identifying peculiar changes of the ambient scene radiance. A form of stereo-like viewing with the dual aperture differential imager offers rapid means to identify abrupt edges or discontinuities in low contrast or dense scene clutter

thermal images. While spatial imaging resolution is lower than that of infrared (IR), the techniques of PMMW imaging would be nearly unsusceptible to simple camouflage masking or light overlays of windblown dust and dry dirt. PMMW imaging with polarimetry can provide visually intuitive imagery, and has a more robust capability to image through simple obscurants that will blind the IR and see volumetric thermal signatures under visually opaque coverings in many circumstances that will nullify the higher spatial resolution advantages of panchromatic or IR imaging systems. The coming decade of technological improvements in low noise figure mm-wave electronics and radio frequency-to-optical conversion technologies would suggest excellent headroom to significantly improve the sensitivity and speed of polarimetric imaging recounted in this report.



## Acronyms and Abbreviations

ADC	analog-to-digital converter
AOI	area of interest
CMB	cosmic microwave background
CMBR	cosmic microwave background radiation
CMOS	complementary metal-oxide semiconductor
cross-pol	cross-polarization
dB	decibel
dBm	decibel referenced to 1 mW
DOE	U.S. Department of Energy
efl	effective focal length
FOV	field-of-view
GSD	ground-separation distance
HEMT	high-electron mobility transistor
HPCR	heterodyne polarization combination radiometer
HPF	high-pass filter
HWHM	half width at half maximum
I, Q, U, V	Stokes parameters 1, 2, 3, 4, respectively
IED	improvised explosive device
IF	intermediate frequency
IR	infrared
LBT	large binocular telescope
LCP	left circularly polarized
LNA	low-noise amplifier
LO	local oscillator
LWIR	long-wave infrared
MIA	multivariate image analysis
MMIC	microwave monolithic integrated circuit
mm-wave	millimeter-wave
NASA	National Aeronautics and Space Administration
NEDT	noise equivalent differential temperature
NIST	National Institute of Standards & Technology
OAP	off-axis parabola
OMT	orthomode transducer
p-p	peak-to-peak
PCA	principal component analysis
PMMW	passive millimeter-wave

PNNL	Pacific Northwest National Laboratory
QWP	quarter-wave plate
RHCP	right-hand circularly polarized
RF	radio-frequency
RGB	red, green, blue
SBIR	Small Business Innovation Research
SNR	signal-to-noise ratio
SPDT	single-pole double-throw (i.e., one input terminal, two selectable output terminals)
TES	transition edge sensor
$T_R$	receiver temperature
TTL	transistor-transistor logic
VNA	vector network analyzer
WGP	wire grid polarizer
WMAP	Wilkinson microwave anisotropy probe

# Contents

Summary .....	iii
Acronyms and Abbreviations .....	vii
1.0 Introduction .....	1.1
1.1 The Physics .....	1.1
1.2 The Goals .....	1.2
1.3 First 1.5 Years of Work to Understand Polarimetric Phenomenology .....	1.3
1.4 Final 1.5 Years of Study to Evaluate Coherent Array Imagers .....	1.4
2.0 Background and Overview .....	2.1
3.0 Radiometer .....	3.1
3.1 Overview .....	3.1
3.2 Theory and Design .....	3.1
3.3 Development .....	3.7
3.4 Performance Evaluation of Heterodyne Dicke Switching Radiometer .....	3.10
3.4.1 Component and Section Performance Evaluations .....	3.10
3.4.2 Radiometer System Performance Evaluation .....	3.14
3.5 Differential Radiometer Performance Testing .....	3.17
3.5.1 Millimeter-Wave Section .....	3.17
3.5.2 Microwave Section .....	3.22
3.5.3 Differential Radiometer System Testing .....	3.26
4.0 Optics .....	4.1
4.1 Overview .....	4.1
4.2 Theory and Design .....	4.1
4.2.1 Telescope Components .....	4.1
4.2.2 Designing the Off-Axis Parabolic Antenna .....	4.2
4.2.3 Tolerance Analysis of the Off-Axis Parabolic Antenna .....	4.6
4.2.4 Design of Dragonian Offset Dual Reflector Antennas: Front-Fed and Side-Fed .....	4.9
4.3 Development .....	4.15
4.3.1 Monocular Telescope .....	4.15
5.0 Mechanics .....	5.1
6.0 Electronics .....	6.1
7.0 Software and Data Analysis .....	7.1
7.1 Stokes Parameters and Multivariate Image Analysis .....	7.4
8.0 Calibration .....	8.1
8.1 Radiometric Sensitivity .....	8.2
8.2 Heated Black Body Calibration .....	8.3
8.3 Liquid-Nitrogen Calibration .....	8.3

8.4	Coherent Polarization Generator Calibration .....	8.5
8.5	Design of a Quarter-Wave Plate Using Simulated Dielectrics.....	8.6
8.5.1	Introduction .....	8.6
8.5.2	Quarter-Wave Plate Design.....	8.7
8.5.3	Groove Design.....	8.7
8.6	Establishment of Calibration Protocols .....	8.10
9.0	Monocular System.....	9.1
9.1	Overview .....	9.1
9.2	Development of the Monocular System.....	9.1
9.3	Measurements with the Monocular System .....	9.3
9.3.1	Initial Measurements .....	9.3
9.3.2	Elevated Platform Measurements.....	9.6
9.3.3	Characterization and Resolution Measurements .....	9.7
9.3.4	Long-Distance Measurements .....	9.11
9.4	Near-Field Imaging Results .....	9.13
10.0	Binocular Differential System .....	10.1
10.1	Overview .....	10.1
10.2	Development of the Binocular System.....	10.4
10.3	Measurements with the Binocular System .....	10.14
10.3.1	CSF Scan at Ground Level.....	10.14
10.3.2	Elevated Scan of Grassy Area East of EDL, PNNL.....	10.19
11.0	Real-Time System Concept.....	11.1
11.1	Introduction .....	11.1
11.2	Mirror Scanning .....	11.1
11.2.1	Whisk Broom Scanning .....	11.1
11.2.2	Two-Dimensional Mirror Scanning .....	11.2
11.3	Array Imagers.....	11.2
11.3.1	Coarse Arrays of Receivers.....	11.2
11.3.2	Solid-State Arrays .....	11.5
12.0	Conclusions .....	12.1
12.1	Notable Technical Accomplishments.....	12.1
12.2	Future Plans.....	12.2
13.0	References .....	13.1
	Appendix A Definitions .....	A.1
	Appendix B Presentations.....	B.1
	Appendix C Administrative Information .....	C.1
	Appendix D Radiometer Components .....	D.1
	Appendix E Electronic Diagrams .....	E.1
	Appendix F Fully Polarimetric Radiometer Imaging Sets.....	F.1

Appendix G Binocular Imaging Trade-Offs for Aircraft..... G.1  
Appendix H Possible NNSA Applications for PMMW Imaging ..... H.1

# Figures

2.1	Monocular Telescope in Use at Remote Hilltop Location.....	2.3
2.2	Binocular Differential System in Use on Scissor Lift at PNNL Grounds.....	2.3
3.1	Simplified Schematic of the Fully-Polarimetric W-band Radiometer.....	3.4
3.2	Radiometer as Mounted on Monocular Telescope .....	3.5
3.3	Dual Radiometer Photograph.....	3.6
3.4	Dual Radiometer Block Diagram.....	3.6
3.5	Polarimeter Network: Labeled Pictorial Diagram .....	3.8
3.6	Configured mm-wave HPCR System .....	3.9
3.7	Block Diagram of the Phase Combination Network.....	3.13
3.8	Microwave Phase Combining Network Test Arrangement .....	3.14
3.9	Radiometer Response to a $+45^\circ$ Signal.....	3.15
3.10	Radiometer Response to a $-45^\circ$ Signal.....	3.16
3.11	Radiometer Response to a Right-Hand Circularly Polarized Signal .....	3.16
3.12	Differential Radiometer Front End .....	3.17
3.13	Horizontal and Vertical Channel Measurements for OMT 1.....	3.19
3.14	Horizontal Channels: Power Measurement Comparison .....	3.20
3.15	Vertical Channels: Power Measurement Comparison .....	3.21
3.16	OMT 1, H and V Phase Comparison .....	3.21
3.17	OMT 2, H and V Phase Comparison .....	3.22
3.18	Microwave Filtering and Amplification Stage.....	3.23
3.19	Microwave Phase-Combination Network for the Differential Radiometer .....	3.24
3.20	Microwave Phase Matching Test Arrangement for Differential Radiometer.....	3.25
3.21	Transmitting V into OMT 1 .....	3.27
3.22	Transmitting H into OMT 1 .....	3.27
3.23	Transmitting $+45$ into OMT 1.....	3.28
3.24	Transmitting $-45$ into OMT 1.....	3.28
3.25	Transmitting RHCP into OMT 1 .....	3.29
3.26	Transmitting V into OMT 2.....	3.29
3.27	Transmitting H into OMT 2.....	3.30
3.28	Transmitting $+45$ into OMT 2.....	3.30
3.29	Transmitting $-45$ into OMT 2.....	3.31
3.30	Transmitting RHCP into OMT 2 .....	3.31
4.1	A Drawing of the Off-Axis Parabola Proposed for the Single Reflector mm-wave Polarimeter.....	4.3
4.2	Plot of the Gaussian Beam Along with Reference Marks Where It Impinges Upon the OAP .....	4.4
4.3	Intensity Plots Showing the Results for an Input Initially Polarized in the y-direction.....	4.4

4.4	Log Plot Showing the Intensity of the y- or Vertically-Polarized Input Field at the Image Plane of the OAP .....	4.5
4.5	Log Plot Showing the Intensity of the x- or Horizontally-Polarized Field Produced by Cross Polarization of the Vertically Polarized Input Field .....	4.5
4.6	Plots Showing the Log Intensity and Linear Intensity of the Focused mm-wave Beam at the Input to the Waveguide .....	4.6
4.7	A Plot of Waveguide Coupling Efficiency Versus Waveguide Tilt for the mm-wave Receiver System .....	4.7
4.8	A Plot of Waveguide Coupling Efficiency Versus Waveguide Lateral Displacement about the x- and y-axes for the mm-wave Receiver System.....	4.8
4.9	Plot Showing the Effect of Defocus or Axial Displacement of the Waveguide Entrance Aperture on Waveguide Coupling Efficiency.....	4.8
4.10	Diagram of a Dual-Offset Reflector with Design Parameter .....	4.10
4.11	Diagram Showing the Side-Fed Dragonian Offset Reflector Antenna Optimized Using Zemax .....	4.11
4.12	The Log Intensity Plot for the y-polarization Field of the Side-Fed Dragonian Reflector of the $E_y$ Field Component.....	4.12
4.13	The Log Intensity Plot for the x-polarization Field ( $E_x$ ) of the Side-Fed Dragonian Reflector.....	4.12
4.14	Layout of the Front-Fed Dragonian Offset Reflector .....	4.14
4.15	Log Intensity Plot of the Front-Fed Dragonian Showing the Amount of Linearly Polarized Light Contained in the $E_y$ Field .....	4.14
4.16	Log Intensity Plot for the Front-Fed Dragonian Reflector Showing the Distribution of Linearly Polarized Light in the $E_x$ Field Leaking into the Orthogonal Polarization State with Respect to the Input Beam .....	4.15
4.17	Single Mirror OAP Design—Isometric and Front Views.....	4.16
4.18	Single Mirror OAP Mounted to Tripod .....	4.17
4.19	Computer/Motor-Controlled Gimbal .....	4.18
4.20	The mm-wave Polarimeter Receiver Integrated into the OAP Scanner .....	4.19
4.21	Complete Integrated Polarimeter System .....	4.20
5.1	CAD Drawing of the Monocular Telescope System .....	5.1
5.2	Monocular Telescope Performing Scan.....	5.2
5.3	Custom-Built Frame with Binocular Telescope Mounted .....	5.3
6.1	Block Diagram of the Roving Eye Electronics System .....	6.1
7.1	AhisWin Example Screen Shot.....	7.2
7.2	ENVI Example Screen Shot.....	7.3
7.3	Overlay of Colorized Polarization Channels with Gray-Scale Intensity Channel .....	7.4
8.1	Coherent Polarization Generator for Calibrating the mm-wave HPCR.....	8.1
8.2	Coherent Polarization Generator.....	8.2
8.3	Incoherent Polarimetric Calibration Source.....	8.3
8.4	Liquid-Nitrogen Calibration of Dual Radiometer.....	8.4
8.5	Liquid-Nitrogen Calibration of Dual Radiometer: Detail of Horn and Turning Mirror .....	8.4

8.6	Coherent Polarization Generator: Horizontal Channel Phase Measurement .....	8.5
8.7	Coherent Polarization Generator: Vertical Channel Phase Measurement .....	8.6
8.8	Calculation of $n_x$ and $n_y$ as a Function of Duty Cycle for the Land and Groove Structure of the Wave Plate Surface.....	8.8
8.9	The Plot Above Showing the Value of $\Delta n_{xy}$ Versus the Duty Cycle of the Land/Groove Structure Reveals the Maximum Value Occurs at 0.56 .....	8.8
8.10	Detailed Drawing Showing the Land and Groove Structure of the Quarter-Wave Plate Design .....	8.9
8.11	Fabricated 6-in.-Diameter Quarter-Wave Plate .....	8.10
8.12	Field Calibration Device .....	8.11
9.1	Millimeter-Wave Polarimeter Receiver Staged on Scissor Jack.....	9.1
9.2	Outside Imaging Study Setup of mm-wave Polarimeter Receiver System.....	9.2
9.3	Visible Photo and Passive-mm-wave-Polarimeter Image of PNNL Parking Lot and Building .....	9.2
9.4	Visible Image for Polarimetric Radiometer Imaging Study with Blackbody Radiator in Foreground.....	9.4
9.5	Stokes Parameters of Passive Polarimetric Radiometer Imaging Results.....	9.5
9.6	Stokes V Channel with the Gray Scale Stretched, as Shown in the Histogram, to Show Only the High-Amplitude Circularly Polarized Data .....	9.5
9.7	Radiometer and OAP Scanner Elevated 36 ft on Scissor Jack .....	9.6
9.8	Wide-Angle Image of Sample Sand Box.....	9.7
9.9	Nighttime Imaging Results of Optical, LWIR, and Passive Millimeter Wave .....	9.8
9.10	Stokes I Image with Feature Overlays and Stokes I-V Scanner Plot.....	9.9
9.11	Resolution Target Pattern Configuration .....	9.10
9.12	Finite Conjugate Test Setup.....	9.10
9.13	Passive Millimeter-Wave Imaging Results of Resolution Pattern Using Various OD Pipes .....	9.11
9.14	Benton City, Washington, from McBee Mountain, with the Yakima River in the Mid-Ground and Rattlesnake Mountain in the Background .....	9.12
9.15	Overlay of mm-wave Data at 50% Opacity on the Photograph.....	9.12
9.16	Overlay of mm-wave Data at 100% Opacity .....	9.13
9.17	Scanning Buried Pipes in Volleyball Court .....	9.14
9.18	Pipe Set Mounted to a Polystyrene Foam Block.....	9.15
9.19	Millimeter-Wave Image of Pipe Set Mounted to Polystyrene Foam Block .....	9.15
9.20	Pipe Set, Laid in Trench, Partially Covered with Quartz Sand.....	9.16
9.21	Millimeter-Wave Scan of Pipe Set, Laid in Trench, Partially Covered with Quartz Sand .....	9.16
9.22	Pipe Set, Fully Buried Under Quartz Sand, with Markers on Surface to Aid in Locating Boundaries of Trench.....	9.17
9.23	Scan of Buried Pipes and Surrounding Markers .....	9.17
9.24	Scan of Buried Pipes (left). Same data as the preceding figure, but presented as the I image overlaid with red markings derived from a region of interest on a scatter plot (right) of I versus Q.....	9.18

9.25	Scan of Buried Pipes (left). Same data as the preceding figure, but presented as the I image overlaid with red markings derived from a region of interest on a scatter plot (right) of I versus V.....	9.19
9.26	Motorcycle and Scanner .....	9.20
9.27	Motorcycle: Visible and mm-wave Intensity.....	9.22
9.28	Motorcycle in False Color Non-Intensity mm-wave Channels.....	9.23
10.1	Ray-Trace for Object at a Distance of 20 m and Mirror Separation of 1 m.....	10.2
10.2	Close-up View of Ray Trace Near the Turning Mirrors and Horns, for Object at a Distance of 20 m and Mirror Separation of 1 m .....	10.2
10.3	Beam Footprint on Turning Mirror, for Object at a Distance of 20 m and Mirror Separation of 1 m.....	10.3
10.4	Beam footprint on Turning Mirror for Convergence Distances of 20, 50, 100, and 500 Meters .....	10.3
10.5	Side-fed Dragone-Mizuguchi Offset Dual Reflector Antennas Configured for Bracewell Nulling Imaging Experiments.....	10.4
10.6	Initial Structure Support Design for Mounting the Dragone-Mizuguchi Offset Dual Reflector Antennas.....	10.5
10.7	Second Structure Support Design for Mounting the Dragone-Mizuguchi Offset Dual Reflector Antennas.....	10.6
10.8	Initial Concept for Dual Pseudo-Differential System .....	10.6
10.9	Intermediate Conceptual Design of the Dual Reflector Scanning Telescope and the Reflector Ray Trace Patterns of the Dual Off-Axis Reflector Parabolas Design .....	10.7
10.10	Final Design Depiction of the Dual Reflector Scanning Telescope Using Dual Off-Axis Reflector Parabolas .....	10.7
10.11	Assembled Binocular Differential Radiometer Dual Reflector Scanning Telescope .....	10.8
10.12	Modified Polarimeter Radiometer with Two Antenna Feeds and Single-Mirror OAP .....	10.8
10.13	Dual System with 750-mm Separation .....	10.9
10.14	Side-Fed Dragone-Mizuguchi Offset Dual Reflector Antenna Test Fixture CAD Illustration.....	10.10
10.15	Dual Antenna Test Fixture, Showing Reflections from Flash and Reflections of Mirrors.....	10.11
10.16	Dual Antenna Test Fixture Angular Adjustment Mechanism, Showing One of Its Two Axes .....	10.12
10.17	Reconfigured Differential Radiometer.....	10.13
10.18	Dual Radiometer Scanning the CSF Building .....	10.15
10.19	Dual Radiometer Scanner Aimed at CSF Building .....	10.15
10.20	CSF Building from Viewpoint of Scanner.....	10.16
10.21	CSF Building, Differential Binocular Intensity (I) Plot.....	10.16
10.22	CSF Building, Differential Binocular Vertical/Horizontal Polarization (Q) Plot.....	10.17
10.23	CSF Building, Differential Binocular Stokes IQU Parameters Mapped into RGB Channels, Respectively .....	10.18
10.24	CSF Building, Differential Binocular IQU Plot Overlaid on Visible-Wavelength Optical Image .....	10.18

10.25	Radiometer Viewed from the Northeast, with EDL at Right and PSL at Left.....	10.19
10.26	Radiometer Viewed from the East, Looking Across the Cooling Ponds.....	10.20
10.27	Radiometer Viewed from the South, with CSF in Background, and In-Line-Pipe Target in Foreground.....	10.20
10.28	View Looking South from the Radiometer Platform.....	10.21
10.29	Differential mm-wave Scan of the Region Shown in the Previous Image.....	10.22
10.30	Overlay of the Optical Image and the mm-wave Image .....	10.23
10.31	Stokes V Parameter Image of the Same Scan as Above .....	10.24
11.1	Log-Log Plot Showing the Time Duration Needed to Acquire an $80 \times 80$ Pixel Image with 0.5-Second Overhead per Pixel Acquisition.....	11.3
11.2	Unit Cell of Two Fixed Horns (blue and red circles) Showing How They Must Be Moved to Obtain the Maximum Imaging Resolution Offered by a 982.5-mm-Focal-Length Telescope Operating in the W Band .....	11.4
11.3	Plot Showing the Effect on Strehl Ratio as the Off-Axis Image or Field Height is Increased from Zero to 96 mm for the Off-Axis Parabola.....	11.5
11.4	Plot Showing the Effect on Strehl Ratio as the Off-Axis Image or Field Height is Increased from zero for 300 mm for the Two-Element f/4 Dragone Design.....	11.5

## Tables

3.1	Microwave Phase Combination Network Phase Measurement Results .....	3.14
3.2	Microwave Network Phase Measurements for Differential Radiometer .....	3.26

# 1.0 Introduction

## 1.1 The Physics

Passive millimeter-wave (PMMW) imaging is an important complementary method to infrared (IR) thermography-radiometry for measuring emitted thermal energy from natural surfaces at ambient temperatures. Anyone who has viewed outdoor metal structures under clear-sky conditions with a thermal IR imager will quickly note that relatively unoxidized, smooth metal objects stand out as the “coldest” ambient objects in the radiometric scene, unless they are heavily corroded, painted with polymeric coatings, or wetted. Then such metal objects are displayed as nearly ambient warmer objects. Unlike IR thermal sensing, PMMW imaging can see corroded, badly pitted, painted, or most camouflaged metals with nearly 230 K of thermal contrast under clear skies, unless the dielectric paints, overlaying grit/grime and/or camo-layer(s) are very thick. Likewise, wet or pooled water surfaces appear radiometrically cold when viewed with PMMW radiometers, but as warm as the ambient surroundings if studied with IR radiometers. As such, PMMW imaging is an excellent complementary technique for identifying covered metals and/or measuring residual soil moisture in many circumstances where IR thermography is not well suited.

There are several excellent references discussing PMMW imaging advantages for persistent situational surveillance or even monitoring hidden weapons under thick clothing, camouflage, and other such defenses. Various references give good generalist descriptions of PMMW imaging principles (Lettington et al. 2003; Yujiri et al. 2003; Peichl et al. 2007; Brooker 2008; Daniels 2009), while Siegel (2002) gives an overview of “terahertz” imaging that also discusses sub-mm-wave imaging with electromagnetic wavelengths between 1 mm and 3 mm that are often considered terahertz wavelengths. Brooker (2008) provides a novel sensors perspective for detecting hidden metal by anti-tank missiles, smart mortar shells, and sub-munitions that resort to strictly passive MMW-radiometric tracking and detection algorithms during their final phases of engagement. The problem of discovering and homing onto hidden metal surfaces in a large background of vegetative or rocky scene clutter or deliberate camouflage is actually a distinct application area of PMMW terminal guidance, known as detection. Even unsophisticated small-aperture PMMW quadrant imagers can detect relatively small metal patches with effective contrast. This is due to the low apparent temperature of the reflected overhead cool sky that is efficiently scattered or reflected into the field-of-view of down-looking PMMW imagers. This radiometric advantage of PMMW sensing can be used regardless of whether the metal objects are heavily painted or even oxidized or heavily roughened. In contrast, IR signatures of oxidized metals are typically low and can be further depressed to match that of soils and ambient surroundings using a large variety of thin polymeric paints or masking overlayers at ambient temperature. It was this strength of PMMW imaging that was proposed to find metal structures or polar liquid spills in a clutter of ambient scene emissions.

While the resolvable temperature precision of MMW-radiometers (noise-equivalent delta-T, abbreviated NEDT) is slightly worse (about 0.1°C), and the frame updates are noticeably slower, than comparable IR thermography,<sup>(a)</sup> PMMW imaging is typically quite immune to humidity and precipitation

---

(a) Modern uncooled IR receivers using microbolometer-based focal plane arrays can have their relative frame images calibrated to NEDT ~ 30 mK, and operate with frame rates ~30 Hz for 480 by 640 sized formats.

effects when exploited at non-resonant frequencies below about 150 GHz. Ground imaging from space is possible at these lower mm-wave frequencies. There are several clean atmospheric windows that are devoid of permanent-dipole molecular absorbers: in particular, the band from about 85 to 105 GHz (W-band) has excellent clarity under nearly all reasonable atmospheric conditions except heavy rain (more than 100 mm/hour), or with extreme total humidity typical of the tropics (more than 55 mm of total integrated water vapor column). At microwave and even the mm-wave wavelengths greater than about 2 mm, the effects of elastic scatter by small hydrometeors (fog, rain less than 50 mm/hour, ice or snow particles smaller than 500  $\mu\text{m}$ ) or dry aerosols is still low, because the Rayleigh and Mie scattering processes are negligible and low, respectively. Also, the millimeter-wave (mm-wave) wavelengths are fairly large compared to the size of the typical airborne scatterers that have reasonable number density loadings, so it is rare under most natural conditions that particle size and suspended density can support strong Mie scatter to block the W-band or Ka-band, etc. Thus, PMMW imaging systems can provide useful surveillance advantages over thermal IR to observe hidden thermal signatures through many man-made obscurants, fog, dust, even blowing sand storms, or vehicular-induced brown-outs and, if the soil is dry, PMMW imaging can potentially be an effective method to see polar liquid spills or metals buried beneath several centimeters of quartzite- or silica-rich dry soil coverings

Even in very overcast rainy conditions, metals will stand out under almost all atmospheric conditions using PMMW imaging, with apparent cooler scene radiance (brightness temperature differentials) by up to 30 K or more.<sup>(a)</sup> Thermal contrast would be about 30 K against pooled water under standard class rains, and more than 40 K against wet concrete, soils, or vegetation. Under overcast or standard radiative-fog conditions, metals can often show more than 100 K thermal contrast, with adjacent pooled water causing the lowest contrast difference of about 100 K, and for vegetation scene clutter nearly 200 K differentials are likely. Under clear conditions, PMMW imaging can be quite effective for observing and quantifying the thermal profiles of natural scenes near 300 K. Calibrated thermal profiles can be provided with good precision: NEDT about 0.3 K at frame rates of 10 Hz or more for room temperature imagers. Space-borne mm-wave radiometers with front-end cooling can allow radiometric sensitivity for air-column temperature profiling, sea-surface temperature, and wind direction profiling with minimum resolvable temperature differentials of about 0.3 K, albeit over large poorly resolved spatial patches of more than 1 km in ground-separation distance (GSD). GSDs of about 1 km are feasible at 90 GHz using 2-m-class reflector dishes in low earth orbit, so the natural aspect of this work was to see if these systems could be advanced—in concept—to observe much smaller metal structures or novel non-natural polarimetric signatures of man-made reflective surfaces in a single pixel. For example, corrugated metal porticos are often constructed over the entrances to underground facilities (their adits) burrowed into wadi channels in the middle-east and then overlaid with a coating of native dry soil. One anticipates from mm-wave imaging of buried metals in dry soils that these objects might be discernible as novelties, both in terms of reduced scene radiance but also due to effects of polarization change as a consequence of their scattering properties from the periodic ridges of the metal roofing panels.

## 1.2 The Goals

With this type of scenario in mind, we undertook to devise modern PMMW imaging constructs based on recent developments from astronomy and astrophysics. We specifically hoped to see non-natural

---

(a) In the mm-wave wavelengths, the spectral radiance falls in the Rayleigh-Jeans limit for black-body emission, and can be described as a scalar power term directly proportional to temperature.

changes induced by man-made disturbances in otherwise natural scenes. Our first-year effort looked at this phenomenology and verified that there is a wealth of polarization signatures to exploit. In the manner of multi-thermal imaging, we found that making simultaneous measurements of polarization anisotropies (using the four Stokes vector measurements of electromagnetic electric fields), it is possible to increase the number of experimental channels to better identify small scene anomalies. The more ambitious part of our work was to look at significantly improving the speed of large area mapping. The ultimate desire would be to effect sub-pixel identifications of polarization anisotropies and to increase in-scene identifications of man-made objects or disturbances on the fly. This part of the work was eventually redirected in the second year based on new guidance and budgeting constraints. Nevertheless, we will outline the original goals for completeness and later summarize a recovery strategy at the end of this report.

We initially wanted to address two shortcomings for the existing space-borne PMMW imagers: spatial resolution and speed of imaging to map larger swaths of a scene at potentially higher spatial resolution. Radiometric sensitivity, the ability to spot small temperature differentials, is already well handled by the WindSat series of PMMW imagers and polarimeters developed for the Navy, as they use cooled front ends to achieve radiometer system temperatures (a measure of instrumental noise) less than 150 K (Gaiser et al. 2004; Bettenhausen et al. 2006). By having a system temperature below that of the scene, one can observe lower scene brightness temperatures with better signal-to-noise ratio (SNR). Lower instrument receiver temperatures ( $T_R$ ) will give greatest scene contrast while typically producing smaller offsets in calibrated absolute temperature profiles. Radiative cooling in space is an efficient method of reducing system noise from the front-end sensors' optics and feed-horns used to collect the mm-wave radiation. Reducing the front-end self-emission is also feasible with low-noise heterodyne receivers and has been demonstrated when studying the cold 2.7 K remnant of the cosmic microwave background radiation (CMBR) with earth-based sensors (Webber and Pospieszalski 2002). This has been demonstrated with a large variety of CMBR imaging systems operated in clear viewing environments, including urban university sites. Because the results of these techniques are already well developed and published, we decided to refocus our Year 2 efforts on improving spatial resolution and identifying high-contrast, sub-pixel polarimetric effects of scenarios that might improve wide area searches for weak anomalies on the scale of 30 m GSD. This change of plan was briefed to the U.S. Department of Energy (DOE) review committee (Schubert committee) in summer 2010. The Schubert committee endorsed the idea of exploiting direct optical imaging with interferometric additive techniques of beam combining. We were not able to show true coherent differential measurements, but found that even incoherent differential analysis could improve upon the sub-pixel spatial resolution seen with polarimetric signatures. We briefly review the findings of our field data developed in the first 1.5 years of our work to give context to our ultimate applications.

### 1.3 First 1.5 Years of Work to Understand Polarimetric Phenomenology

It was observed, early in our work, that polarization anomalies can be seen with sub-Rayleigh geometric resolution.<sup>(a)</sup> That is, objects with a solid angle less than that defined by our systems' detector

---

(a) The Rayleigh limit for angular resolution with our single aperture PMMW-imager, given as  $\sim 2 \cdot \lambda / D$ , at some typical range  $R$  was often better than classically expected for far-field limited measurements,

solid angle projected to the scene were observable when the full polarization map of a scene was analyzed using multispectral imaging techniques. In effect, apparent resolution of an anomaly can be enhanced if its contrast SNR is high, and this was confirmed. Reflected sky radiance from small-gauge twisted wire pairs, small pipes, man-hole covers with periodic ridges, and transitory depressions of grass can all result in novel polarization changes, even when their cross track spatial dimensions are less than one-sixth of the Rayleigh limit for geometric resolution.

As noted in the *Handbook of Military Infrared Technology* (Wolfe 1965, p. 753), “instantaneous resolution is related to the minimum detectable signal level and is limited to the resolution area of the detector. In the presence of a strong signal, however, full response need not be achieved to define an edge. ... the usable resolution solid angle varies inversely as the contrast signal-to-noise ratio so that a doubling of signal-to-noise ratio contains information allowing half the resolution of an isolated edge.” In effect, the Rayleigh limit for observable resolution assuming two closely spaced quasi-point-like sources can be improved if there is a large contrast difference along an edge or vertex. This can be observed for example by examining commercial Ikonos 0.8-m resolution images (Dial et al. 2003) (TerraView, FAS and Global Security provide some examples for study). When studying panchromatic images of the earth, one will often note that sharp contrasted edges and corners can be well resolved below the aforementioned Rayleigh resolution limit of 0.8 m, depending on the level of contrast presented. Having confirmed this analogous capability to see edges and other abrupt changes of polarimetric scene contrast, we turned our efforts to enhancing the scene contrast using quasi-imaging techniques proposed for mapping distant astronomical anomalies. We also looked at how these techniques might be scaled for wide-area searches, possibly by high-altitude, long-endurance aircraft.

## 1.4 Final 1.5 Years of Study to Evaluate Coherent Array Imagers

The latter half of work under this project was spent looking at how to do quasi-optical “additive interferometric” imaging with two separated apertures (by means of either Michelson or Fizeau beam combining), or whether sparse synthetic aperture imaging made better sense. The life-cycle plan had proposed Fizeau-type additive beam combining, sometimes known as Bracewell nulling, which is used effectively in the IR to study small moons in our solar system and search for exosolar planetary systems in distant solar systems. Unlike a single-aperture imaging system, interferometric beam analysis from two (or more; Kendrick et al. 2006) collection apertures allows an instantaneous differential measurement to be made concerning the fringe visibility of a “beam pattern” (Korotkov et al. 2006; Tucker et al. 2008). This allows both better spatial resolution and polarimetric precision to be achieved simultaneously, with spatial resolution being improved sometimes by  $2L/D$  at about 10 for a relatively small baseline separation  $L$  of two apertures of  $D$  diameter separated by  $2D$  between centers. This paradigm is effective for direct detection with photon detectors or bolometers but turns out to be a complex signal plumbing issue to implement with heterodyne receivers for more than a few pixels. Heterodyne reception would be needed in near-term operational PMMW imagers, because direct detection requires stringent cooling of a detector array to less than 4 K to work well.

One of the principal investigators, Dr. Bruce Bernacki, noted that Prof. Dennis Prather at the University of Delaware was making excellent progress with dense-array synthetic aperture imaging in the

---

and even sub-pixel detection was possible when near-field optical distortion was present in our early field trials.

atmospherically clean Ka-band (near 37 GHz) and his “multiplicative interferometric” techniques could potentially be adapted to work up beyond the 100-GHz band (W-band) with wide bandwidths. Thus, we have entered into collaboration with Prof. Prather’s team and encouraged them to apply for a DOE-Small Business Innovation Research (SBIR) project to extend their work to the W-band. Their SBIR proposal has been awarded and we are now assessing the likelihood that their planar array imager technology could be adapted for higher spatial resolution imaging at frequencies above 85 GHz. Their methods of distributed optical-radio-frequency (RF) heterodyne receivers would be an ideal way to make wholly passive mm-wave imagers for aircraft operations or folded large-extension panel space-borne array imagers, without any need for exotic cryo-cooling systems.

It was also decided that we should look at two-aperture quasi-optical beam combining to determine if we could achieve wide field imaging of sub-pixel disturbances, and whether improved angular resolution of these fringe detection techniques, given by  $\lambda/L'$ , where  $\lambda$  is the wavelength and  $L'$  is the full separation of the two apertures, holds when doing full Stokes analysis. Simulations of IR beam combining with the large binocular telescope (LBT) have shown the ability to see sub-pixel scale features in intensity maps; we wanted to confirm if equally compelling polarimetric signatures could also be recovered with better spatial resolution using two widely spaced apertures. Fringe imaging by additive interferometric beam summing has been demonstrated in the mm-wave using small separated horns (smaller than 1 m), but to our knowledge, no studies of fully polarimetric additive interferometric beam-combining have been done with large 0.5-m apertures separated by over 1 m. The Wilkinson microwave anisotropy probe (WMAP) imager is a notable pseudo “additive beam” correlator, but its adaptation to do full polarimetry appears complex and expensive at this time.

The basic layout for the design we had in mind is shown in Slide 9 of Angel (2000), which follows the design effort of the LBT that performs additive interferometric studies of IR signals. Very little information about the technical feasibility of imaging extended complex diffuse sources exists. However, a preliminary example of modeling for this paradigm (in the IR) is shown in Slide 12 of Angel (2000). This work would indicate that since the Fizeau method of additive beam interferometry has a wide bandwidth zero-order interference fringe, we surmise that initial reconstruction of mm-wave surfaces could be handled in turn, using a superposition of multiple looks with a multi-line array.

The other matter concerned understanding the detector architectures that could be used to do this type of imaging cost effectively. Two techniques of focal plane array imaging are used for sensitive additive-beam detection: either heterodyne or bolometric receivers work. Layout of quasi-optical Fizeau beam combining is most often carried out with bolometric imaging arrays and this is the method preferred by the academic CMBR community. It is low loss, but requires expensive cooling to effect properly through all stages of the beam combining and their polarization analyses.

In their simplest implementations as total power receivers, bolometer-based PMMW imagers perform much like thermal (calorimetric) IR imagers that use microbolometers, in that total received power is studied. IR bolometers can work well at room temperature whereas mm-wave bolometers need to operate at quite low temperatures just to work as mm-wave sensors. To make an array work at background-limited performance like that of optical or IR beam combining imagers requires less than liquid helium temperatures. For comparison, the temperature of the receiver elements must be such that their peak self-emitted photon energies are much less than the photon energy ( $kT = hv$ ) being analyzed; for 100-GHz photons, this equivalent peak temperature is 8 K for the instrumental radiation brightness to be equivalent

to the source. Heterodyne receivers can maintain low self-emission effects without the need for such cooling, so we reviewed these techniques for beam combining.

Since about 2000 there has been an explosion of solid-state mm-wave electronics that can operate uncooled with effectively low noise factors  $N$  in the mm-wave ( $N = 10^{\lceil \log_{\alpha}/10 \rceil}$ , where  $\alpha$  is defined as the net conversion and/or propagation losses). Practical mm-wave electronics typically can give equivalent receiver temperatures  $T_R < 1,500$  K.<sup>(a)</sup> The main parameter in any radiometer design is the radiometric sensitivity of the passive receiver architecture and its system losses that act between the receiver's rectification conversion stage and the target under study. The minimum resolvable temperature differential sensitivity for a radiometer with zero photon gain before the down-conversion that measures total power from an ambient surface at  $T_A$  is given as  $M \cdot (T_R + T_A) / \sqrt{B\tau}$  (Ulaby et al. 1981). Here  $M$  is the modulation constant (e.g., 1 for total power radiometer with direct rectification, 2 for Dicke switched comparator with reference at  $T_A$ ),  $B$  is the electromagnetic noise bandwidth ( $\pi/2 \cdot [-3$  dB] passband) being received (Hz), and  $\tau$  the post detection integration time (s). Often the net system temperature  $T_{\text{sys}} = (T_R + T_A)$  is noted for shorthand in many literature discussions, and typically is instrument dominated when the net receiver losses exceed about 6 dB.<sup>(b)</sup> Quite recently, complementary metal-oxide semiconductor (CMOS)-based mm-wave chipsets have become available that can provide a  $T_R$  of less than 2,000 K and steady progress continues with III-V semiconductor electronics that can push  $T_R$  below 100 K with modest front-end cooling, so the matter of additive interferometric beam combining and full polarimetric analysis may become technically feasible in the next few years.

The layout of the final report gives an overview of the radiometer layouts (monocular and binocular) that were used to understand the matters of differential beam combining (Section 2.0), the basic radiometer design to do full polarimetry in order to understand scene effects (Section 3.0), optical designs of the collection dishes, including a detailed study of how to make low cross polarization telescopes for a whiskbroom scanner (Section 4.0), the mechanical needs to scan the radiometers which indicate that it would be possible to build and suitably scan and/or jiggle a long baseline two-aperture binocular system (Section 5.0), the control electronics (Section 6.0), the scanning control software and basic image analysis codes (Section 7.0), methods of providing radiometric temperature calibrations and techniques to calibrate the polarimeter's vector analysis of the full Stokes parameters (Section 8.0), a compendium of field data taken with the monocular system (Section 9.0), a more detailed discussion of the binocular system and some of its early results from field testing (Section 10.0), and a brief discussion of the means to properly use the binocular system as a whiskbroom scanner, which could be built into the center pod of a high altitude long endurance aircraft for future tests of DOE relevant sites (Section 11.0). A conclusions section is provided to give a cursory understanding of the milestones accomplished. In Appendices G and H, we discuss how the binocular imager could be made to do wide area searches with a small imaging array (G), and where we think this type of imaging would benefit DOE missions (H).

- 
- (a) For example, if a system had a net loss  $\alpha$  of 4.86 dB to collect, down-convert and rectify the MMW signal to a quasi-dc signal, then the receiver's system temperature would be defined as  $T_R = (N-1) \cdot 290$  K, or 600 K. In electrical engineering convention, ambient reference temperature for noise calculations is defined at 290 K.
- (b) The receiver temperature is calculated as  $(10^{\lceil \alpha(\text{dB})/10 \rceil} - 1) \cdot 290$ , where  $\alpha$  is the sum of antenna feed losses (logarithmic noise figure (NF) in dB), front-end MMW-amplifier NF, mixer (double-sideband) NF, and intermediate frequency (IF) noise figure. Typically  $\alpha \sim 8$  dB of net loss or total NF for uncooled MMW radiometers, which results in a receiver temperature  $T_R \approx 1540$  K.

## 2.0 Background and Overview

Persistent broad area search for cueing requires extremely high dynamic range for textural and thermal contrast analysis under adverse seeing conditions. The enormous scope to remotely observe large areas needs to be offset by filtering for sub-pixel anomalies. This project will build a passive millimeter-wave (mm-wave) imaging polarimeter for identifying jarring discontinuities in thermal scene clutter. By using balanced methods of differential polarimetry, abrupt yet small changes of scene thermal noise and/or polarization irregularities are detectable at a sub-pixel level. This imager is meant to greatly enhance contrast for man-made novelties of changing scene radiance. It is intended for use by the U.S. Department of Energy's NA-22 mission programs and other United States Government agencies such as the Department of Defense, the Defense Intelligence Agency, and their operational entities.

The technical challenge of broad area search is timely coverage of large tracts of land or sea with sufficient spatial resolution and sensitivity to detect an anomaly (e.g., undeclared nuclear facility). As stated, the challenge is open-ended and one must define or put real numbers to terms such as "large tracts of land." To some extent, the values of these terms will be mission-specific. Still, one can construct a general argument as follows. Given a large area to search (the state of Nevada, 250,000 km<sup>2</sup>), what are the technology requirements to detect an anomaly (small uranium centrifuge facility, 1,000 m<sup>2</sup>)? At first glance it may appear that one needs spatial resolution on the order of 1,000 m<sup>2</sup> (about 30-m ground sample distance), but this is in fact misleading and will depend on what anomaly is being detected and the sensitivity of the sensor. For instance, thermal signatures can be used as anomaly indicators and with sufficient sensitivity, the physical structure representing the anomaly can be significantly smaller than the individual sensor pixel size. In the case given above, the enrichment facility occupies an area of approximately one part in a billion of the total area to be searched. For example, an imaging system with a spatial resolution of 1 km<sup>2</sup> may be plausible to search for a small enrichment facility, even though it occupies one one-thousandth of an individual pixel. To achieve this, the technical challenge is thus one of developing a sensor capable of detecting anomalies that occupy a small fraction of a pixel (sub-pixel)—that is, with sensitivity to the anomaly being orders of magnitude greater than sensitivity to other features.

This research addressed a passive, millimeter-wave-based imaging sensor specifically focused on broad-area search for cueing of more directed assets. A passive, mm-wave imager combines desirable attributes of both synthetic-aperture radar and passive hyper-spectral systems, such as all-weather operations and potentially extremely sensitive thermal imaging or emissivity-differential contrast identifications – useful, say, for quickly detecting metals covered with dust, paints, or camouflage fabrics. Millimeter-wave radiometers can also make sensitive measurements of polarization anisotropies such as is caused by liquid coatings or moisture on/in surfaces, or disturbances to the natural texture of soils and fields by repeated traffic. While a thermal- or polarization-change signature is not always indicative of specific operations, specificity must be sacrificed to achieve broad area searching capabilities. Once a search is narrowed to about 1 km<sup>2</sup>, a significant number of existing assets that are capable of site characterization can be cued.

The objective of this research was to develop a passive-imaging mm-wave polarimeter system that gives both real-time thermal contrast images and certain (Stokes) parameters of polarization analysis on-the-fly. The work began by developing an imaging 1D focal-plane radiometer-polarimeter system for doing scans of thermal and polarization changes. The target system (to be developed in future work) is

meant for deployment at stand-off ranges of 10 km or more. It is intended to passively map facility and effluent absolute temperatures and the extent of their thermal distributions, or provide persistent monitoring of facilities during bad weather (haze, dust, fog, moderate rain) and/or deliberate obscurations that would occlude infrared (IR) thermal imaging. The system will utilize advances in mm-wave imaging and on-the-fly correlation polarimetry in the 95-GHz range that are now practical for airborne surveillance. The goal for the target system's angular resolution was to achieve less than 5 mrad with 1-m-class antennas, and absolute temperature accuracy on the order of 1K. The goal for radiometric sensitivity to variances of surface or plume temperature was to reach better than 0.05 K/ $\sqrt{\text{Hz}}$  per pixel. The final demonstrator system permits exploration of the use of coherent differential correlations to highlight unusual polarization anisotropies, such as ellipticity changes due to sharp surface discontinuities, liquid spills/moisture on surfaces, or camouflaged metals. Monitoring quickly changing polarization correlations can cue man-made disturbances; they typically affect certain differential states of polarization. This would likely also improve on-the fly coherent sensing of aerosol plumes (and possibly their fallout patterns), and also discern disturbances of soil, etc., by observing subtle changes in upwelling radiated and reflected skyshine radiance. Detecting and cataloging how abrupt sub-pixel changes of temperature/emissivity can be seen in complex scenes was a parallel science effort of this work.

Achieving the project objectives required building several systems and numerous system components, some of which were incorporated into a system and some of which were used for stand-alone tests. For presentation purposes the project objectives and accomplishments have been described under the headings of Radiometer, Optics, Mechanics, Electronics, Software and Data Analysis, Calibration, Monocular System, Binocular Differential System, and Real-Time System Concept. Nevertheless, all the components of the systems are interactive, and in the course of research, elements were sometimes moved from one system to another. Thus the various report sections do not stand alone, and sometimes the decision of where to place certain information, or how often to repeat it, has been difficult and may seem arbitrary. A preliminary scan through the headings, figures, and tables should help the reader to gain an overview of the report and find the information of greatest interest. Appendices have been used to provide additional information such as definitions, presentations, and administrative details.

Demonstrated angular resolution of the single-reflector demonstrator system is 6.4 mrad. Its temperature sensitivity is given by a noise equivalent differential temperature (NEDT) of 0.2 K with a noise figure of 8.5 dB.

Figure 2.1 shows the monocular telescope in use; Figure 2.2 shows the binocular differential telescope in use.



**Figure 2.1.** Monocular Telescope in Use at Remote Hilltop Location



**Figure 2.2.** Binocular Differential System in Use on Scissor Lift at PNNL Grounds



## 3.0 Radiometer

### 3.1 Overview

The heart of the system is the radiometer, which is designed to perform full polarimetric radiometry, also referred to as polarimetry. It comprises passive and active microwave elements and is mounted integrally to the optical and mechanical systems. The optical elements focus energy representing a single mm-wave pixel onto the radiometer's receiver horn. The microwave elements separate this signal into its polarization components and convert it to a set of analog voltages that are digitized and recorded by the electronic and software subsystems. It is a heterodyne radiometer that produces a 6 GHz intermediate frequency (IF) with 4 GHz of bandwidth, resulting in an NEDT of less than 200 mK.

The radiometer specifications are as follows:

- Frequency range: 91–95 GHz
- Center frequency: 93 GHz
- Bandwidth: 4 GHz
- Local oscillator frequency: 87 GHz
- Lower sideband (reject): 79–83 GHz
- IF frequency: 4–8 GHz

The radiometer components are as follows:

- Ortho-mode transducer (OMT)
- Single-Pole Double -Throw (SPDT) waveguide switches
- Reference loads – use normal waveguide termination
- Low noise amplifiers (LNA)
- Isolators
- High-pass filters
- Mixers
- Phase shifters
- Magic-T splitter
- Gunn Oscillator (local oscillator; LO)

Details of these components are provided in Appendix D.

### 3.2 Theory and Design

The purpose of the radiometer is to detect the polarization components of the mm-wave signal and convert them to electrical signals that can be digitally recorded in order to form images.

The PMMW system was designed to study the phenomenology of passive millimeter-wave emissions and reflections from various man-made and natural environmental features. Polarimetric effects are of particular interest since these are expected to provide the greatest distinction between natural and manmade features. A fully-polarimetric radiometer was desired in order to measure the complete state of polarization, which contains all of the available information. The end application is for airborne remote sensing; however, the experimental radiometer does not need to scan quickly, because it will be used exclusively for ground-based field experiments of static scenes. These experiments can achieve a high signal-to-noise performance by using longer integration times, and correspondingly slower scanning. For these reasons, a mechanically scanned fully polarimetric radiometer was desired.

A center frequency in the W-band (75–110 GHz) near 94 GHz was chosen for several reasons. Components are widely available and at reasonable cost at this frequency range, including relatively high-performance low-noise amplifiers. Operation at this frequency is relatively insensitive to absorption from water. Finally, this frequency is high enough to allow reasonably wide bandwidths, good passive emission strength, and high angular resolution.

A fully polarimetric radiometer can be formed using outputs from a single antenna through the use of an OMT. This transducer can separate the received signal into horizontal and vertical polarized components. The Stokes Parameters can be defined in terms of the sampled electric field components (Collett, 2011)  $E_H$  and  $E_V$  as

$$\begin{aligned}
 I &= \langle E_V^2 \rangle + \langle E_H^2 \rangle \\
 Q &= \langle E_V^2 \rangle - \langle E_H^2 \rangle \\
 U &= 2 \operatorname{Re} \langle E_V E_H^* \rangle \\
 V &= 2 \operatorname{Im} \langle E_V E_H^* \rangle
 \end{aligned} \tag{3.1}$$

Six power measurements can be used to determine the Stokes Parameters. These measurements essentially sample the vertical, horizontal, 45 degree, and  $-45$  degree linearly polarized components and the left and right circularly polarized components and are defined as

$$\begin{aligned}
 T_V &= \langle E_V^2 \rangle \\
 T_H &= \langle E_H^2 \rangle \\
 T_{+45^\circ} &= \frac{1}{2} \langle (E_V + E_H)(E_V + E_H)^* \rangle = \frac{1}{2} \langle E_V^2 + 2 \operatorname{Re}(E_V E_H^*) + E_H^2 \rangle \\
 T_{-45^\circ} &= \frac{1}{2} \langle (E_V - E_H)(E_V - E_H)^* \rangle = \frac{1}{2} \langle E_V^2 - 2 \operatorname{Re}(E_V E_H^*) + E_H^2 \rangle \\
 T_r &= \frac{1}{2} \langle (E_V + jE_H)(E_V + jE_H)^* \rangle = \frac{1}{2} \langle E_V^2 - 2 \operatorname{Im}(E_V E_H^*) + E_H^2 \rangle \\
 T_l &= \frac{1}{2} \langle (E_V - jE_H)(E_V - jE_H)^* \rangle = \frac{1}{2} \langle E_V^2 + 2 \operatorname{Im}(E_V E_H^*) + E_H^2 \rangle
 \end{aligned} \tag{3.2}$$

The Stokes Parameters are then expressed as

$$\begin{aligned}
I &= T_V + T_H \\
Q &= T_V - T_H \\
U &= T_{45^\circ} = T_{-45^\circ} \\
V &= T_l - T_r
\end{aligned}
\tag{3.3}$$

A polarization combination radiometer measures the six power levels defined in Eq. (3.2). This can be accomplished using the architecture described by (Skou et al. 1999) and depicted in Figure 2 of that paper. This architecture coherently combines in-phase and quadrature samples of the horizontal and vertical components and then detects the resulting average power levels using power-law detectors.

The architecture used by Skou would be difficult to fabricate directly in W-band, so a heterodyne architecture was employed. A heterodyne architecture uses mixers to coherently down-convert the radiation at the higher frequency millimeter-wave band to a lower IF in the microwave range. Components are more widely available in the microwave range and can be connected using flexible coaxial cables, which are easier to use than rigid metallic waveguides.

In radiometer systems the input signal is very low power, on the order of nanowatts, and the signal can be very hard to distinguish from the noise in a single-ended detection system. Therefore, Dicke switching was employed in the design, to reduce or eliminate sensitivity to amplifier gain fluctuations and other sources of low-frequency drift. A Dicke-switched radiometer rapidly switches the input between a reference load  $V_{ref}$  and the antenna  $V_{ant}$  to allow narrowband lock-in amplifier techniques to sensitively detect only the difference between the load signal and the antenna signal. The switching frequency must be such that

$$f_{switch} \geq 2 * f_{gv}$$

where  $f_{switch}$  is the frequency applied to the W-band switches and  $f_{gv}$  is the highest significant frequency in the system gain variation spectrum. If this is the case, the system gain will be constant for comparing  $V_{ant}$  to  $V_{ref}$  for each cycle. The upper limit of the gain variation spectrum is assumed to be on the order of 10 Hz (Ulaby et al. 1981, p. 396), so a switching frequency of 1 kHz was selected, ensuring that the system gain fluctuations would have little to no effect on sensitivity.

The system specifications were chosen as follows:

Architecture:	Fully polarimetric, Dicke-switching, heterodyne, polarization combining radiometer
Center frequency:	93 GHz
Bandwidth:	2–4 GHz
Intermediate frequency (IF):	6 GHz
Local oscillator (LO) frequency:	87 GHz

A simplified schematic of the final design is shown in Figure 3.1. This radiometer design uses a feed horn with circular waveguide output coupled to an OMT. The horizontal and vertical components are then amplified, isolated, and bandpass-filtered prior to being mixed down to the IF using an 87-GHz Gunn oscillator coupled through adjustable phase shifters. After down-conversion to the IF, these signals are further amplified and filtered. After this conditioning the components pass through the polarization

combining network and are detected using six diode detectors. Not shown are six lock-in amplifiers used to sensitively detect the output at the Dicke-switching frequency.

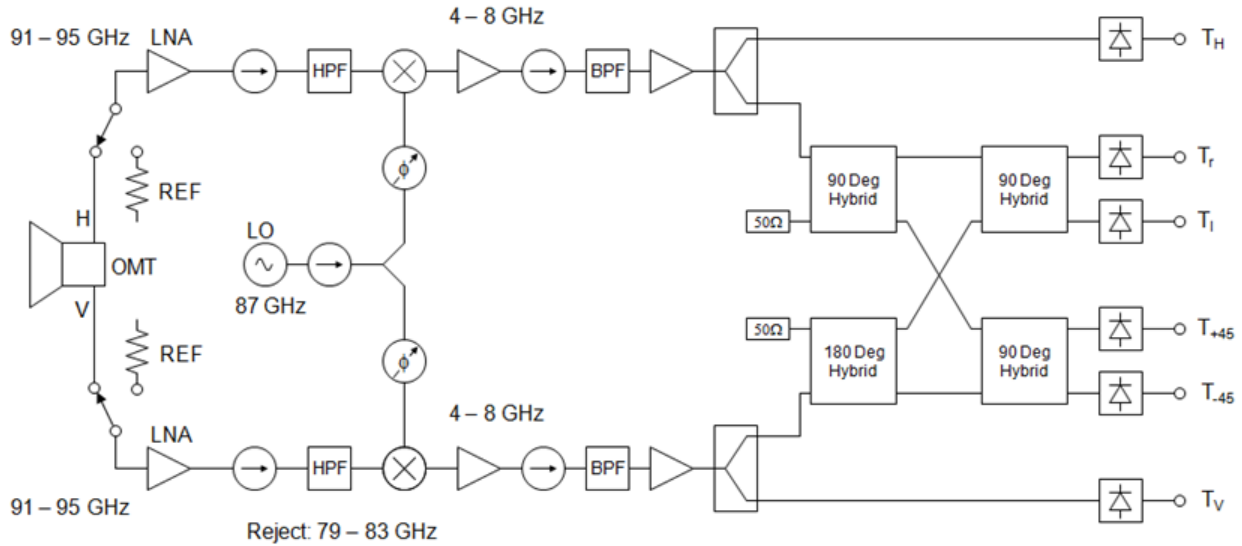


**Figure 3.1.** Simplified Schematic of the Fully-Polarimetric W-band Radiometer

The sensitivity of a Dicke switching radiometer can be expressed in terms of a NEDT. This NEDT is nominally,

$$NEDT = 2 \frac{T_R}{\sqrt{\tau B}} \quad (3.4)$$

where  $T_R$  is the noise temperature of the receiver,  $B$  is the bandwidth of the detected signal,  $\tau$  is the integration time, and the factor of 2 comes from only looking at the scene half the time. The noise temperature can be expressed as

$$T_R = (F - 1)T_0 \quad (3.5)$$

where  $F$  is the noise figure of the system and  $T_0$  is the nominal temperature. For our system, the noise figure is 8.517 dB which yields  $F= 7.107$ . Other parameters are nominally  $T_0 \approx 293$  K,  $B = 2 \times 10^9$  Hz, and  $\tau = 0.3$  sec. This yields an NEDT of 0.146 K.

The single and differential radiometers are somewhat different in design. The single radiometer, shown pictorially in Figure 3.2, is described first, briefly reiterating the description above. The front end of the radiometer is a circular horn, which preserves all of the polarization components. The horn is connected to an OMT, which splits the signal into horizontal and vertically polarized components. Each OMT output is connected via a rectangular waveguide to a Dicke switch, which switches between the input signal and a reference load, in order to minimize the effects of amplifier drift. One of the waveguides has a 90-degree twist to provide the correct polarization for the remaining stages. After the Dicke switch are a low-noise amplifier and high-pass filter, followed by a mixer connected to an 87-GHz

local oscillator. The 4–8 GHz signal is further amplified and band-pass filtered. A final amplification stage is followed by a network of 90-degree and 180-degree hybrid couplers to extract the circular and diagonal polarization components.

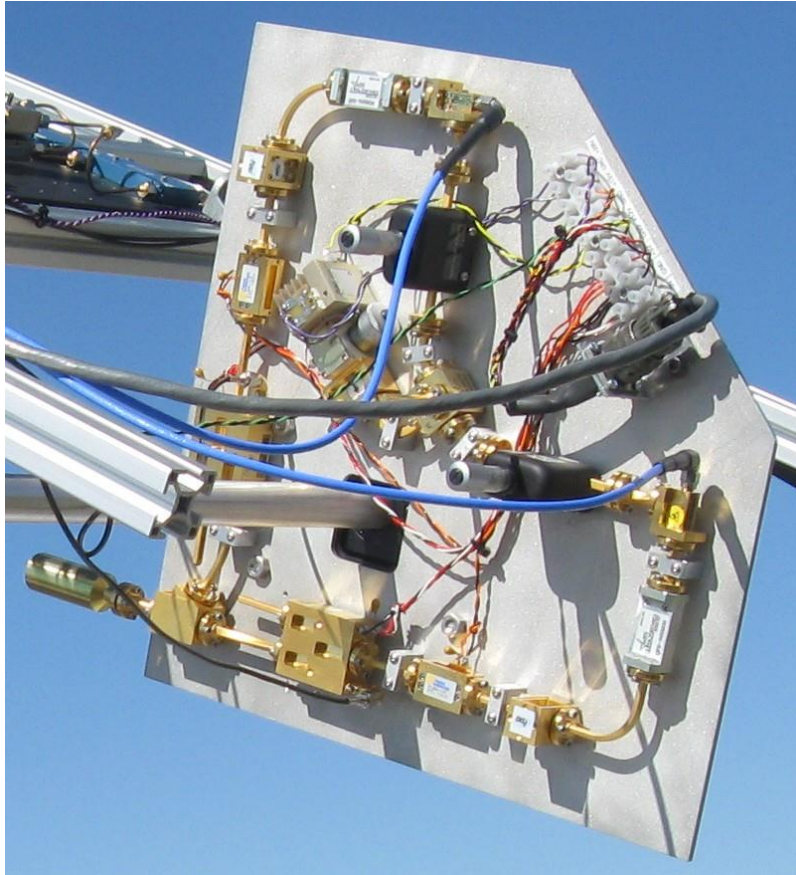


**Figure 3.2.** Radiometer as Mounted on Monocular Telescope

In order to carry out phenomenological studies, a fully polarimetric design is needed. The W-band (75–110 GHz) was selected as a band that provides high resolution and good sensitivity, and for which components are available. A desire for design simplicity motivated the polarization combination network, using heterodyne architecture. Dicke switches between the antenna and a reference load are used to minimize gain fluctuations and drift.

The critical components are the conical horn antenna and circular waveguide; the W-band low-noise amplifiers, and the local oscillator. The antenna is matched to the 50-cm reflector with an edge taper of approximately  $-12$  dB. The low-noise amplifiers, from Farran Technologies, have a 5.0 dB noise figure. The local oscillator, from HXI, is a temperature-stabilized 87-GHz Gunn-diode design with an integral isolator.

The radiometer is designed for compactness. The H and V path lengths are minimized and matched. In the IF stage, line stretchers are used to fine-tune path lengths for phase matching.

The dual radiometer differs from the single-antenna radiometer in using the second antenna, instead of a static load, for the reference signal. A photograph is shown in Figure 3.3. A block diagram is shown in Figure 3.4.

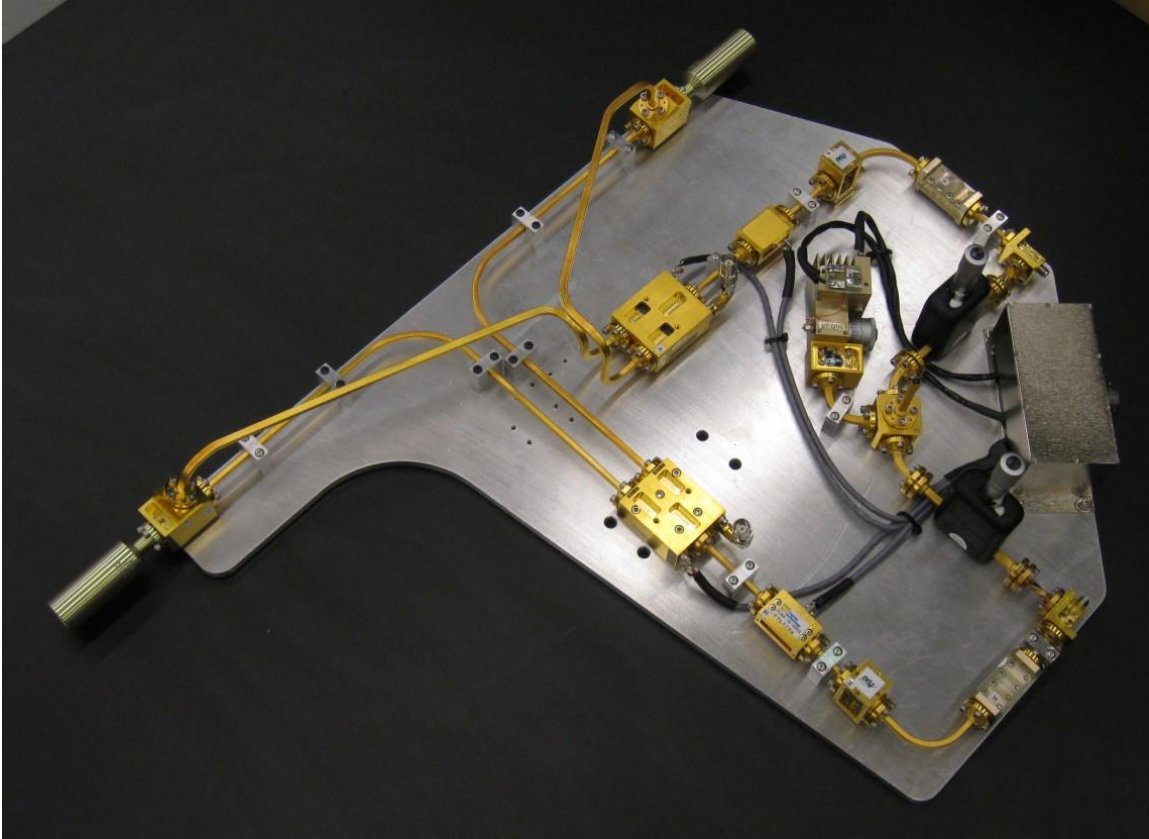


**Figure 3.3.** Dual Radiometer Photograph

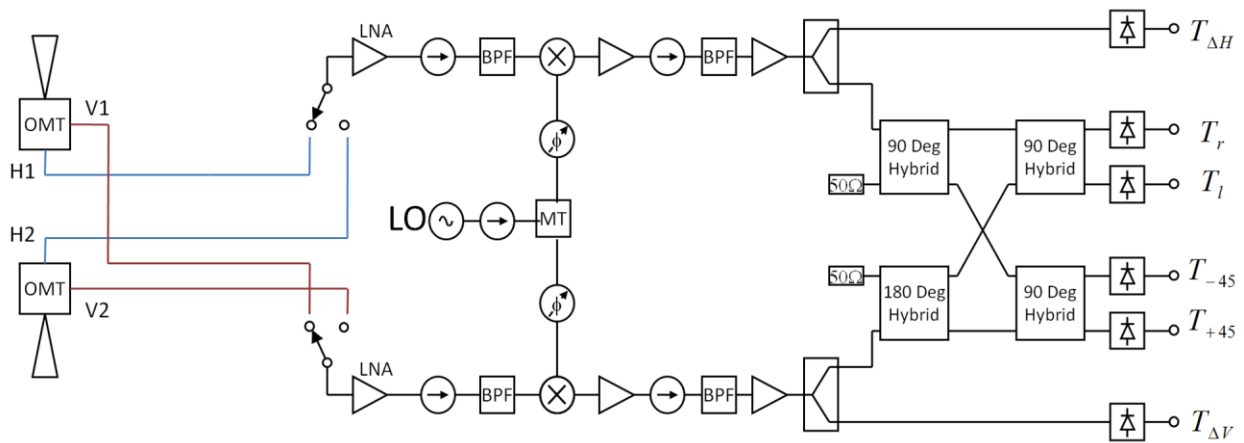


**Figure 3.4.** Dual Radiometer Block Diagram

### 3.3 Development

Millimeter-wave polarimeter designs were studied from various design configurations in the open literature. Based on this literature search, a design trade study was conducted to determine the optimum single channel polarimeter design to meet the phenomenology research needs of Phase I. The polarimeter design is shown previously in Figure 3.1; it is called a Millimeter-wave Heterodyne Polarization Combination Radiometer. This polarimeter provides all four Stokes parameters, as described earlier. It uses LNAs and Dicke switches in the radiometer front end (left side) to optimize measurement sensitivity. Some of the other polarimeter designs did not provide all four Stokes parameters or the front-end sensitivity. One downside to this design, however, is the limited bandwidth of the polarizing combining network shown after the mix-down to the IF. Other millimeter wave polarimeter designs that were studied include Millimeter-wave Parallel Receiver Polarization Combining Radiometer and Millimeter-wave Heterodyne Correlation Radiometer.

Because the Millimeter-wave Heterodyne Polarization Combination Radiometer (mm-wave HPCR) provides all four Stokes parameter, this design was used in Phase I to determine the most useful Stokes parameter(s) for broad area novelty search, allowing us to tailor our polarimeter and array designs in future Phases II and III to the most sensitive polarimeter imaging system.

Commercial vendors and millimeter-wave components to fabricate this system were identified. Some of these components had lead times of two to four months, and one was an international purchase (from Ireland), all of which slowed the initial construction. Although many of the components were in the vendor catalog, they were not “on-the-shelf” and had to be fabricated when ordered. The LNA from a company in England was not delivered by the time all other components were received. However, we purchased an alternative LNA from another vendor that was used to fabricate the polarimeter prototype and perform preliminary measurements until the better-quality LNA came in from the Farran Technologies.

One critical component that determines the overall polarimetric system performance is the OMT. In our initial vendor search for this component, we were unable to obtain commercial OMTs with cross-polarization (cross-pol) isolation of  $-40$  dB. However, we were able to locate an OMT with excellent cross-pol isolation from the National Radio Astronomy Observatory and we received rapid delivery of it. This OMT, according to our test measurements, met the cross-pol isolation performance that we needed. Several spares were purchased after we confirmed that their OMT met our needs. In the future, another source will be needed, since they are no longer producing this component. A pictorial diagram of the radiometer front end is shown in Figure 3.5.

The Microwave Polarization Combining Network shown on the right side of the block diagram design (after the mixers in Figure 3.1) was assembled and tested in the laboratory. This network provides all four Stokes parameters when combined with the Dicke Switching Heterodyne front end.

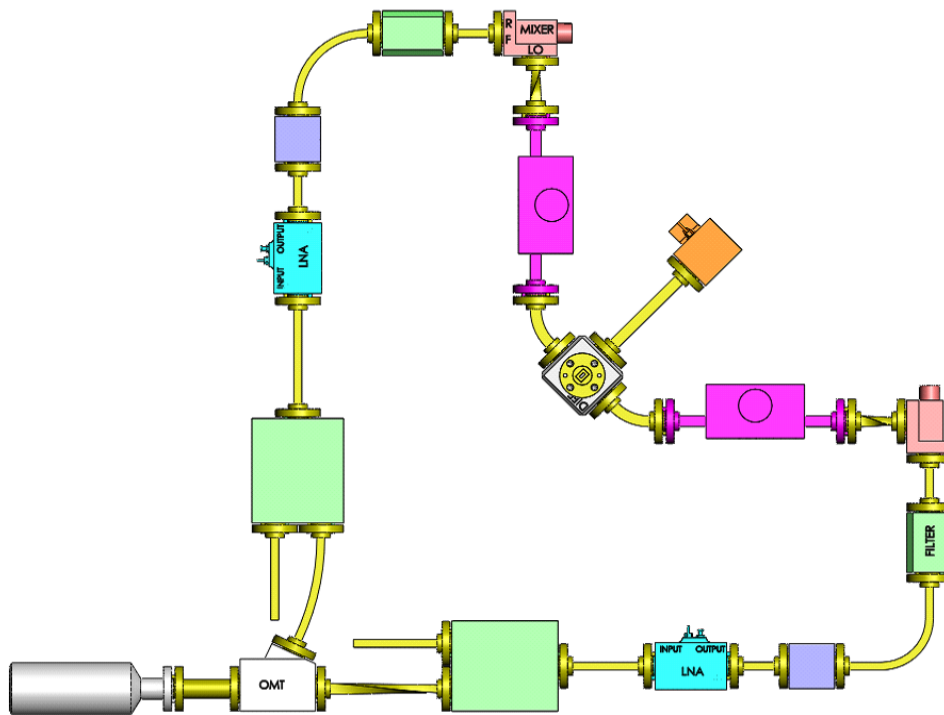


**Figure 3.5.** Polarimeter Network: Labeled Pictorial Diagram

Figure 3.6 shows the initially configured mm-wave HPCR system. Six FEMTO lock-in amplifiers are used in the system. All six channels of the mm-wave HPCR were tested and have good response. The H and V channels are both very responsive and have about the same sensitivity.

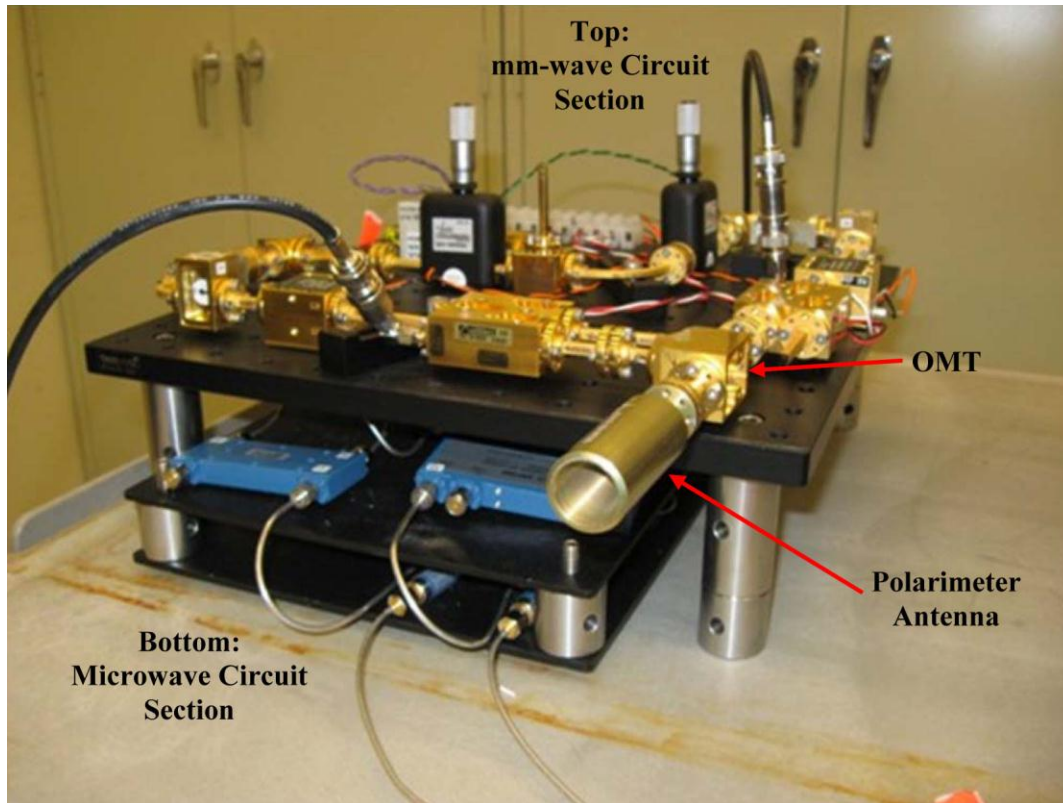


**Figure 3.6.** Configured mm-wave HPCR System

The radiometer as mounted in the telescope is shown in Figure 2.1 and in more detail in Figure 3.2.

This research was targeted toward downward-looking aerial surveillance. It was challenging to mimic these conditions in terrestrial experiments. Lifts and mountainsides were used to achieve some elevation for field imaging. Imaging studies using the monocular system included assessing system resolution, sensitivity, and phenomenology. Elevated imaging with the differential radiometer system using a scissor lift platform was performed in 2011. The best polarimetric signatures are expected at fairly high depression angles (45 to 60 degrees below flight line). At present we can cost-effectively obtain 30° to 45° depression angles with the scissors lift, and less than 20° using natural scenes from hillside vantages. A calibration matrix for the differential radiometer system was planned, in order to pull out the much weaker signatures obtained at lower depression angles less than 45°, but additional equipment needed to develop this matrix would have been prohibitively expensive, and so it was not developed.

Throughout the project, we developed collaborative relationships with Universities, National Aeronautics and Space Administration (NASA), other government labs (National Institute of Standards & Technology; NIST) and industry to obtain and evaluate state-of-the-art front-end hybrid components and partial radiometric modules that fully integrate the electronics with waveguide feeds and OMTs. We looked at making 1D or 2D focal plane arrays using compact mm-wave versions of microwave monolithic integrated circuit (MMIC) chips as one option to increase the rate of sensor imaging. Alternatively, a more complete method to do full polarimetric imaging is with correlation interferometry,

but the electronics required to do traditional correlations would be expensive and daunting to ‘plumb’ with RF-waveguides. Our team identified a novel method to do optical correlations that would scale more effectively for large arrays and is quite cost effective. We engaged in a collaboration to do optical signal conversion of the mm-wave energy using telecom upconversion techniques in fiber optical systems.

We collaborated with University of Delaware and Phase Sensitive Innovations to investigate optical up-conversion methods for coherent phased arrays and all-optical signal processing. Dr. Dennis Prather and John Wilson from the University of Delaware visited Pacific Northwest National Laboratory (PNNL) in late June 2011 and gave an extensive presentation on their work.

We investigated 4- to 8-element millimeter-wave focal plane arrays in collaboration with HRL Laboratories and NIST using their proprietary designs.

Two PNNL staff members attended the 2009 International Microwave Symposium in Boston to review microwave and millimeter-wave component research developments, consult with millimeter-wave component vendors, and to initiate collaborative relationships with universities, NASA, other government laboratories, and industry.

## **3.4 Performance Evaluation of Heterodyne Dicke Switching Radiometer**

### **3.4.1 Component and Section Performance Evaluations**

Performance evaluation began at the component level, verifying that each component performed according to vendor specifications, in order to accurately characterize the noise figure of our W-band system. The instrument used to verify system performance was an Agilent Technologies vector network analyzer, which has W-band port extensions on it, allowing for 75- to 110-GHz S-parameter measurements. A two port w-band calibration was performed, isolating the bandwidth of interest for our radiometer, 91 to 95 GHz, measuring system reflections,  $S_{11}$ , down to -80dB . Providing a good calibration allowed us to accurately characterize both the individual performance of our W-band components and their interaction with each other on a system level.

The critical components in the W-band system that would significantly contribute to the noise figure are the single-pole double-throw electronic switch (SPDT), the low-noise amplifier (LNA), and the mixer. To characterize the noise figure of the SPDT, it is necessary to perform an  $S_{11}$  and  $S_{21}$  measurement for both input ports on the SPDT. The switch is driven by a transistor-transistor logic (TTL) signal, which, on the radiometer, is a square wave with a 2.5 V peak-to-peak (p-p) amplitude and a frequency of 1 kHz. For the performance evaluation, a constant voltage was applied to the TTL input to measure the reflection, transmission, and isolation for a single port, then connect the W-band module of the vector network analyzer (VNA) to port 2 on the SPDT and repeat the measurements. The performance results measured on the SPDT were as follows:

- reflection: -14 to -8 dB
- isolation: 20 dB

- transmission loss:  $-2.6$  dB

The contributed noise figure from the switch is equal to the transmission loss through the switch, and therefore the noise factor of the SPDT is 2.6 dB. This is of particular note because the noise figure of the system contributes to the overall sensitivity of the radiometer.

Measurements for the LNA were also performed using the previous calibration file, and the gain of the LNAs was verified by adjusting the attenuation on the W-band modules. The measured gain across the bandwidth of interest was  $27.2 \pm 0.5$  dB. A noise figure measurement of a W-band LNA requires a precise noise-figure measurement system, and unfortunately we were unable to perform this measurement to verify the noise figure performance of the Farran W-band LNAs due to lack of equipment in house. The vendor's listed noise figure of the amplifier across our bandwidth is 4.5 dB.

The performance characteristics of interest for the W-band mixer are conversion loss and reflection. Because our mixer is not powered, it requires a bias provided by the local oscillator (LO) signal. An LO signal having an amplitude greater than 12 dBm is required to drive the mixer diodes. The specified and claimed insertion loss by the manufacturer was 8.5 dB. Insertion loss was measured and characterized by using the W-band module of the VNA to provide the radio-frequency (RF) signal at a measured power level using a calibrated W-band power meter. Next, the LO was driven by the Gunn oscillator to be used for the radiometer system. The IF signal was measured using a real-time spectrum analyzer covering the center frequency of the bandwidth of interest. The measured reflected signal for the mixer was on the order of  $-6$  dB with a conversion loss of 9.5 dB.

The noise contributed by the passive components in the W-band system can be equated to the insertion loss associated with each of the devices. The measured noise figure is on the order of 0.2 dB for the OMT, 0.7 dB for the filter, and 0.5 dB for the isolator, in addition to waveguide losses. The loss associated with WR-10 waveguide at 90 GHz is 2.69 dB/m, according to Microwaves101.com [<http://www.microwaves101.com/encyclopedia/waveguideloss.cfm>]. The noise figure of cascading amplifiers can be calculated using the Friis formula (McClaning et al. 1959),

$$F = F_{p1} + \frac{F_{p2} - 1}{G_{p1}} + \frac{F_{p3} - 1}{G_{p1}G_{p2}} + \dots + \frac{F_{pn} - 1}{G_{p1}G_{p2}\dots G_{pn}} \quad (3.6)$$

This formula yields a noise figure 8.517 dB for the mm-wave section of the radiometer. It is generally assumed that the noise figure contributions from components after the first amplifier are not significant, because the noise from the components before the amplifier has a gain factor of 100–1000 times the noise downstream.

Once each of the W-band components was characterized, full system measurements were performed to phase-match the horizontal and vertical mm-wave sections of the radiometer. Phase matching was performed using the complete assembly of the mm-wave section of the radiometer minus the corrugated feed horn. The phase was measured from the input to the OMT to the waveguide flange just before the mixer, using the Agilent VNA. The phase was characterized by setting a single electrical delay for the horizontal channel; setting the electrical delay allowed for viewing the phase across the relevant bandwidth in a more linear way. Then keeping this same electrical delay, the phase associated with the vertical channel was measured. Phase differences were accounted for by adding W-band shims into the

channel that was behind in the phase measurement. Note that a phase shifter could not be used because the electrical delay associated with a phase shifter is not linear with frequency, and therefore it is not useful in trying to match the phase across a wide bandwidth. The maximum phase difference between the horizontal and vertical channels measured across the 2 GHz of bandwidth was 10 degrees. Note that the non-linearity of the phase response across the given bandwidth is due to the non-linearity in the mm-wave devices. Also of interest for the horizontal and vertical channels are their total respective gains. However, since the focus of this radiometer is fully polarimetric measurements, phase matching is prioritized above power matching. Gain inconsistencies can be accounted for and adjusted in calibration matrices after signal detection. The power-level variation between the horizontal and vertical channels was measured using a spectrum analyzer and matched using microwave attenuators to 0.1 dB.

After the phase was matched in the mm-wave arms for the RF signal, the 87-GHz LO signal needed to be matched for both the horizontal and vertical LO arms. This was done using the same method used for matching the phase in the horizontal and vertical mm-wave RF sections of the radiometer. The tolerance achieved for phase matching in the LO section was 1 degree, which is quite good.

Performance evaluation of the microwave section components was performed to verify that they met the manufacturer's specifications. This evaluation was performed using an Agilent Technologies VNA. Calibration sets were created for the bandwidth of interest. The components in the microwave section are medium power amplifiers, filters, isolators, splitters, 90° phase shifters, 180° phase shifters, and detectors. As discussed in the previous paragraphs, noise figure contributions from components after initial amplification are negligible, and therefore the noise contribution of the microwave section was not characterized.

Gain and phase measurements were performed on the first part of the microwave section, which includes the amplification filtering and isolation. These set of measurements were straightforward, using a single electrical delay and signal amplitude that would not saturate the series of amplifiers. The filters were verified as having a pass band of 5–7 GHz. The power was matched between the horizontal and vertical channel to 0.1 dB by inserting microwave attenuators.

The second section of the microwave portion of the radiometer is the phase combination network, shown in the block diagram in Figure 3.7.

The phase-combination network recombines the horizontal and vertical signals using phase-shifting hybrids. The recombined signals allow for the extraction of the polarization signatures included in the total brightness temperature.

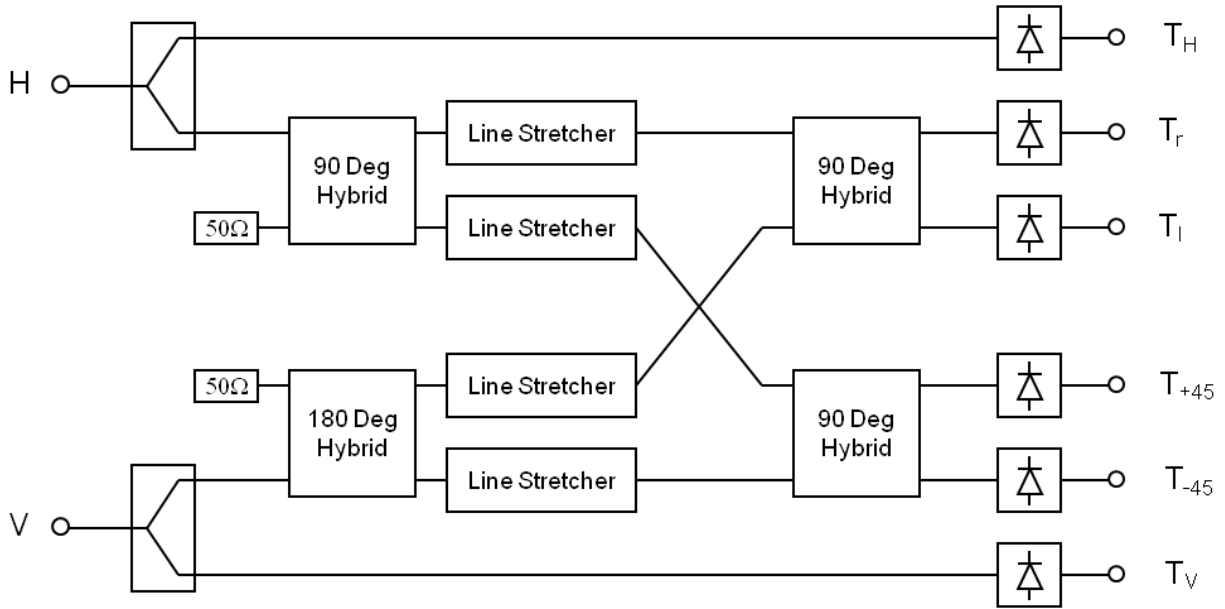


**Figure 3.7.** Block Diagram of the Phase Combination Network

The phase accuracy of the 90° and 180° hybrids is listed to 3°; using line stretchers between the series of hybrids to perform fine phase adjustments, the assumed accuracy limitation was 3°. Matrices characterizing each hybrid were developed and used to arrange the order and interconnections of the phase-matching network. The hybrid matrices and resulting phase relationships for H and V for each of the four recombined signals are as follows:

$$\frac{1}{\sqrt{2}} \begin{vmatrix} 0 & 1 & j & 0 \\ 1 & 0 & 0 & j \\ j & 0 & 0 & 1 \\ 0 & j & 1 & 0 \end{vmatrix} \quad 90^\circ \text{ hybrid}$$

$$\frac{1}{\sqrt{2}} \begin{vmatrix} 0 & 1 & -1 & 0 \\ 1 & 0 & 0 & -1 \\ 1 & 0 & 0 & 1 \\ 0 & 1 & 1 & 0 \end{vmatrix} \quad 180^\circ \text{ hybrid}$$

$$T_r = \frac{1}{2}(V_H + jV_V) \quad (3.7)$$

$$T_l = \frac{1}{2}(jV_H + V_V) \quad (3.8)$$

$$T_{+45} = -\frac{1}{2}(V_H + V_V) \quad (3.9)$$

$$T_{-45} = -\frac{j}{2}(-V_H + V_V) \quad (3.10)$$

Using the Agilent Technologies VNA and a constant electrical delay, the phases were measured for each of the channels. The test arrangement is shown in Figure 3.8. The phase was adjusted and optimized for each channel using the microwave line stretchers.

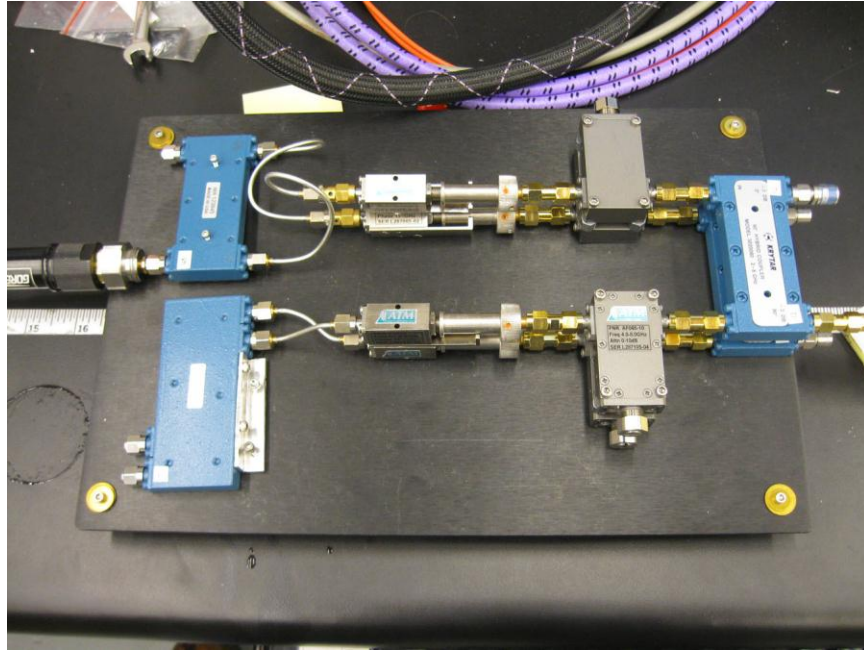


**Figure 3.8.** Microwave Phase Combining Network Test Arrangement

The theoretical and measured values for the microwave phase combination network are given in Table 3.1, showing very good agreement.

**Table 3.1.** Microwave Phase Combining Network Phase Measurement Results

	$V_V$		$V_H$	
	Calculated	Measured	Calculated	Measured
$T_l$	0	-1.93	90	89.95
$T_r$	90	90.02	0	1.82
$T_{+45}$	180	179.12	180	-178.38
$T_{-45}$	-90	90.37	90	90.046

### 3.4.2 Radiometer System Performance Evaluation

After all the components and sections were evaluated, the system was evaluated as a whole. This was done by combining the mm-wave and microwave sections, detecting the output, and comparing the input

signal to the reference loads at the lock-in amplifiers. The parameters of interest in particular with a fully polarimetric Dicke switching radiometer are the isolation between the polarization channels. The Dicke switching radiometer design is intended to cancel the gain fluctuations that occur in the system. Absolute power measurements were not performed, but rather power measurements of each channel relative to other channels, in order to determine isolation. The network analyzer was used as a transmission source in conjunction with a linear W-band horn to measure the linear polarization channels, and with a coherent circular polarization generator to verify performance of the circular polarization channels.

Shown below are the performance measurements for all six channels of the radiometer. The radiometer is given three different polarizations as input, targeting specific channels. Note that H and V were not presented, due to their isolation being set by the OMT and being greater than 40 dB, and that the circular polarization source presents only right-hand circularly polarized signals.

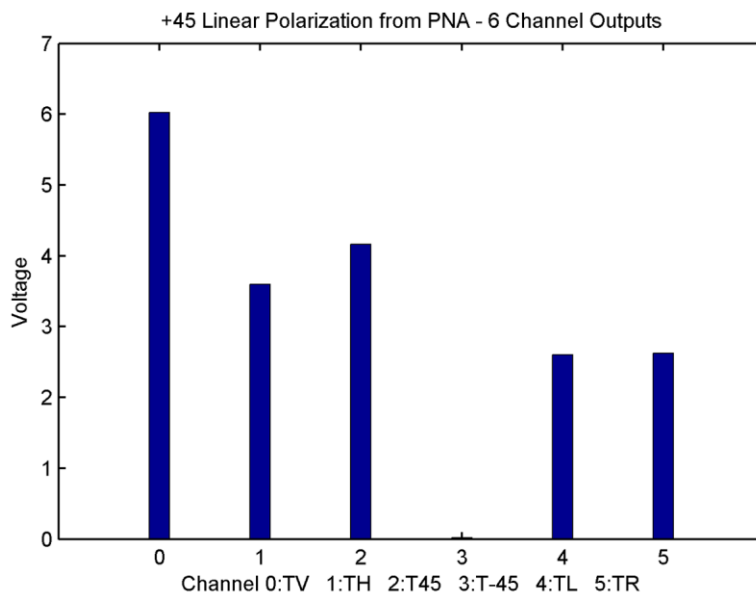


**Figure 3.9.** Radiometer Response to a +45° Signal

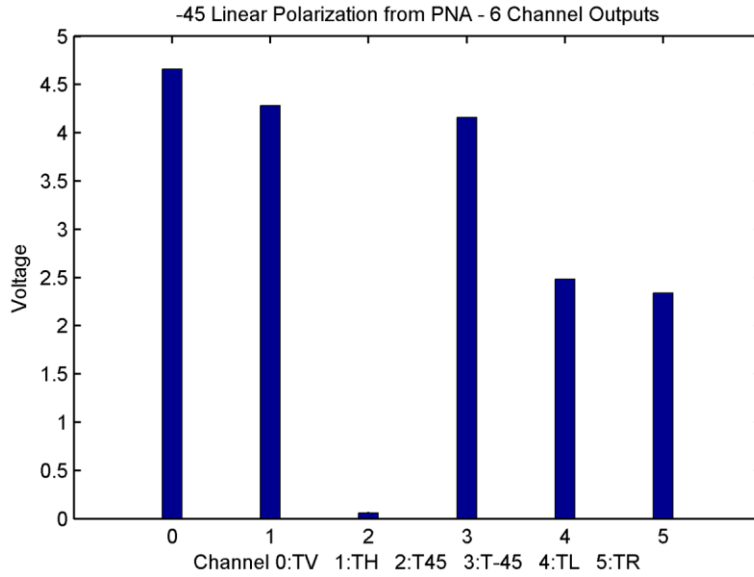


**Figure 3.10.** Radiometer Response to a  $-45^\circ$  Signal

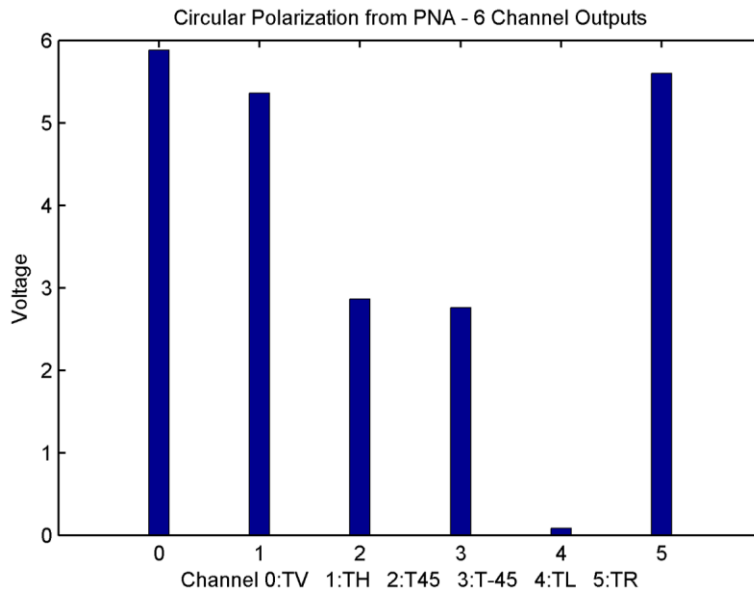


**Figure 3.11.** Radiometer Response to a Right-Hand Circularly Polarized Signal

Note the nulling of the channel that is complementary to the presented signal. There is good isolation between polarization sets. Note that the vertical and horizontal channels are (overall) stronger than the other channels. This is because the H and V channels do not travel through the hybrids, line stretchers, and variable attenuators, and thus have roughly 9 dB less loss.

In light of the responses in the six channels with respect to the polarization of the presented signal, the radiometer was determined to have sufficient isolation and polarization distinction and was deployed for field testing.

### 3.5 Differential Radiometer Performance Testing

The differential radiometer was constructed using a design platform similar to the original Dicke switching radiometer.

#### 3.5.1 Millimeter-Wave Section

The differential radiometer employs the same mm-wave section components after the switches and uses the same microwave phase combination network. However, the mm-wave design prior to the switches consists of two inputs each, for both the horizontal and vertical, comparing the detected brightness temperatures received by the two inputs. The design of the differential radiometer front end is shown in Figure 3.12.

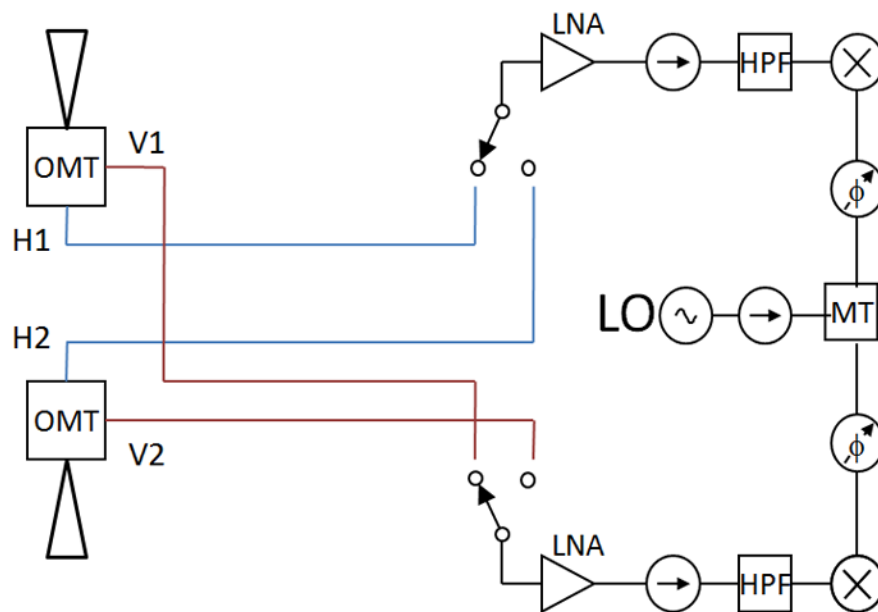


**Figure 3.12.** Differential Radiometer Front End

The system performance parameters of concern are phase matching between the horizontal channels (H1 and H2) and their corresponding vertical channels (V1 and V2), matching of the power between both horizontal and both vertical arms, and system noise temperature. The noise temperature is of significance because the noise figure of the system contributes to the overall sensitivity of the radiometer.

It is important to note that since the signal subtraction is occurring post detection at the lock-in amplifier level, the subtraction is incoherent, meaning it does not take phase into account. Therefore, matching the phases between the horizontal channels or between the vertical channels is not necessary.

Power matching between the horizontal channels and between the vertical channels is necessary for subtraction; that is, it is necessary that 0 volts in H1 correspond to 0 volts in H2. However, the power offsets can be removed after signal detection via calibration matrices.

The testing performed on the differential radiometer began at the component level, characterizing each component to ensure that it met manufacture specification and measuring its noise figure. The mm-wave components that were characterized are the OMT, SPDT, LNA, isolator, high-pass filter (HPF), mixer, and W-band waveguide. All components were provided by the same manufacturers as in the single-ended radiometer design described in Section 3.2, and were characterized using the same methods. The noise figures for most of the devices are equal to their insertion losses.

The critical components in the W-band system that would significantly contribute to the noise figure are the SPDT, the LNA, and the mixer. To characterize the noise figure of the SPDT, it is necessary to perform an  $S_{11}$  and  $S_{21}$  measurement for both input ports on the SPDT. The switch is driven by a TTL signal: a square wave with a 2.5 V p-p amplitude and a frequency of 1 kHz. For the performance evaluation, the SPDT was biased to the channel under test to measure the reflection, transmission, and isolation for a single channel. The SPDT was connected to the W-band module of the VNA, using a W-band calibration for our bandwidth of interest. S-parameter measurements were taken for both switch inputs. The performance results measured on the SPDT were as follows:

- reflection:  $-16$  to  $-8$  dB
- isolation: 21.7 dB
- transmission loss:  $-2.61$  dB

The contributed noise factor from the switch is equal to the transmission loss through the switch, and therefore the noise factor of the SPDT is 2.61dB.

Measurements for the LNA were also performed using the calibration file previously used on the original radiometer, and the gain of the LNAs was verified by adjusting the attenuation on the W-band modules. The measured gain across the bandwidth of interest was  $27.7 \pm 0.5$  dB. A noise figure measurement of a W-band LNA requires a precise noise figure measurement system, and unfortunately we were unable to perform this measurement to verify the noise figure performance of the Farran W-band LNAs, due to our not having the equipment needed to perform noise figure measurements. The vendor's listed noise figure of the amplifier across our bandwidth is 4.5 dB.

The performance characteristics of interest for the W-band mixer are conversion loss and reflection. Since our mixer is not powered, it requires a bias provided by the LO signal. An LO signal having an amplitude greater than 12 dBm is required to drive the mixer diodes. The specified and claimed insertion loss by the manufacturer was 8.5 dB. Insertion loss was measured and characterized by using the W-band module of the VNA to provide the RF signal at a measured power level using a calibrated W-band power meter. Next, the LO was driven by the Gunn oscillator to be used for the radiometer system. The IF signal was measured using a real-time spectrum analyzer viewing the center frequency of the bandwidth of interest. The measured reflected signal for the mixer was on the order of  $-6$  dB with a conversion loss of 9.5 dB.

The noise figure contributed by the passive components in the W-band system can be equated to the insertion loss associated with each of the devices. The measured noise figure is on the order of 0.2 dB for

the OMT, 0.51 dB for the filter, and 0.4 dB for the isolator, in addition to waveguide losses. The loss associated with WR-10 waveguide at 90 GHz is 2.69dB/m according to Microwaves101.com. The noise figure of cascading amplifiers can be calculated using the Friis formula (McClaning et al. 1959),

$$F = F_{p1} + \frac{F_{p2} - 1}{G_{p1}} + \frac{F_{p3} - 1}{G_{p1}G_{p2}} + \dots + \frac{F_{pn} - 1}{G_{p1}G_{p2}\dots G_{pn}} \quad (3.11)$$

This formula yields a noise figure of 9.12 dB for the mm-wave section of the radiometer. It is generally assumed that the noise figure contributions from components after the first amplifier are not significant, because the noise from the components before the amplifier has a gain factor of 100–1000 times the noise downstream; however, the noise figures from all the mm-wave components and waveguide are taken into account. The reason that the noise figure of the differential radiometer is higher than the original radiometer is the long waveguide path length upstream of the LNA, which causes the noise figure contributions of the long waveguide sections to be amplified, giving them a significant impact on the system’s noise figure.

Once the components of the mm-wave section were characterized and the noise figure calculated, the phases and powers were matched between the two horizontal and two vertical channels. The challenge in matching both the phase and power across a given bandwidth is that any shims inserted to cause a full-band linear phase shift will also cause additional loss; therefore, achieving both equal phase and equal power was nearly impossible for all channels. The power for each channel was matched as well as possible, but the phase was chosen as the key parameter, due to the fully polarimetric nature of the differential radiometer. The test arrangement for measuring both the power and the phase for the horizontal and vertical channels is shown in Figure 3.13. Note that the images show measurements only for OMT 1; a similar arrangement was used for OMT 2.

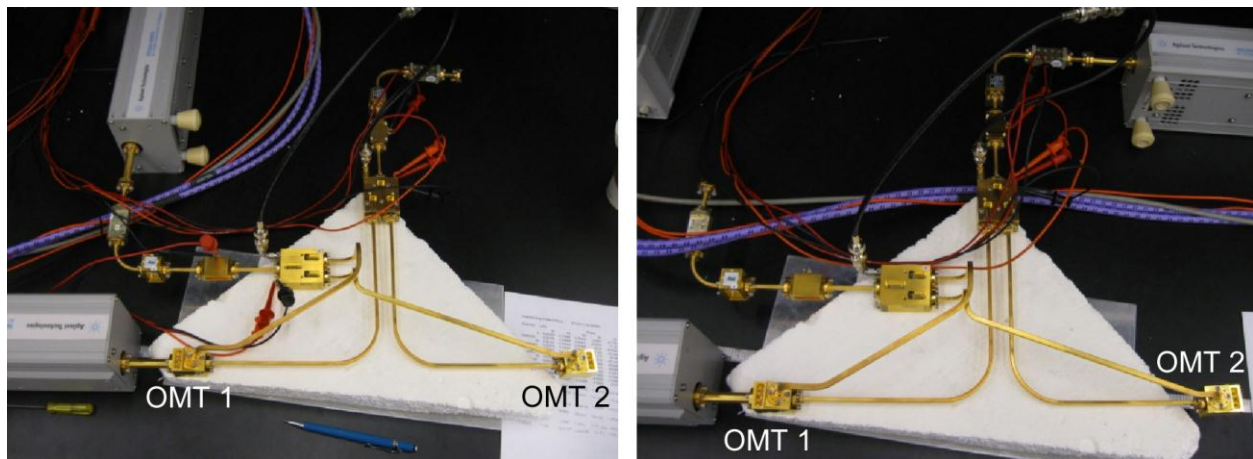


**Figure 3.13.** Horizontal and Vertical Channel Measurements for OMT 1. Horizontal setup at left, vertical setup at right.

The power and phase relationships required for incoherent differential fully polarimetric measurements are as follows, where  $S$  refers to the signal power,  $\varphi$  refers to phase, and subscripts 1 and 2 refer to OMT 1 and 2, respectively.

$$\begin{aligned}
 S_{H1} &= S_{H2} \\
 S_{V1} &= S_{V2} \\
 \varphi_{H1} &= \varphi_{V1} \\
 \varphi_{H2} &= \varphi_{V2}
 \end{aligned}
 \tag{3.12}$$

Since the differential measurements are not coherent, meaning the subtraction does not take phase into account, and takes place post signal detection, it is necessary only to match the phases within the respective OMTs, H1 to V1 and H2 to V2, and it is not necessary to match H1 to H2 and V1 to V2. The resulting phase and power measurements, after adding W-band shims into each line to minimize the phase and power differences, are shown in Figures 3.14 through 3.17. The frequency band of interest is 92–94 GHz, as indicated by the vertical dashed lines. The horizontal dashed lines indicate the minima and maxima over that band.

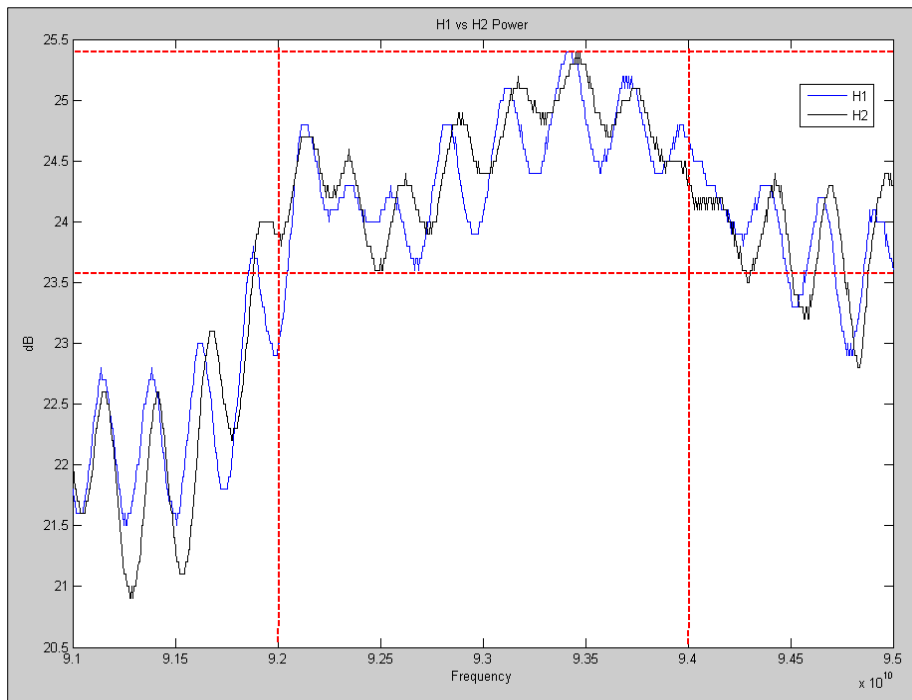


**Figure 3.14.** Horizontal Channels: Power Measurement Comparison—H1 average over associated bandwidth: 24.15 dB; H2 average over associated bandwidth: 24.27 dB

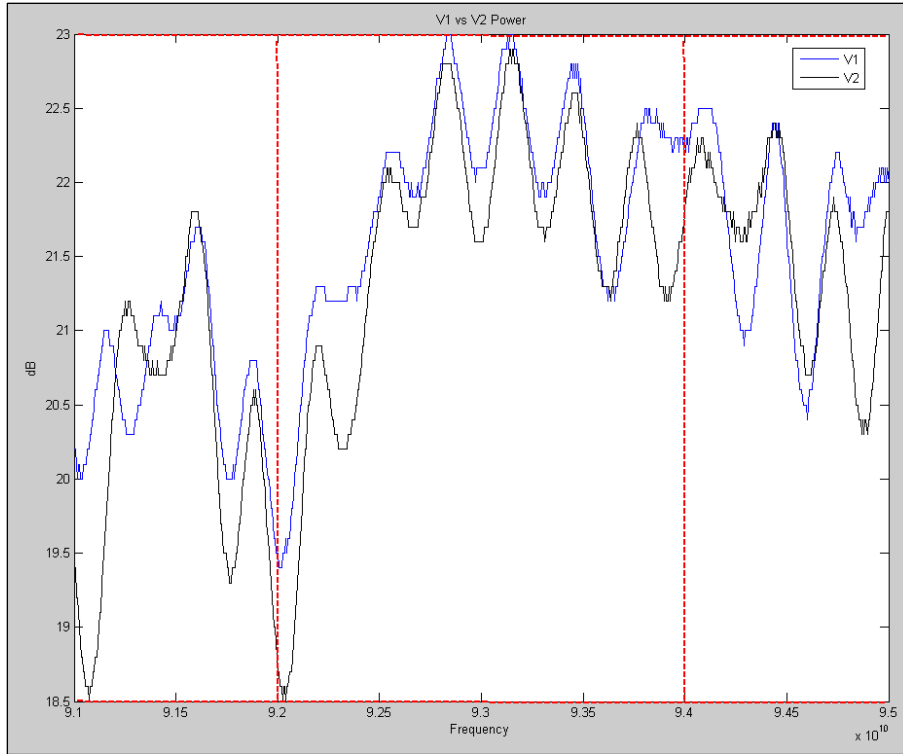


**Figure 3.15.** Vertical Channels: Power Measurement Comparison—V1 average over associated bandwidth: 21.61dB; V2 average over associated bandwidth: 21.16dB

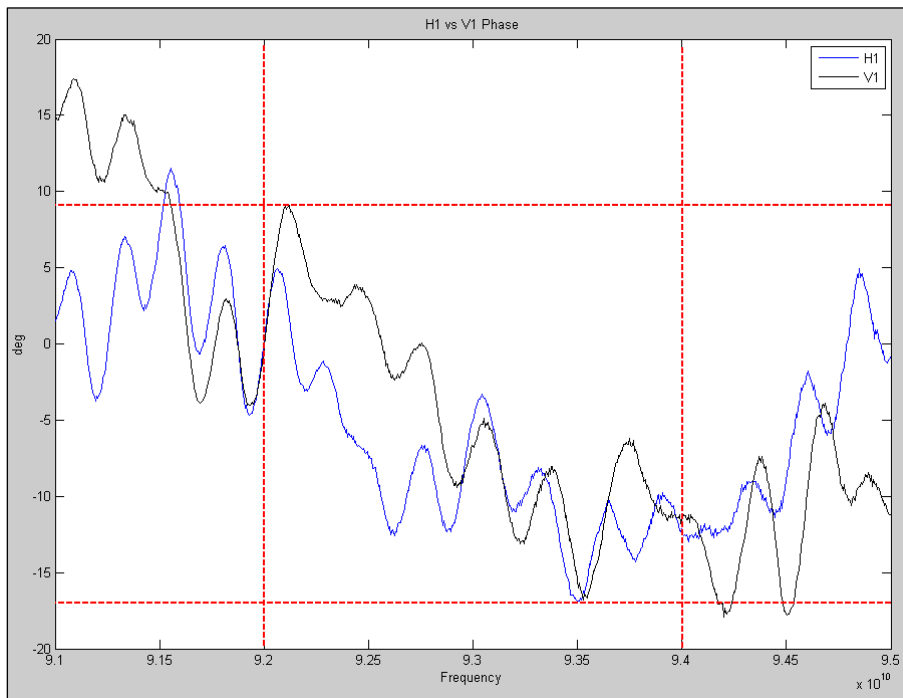


**Figure 3.16.** OMT 1, H and V Phase Comparison

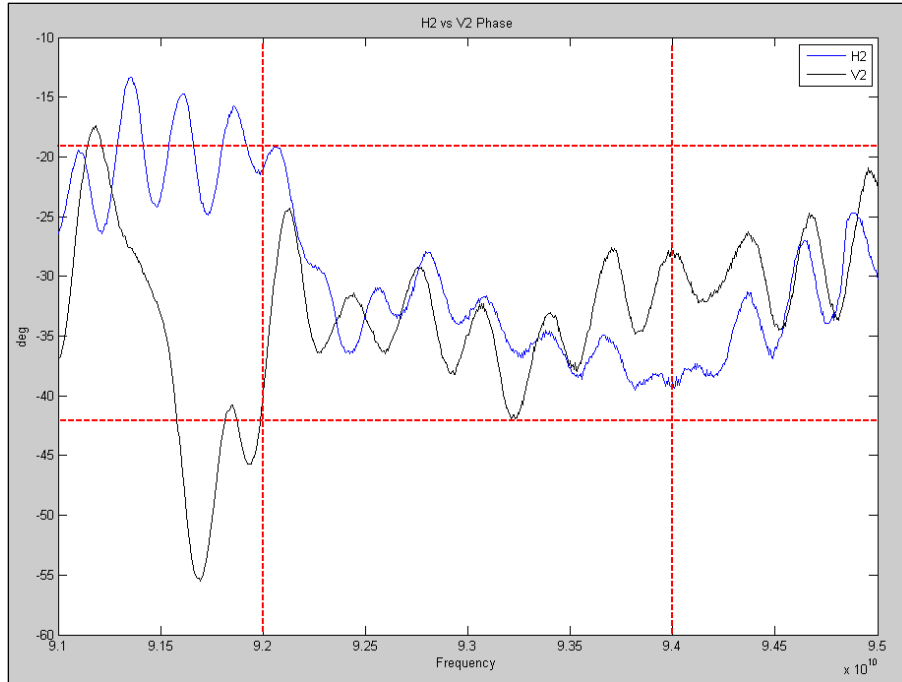


**Figure 3.17.** OMT 2, H and V Phase Comparison

These measurements show that there is a difference in power between the horizontal and vertical channels of  $-0.1253$  dB and  $0.4507$  dB, respectively. The phase measurements show an average phase offset of  $-4^\circ$  and  $4^\circ$  for OMTs 1 and 2, respectively. The oscillations over frequency in the phase and power are probably due to reflections at the waveguide connections and impedance mismatch at the SPTDs.

### 3.5.2 Microwave Section

The microwave section consists of two isolated parts: the amplification/filtering stage and the phase combination network. The attributes of focus are matching the power levels and phase of the H and V channels.

The first section that was tested was the amplification and filtering stage. To accurately characterize the gains and phases of each channel, a 4–8-GHz calibration set was created on the VNA. Shown in Figure 3.18 is the system under test.

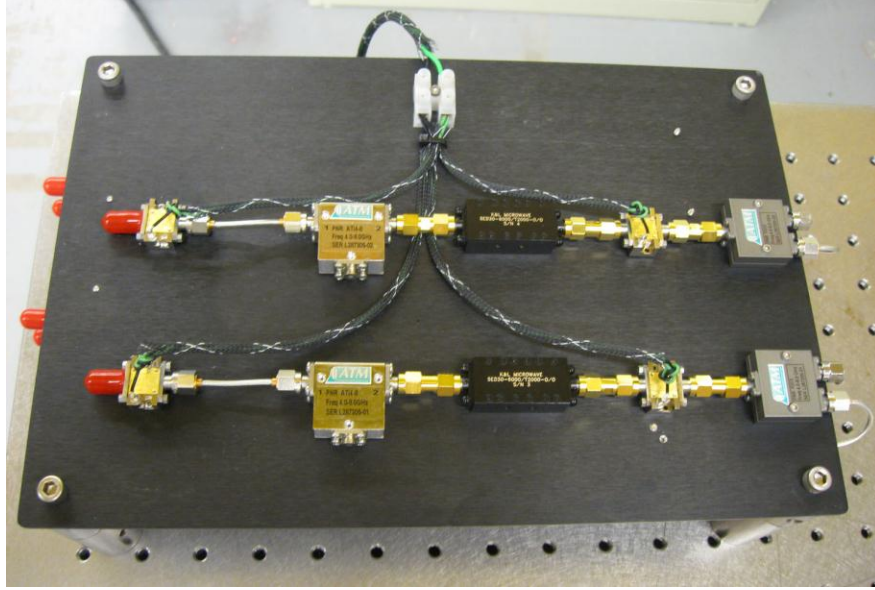


**Figure 3.18.** Microwave Filtering and Amplification Stage

S-parameter transmission measurements were transformed into the time domain, measuring both the amplitude and time delay delta, which can be equated to a phase delta. The measurement results and calculations for the variations between channels are shown below, where S refers to the relative power measured by the VNA, d refers to the distance travelled measured by the VNA using the electrical delay and velocity factor of coaxial cable, and  $\Delta\phi$  is the phase difference between the H and V channels.

$$S_H = -6.8689dB$$

$$S_V = -6.7735dB$$

$$\Delta S = 0.0954dB$$

$$d_H = 645.30mm$$

$$d_V = 645.57mm$$

$$\Delta d = 0.27mm$$

$$\Delta\phi = 360 * \frac{\Delta d}{\left(\frac{\lambda}{v_f}\right)}$$

$$\Delta\phi = 360 * \frac{0.27mm}{50mm/0.7} \tag{3.13}$$

$$\Delta\phi = 1.3608^\circ$$

A relative power variation of 0.1 dB is quite good, and a phase difference of 1.36 degrees will still allow accurate characterization of the unique polarization signatures of the received signal.

The second section, the microwave phase-combination network, was tested using the same VNA calibration set. Figure 3.19 shows a schematic of the microwave phase-combination network for the differential radiometer. Note that it is of the same design as that used in the single-ended radiometer.

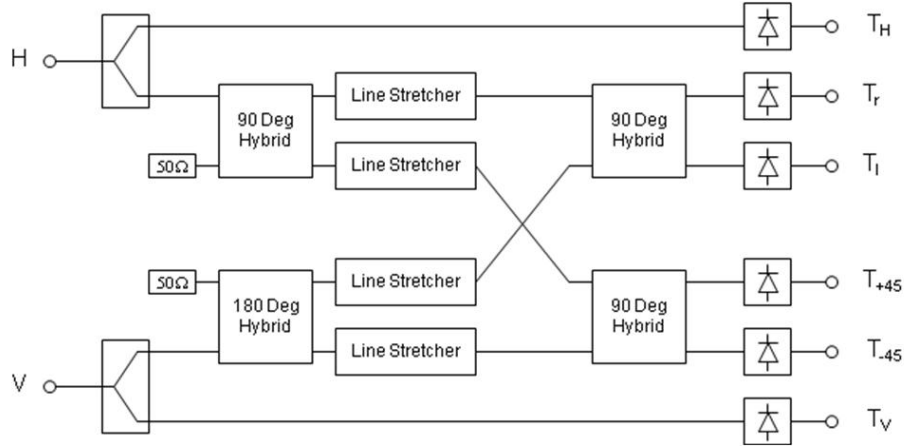


**Figure 3.19.** Microwave Phase-Combination Network for the Differential Radiometer

The phase-combination network recombines the horizontal and vertical signals using phase-shifting hybrids. The recombined signals allow for the extraction of the polarization signatures included in the total brightness temperature.

The phase accuracy of the 90- and 180-degree hybrids is listed as 3°; using line stretchers between the series of hybrids to perform fine-phase adjustments, the assumed accuracy limitation was 3°. Matrices characterizing each hybrid were developed and used to arrange the order and interconnections of the phase-matching network. The hybrid matrices and resulting phase relationships for H and V for each of the four recombined signals are as follows:

$$\frac{1}{\sqrt{2}} \begin{vmatrix} 0 & 1 & j & 0 \\ 1 & 0 & 0 & j \\ j & 0 & 0 & 1 \\ 0 & j & 1 & 0 \end{vmatrix} \quad 90^\circ \text{ hybrid}$$

$$\frac{1}{\sqrt{2}} \begin{vmatrix} 0 & 1 & -1 & 0 \\ 1 & 0 & 0 & -1 \\ 1 & 0 & 0 & 1 \\ 0 & 1 & 1 & 0 \end{vmatrix} \quad 180^\circ \text{ hybrid}$$

$$T_r = \frac{1}{2}(V_H + jV_V) \quad (3.14)$$

$$T_i = \frac{1}{2}(jV_H + V_V) \quad (3.15)$$

$$T_{+45} = -\frac{1}{2}(V_H + V_V) \quad (3.16)$$

$$T_{-45} = -\frac{j}{2}(-V_H + V_V) \quad (3.17)$$

Measurements were taken from the inputs of the hybrids to the output of the second set of 90-degree hybrids, using the setup shown in Figure 3.20. During the transmission measurement, all outputs and inputs not being measured were terminated with 50-ohm loads, as it was found that leaving the outputs and inputs open allowed for significant reflections, which influenced phase measurements. Phase measurements were taken using a single electrical delay to flatten phase values across the bandwidth. Once the electrical delay was set, it was not adjusted for the remainder of the measurements. For this phase-matching network, an electrical delay of 2.980986 nanoseconds was used. The phase differences between the channels were measured and are shown in Table 3.2 below.

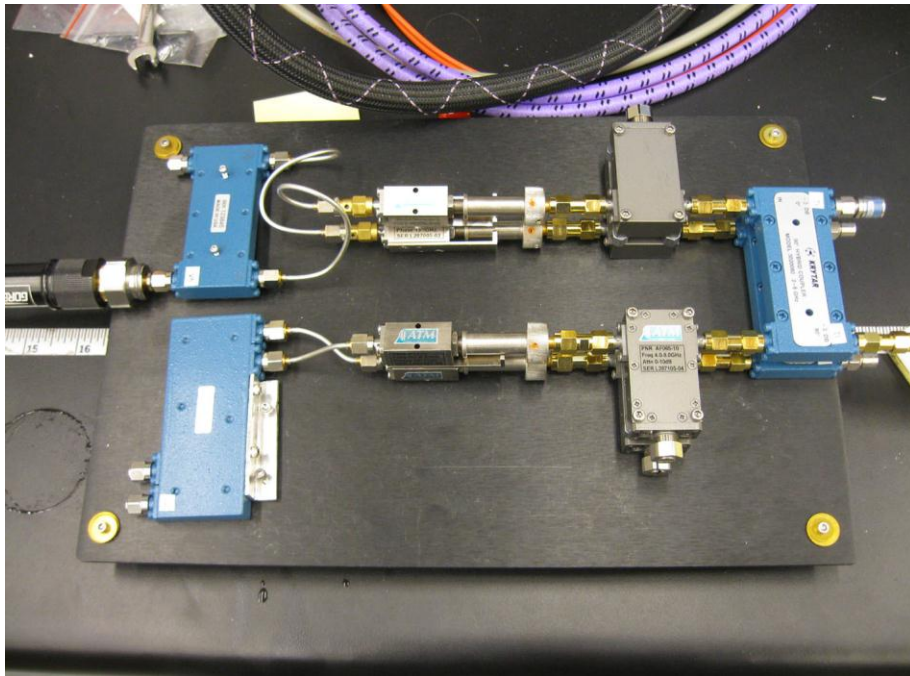


**Figure 3.20.** Microwave Phase Matching Test Arrangement for Differential Radiometer

**Table 3.2.** Microwave Network Phase Measurements for Differential Radiometer

	$V_V$		$V_H$	
	Calculated	Measured	Calculated	Measured
$T_1$	0	0.0592	90	90.077
$T_r$	90	90.23	0	1.0194
$T_{+45}$	180	179.16	180	179.67
$T_{-45}$	-90	-90.162	90	91.014

There is good agreement between the calculated and measured phases for all channels.

Once the mm-wave and both microwave sections were characterized, the radiometer system was fully assembled and tested on a system level.

### 3.5.3 Differential Radiometer System Testing

To test the differential radiometer as a system and assure accurate analysis of the differential data, the inputs associated with the two OMTs were isolated. This was accomplished by removing the inputs of the other OMT and replacing them with linear W-band reference loads into the SPDTs. In this configuration, there is a known ambient source, with no unpredictable polarization effects, to which the input data is compared. The VNA was used as a source to present the radiometer with a single-frequency 93-GHz signal at different polarizations: H, V, +45, -45, and right-hand circularly polarized (RHCP). The angular orientation of the VNA source was measured to be within  $\pm 0.1^\circ$  with respect to the radiometer OMT. To further extract the polarization measurements, ambient measurements were taken and subtracted from all transmission measurements. Also, the lock-in amplifiers were set at a time constant of 300 ms with a sensitivity of 300 mV.

Results from this measurement study are shown in Figures 3.21 through 3.30, for all five measurements and for both OMT inputs.

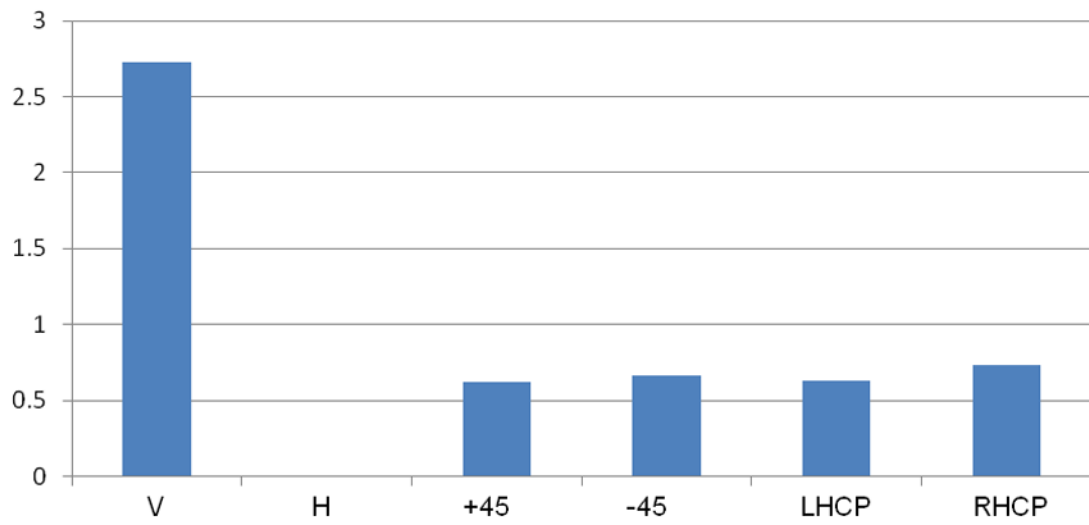


**Figure 3.21.** Transmitting V into OMT 1

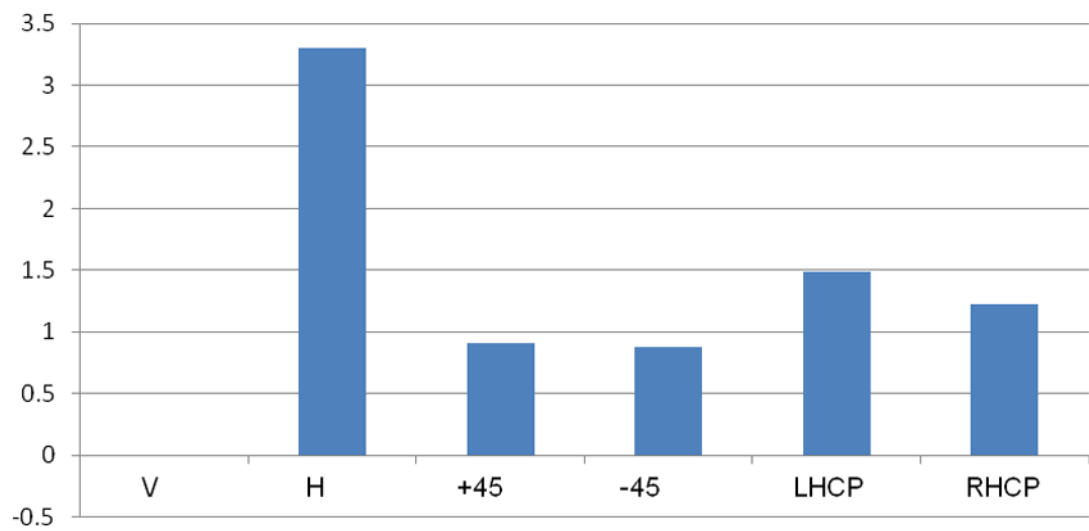


**Figure 3.22.** Transmitting H into OMT 1

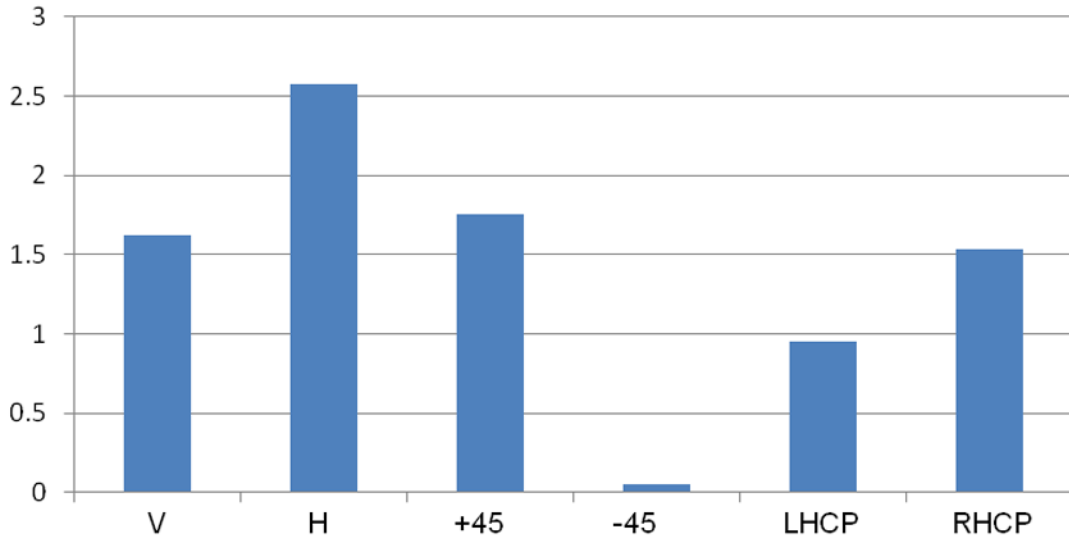


**Figure 3.23.** Transmitting +45 into OMT 1

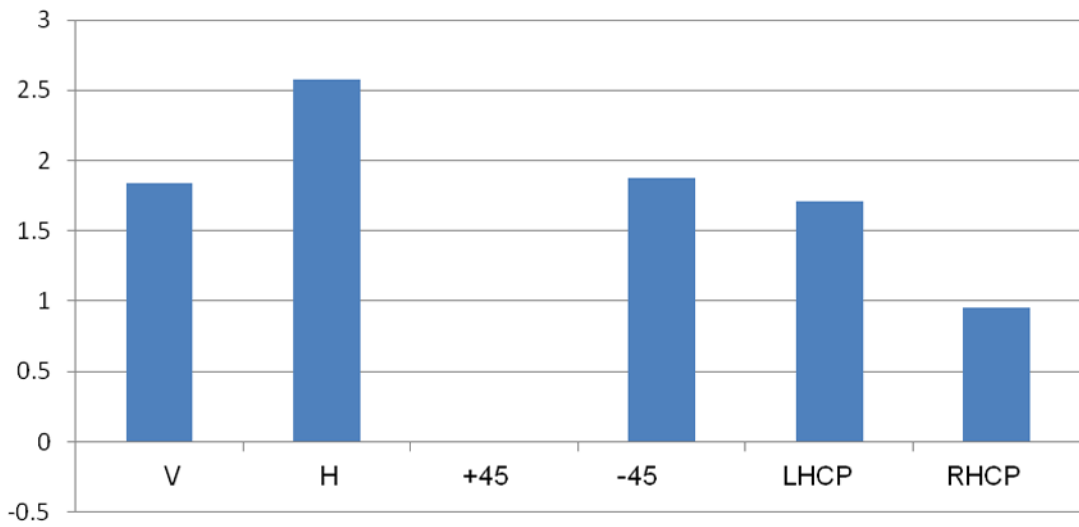


**Figure 3.24.** Transmitting -45 into OMT 1

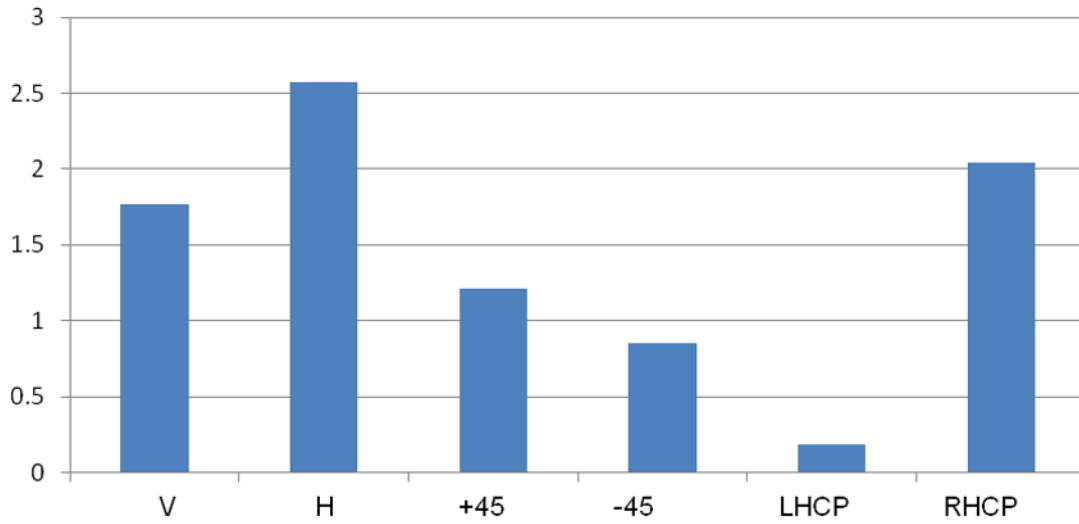


**Figure 3.25.** Transmitting RHCP into OMT 1

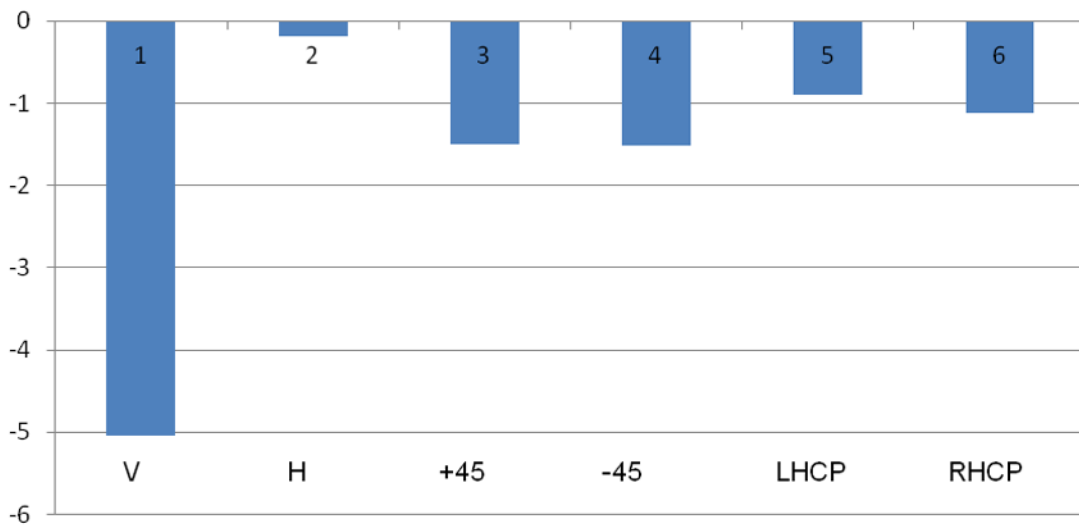


**Figure 3.26.** Transmitting V into OMT 2

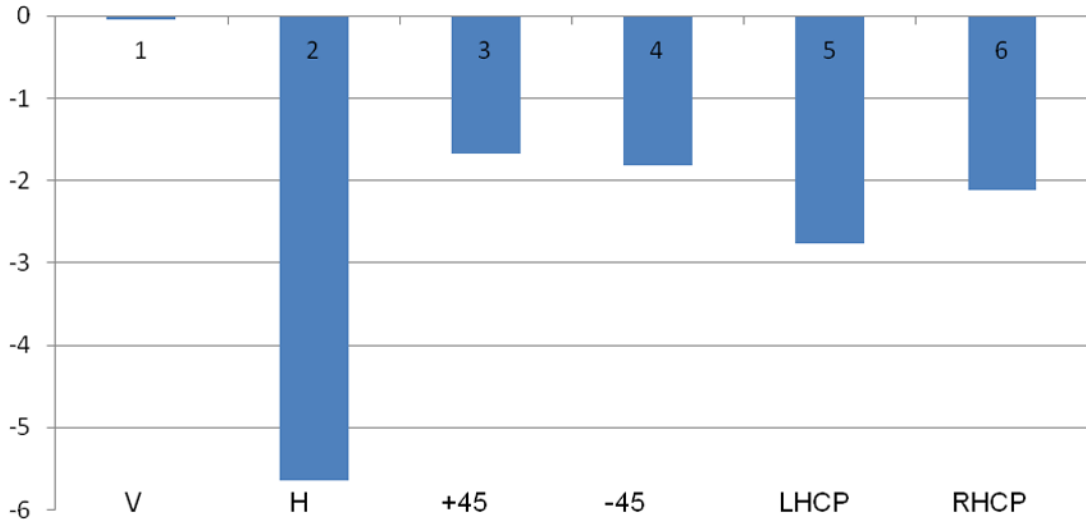


**Figure 3.27.** Transmitting H into OMT 2

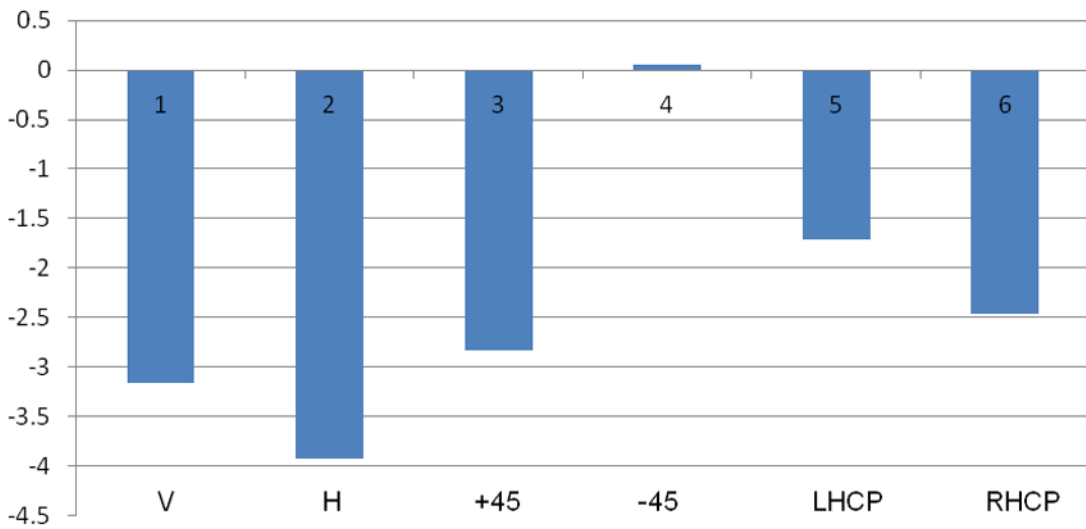


**Figure 3.28.** Transmitting +45 into OMT 2

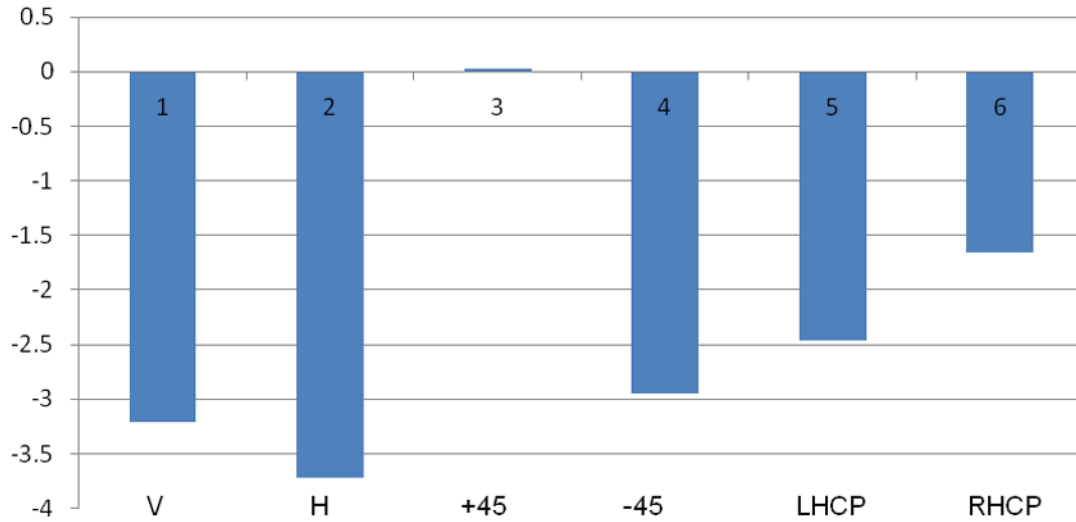


**Figure 3.29.** Transmitting -45 into OMT 2

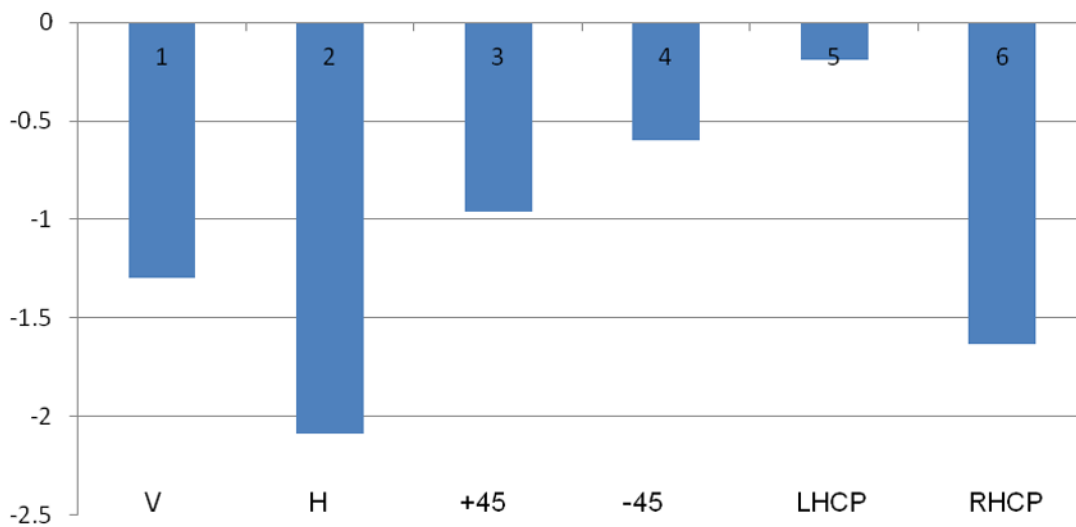


**Figure 3.30.** Transmitting RHCP into OMT 2

As mentioned in the analysis of the single-ended radiometer results, the vertical and horizontal channels are (overall) stronger than the other channels, because the H and V channels do not travel through the hybrids, line stretchers, and variable attenuators, and thus have less loss.

In light of the distinct responses of the polarization channels with respect to the transmitted signals, the fully polarimetric differential radiometer was deemed operational and the experimental work proceeded to field testing, as described in other sections of this report.



## 4.0 Optics

### 4.1 Overview

The optics in this system consist of a parabolic or ellipsoidal reflector that focuses the radiation from the direction of interest onto the horn of the radiometer. We refer to this arrangement as a telescope operating in the mm-wave region. For nearby objects, up to a few meters distant, an ellipsoidal design is used; for distant scenes, an off-axis parabolic design is used.

### 4.2 Theory and Design

#### 4.2.1 Telescope Components

PNNL designed a laboratory-style 0.5–1.0 meter scanning telescope for use with the mm-wave HPCR for conducting radiometric polarization imaging studies both indoors and outdoors. The development of this scanner was based on the design and fabrication costs versus project budget constraints. We investigated three basic telescope designs for cross-polarization isolation. A summary is as follows:

- Three basic designs were investigated:
  - Single unobscured reflector
    - Off-axis parabola (OAP)
  - Two-mirror unobscured reflector
    - Offset Gregorian
      - confocal off-axis parabolic primary and ellipsoidal secondary
    - Offset Dragone-Mizuguchi (side fed)
      - confocal off-axis parabolic primary and tilted hyperboloidal secondary
- Performance of the three designs in suppressing cross-polarization terms:
  - OAP:  $-34.1$  dB
  - Offset Gregorian:  $-39.2$  dB
  - Offset Dragone-Mizuguchi:  $-45.7$  dB
- Conclusions:
  - The two-mirror designs are equally difficult to fabricate and align, so we selected the offset two-mirror Dragone-Mizuguchi-type design, for its superior cross-polarization performance.
  - The single-mirror OAP performance is about 10 dB worse than the Dragone-Mizuguchi reflector, but due to its simplicity it was selected for proof-of-concept work

## 4.2.2 Designing the Off-Axis Parabolic Antenna

### 4.2.2.1 Introduction

An off-axis parabolic (OAP) reflector is required for a passive mm-wave polarimeter designed to operate at a wavelength of 3.2 mm (93 GHz), and have a 500-mm input aperture. The desired beam profile must have an edge taper of  $-12$  dB. Edge taper is defined as:

$$ET = 10 \log \left[ \frac{I_{edge}}{I_{max}} \right]. \quad (4.1)$$

For the  $-12$  dB edge taper specification, the signal intensity is reduced to 6.3% of the maximum at the edge of the beam.

Since the instrument will be used to extract the Stokes Vectors from mm wave energy passively collected from a scene, polarization purity in the received beam is paramount. However, there are no degrees of freedom in a single collector design to optimize this parameter, so we are left with designing the reflector and then analyzing the amount of polarization leakage in the resulting design. The user must then determine if this level of performance will be adequate for the application.

### 4.2.2.2 Design

To match the waveguide to the parabolic antenna, we need to ensure that the antenna, or telescope aperture, is optimally filled to correctly mode match to the waveguide and to provide the desired side lobe intensity. Working from the waveguide outwards towards the scene at infinity, we can propagate a Gaussian beam with the correct divergence and determine the necessary focal length required to meet the  $-12$  dB specification at the mirror surface. The waveguide has a full width half maximum divergence of  $14.3^\circ$  which means a half angle divergence of  $14.3^\circ$  to obtain a  $-12$  dB edge taper at the mirror. Therefore, the effective focal length (efl) must be

$$efl = \frac{250 \text{ mm}}{\tan[14.3^\circ]} = 982.5 \text{ mm}. \quad (4.2)$$

The resulting F/# for the design is F/2.1. Since the design is a simple single mirror parabolic reflector, we know by inspection that the radius of curvature must be twice the focal length, or 1965.1 mm. The conic constant, is of course,  $-1$ , since the surface is parabolic. The conic constant is related to the eccentricity parameter from analytic geometry using the following relationship:

$$k = -\varepsilon^2. \quad (4.3)$$

By entering these values into the general sag or z-profile equation for on-axis conic sections we have:

$$z(r) = \frac{\frac{r^2}{R}}{1 + \sqrt{1 - (1+k)\frac{r^2}{R^2}}} = \frac{r^2}{2R}; r^2 = x^2 + y^2. \quad (4.4)$$

In this expression,  $R$  is the radius of curvature of the parent spherical surface, and  $k$  is the conic constant of the parabola.

The parabola must be fabricated off axis by an amount at least equal to the beam radius, which is 250 mm in this case, in order that the detector does not obscure the input beam. However, at this limit, there would be no room to insert the waveguide at the reflector's focus without partially obscuring the incident beam. Therefore, we ensure that the physical diameter of the off-axis parabola is a bit larger than the clear aperture size that we need in order to minimize fabrication artifacts at the periphery of the reflector, and therefore we increase the aperture of the design by 100 mm to give 50 mm of guard band around the periphery of the optic. This means we now have a physical diameter of 600 mm. We arbitrarily add some additional clearance of 75 mm at the base of the parabola to permit sufficient clearance for the waveguide and select an offset height of 375 mm for the center of the OAP, which provides for 125 mm of clearance from the edge of the entrance beam to the focus. A drawing of the proposed design is shown in Figure 4.1. The design is shown with a squared-off rear surface. Since the maximum sag of the surface is 115.9 mm at the upper edge of the optic ( $y = 675$  mm), the OAP base dimension at its thickest point at the top of the optic must account for the thickness required at the bottom optic edge plus 80.3 mm. If we choose 20 mm or so for the central thickness at the bottom edge, the thickness at the top edge should be approximately 100 mm. These numbers can vary depending on the advice of the mechanical designer when rigidity and weight of the reflector are considered and the exact values chosen do not influence the basic optical function of the reflector; they affect mounting and stability requirements.

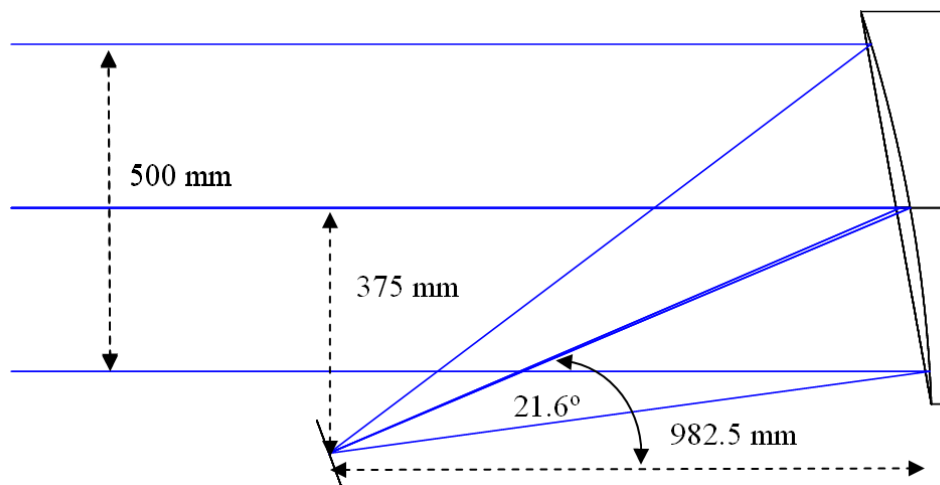


**Figure 4.1.** A Drawing of the Off-Axis Parabola Proposed for the Single Reflector mm-wave Polarimeter. The off-axis height is 375 mm, the input beam diameter is 500 mm, and the physical aperture of the parabolic surface is 600 mm.

#### 4.2.2.3 Optical Performance

If we assume that the half angle to achieve a  $-12$  dB edge taper is  $14.3^\circ$ , and furthermore, that the beam is essentially Gaussian, the  $1/e^2$  half angle is  $12.1^\circ$ . If we propagate a Gaussian beam with x- and y-

half with  $1/e^2$  divergence  $12.1^\circ$  half angles from the waveguide to the mirror surface, we should achieve the desired edge taper of  $-12$  dB at the telescope mirror, as shown in Figure 4.2.

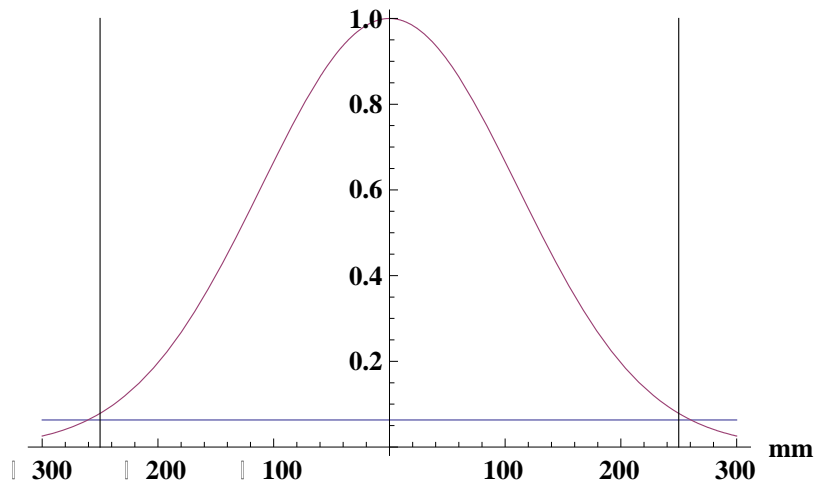


**Figure 4.2.** Plot of the Gaussian Beam Along with Reference Marks Where It Impinges Upon the OAP. The vertical lines denote the edges of the OAP clear aperture, while the horizontal line shows the  $-12$  dB intensity level of the beam.

Reversing the direction of mm wave energy, if we image an object at infinity onto the entrance plane of the waveguide, we obtain the intensity plots shown in Figure 4.3 for a y-polarized input field.

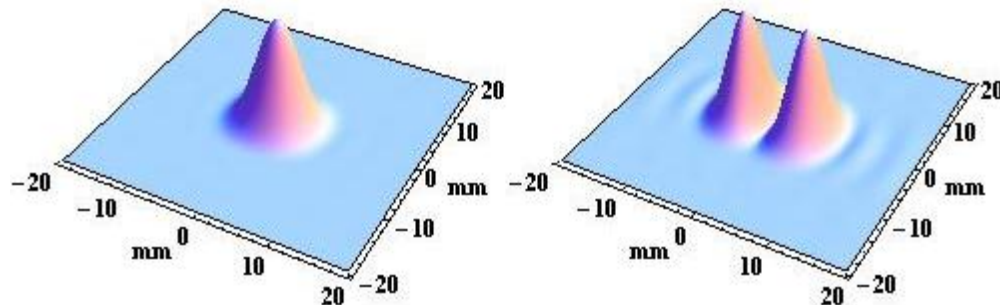


**Figure 4.3.** Intensity Plots Showing the Results for an Input Initially Polarized in the y-direction (vertically). The plot at the left shows the y field, the plot at right, the orthogonally-polarized x field. The relative powers are such that the cross polarized field is  $-34.2$  dB down from the vertically polarized field.

The cross polarized field is down  $-34.2$  dB from the nominal vertically- or y-polarized input field. We found that the cross polarization extinction was about 5 dB better in the slower F/2.8 design found earlier, and this is due to the smaller F/# of this design when compared with an F/2.8 design. The smaller F/# surface results in steeper angles of incidence on the reflector surface which contribute to additional polarization conversion. Slices of the intensity profile through each pattern's center are also plotted on a

logarithmic scale (Figures 4.4 and 4.5) to highlight details of the two orthogonal polarization intensities at the focal plane.

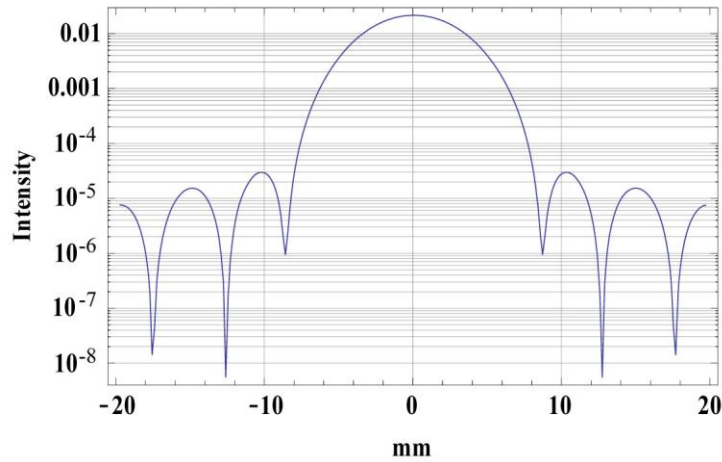


**Figure 4.4.** Log Plot Showing the Intensity of the y- or Vertically-Polarized Input Field at the Image Plane of the OAP

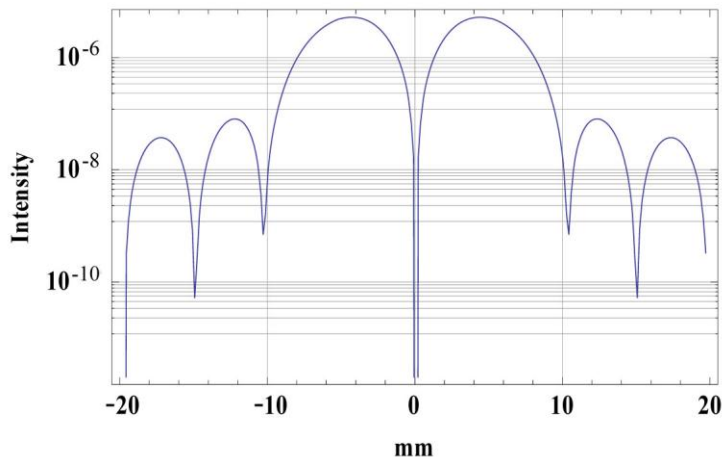


**Figure 4.5.** Log Plot Showing the Intensity of the x- or Horizontally-Polarized Field Produced by Cross Polarization of the Vertically Polarized Input Field

#### 4.2.2.4 Summary

An F/2.1 off-axis parabola design was presented having a 500-mm clear aperture and 982.5-mm focal length. A 600-mm-diameter section of the parabola is used that is displaced 375 mm from the nominal axis of the parent surface. The F/# of the design matches the  $-12$  dB edge taper of the detector for optimal mode matching, and the reflector exhibits a polarization extinction of  $-34.2$  dB in the cross polarization field when the telescope is illuminated with a linearly polarized beam aligned with the vertical (y-axis). The polarization extinction figure of merit is about 5 dB worse than that shown in the

previous design, but is due solely to the lower F/# (shorter focal length with same input aperture diameter) of this design that was optimized to critically fill the detector waveguide for optimum mode matching and acceptable side lobe intensity.

### 4.2.3 Tolerance Analysis of the Off-Axis Parabolic Antenna

#### 4.2.3.1 Introduction

The single reflector PMMR design consists of an OAP with a 500-mm aperture,  $-1965.09$ -mm radius of curvature, conic constant of  $-1$ , and an off axis height of 375 mm. The resulting focal length is then  $R/2$  or 982.5 mm. These values were arrived at by assuming a feed horn (detector) with a half width at half maximum (HWHM) divergence of  $14.3^\circ$  to ensure a  $-12$  dB edge taper at the 500-mm aperture.

#### 4.2.3.2 Model Parameters

Coupling efficiency was modeled using the physical optics option of Zemax in which the waveguide parameters were specified to have a Gaussian angle acceptance of  $\pm 12.1^\circ$ . This is the  $1/e^2$  divergence of the feed horn specified above. Additionally, an aperture having a 7-mm radius was placed in front of the waveguide as this radius is the limit at which the intensity of the impinging beam falls to  $-12$  dB of its maximum value. The  $1/e^2$  radius of the beam at focus is 5.5 mm, found from fitting a Gaussian to the input beam at focus.

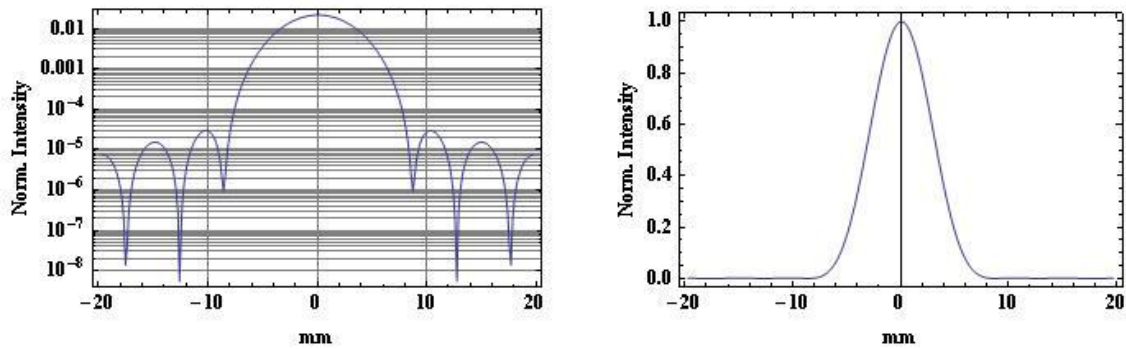


**Figure 4.6.** Plots Showing the Log Intensity and Linear Intensity of the Focused mm-wave Beam at the Input to the Waveguide

#### 4.2.3.3 Tolerance Analysis

In order to investigate the precision with which the feed horn must be positioned, the waveguide coupling feature of the physical optics propagation option was used under control of a macro to vary the angular orientation of the waveguide, as well as its lateral displacement. Additionally, the focal position of the waveguide was varied to determine the sensitivity of the system to focal displacements.

## Angular Misalignment

In the measurement shown in Figure 4.7, the waveguide is tilted about its entrance aperture such that there is no attendant lateral misalignment. It can be seen that approximately  $\pm 9.5^\circ$  can be tolerated until the signal falls to about  $-3$  dB below its peak value.

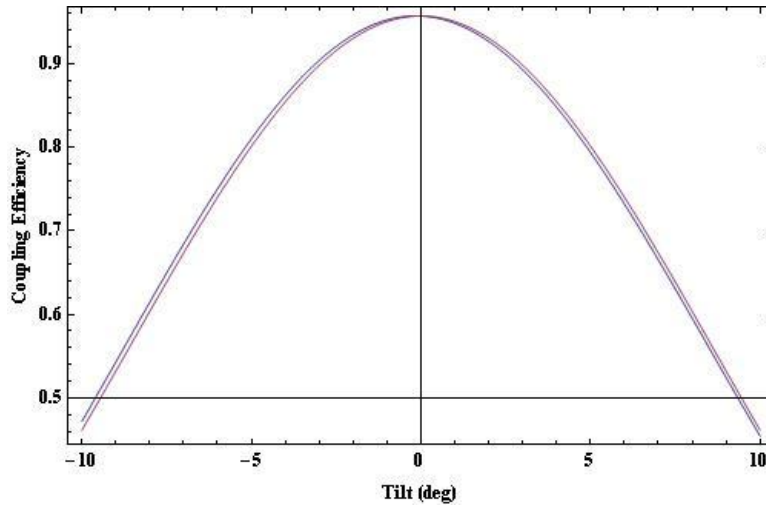


**Figure 4.7.** A Plot of Waveguide Coupling Efficiency Versus Waveguide Tilt for the mm-wave Receiver System. Note that the waveguide can tolerate approximately  $\pm 9.5^\circ$  of tilt before the coupling efficiency drops to about half of its peak value. There is a slight difference between tilts about the x- and y-axes, but not so much as to be significant.

## Lateral Misalignment

In this case, the waveguide is displaced laterally about the aperture center while the waveguide coupling efficiency is calculated. Note that approximately  $\pm 4$  mm of lateral misalignment can be tolerated with a  $-3$  dB drop in coupling efficiency.

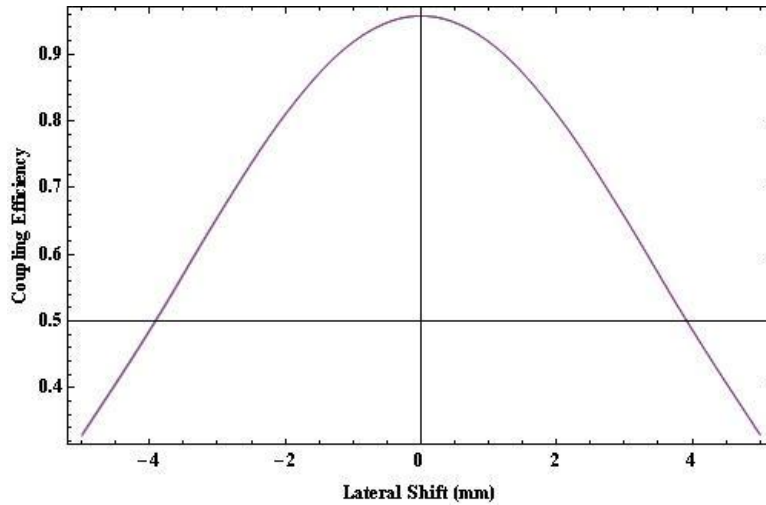


**Figure 4.8.** A Plot of Waveguide Coupling Efficiency Versus Waveguide Lateral Displacement about the x- and y-axes for the mm-wave Receiver System. The waveguide receiver can tolerate approximately  $\pm 4$  mm of lateral shift before the coupling efficiency is reduced by  $-3$  dB.

### Axial Misalignment

In the case of axial misalignment, the position of the waveguide entrance is varied along the system axis to gauge the effects of non-optimum focus on the coupling efficiency.

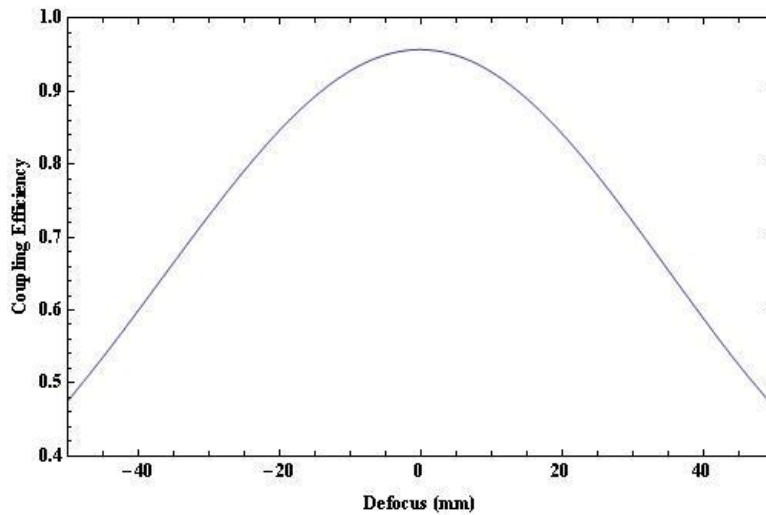


**Figure 4.9.** Plot Showing the Effect of Defocus or Axial Displacement of the Waveguide Entrance Aperture on Waveguide Coupling Efficiency. Almost  $\pm 50$  mm of axial displacement is required to reduce the coupling efficiency by  $-3$  dB.

#### 4.2.3.4 Summary

The single reflector OAP design for the PMMR prototype was examined for sensitivity to misalignment using the metric of waveguide coupling efficiency. In general, the system is relatively insensitive to misalignment in that  $\pm 9.5^\circ$  of tilt,  $\pm 4$  mm of lateral displacement and  $\pm 50$  mm of displacement must occur to reduce the peak coupling efficient to half of its maximum value. Therefore, tilt can likely be accommodated by a relatively crude adjustment, as can axial alignment. Lateral adjustment may be well served by use of a linear stage to control that degree of freedom.

### 4.2.4 Design of Dragonian Offset Dual Reflector Antennas: Front-Fed and Side-Fed

#### 4.2.4.1 Introduction

The seminal paper by Dragone (1978) describes the method of combining two or more confocal conic reflectors to ensure circular symmetry and reduce cross-polarization effects, and builds on Mizuguchi et al.'s earlier work (Mizuguchi et al. 1978). Dragone's arguments are based upon geometrical optics and are somewhat graphical in nature, which does not lend itself to performance- or specification-driven design. Fortunately, later authors, notably Chang and Prata (2004) and Granet (2001) have taken the concepts formulated by Dragone and derived analytical expressions that allow one to design a reflector system having minimum cross-polarization. Both authors require some starting parameters, such as system aperture  $D$ , feed divergence angle  $\theta_e$ , angular orientation of the feed or detector  $\theta_c$ , an estimate of the separation distance between the primary and secondary reflector  $l$ , and  $\alpha$ , the tilt angle of the principal ray of the secondary reflector. A graphic showing the antenna geometry and design parameters from Chang and Prata (2004) is shown in Figure 4.10. The parameters calculated using the expressions from Chang and Prata (2004) are then entered into the Zemax optical design program after they are converted into parameters that are suited to optical design as a starting point. The design is then optimized while the separation distance between the primary and secondary, the separation distance between the secondary and the focal plane, the offset of the secondary reflector and the secondary tilt angle are allowed to vary. Diffraction calculations are then performed using polarized input to determine the amount of cross-polarization that results in the final design.

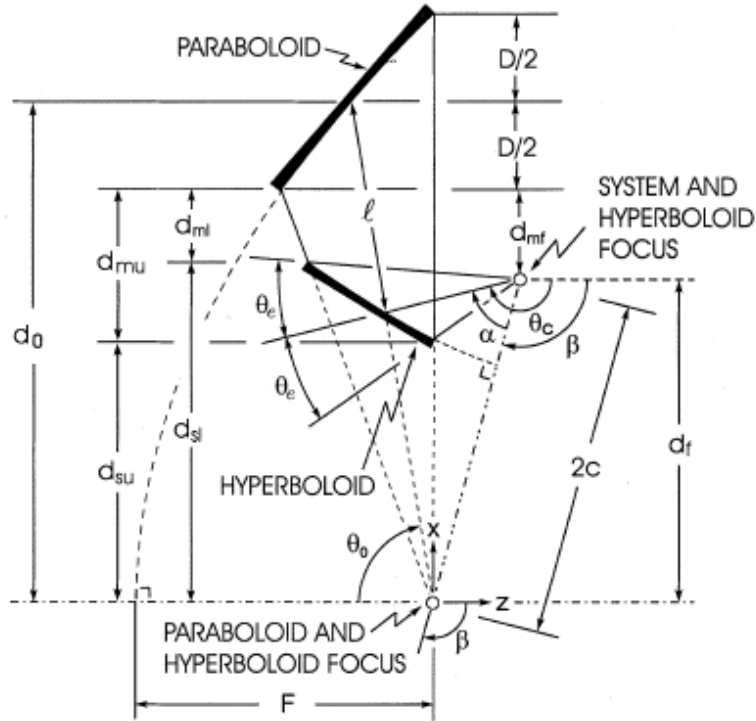


**Figure 4.10.** Diagram of a Dual-Offset Reflector with Design Parameters. (Chang and Prata 2004, Figure 3; reproduced with permission from IEEE. IEEE© 2004.)

Multiple reflector telescopes are preferred for reducing cross-polarization effects due to their symmetry when compared with single reflector designs. The original motivation was to permit the transmission of two orthogonally polarized beams using the same antenna, but lately, have been rediscovered for research into the cosmic microwave background (CMB).

#### 4.2.4.2 Dragonian Designs

##### Side-Fed Variant

The initial design parameters below were used in the design of the side-fed Dragonian antenna.

Parameter	Front-Fed Type
D	500 mm
$\theta_e$	14.3°
$\theta_c$	-90°
l	500 mm
$\alpha$	-25°

After following the procedure in the Chang paper, the following parameters were calculated using the initial values.

Parameter	Side-Fed Type
$\beta$	$-65^\circ$
k (conic constant secondary)	-4.27432
R (primary-parabola)	4273.87 mm
F (primary)	2136.94 mm
r (secondary hyperboloid)	2342.1 mm
f (secondary)	763.535 mm
$d_0$ (parabola offset)	2280.93 mm
$d_{cf}$ (distance from edge ray to focus)	149.622 mm
$d_{cs}$ (clearance between primary and secondary)	99.03 mm

After optimization to minimize spot size or wave front variance, as well as minimizing the intensity in the cross polarization field, the design that resulted is shown in Figure 4.11. The primary has a clear aperture of 500 mm, and a physical aperture of 600 mm. The secondary has a clear aperture of 450 mm and a physical aperture of 500 mm. The system F/# is F/2.03, with an effective focal length of 1198.5 mm.

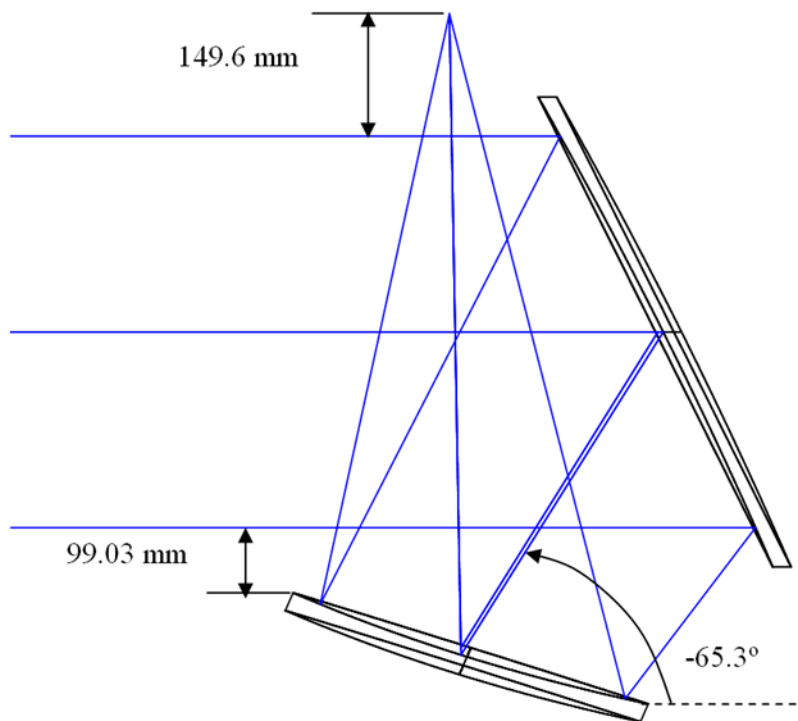


**Figure 4.11.** Diagram Showing the Side-Fed Dragonian Offset Reflector Antenna Optimized Using Zemax. The secondary is nearly the same size as the primary, which is typical of these designs.

The side-fed design was illuminated with a linearly polarized beam aligned with the y-axis with  $1/e^2$  width that ensured a  $-12$  dB edge taper, and which resulted in the intensity profile for the  $E_y$  field shown

in Figure 4.12 and  $E_x$  field shown in Figure 4.13. The cross-polarization component is found to be down  $-47$  dB using the diffraction modeling feature of Zemax.

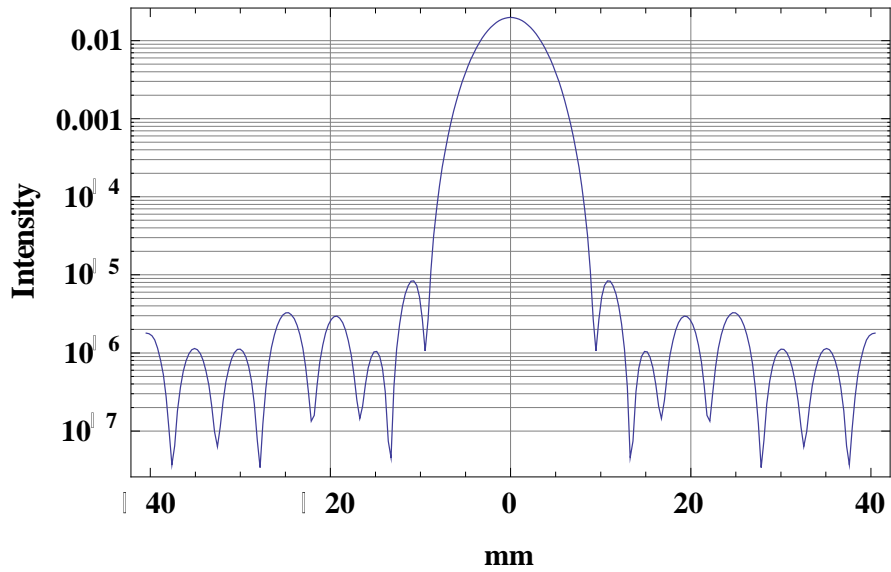


**Figure 4.12.** The Log Intensity Plot for the y-polarization Field of the Side-Fed Dragonian Reflector of the  $E_y$  Field Component. The total intensity is 0.975257 watts.

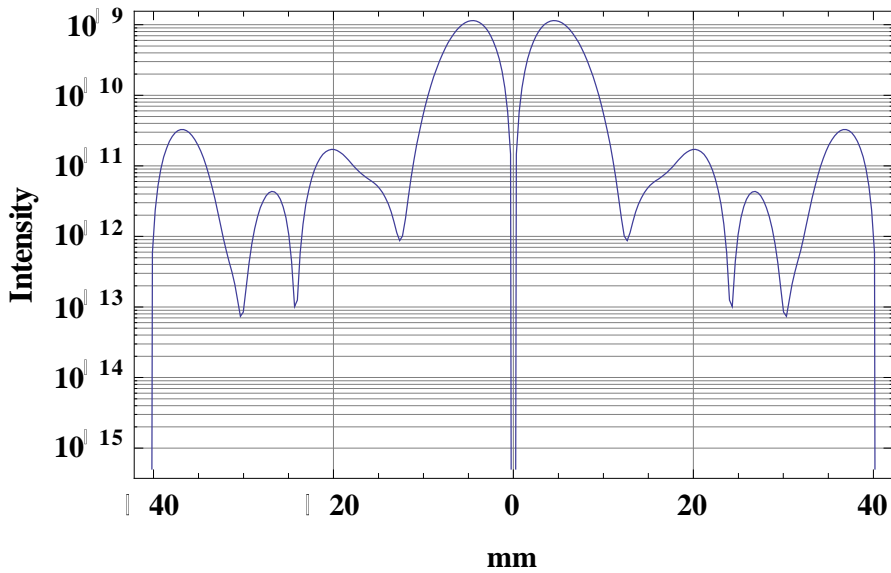


**Figure 4.13.** The Log Intensity Plot for the x-polarization Field ( $E_x$ ) of the Side-Fed Dragonian Reflector. The total intensity is  $1.9135 \times 10^{-5}$  watts.

## Front-Fed Variant

The initial parameters shown in the table below were used to initiate calculations for the Dragonian front-fed variant.

Parameter	Front-Fed Type
D	500 mm
$\theta_e$	14.3°
$\theta_c$	-170°
l	600 mm
$\alpha$	-60°

Once again, after following the procedure in the Chang paper, the following parameters were calculated using the initial values in the table above. These values were used to construct a model in Zemax and the system was optimized to minimize wave front error and energy contained in the cross polarization component.

Parameter	Side-Fed Type
$\beta$	-110°
k (conic constant secondary)	-5.55638
R (primary-parabola)	2162.47 mm
F (primary)	1081.23 mm
r (secondary hyperboloid)	1502.72 mm
f (secondary)	447.611 mm
$d_0$ (parabola offset)	1937.37 mm
$d_{cf}$ (distance from edge ray to focus)	226.628 mm
$d_{cs}$ (clearance between primary and secondary)	158.836 mm

The final design is shown below. The final design is F/2.03 and has an effective focal length of 2182.9 mm. The primary reflector has a clear aperture of 500 mm and 600 mm physical aperture. The secondary also has a 500 mm clear aperture and 600 mm physical aperture.

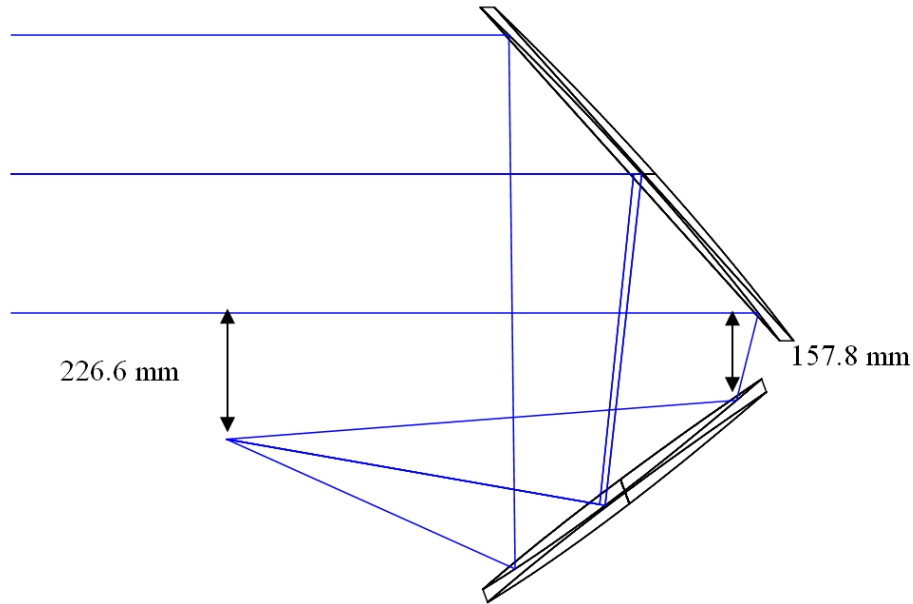


**Figure 4.14.** Layout of the Front-Fed Dragonian Offset Reflector

As was the case for the side-fed variant, the front-fed Dragonian antenna was illuminated with a linearly polarized beam oriented parallel to the  $y$ -axis and diffraction calculations were done for the  $E_y$  and  $E_x$  fields respectively to determine the amount of leakage into the orthogonal polarization component. The results of these calculations are shown in Figure 4.15 and Figure 4.16. The cross-polarized component was down  $-50$  dB with respect to the input polarization.

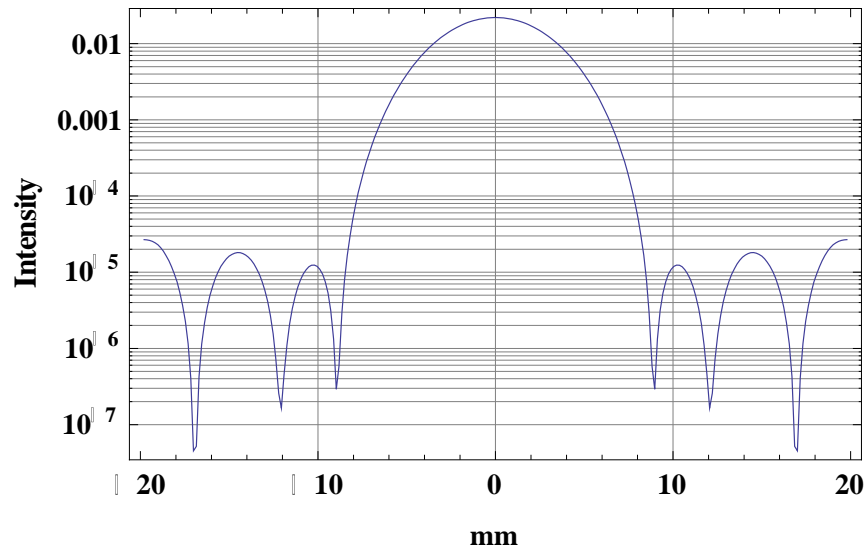


**Figure 4.15.** Log Intensity Plot of the Front-Fed Dragonian Showing the Amount of Linearly Polarized Light Contained in the  $E_y$  Field. The total intensity is 0.97503 watts.

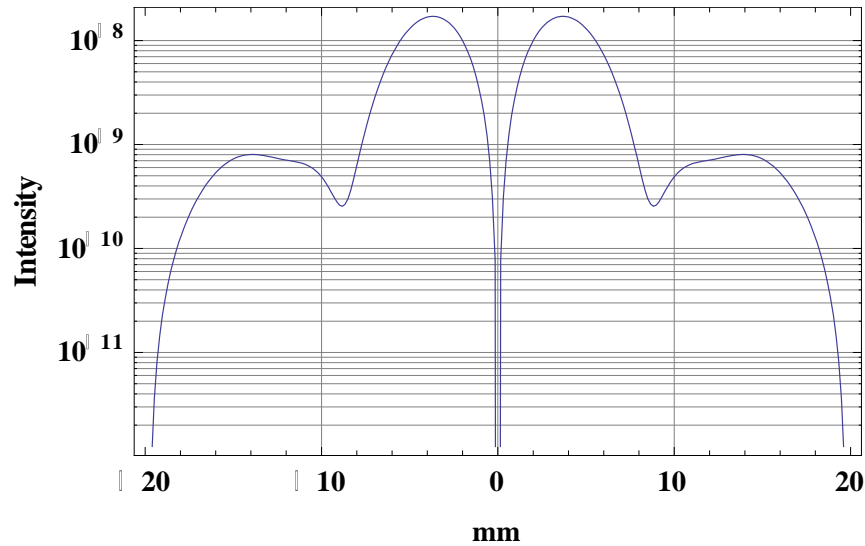


**Figure 4.16.** Log Intensity Plot for the Front-Fed Dragonian Reflector Showing the Distribution of Linearly Polarized Light in the  $E_x$  Field Leaking into the Orthogonal Polarization State with Respect to the Input Beam. The total intensity is  $9.2509 \times 10^{-6}$ .

#### 4.2.4.3 Conclusions

Two examples of offset reflector antenna designs were presented that meet the Dragone criteria for symmetry and produce very low cross-polarization leakage: the side-fed and front-fed Dragonian offset dual reflectors. Both designs consist of an off-axis parabolic primary mirror and hyperboloidal secondary that is also off-axis and tilted to help reduce the polarization mixing found in single reflector and non-Dragonian offset dual reflector designs, such as the offset Gregorian or Cassegrain designs. The original paper by Dragone described the method for producing design having low cross-polarization that relied heavily on symmetry arguments buttressed by trigonometry and ray tracing to demonstrate and prove the approach. Later authors used the basis of his ideas to derive analytical expressions needed to methodically design antennas meeting specific design criteria.

Both designs have nearly equal-sized primary and secondary mirrors that are approximately 0.5 m in diameter. The side-fed version is less flexible than the front-fed variant with respect to feed horn choice as only a limited range of horn divergences can be accommodated that do not result in beam obscuration. However, it appears that more compact mechanical designs can result from the side-fed variant which may give a slight edge from an instrument design standpoint. However, the front-fed design presented here has  $-50$  dB cross-polarization performance, which is  $-3$  dB lower than the side-fed design, and would be the clear choice if the best cross-polarization performance is desired.

### 4.3 Development

#### 4.3.1 Monocular Telescope

A single-mirror OAP was designed and fabricated to perform proof-of-concept work. Figure 4.17 shows the initial design drawings for this telescope. A Dragone-Mizuguchi-type telescope was also

designed and two mirrors were fabricated. The mechanical structure and platform are designed to work with both the single-mirror OAP and the Dragone-Mizuguchi design.

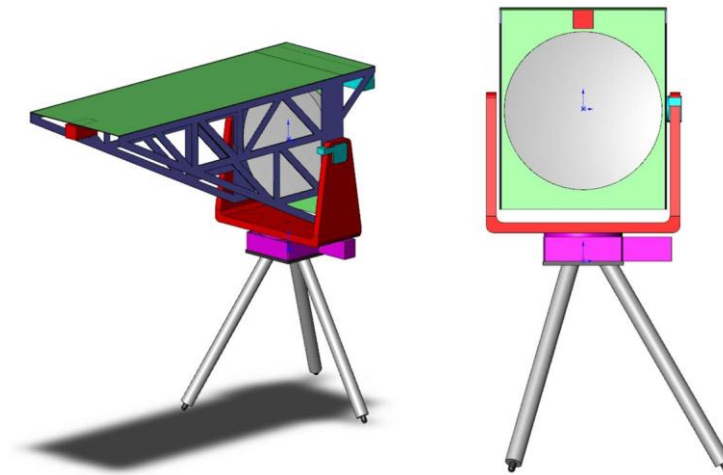


**Figure 4.17.** Single Mirror OAP Design—Isometric and Front Views

The initial mechanical design work for the telescope was as follows:

- Developed a specification for the scanning mechanism based on a gimbal concept
- Obtained a quotation from Parker Automation that is partially responsive to the specification
- Issued comments to Parker Automation to address noncompliant areas
- Completed conceptual design of gimbal scanner for single mirror reflector design
- Prepare procurement package for gimbal and performing preliminary design of scanner

A single-reflector mm-Wave receiver tolerance analysis on OAP design is shown in Figure 3.1. The single-reflector polarimeter design consists of an OAP with a 500-mm aperture,  $-1965.09$  mm radius of curvature  $R$ , conic constant of  $-1$ , and an off-axis height of 375 mm. The resulting focal length is then  $R/2$  or 982.5 mm. These values were arrived at by assuming a feed horn (detector) with a HWHM divergence of  $14.3^\circ$  to ensure a  $-12$  dB edge taper at the 500-mm aperture.

The summary of this analysis was that the single reflector OAP prototype was examined for sensitivity to misalignment using the metric of waveguide coupling efficiency. In general, the system is relatively insensitive to misalignment in that  $\pm 9.5^\circ$  of tilt,  $\pm 4$  mm of lateral displacement and  $\pm 50$  mm of displacement must occur to reduce the peak coupling efficient to half of its maximum value. Therefore, tilt can be accommodated by a relatively crude adjustment, as can axial alignment. Lateral adjustment is well served by use of a linear stage to control that degree of freedom. This system is designed for robust and stable performance in the field. It allows for stable imaging of static field objects under many conditions to assess the degree of natural depolarization or change of polarization of test objects against many backgrounds.

The mechanical design work for the OAP mirror was completed at PNNL and a vendor (Olympus Controls) fabricated it. The mechanical scanner was assembled separately.

Figure 4.18 shows the single mirror OAP mounted temporarily to the system tripod and radiometer support structure. This temporary mount was later replaced with the computer/motor control Gimbal which is shown in Figure 4.19. Olympus Controls fabricated the Gimbal and delivered in August 2009. However, on initial system startup, it was determined that the Gimbal was delivered with the wrong elevation (tilt) axis motor and without an internal motor brake to hold the reflector plate in place when power is removed from the motors. These items were swapped out with Olympus Controls and both have been tested and are functioning properly. Limit switches and sample encoders were added to complete the development of the Gimbal positional control. Once these were completed, the Gimbal was mounted on the tripod with the reflector plate mounted to it.

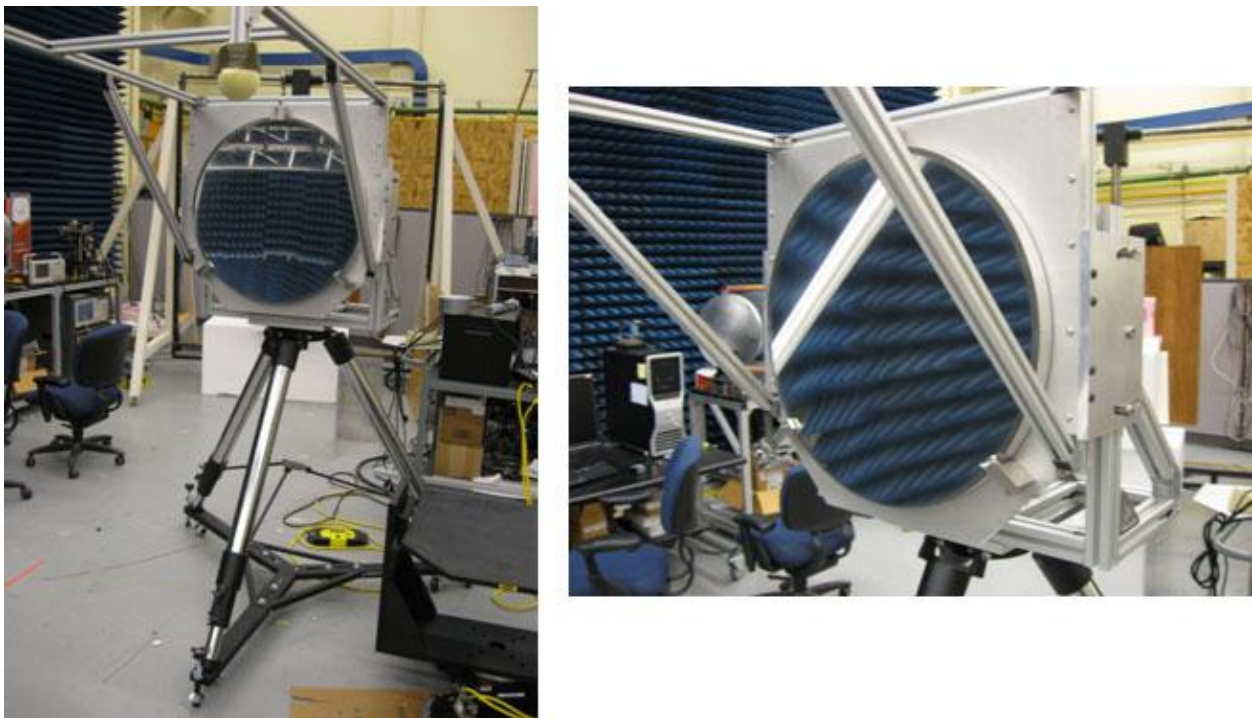


**Figure 4.18.** Single Mirror OAP Mounted to Tripod



**Figure 4.19.** Computer/Motor-Controlled Gimbal

The millimeter wave polarimeter receiver was integrated into the single reflector OAP and computer/motor control scanning (azimuth and elevation) Gimbal as shown in Figure 4.20.

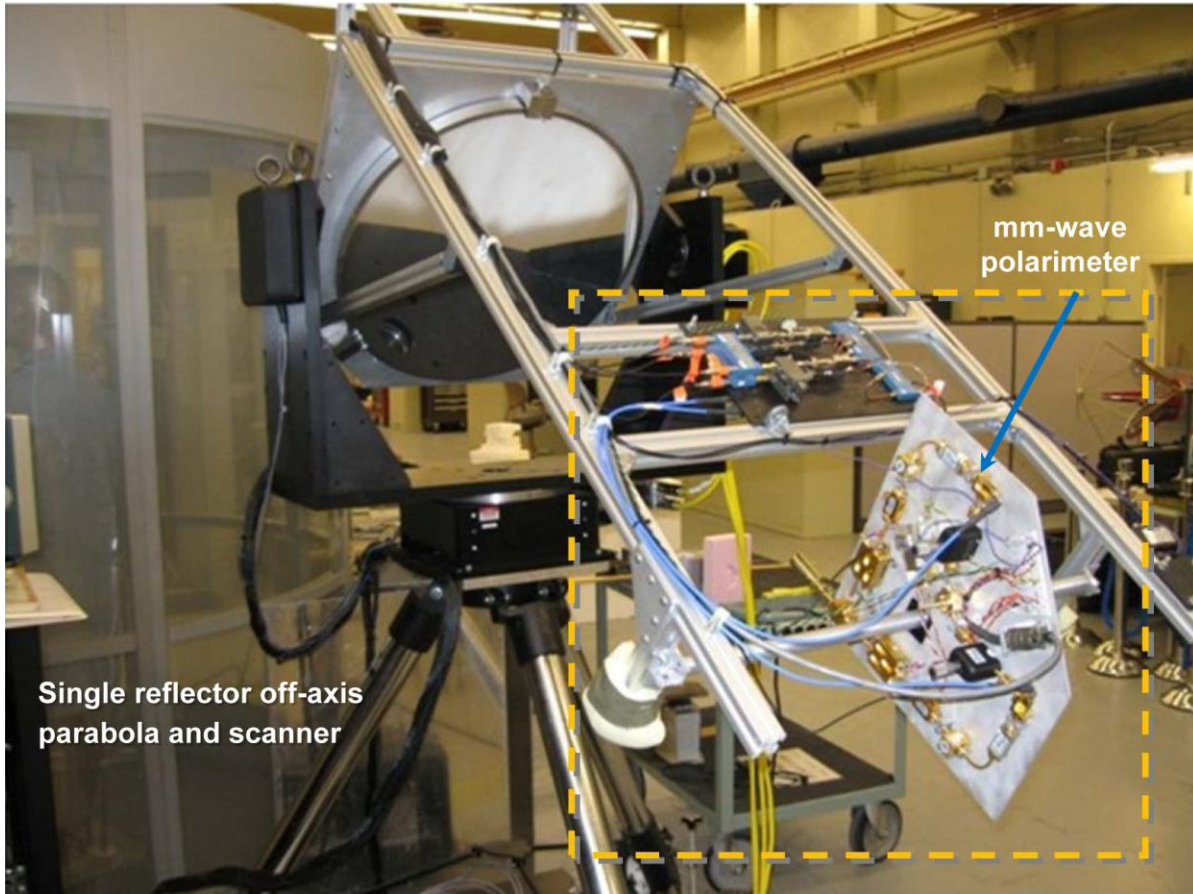


**Figure 4.20.** The mm-wave Polarimeter Receiver Integrated into the OAP Scanner

Six lock-in amplifiers were integrated into a 19-in. instrument rack, which are used to process the six millimeter-wave polarimeter receiver signal channels. Figure 4.21 shows the complete integrated polarimeter system, which includes the millimeter wave polarimeter, OAP single reflector, azimuth and elevation scanner, movable tripod mount, and 19-in. instrument rack. Not shown is the laptop computer which is used to process and display the passive radiometric imaging data.

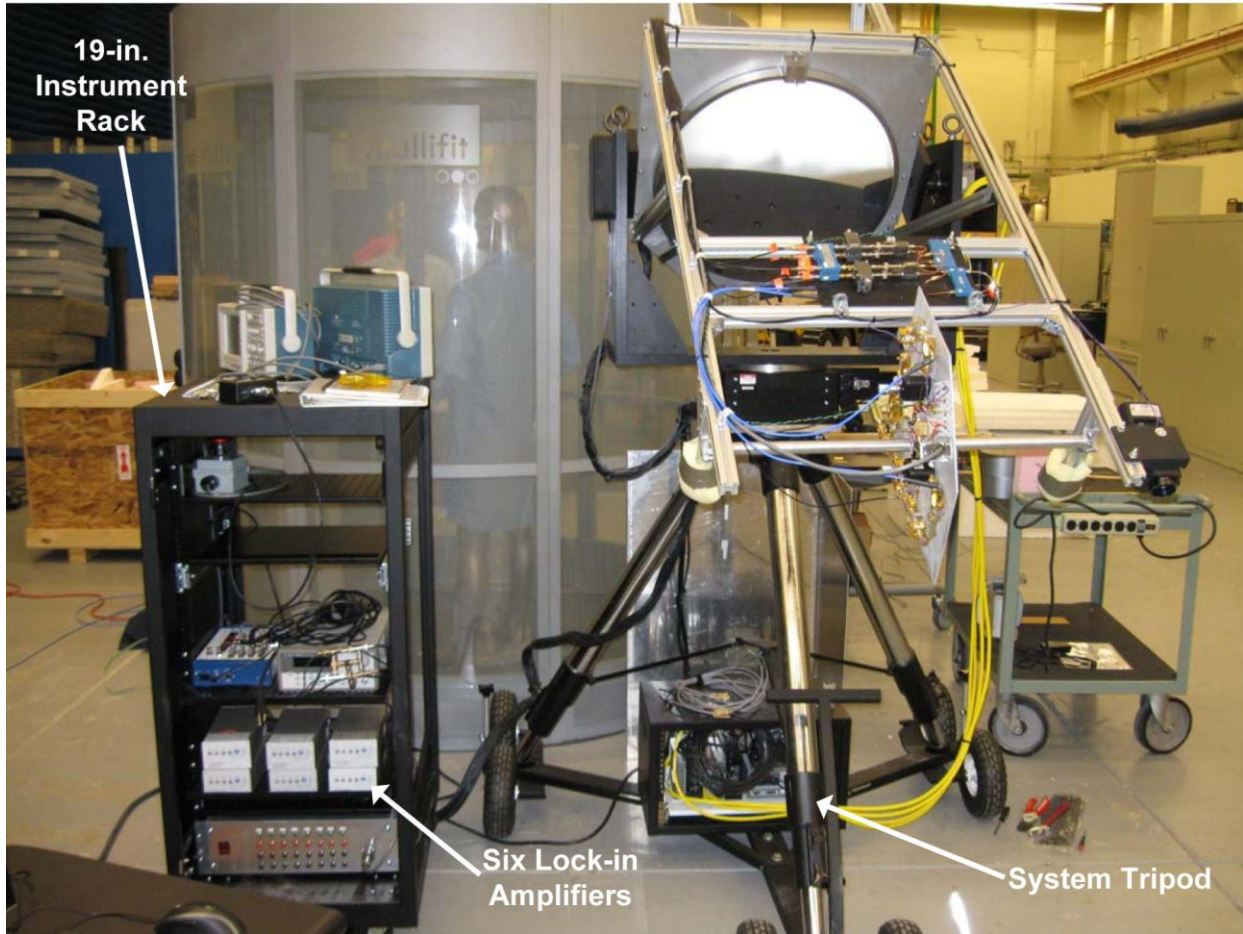


**Figure 4.21.** Complete Integrated Polarimeter System

Initial polarimetric radiometer measurements on the passive receiver were conducted with an active calibration source to determine the sensitivity of the two channels (vertical and horizontal). A PNNL-developed active calibration source is able to provide W-band (93 GHz) vertical and horizontal polarized signals to the receiver to evaluate the sensitivity and performance of the polarimetric radiometer. It was determined that one of the W-band mixers in the radiometer receiver was not performing up to specifications. A replacement mixer was obtained. The radiometer was still able to perform passive measurements with this mixer; however, one channel was not as sensitive as the other, so this degraded full Stokes analysis on early measurements without more elaborate calibration.

## 5.0 Mechanics

The mechanical design of the PMMR systems includes mounting and scanning elements, as well as the physical structure of the optical components.

The initial design used a heavy-duty commercial tripod mounted on a wheeled dolly, suitable for use in and near the laboratory. Mounting elements include tripod, tilt axis, swivel axis, reflector mounting plate, and counterweight.



**Figure 5.1.** CAD Drawing of the Monocular Telescope System



**Figure 5.2.** Monocular Telescope Performing Scan

A later design replaced the tripod with a custom-built frame, shown in Figure 5.3. This design is better suited to transportation by truck for long-distance viewing from an elevated vantage point.



**Figure 5.3.** Custom-Built Frame with Binocular Telescope Mounted



## 6.0 Electronics

The electronic design of the PMMR systems consists of three main functions: motion control of the scanner, data collection, and radiometer. The radiometer design has been discussed in great detail in Section 3.0. This section will cover the remaining two functions: data collection and motion control. The electronics design is the same for both the monocular system and the binocular differential systems. A block diagram is shown in Figure 6.1, and circuit diagrams are shown in Appendix E.

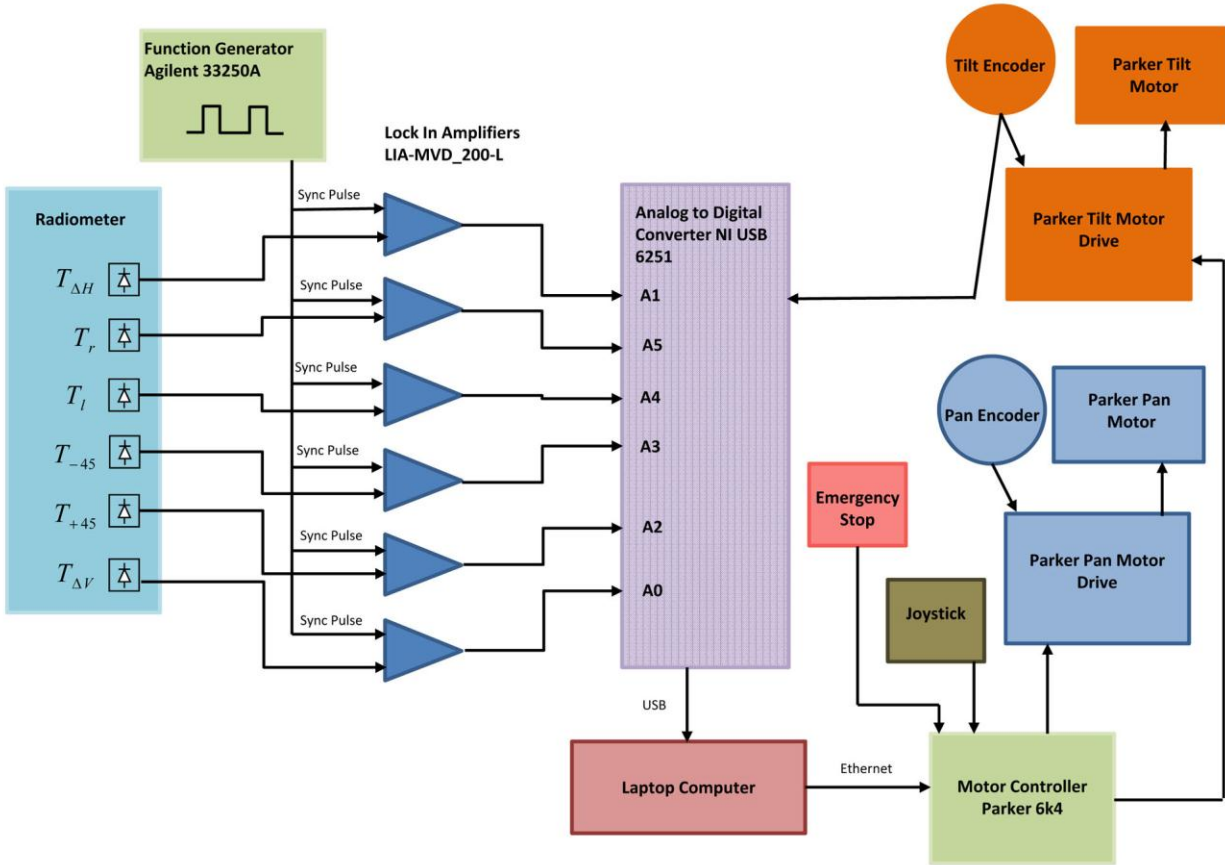


**Figure 6.1.** Block Diagram of the Roving Eye Electronics System

There are six polarization states that are measured by the polarimetric radiometer and are output as analog signals. These signals are right hand ( $T_r$ ), left hand ( $T_l$ ), 0 degrees horizontal ( $T_h$ ), +45 degrees ( $T_{+45}$ ), -45 degree ( $T_{-45}$ ), and 90 degrees vertical, ( $T_v$ ). Each analog signal is sent to a lock-in amplifier, model LIA-MVD-200L, where the signal is amplified and synchronized. An Agilent function generator, model 33250A, is used to generate a sync pulse for each lock in amplifier. The amplified synchronized signal is then sent to an analog-to-digital converter (ADC), National Instruments model USB 6251. The digital data are sent to a laptop connected to the ADC via a USB interface for display and storage. The digitized data are optionally displayed in real time and are stored on the laptop hard drive for post-processing.

Motion control is handled by a Parker motor controller model 6k4. The laptop communicates to the motor controller over an Ethernet connection. The laptop issues commands to the motor controller, which has its own closed-loop system with encoder feedback to control the motor operation based on commands from the laptop for position, velocity, and acceleration. There are two motors with motor drives on the system, one for tilting and one for panning the radiometer. The control has an analog joystick for panning and tilting under manual control. There are limit switches for both pan and tilt set such that motion will not move to a position that may cause damage to the radiometer or electrical wiring. There is an emergency stop button, wired directly into the motor control in a normally closed configuration, which if pressed halts all motion and engages the tilt brake.

The encoders for the pan and tilt motors are quadrature encoders. One phase of the tilt-axis quadrature encoder output is electrically wired to a counter on the ADC. The counter counts pulses as the tilt axis scans in the “up” direction. When the number of pulses counted corresponds to the specified sampling distance, the ADC is triggered by the laptop host software to collect samples from the radiometer signals.

## 7.0 Software and Data Analysis

Two primary software suites are used in data collection and analysis. AhisWin, developed at PNNL for mm-wave work, is used as a data collection and pre-processing tool. ENVI, a commercial application built on Research System's IDL, is used for further processing and image presentation. General-purpose scientific software such as Mathematica, and image processing software such as Adobe Photoshop and IrfanView, are used to determine associations between optical images and mm-wave images, and to collate multiple images.

Figure 7.1 shows a typical screen shot of AhisWin, and Figure 7.2 shows the same file being further processed in ENVI.

A useful technique, shown in Figure 7.2, is to use color for the polarization channels. This can be further enhanced by creating a gray-scale image of the intensity channel, then modulating (overlying) the two, as shown in Figure 7.3.

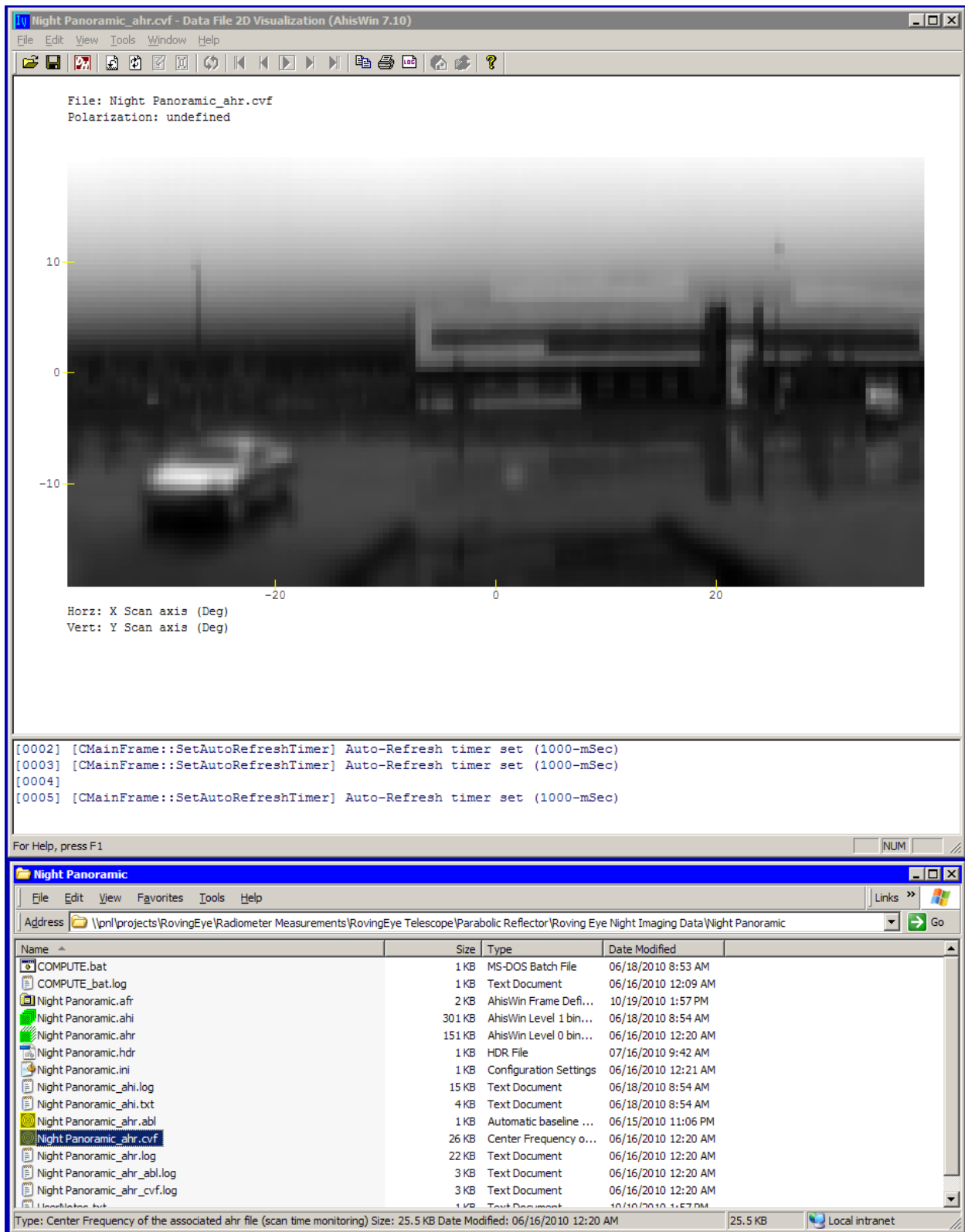


Figure 7.1. AhisWin Example Screen Shot

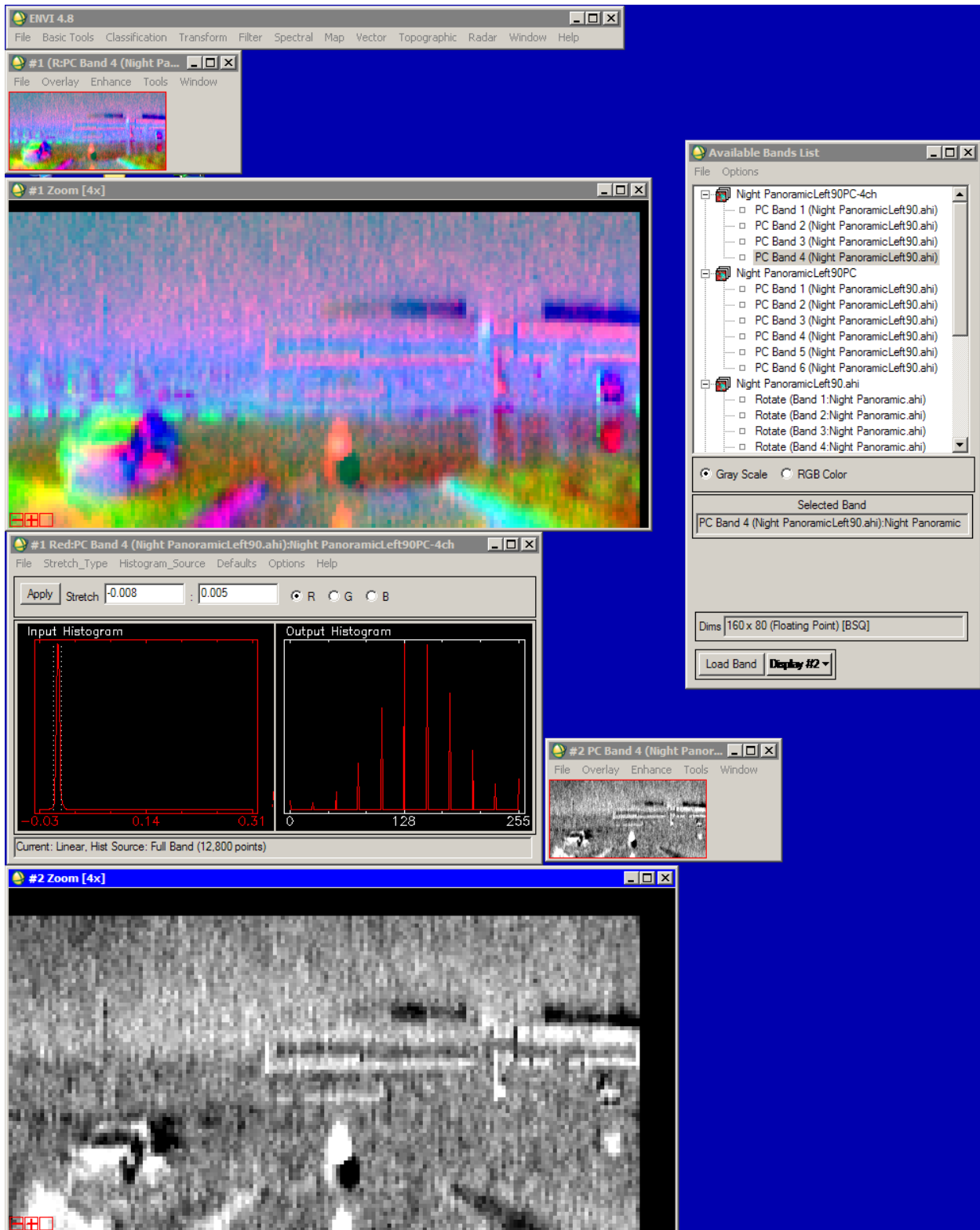


Figure 7.2. ENVI Example Screen Shot



**Figure 7.3.** Overlay of Colorized Polarization Channels with Gray-Scale Intensity Channel

## 7.1 Stokes Parameters and Multivariate Image Analysis

The radiometer data channels are the four linear and two circular polarization states. It is often useful to transform them into Stokes parameters. Another approach is to use multivariate image analysis (MIA). MIA exploits the interplay between spatial (inter-pixel) and statistical (inter-variable) correlations. The main analysis tool is principal component analysis (PCA). The number of components is equal to the number of variables (six in our case). The data are visualized using score plots (two-dimensional scatter plots of one principal component against another). These can be used to examine data structure interactively in the images. It will be seen that PCA provides very similar (but not identical) results to classical Stokes analysis.

## 8.0 Calibration

We conducted a literature search into techniques to calibrate the mm-wave HPCR system in order to develop a means of creating calibration matrices to apply to each of our polarization channels in order to increase our ability to detect small signal responses and filter out contributions from other channels into the channel of interest. We developed preliminary designs to calibrate the mm-wave HPCR. One technique uses a coherent polarization generator shown in Figure 8.1 to calibrate all six polarization states of the polarimetric radiometer. Thermal polarimetric calibration standard techniques have also been investigated. The millimeter-wave components for fabricating the coherent polarization generator were received and assembled together for calibrating the mm-wave HPCR system. Figure 8.2 shows the fabricated coherent polarization generator for calibrating the mm-wave HPCR. This calibrating source creates an accurate single frequency either left hand or right hand circular polarized signal. Adjusting the phase makes it generate either left or right circular polarized signals, which we can use to obtain the appropriate  $T_l$  and  $T_r$  detector outputs of the radiometer.

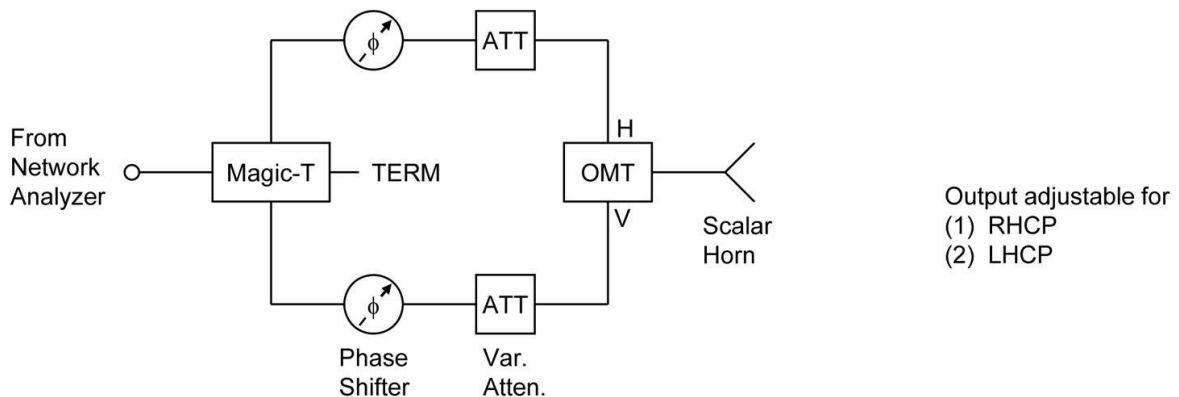


**Figure 8.1.** Coherent Polarization Generator for Calibrating the mm-wave HPCR



**Figure 8.2.** Coherent Polarization Generator

The test system was evaluated with imaging 2-D scanners and calibration equipment. The two channels in the millimeter wave polarimeter receiver (vertical and horizontal) were phase-aligned for optimum signal performance.

## 8.1 Radiometric Sensitivity

The radiometric sensitivity of the radiometer was measured and calculated as follows.

- Measurements were conducted using heated and cooled sources
  - Heated blackbody (~ 50°C) - Section 8.2
  - Liquid nitrogen cooled absorber (cooled blackbody) - Section 8.3
- H channel lock-in output (3 mV scale, t = 300 msec)
  - Signal measured at 169.5 mV/K
  - Noise approximately 18 mV
  - NEDT = 169.6/18 = 0.107 K

$$\text{NEDT} = \frac{2(T_{\text{sys}} + T_0)}{\sqrt{\tau B}}$$

- V channel lock-in output ( 3 mV scale, t = 300 msec)
  - Signal measured at 152.4 mV/K
  - Noise approximately 17 mV

- $NEDT = 152.4/17 = 0.110 \text{ K}$
- Theoretical sensitivity ( $BW = 2 \text{ GHz}$ ,  $t = 300 \text{ msec}$ )
  - $NEDT = 0.146 \text{ K}$

## 8.2 Heated Black Body Calibration

An incoherent polarimetric source (Figure 8.3) was constructed using a black body heated to  $50^\circ\text{C}$ , a linear wire-grid polarizer, and a quarter-wave plate made of sub-wavelength grooved Rexolite.

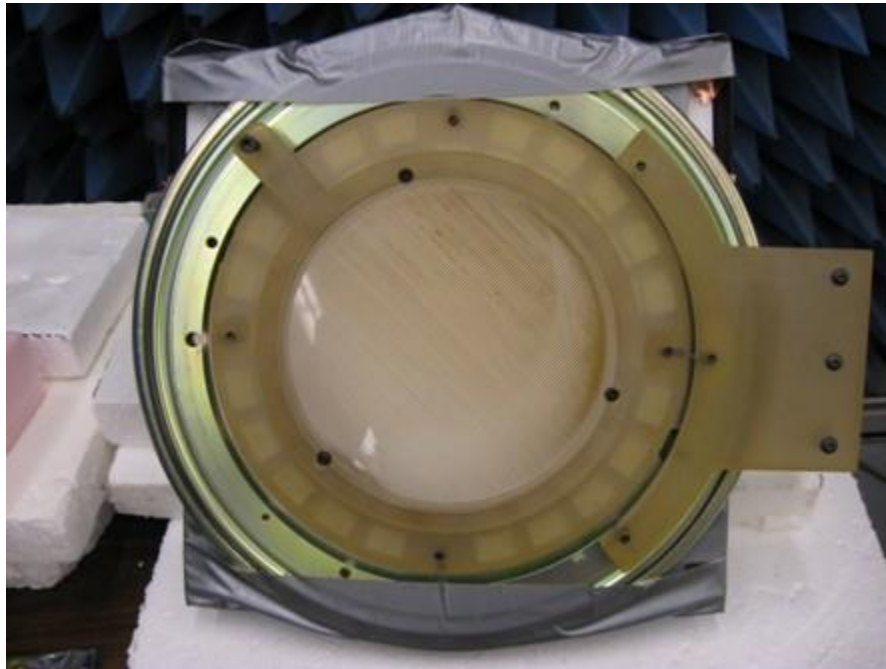


**Figure 8.3.** Incoherent Polarimetric Calibration Source

## 8.3 Liquid-Nitrogen Calibration

Figure 8.4 shows a liquid-nitrogen calibration test of the dual radiometer. Each of the foam cups in the foreground contains liquid nitrogen at ambient pressure. The turning mirrors reflect radiation from the cold surface toward the receiving horns, as shown in detail in Figure 8.5. The parabolic mirrors (seen in the background) are not being used.



**Figure 8.4.** Liquid-Nitrogen Calibration of Dual Radiometer

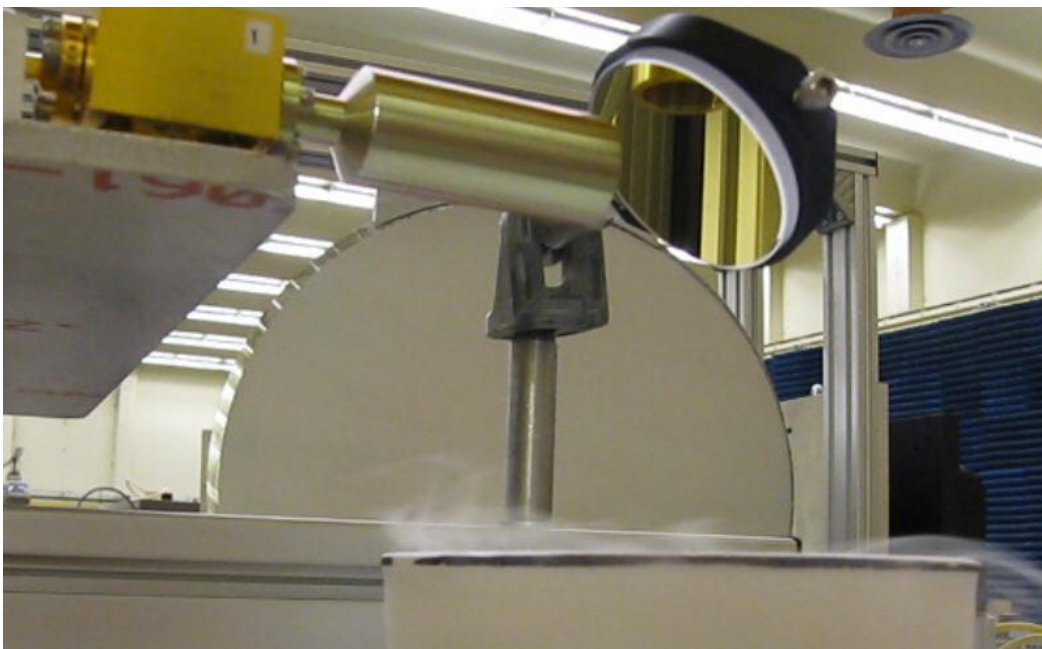


**Figure 8.5.** Liquid-Nitrogen Calibration of Dual Radiometer: Detail of Horn and Turning Mirror

## 8.4 Coherent Polarization Generator Calibration

The coherent polarization generator is used to calibrate the polarimeter, but the generator itself first had to be calibrated. The purpose of the calibration was to introduce a phase shift into the vertical channel such that the phase difference between the horizontal and vertical channels would be exactly  $90^\circ$ . An Agilent E8361A PNA network analyzer was used to perform this calibration.

The measurements were carried out at 93 GHz. The network analyzer's electrical delay was set to adjust the phase of the horizontal channel, which has no phase shifter, to zero degrees. The same electrical delay was used in phase measurements for both horizontal and vertical channels.

The setups for the horizontal and vertical channel phase measurements are shown in Figure 8.6 and Figure 8.7, respectively. To measure each leg, attenuators are placed in the other leg to reduce the unwanted signal to a negligible level (55 to 60 dB below the signal of interest).

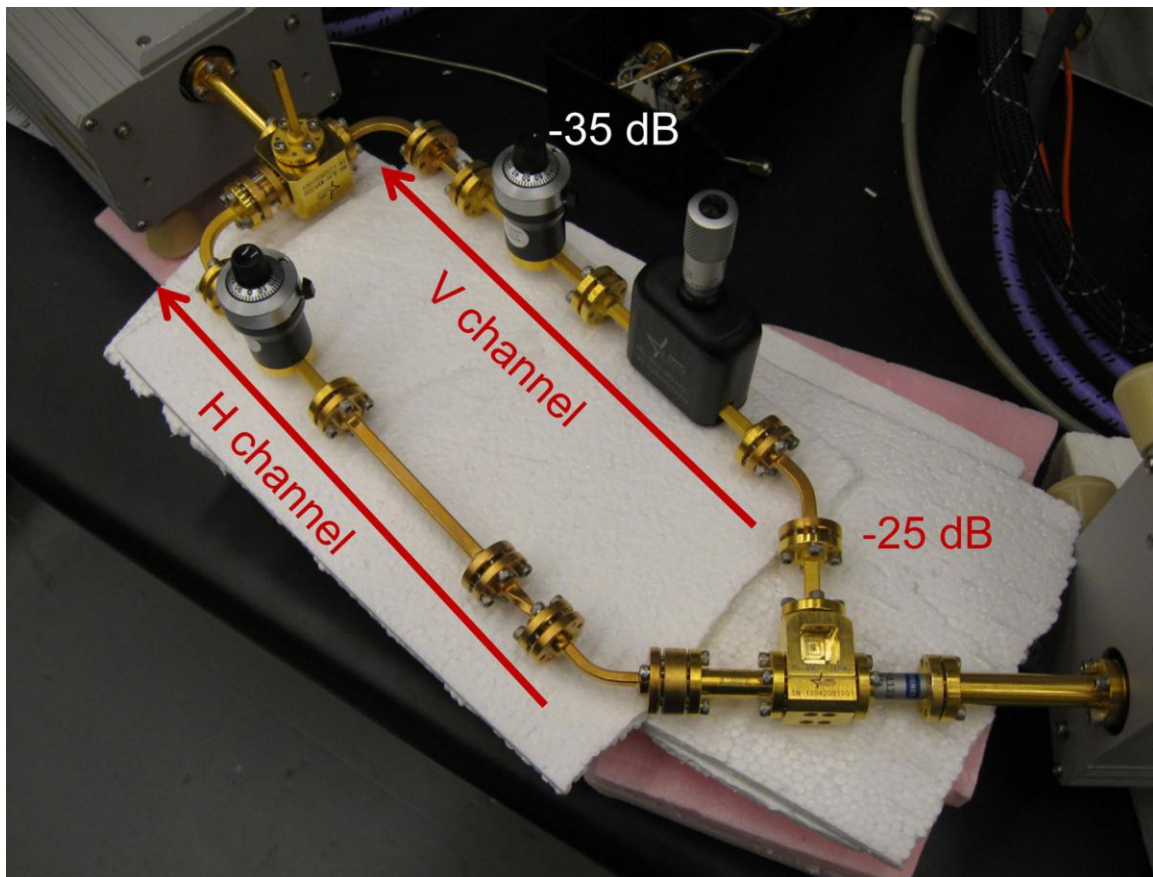


**Figure 8.6.** Coherent Polarization Generator: Horizontal Channel Phase Measurement

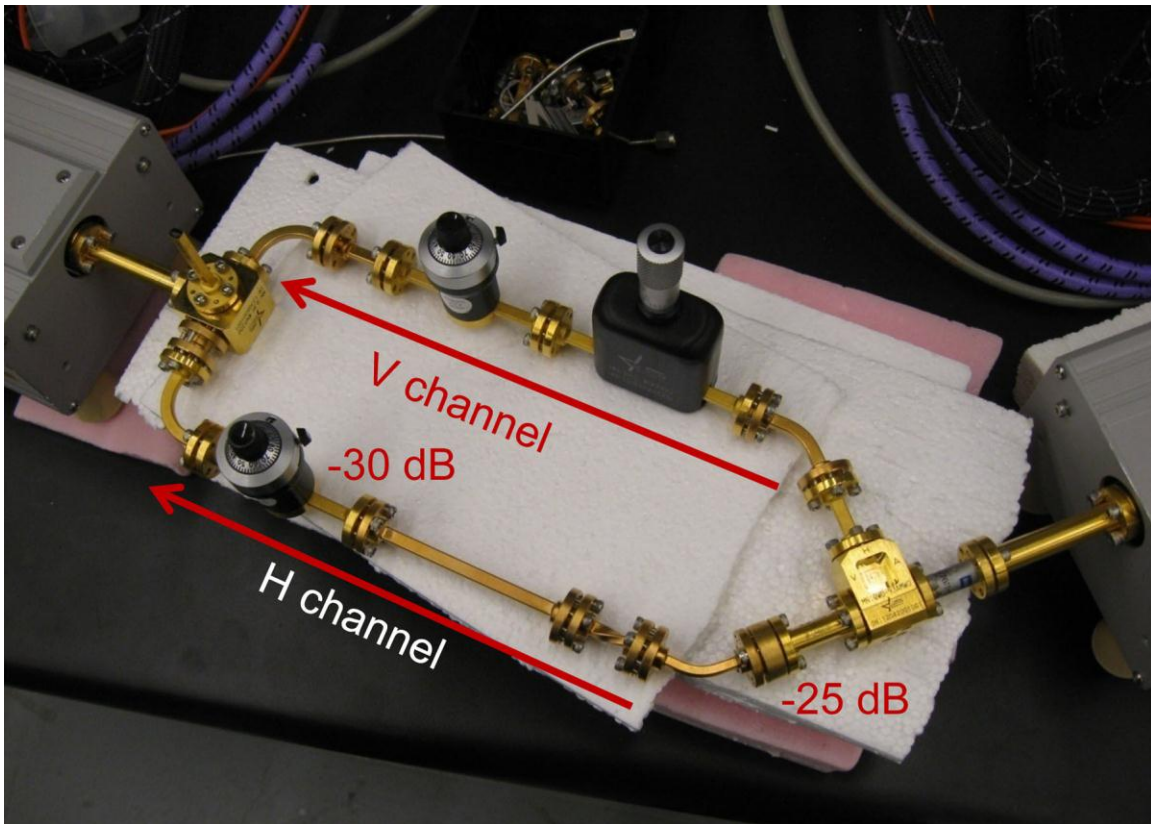


**Figure 8.7.** Coherent Polarization Generator: Vertical Channel Phase Measurement

The phase in the horizontal leg was measured as  $0.195^\circ$ , and in the vertical as  $90.246^\circ$ . The measured phase difference was thus  $90.051^\circ$ , which is acceptably close to the desired value of  $90^\circ$ .

## 8.5 Design of a Quarter-Wave Plate Using Simulated Dielectrics

### 8.5.1 Introduction

Roving Eye is intended to operate in the W-band region of the millimeter wave band, from 91 GHz to 95 GHz. Since this is a full Stokes polarimeter, careful calibration is essential to ensure reliable performance and data integrity. The basic calibration approach is to initially use an active millimeter wave source as a test signal to the polarimeter. This input wave form must be polarized vertically and horizontally with respect to the propagation coordinate frame, at  $\pm 45^\circ$  with respect to the x- and y-axes of this right-handed Cartesian coordinate system, as well as circularly polarized. One obtains circularly polarized electromagnetic wave propagation by transmission of a vertically polarized wave field through a quarter-wave plate oriented at  $45^\circ$  with respect to the vertical axis.

Quarter-wave plates are not readily commercially-available in W-band so we must construct one. As is true in visible optics, one can be made using crystal quartz by controlling the thickness such that the phase difference between light polarized with respect to the x- and y-axis are  $90^\circ$  out of phase. The controlling equation for the phase shift provided by the birefringent wave plate is given below.

$$\Delta\varphi = \frac{2\pi d \Delta n_{xy}}{\lambda} \quad (8.1)$$

At the center frequency of the instrument design, 93 GHz, the  $\Delta n$  of crystal quartz is 0.047. This results in a required thickness of the quartz plate of 17.16 mm to achieve a  $90^\circ$  phase difference. Since the index of quartz at 93 GHz is 2.1, reflective losses from each surface of the plate result in an insertion loss (neglecting absorption losses) of 0.58 dB (power) for each surface, for a total insertion loss of 1.16 dB. Fortunately, there is an alternative method of producing a birefringent surface using the anisotropy provided by grooved sub-wavelength structures in dielectrics that gives us an effective dielectric constant (and hence index of refraction) that is lower than that possible using quartz. The lower refractive index results in lower Fresnel losses due to surface reflections and lowers the insertion loss.

### 8.5.2 Quarter-Wave Plate Design

For the approach using form birefringence, the equation above that describes the phase shift as a function of  $\Delta n$ , component thickness and design wavelength is the same as that using naturally birefringent materials. The difference in the approach using form birefringence is the ability to tailor (within limits) the  $\Delta n$  value depending on the duty cycle of the land and groove structure of the wave plate design. The equations that govern the effective index of the ordinary and extraordinary indices of the simulated dielectric design are given in the equations below (Lahtinen and Hallikainen 2003).

$$\begin{aligned} n_x &= \sqrt{\frac{t_1 \epsilon_1 + t_2 \epsilon_2}{t_1 + t_2}} \\ n_y &= \sqrt{\frac{\epsilon_1 \epsilon_2 (t_1 + t_2)}{t_2 \epsilon_1 + t_1 \epsilon_2}} \end{aligned} \quad (8.2)$$

In these equations,  $\epsilon_2$  is the dielectric constant for the grooves, which is 2.56 for Rexolite, and  $\epsilon_1$  the dielectric constant for the lands, which we assume to be air with a value of 1. The width of the lands is  $t_1$  and the width of the grooves is  $t_2$ . The wave plate is a dielectric slab made of Rexolite 1422 with grooves machined on one face. The group velocities are different from electromagnetic waves polarized parallel and perpendicular to the grooves, which results in a phase shift between the two polarizations (van Vliet and de Graauw 1981).

### 8.5.3 Groove Design

The phase delay imparted by the wave plate is dependent upon the change in index of refraction parallel and perpendicular to the grooves. The plot below shows the indexes as the duty cycle is varied from 0 to 100% for the land.

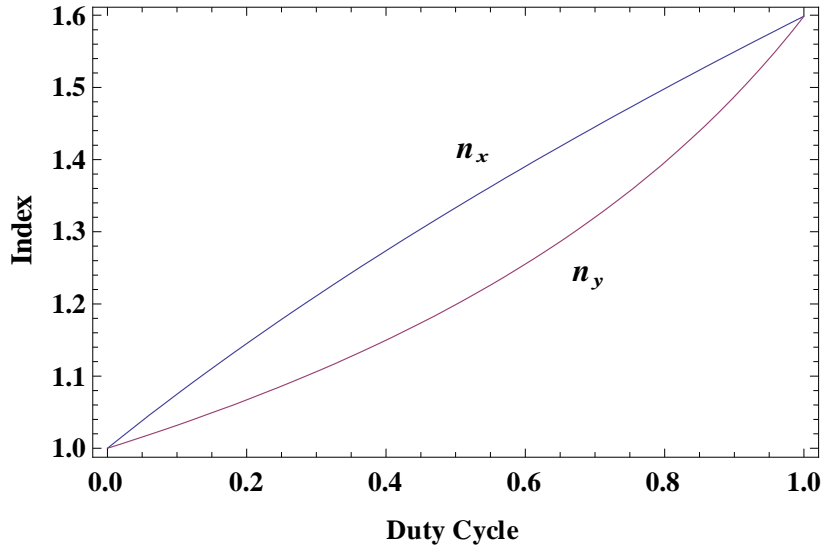


**Figure 8.8.** Calculation of  $n_x$  and  $n_y$  as a Function of Duty Cycle for the Land and Groove Structure of the Wave Plate Surface. One can see that the absolute values of the structures, so long as they are much smaller than the incident radiation wavelength, are not as important as the ratio of land to groove width.

Of course, the item of paramount importance is the quantity  $\Delta n_{xy}$ . As can be seen in Figure 8.9, the maximum value of  $\Delta n_{xy}$  is *nearly* maximum at a duty cycle of 50%, but its true maximum is at a land/groove ratio of 0.56/0.44.

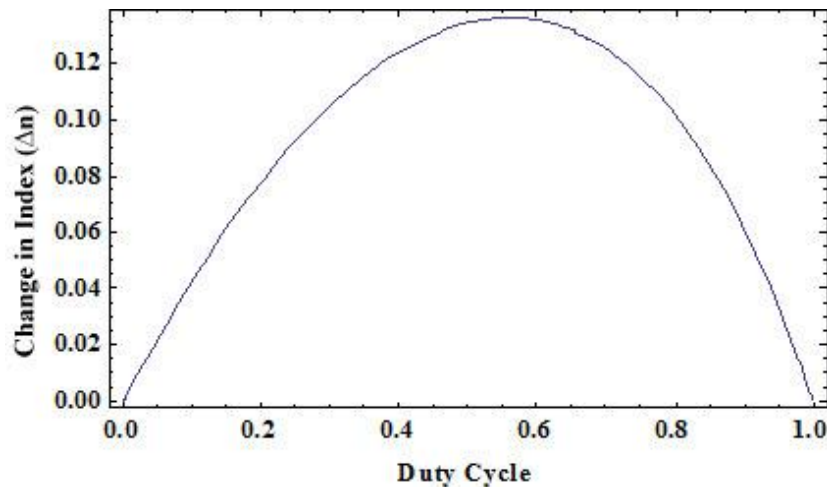


**Figure 8.9.** The Plot Above Showing the Value of  $\Delta n_{xy}$  Versus the Duty Cycle of the Land/Groove Structure Reveals the Maximum Value Occurs at 0.56

To ease manufacturing of the wave plate, we choose a duty cycle of 50%. This will result in a  $\Delta n_{xy}$  value of 0.134. For a design wavelength of 93 GHz, the corresponding wavelength is 3.22 mm.

Additionally, we select a pitch value of  $\lambda/4$  for the land/groove cycle, which has a value of 0.806 mm. We can use the expression below to calculate the required groove depth in Rexolite

$$d = \frac{c\varphi}{2\pi f \Delta n_{xy}}$$

$$d = \frac{3 \cdot 10^{11} \frac{\pi}{2}}{2\pi 93 \cdot 10^9 \cdot 0.134} \quad (8.3)$$

$$d = 5.9999 \text{ mm}$$

Thus, we require a groove depth of 6.00 mm. A cross section of the land and groove profiles is shown in the Figure 8.10 for a portion of the wave plate surface. Approximately 189 grooves must be machined into the surface for a 152.4-mm-diameter component.

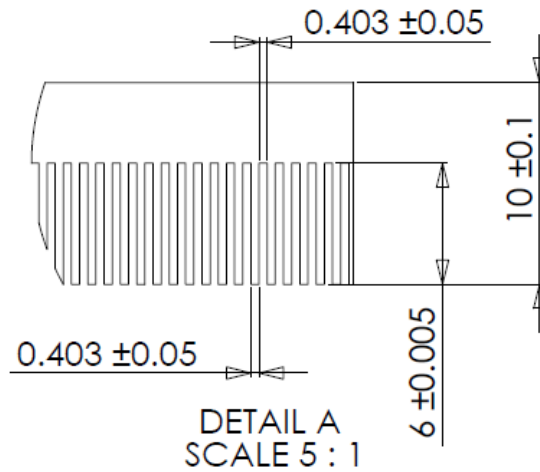


**Figure 8.10.** Detailed Drawing Showing the Land and Groove Structure of the Quarter-Wave Plate Design

The final design is summarized in the table below.

Parameter	OD, mm	CT, mm	Land Width, mm	Groove Width, mm	Groove Depth, mm	Material
Value	152.4 + 0/-0.1	10.0 ± 0.1	0.403 ± 0.050	0.403 ± 0.050	6.000 ± 0.005	Rexolite 1422

Three wire-grid polarizers and three quarter-wave plates were specified, ordered and received to support the calibration of the polarimetric radiometer. These calibration devices are used as field calibration devices for the radiometer. Figure 8.11 shows one of the fabricated 6-in.-diameter quarter-wave plates. The millimeter-wave polarimetric radiometer was calibrated and phase-aligned. In addition, a millimeter-wave noise source was purchased to support field calibration activities.



**Figure 8.11.** Fabricated 6-in.-Diameter Quarter-Wave Plate

## **8.6 Establishment of Calibration Protocols**

Three wire grid polarizers (WGP) were specified and ordered to provide simple field calibrations. The specifications for the WGP are as follows: 6-in. frame wire grid polarizer with 0.001-in. wire diameter 200 wires/inch. Additionally, a quarter-wave plate (QWP) intended for use at millimeter-wave frequencies was designed and a purchase order was placed with American Dicing Inc. to fabricate three of these calibration devices. The WGP and the QWP are used in the calibration of the millimeter wave polarimeter receiver.

We designed a field calibration method to determine the operation of each of the six output channels of the radiometer by presenting two input sources: blackbody and skyshine. The device takes either source as the input and through the combination of a polarizer and quarter-wave plate provides signals to maximize each of the six output channels of the radiometer to ensure its proper operation prior to a field campaign. The field calibration device is shown in Figure 8.12.

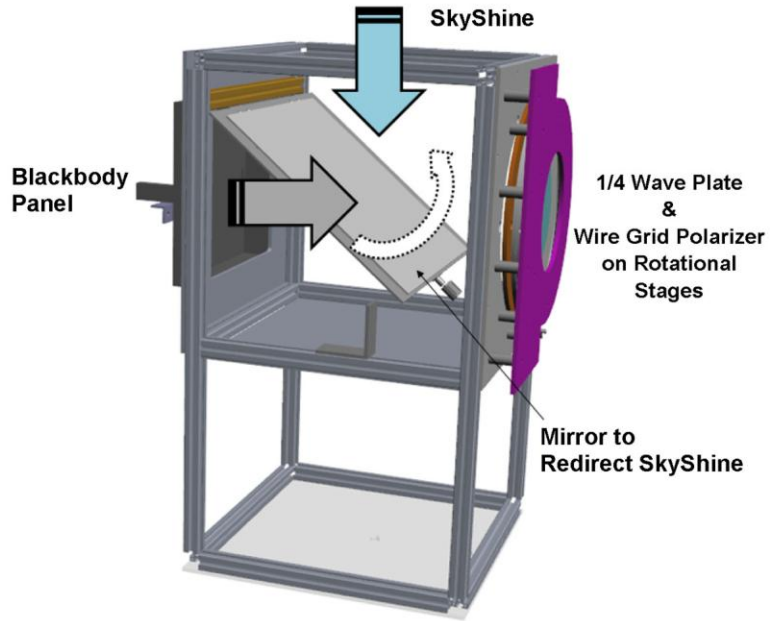


**Figure 8.12.** Field Calibration Device



## 9.0 Monocular System

### 9.1 Overview

The monocular system consists of a single focusing mirror and one or two mm-wave receivers. In most cases the monocular system only performs a single radiometric measurement comparing the received brightness temperature to a reference load. However, to collect differential measurements on the monocular system, the loads on both the horizontal and vertical channels are replaced with a second OMT – horn input.

### 9.2 Development of the Monocular System

The millimeter-wave polarimeter receiver integrated with the single reflector OAP and computer/motor control scanning (azimuth and elevation) was the first system completed. Existing data acquisition software was upgraded to allow for remote scanning operations on an elevated platform. The upgraded software allows for both the millimeter-wave receiver data and optical images to be captured remotely so that an operator is not required to stand on the elevated platform for imaging studies. Figure 9.1 shows the millimeter-wave polarimeter receiver staged on a scissor jack for lookdown imaging experiments.



**Figure 9.1.** Millimeter-Wave Polarimeter Receiver Staged on Scissor Jack

Data acquisition and image display software was modified for the polarimeter. Passive millimeter-wave imaging studies on natural and man-made structures were performed with the system.

Figure 9.2 shows the setup of the first outside imaging experiment with the millimeter wave polarimeter receiver system.

Figure 9.3 shows one of the first passive mm-wave polarimeter images of a PNNL parking lot and building.



**Figure 9.2.** Outside Imaging Study Setup of mm-wave Polarimeter Receiver System



**Figure 9.3.** Visible Photo and Passive-mm-wave-Polarimeter Image of PNNL Parking Lot and Building. The visible photo was taken earlier in the day, so some cars had been moved before the mm-wave image was taken.

## 9.3 Measurements with the Monocular System

### 9.3.1 Initial Measurements

Passive-millimeter-wave imaging studies on natural and man-made structures continued with the single reflector OAP system. Numerous polarimetric imaging studies were conducted with this system as the weather permitted. Figure 9.4 shows the visual scene from one of our passive millimeter-wave imaging experiment setups with a blackbody radiator in the foreground. The blackbody radiator was coupled to a wire grid polarizer and a quarter-wave plate to generate calibrated circular polarized millimeter waves in the polarimetric radiometer field-of-view. Figure 9.5 shows the full Stokes parameters (**I**, **Q**, **U**, **V**) from the radiometer. **I** represents the total power (sum of both the vertical and horizontal electric fields), **Q** represents the difference of the vertical and horizontal power components defined by the image geometry. The **U** Stokes parameter is typically measured by correlating two orthogonal linear polarization states. The **V** Stokes parameter evaluates the differential of the left- and right-hand components of circular polarization, which is why the blackbody radiator with the wire grid polarizer and quarter-wave plate is observable in the **V** imagery. Detail analysis of the Stokes images shown in Figure 9.5 reveals strong horizontal polarization signals in the **Q** image, which is expected. A strong  $+45^\circ$  return is detected in the **U** image originating from the automobile curved windshields, and strong left circularly polarized (LCP) emission is seen in the **V** image in general. Stronger returns emanate from the polarization source, as well as the automobile panels that subtend adequate sky shine. Additionally, the clouds also produce strong circularly polarized image features. These observations were facilitated by stretching the image histograms of the **Q**, **U**, and **V** images (Figure 9.6).



Blackbody radiator with wire-grid polarizer and quarter-wave plate

**Figure 9.4.** Visible Image for Polarimetric Radiometer Imaging Study with Blackbody Radiator in Foreground

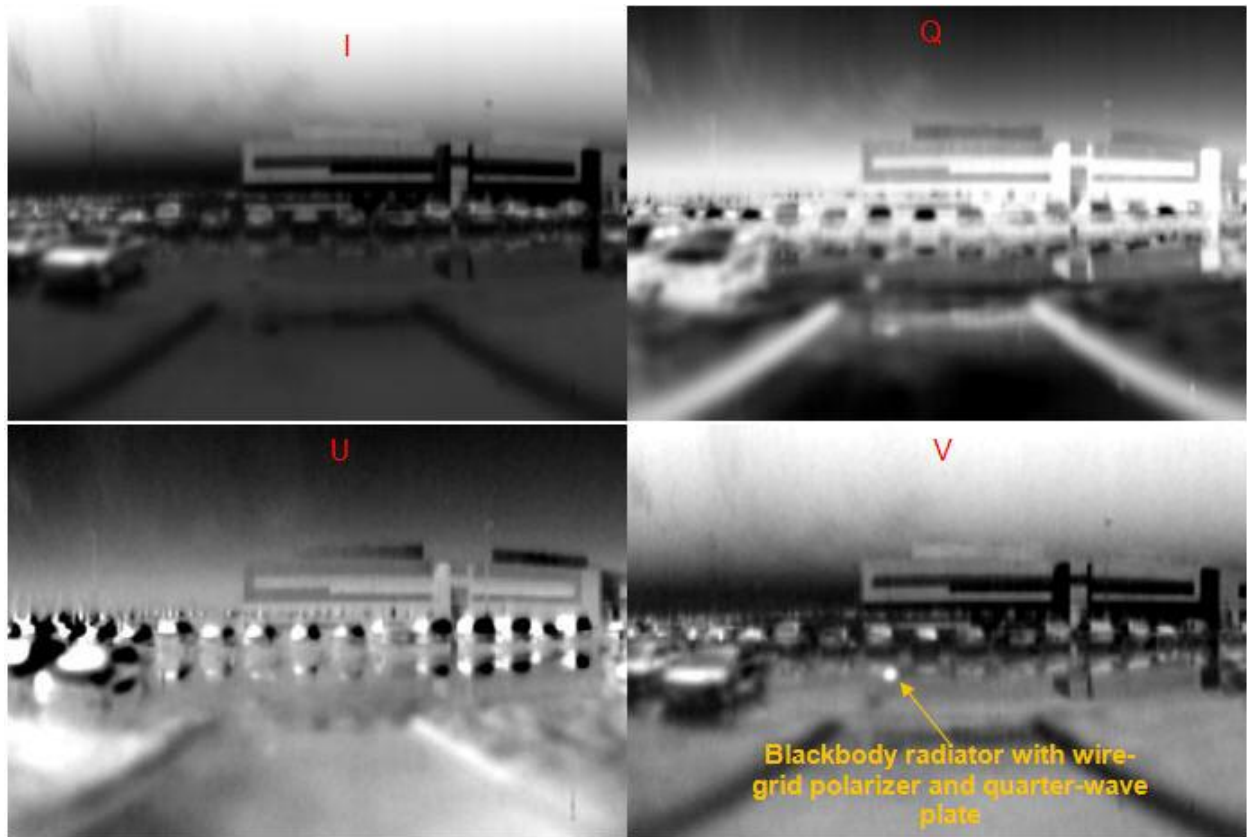


**Figure 9.5.** Stokes Parameters of Passive Polarimetric Radiometer Imaging Results

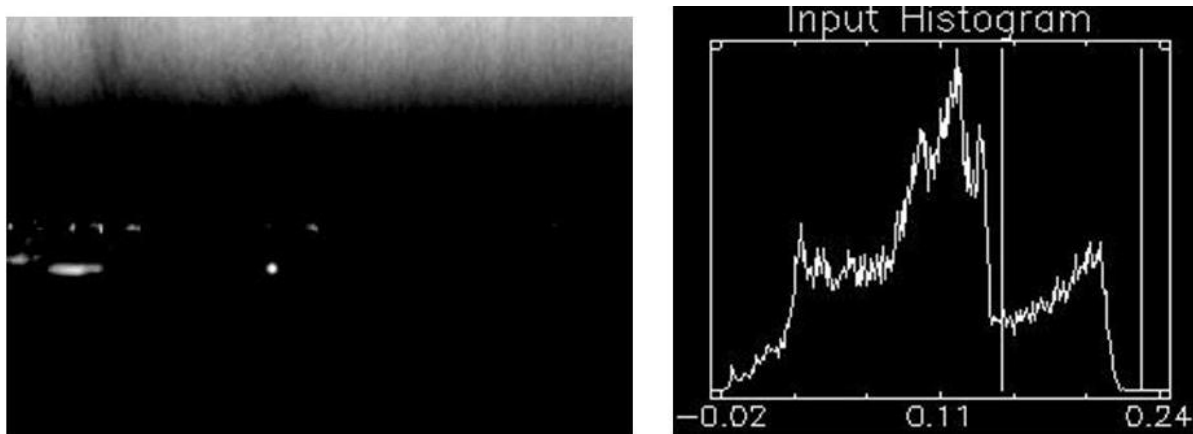


**Figure 9.6.** Stokes V Channel with the Gray Scale Stretched, as Shown in the Histogram, to Show Only the High-Amplitude Circularly Polarized Data

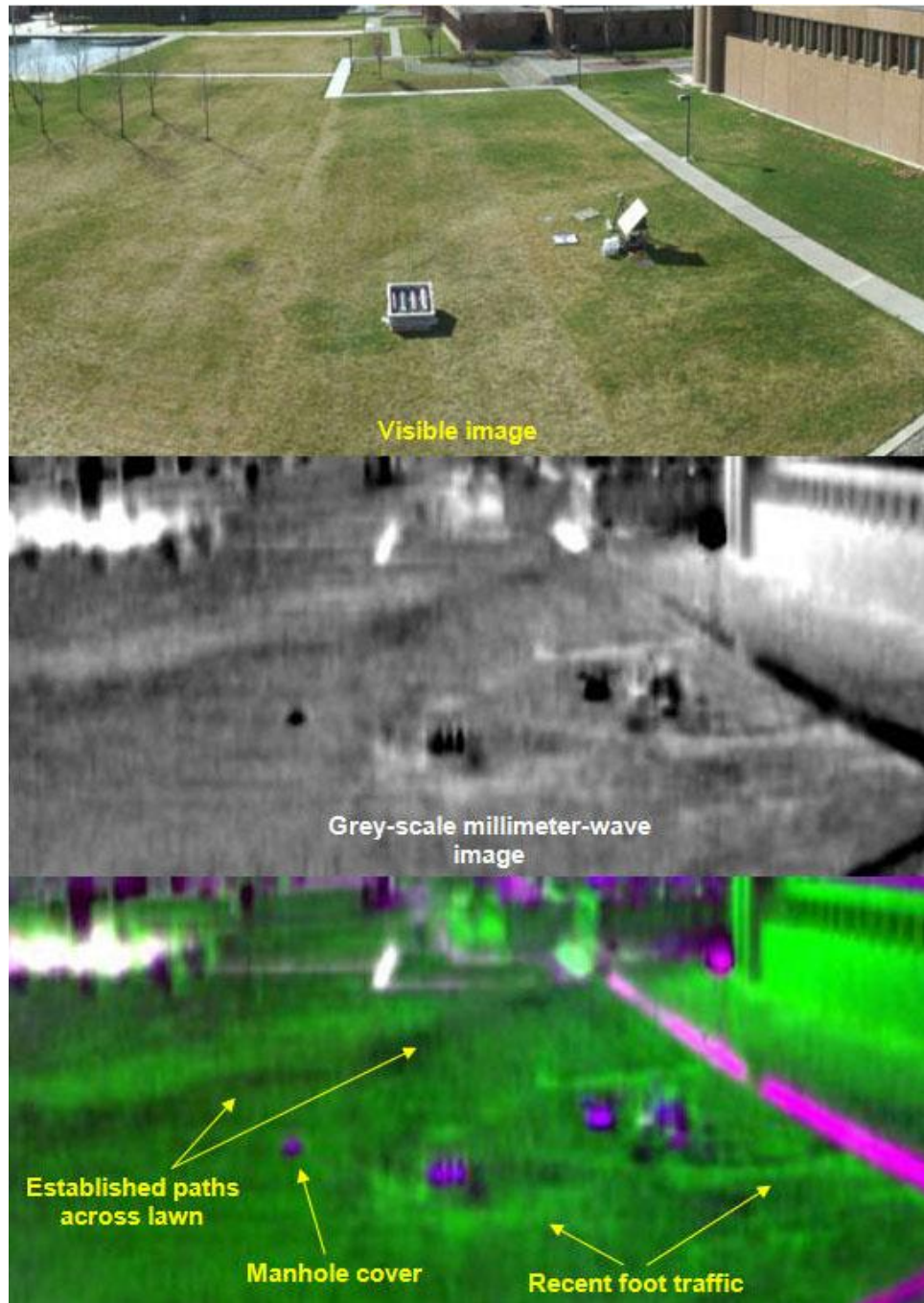
### 9.3.2 Elevated Platform Measurements

We performed numerous look-down imaging studies from an elevated platform (scissor jack) on various liquids (both polar and non-polar) and various structures and objects (both buried under sand and not buried). Figure 9.7 shows the radiometer and the OAP scanner on an elevated platform. The platform was used to simulate an airborne operation. The scissor jack was elevated to 36 ft and the telescope was tilted down by 30 degrees. The sample sand box was tilted up by 12.4 degrees. The distance to the sample box was 60 ft–72 ft.



**Figure 9.7.** Radiometer and OAP Scanner Elevated 36 ft on Scissor Jack

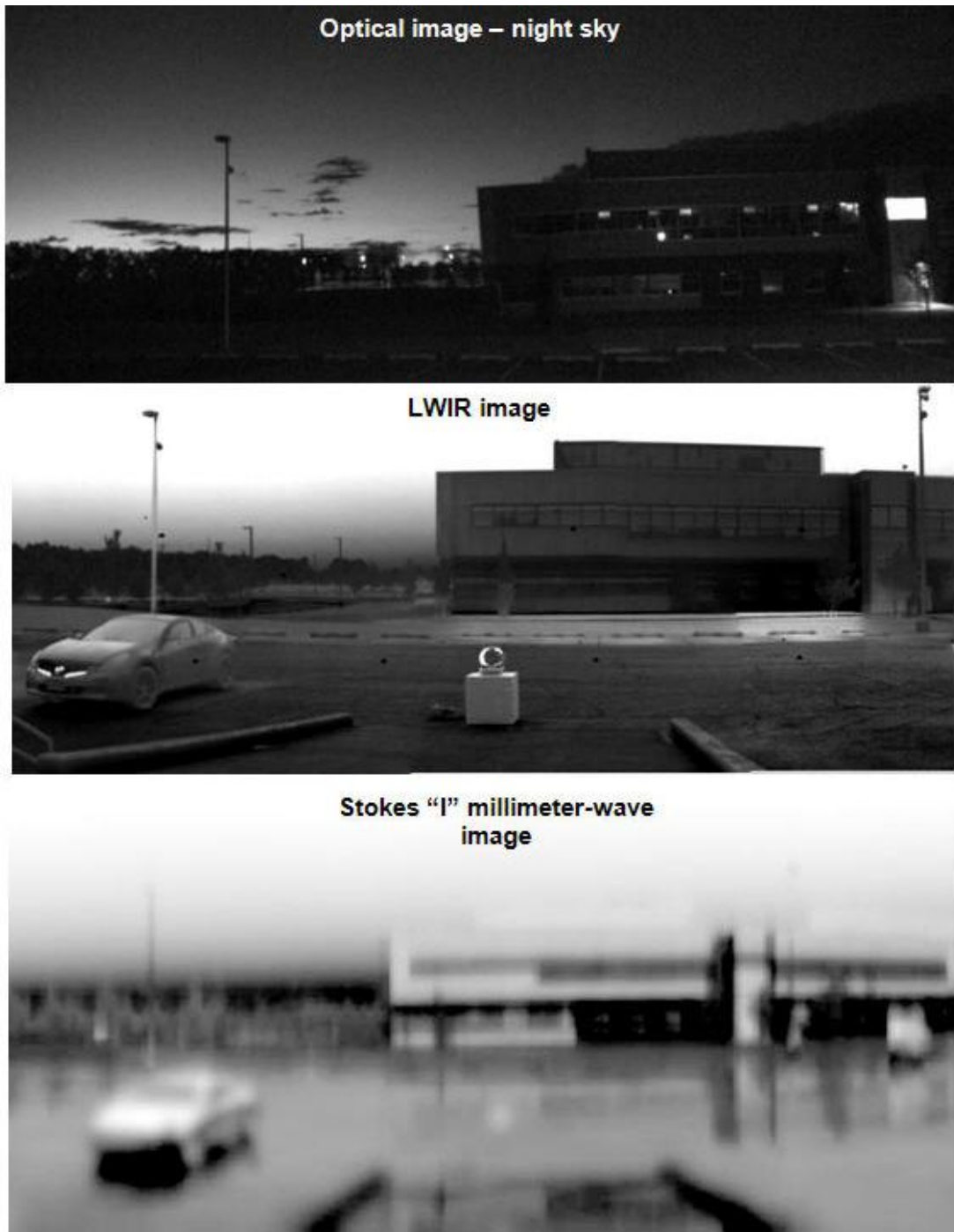
Narrow and wide angle imaging studies were conducted with the polarimetric radiometer and OAP scanner on sample sandbox. Figure 9.8 shows two renderings of a passive millimeter-wave image of sample box and PNNL campus lawn. One image is grey-scale and the other is pseudo-color that highlights the foot traffic in the lawn and some of the metal targets as well.



**Figure 9.8.** Wide-Angle Image of Sample Sand Box (4 pipes in sandbox: 4-, 6-, 6-, 8-in. diameters)  
 Top: visible image, middle: U-channel image, bottom: QUV RGB image.

### 9.3.3 Characterization and Resolution Measurements

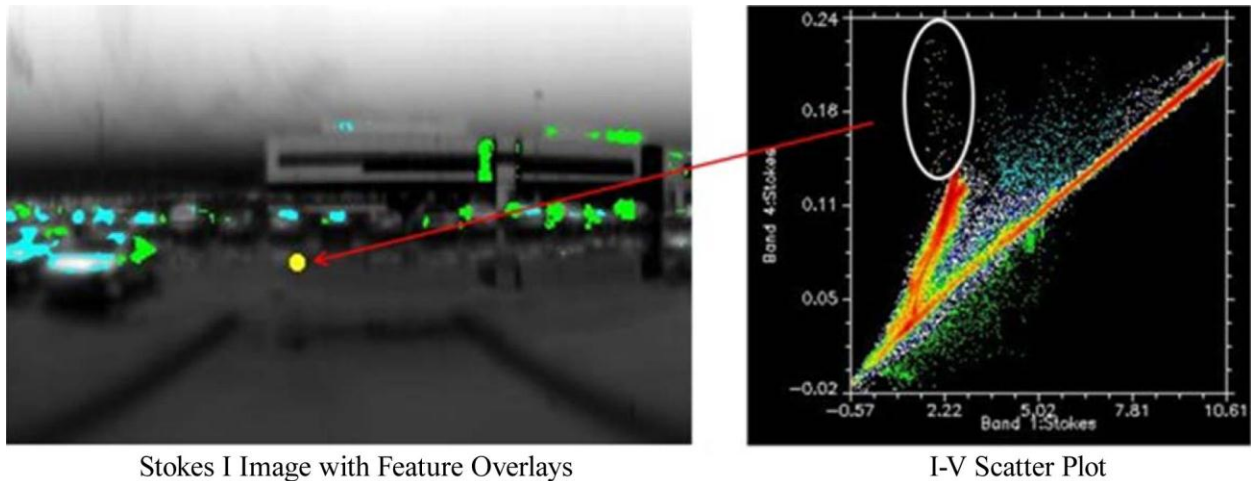
Nighttime imaging studies were conducted with the passive polarimeter radiometer and compared against optical and long wavelength infrared (LWIR) Images. The imaging results are shown in Figure 9.9. The results show that passive millimeter-wave imagers can “see” at night.



**Figure 9.9.** Nighttime Imaging Results of Optical, LWIR, and Passive Millimeter Wave. The brightness was logarithmically stretched in the mm-wave image to exploit the full dynamic range of the scene.

Polarimeter radiometric imaging results were analyzed using both Mathematica-based methods and ENVI, a commercial hyperspectral image processing software package. The image cube produced by the radiometer is analogous to a multispectral image cube and the additional processing necessary to form the

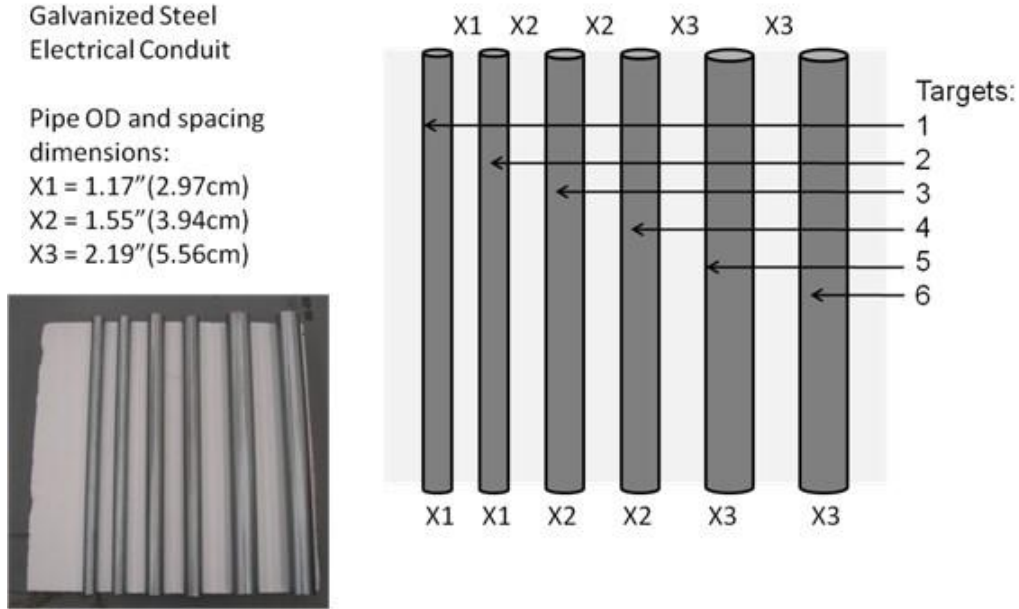
Stokes images and image enhancement methods using the raw polarimeter outputs is easily accomplished using ENVI. Figure 9.10 shows an example of the anomaly detection imaging analysis using a 2D scatter or score plot to identify regions of interest in the V vs. I plot. The density of pixels shows that areas of interest (AOI) lie on the periphery of the densely shaded regions. The AOIs are selected and classified according to the different pixel colors, and the image pixels which map into these AOI are highlighted in the image on the left. We have also shown that methods of MIA based upon principal component analysis and score plots can uncover regions of interest quickly and intuitively as opposed to scene-based analysis. Additionally, the principal components correspond to the Stokes vectors.



**Figure 9.10.** Stokes I Image with Feature Overlays and Stokes I-V Scanner Plot

Imaging studies were also performed using a finite conjugate reflector focusing at 5m. This work was done to address a suggestion of the external review panel that wanted to know what the theoretical spatial resolution is for our polarimetric radiometer. Various imaging studies were conducted on targets consisting of curved surfaces that produce known polarization changes with overhead skyshine. These resolution targets were used to determine the lateral resolution of this passive millimeter-wave system.

Figure 9.11 shows the resolution target geometry and configuration using various diameters of galvanized steel electrical conduit pipes.



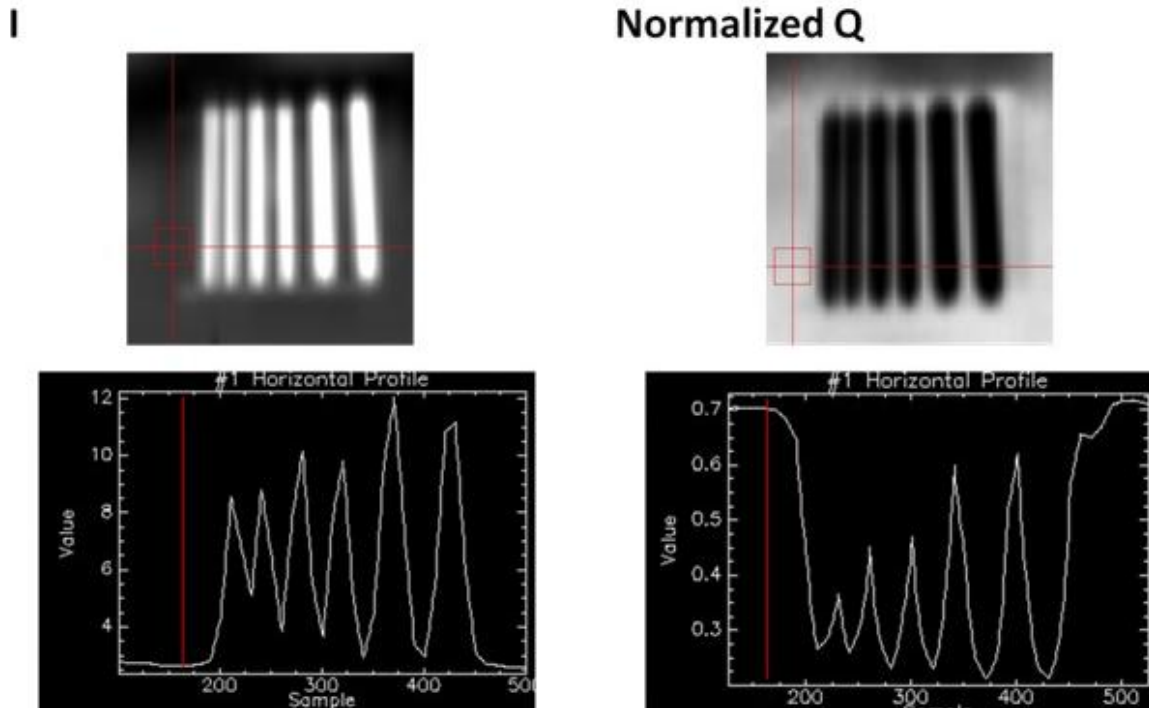
**Figure 9.11.** Resolution Target Pattern Configuration

Figure 9.12 shows the imaging test setup and the radiometer with the finite conjugate (5 meter) reflector surface.



**Figure 9.12.** Finite Conjugate Test Setup

Figure 9.13 shows the imaging results of the finite conjugate reflector mirror. The imaging results shows the amplitude I and normalized Q results (difference between vertical and horizontal projection of the reflected skyshine). As can be observed in the imagery, the finite conjugate reflector mirror can readily obtain lateral resolution on the order of 1.17 in., which is less than  $(\lambda/D) \times 5 \text{ m}$ , the theoretical Rayleigh limit of standard resolution for reflected plane wave radiation.



**Figure 9.13.** Passive Millimeter-Wave Imaging Results of Resolution Pattern Using Various OD Pipes

An extensive library of finite conjugate passive mm-wave images was developed and more images are shown in Appendix F, section F2. Imaging studies include, targets of unique geometry, buried targets, and differential imaging sets.

### 9.3.4 Long-Distance Measurements

Long-distance imaging from a mountain is the nearest approach to airborne imaging attainable with the present system. We used the single-ended radiometer and infinite conjugate (parabola) single element telescope by imaging the Yakima River in the vicinity of Benton City, Washington, from an elevated vantage point on BLM land. Initial results were satisfactory and provided a rich tapestry of natural (water and different vegetation types) and man-made objects (buildings, power lines, and roads). The instrument was truck-mounted and operated by generator power and performed flawlessly. It was hoped to perform further scans from a higher vantage point with fewer foreground obstacles to better simulate airborne operation, but project resources did not permit this. Imaging tests showed definition of terrain orientation, material composition (e.g., water, land, roads), buildings, and vegetation based on the received brightness temperature, as shown in figures 9.14-9.16.

The composite photograph below, Figure 9.14, is a view of Benton City, Washington, looking northeast from McBee Road on McBee Mountain. The following figures (Figure 9.15 and Figure 9.16) show mm-wave data overlaid on the photograph. The data are color-coded by mapping the Stokes V, Q, and I parameters to red, green, and blue (R, G, and B), respectively.



**Figure 9.14.** Benton City, Washington, from McBee Mountain, with the Yakima River in the Mid-Ground and Rattlesnake Mountain in the Background



**Figure 9.15.** Overlay of mm-wave Data at 50% Opacity on the Photograph. The data represent Stokes parameters V, Q, U mapped to red, green, blue (RGB), respectively. The water can be seen to correspond to dark areas. The foreground object is not well registered because of the difference in perspective between the camera and the mm-wave telescope.

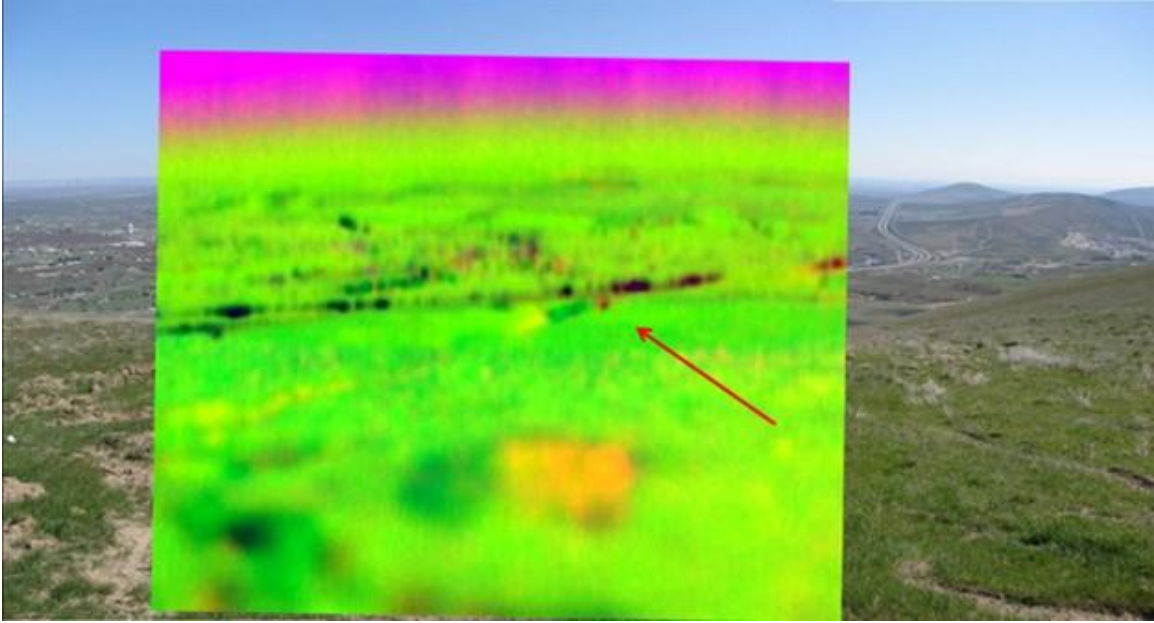


**Figure 9.16.** Overlay of mm-wave Data at 100% Opacity. The arrow indicates an object near the river (near the highway overpass) that is not readily visible in the photograph, but highly visible as a red circle in the V parameter data. Benton City shows up in different colors from the surrounding countryside.

## 9.4 Near-Field Imaging Results

Work was performed for near-field imaging of concealed objects buried in various types of soils using the 5-m focal length finite conjugate imager (ellipsoid). This was accomplished using a vacant volleyball court on PNNL-leased property as well as silica sand kept for experiments of this type. Imaging studies with the finite conjugate single reflector radiometer continued with determining the penetration depth of mm-waves through soils, and various sands (some rich in quartzite are quite transparent, while others richer in iron minerals are actually magnetic – yet surprisingly still ‘transparent’ despite their relatively high losses). As mentioned, further studies of the causes for changing polarization effects of buried objects contribute to understanding how curvature in objects translates to different Stokes representations of the net mm-wave field that is remitted from buried objects. Imaging studies looked at buried pipes, conduits, twisted cables, buried surrogate IEDs, and polar liquid spills including organophosphorus compounds used in reprocessing.

Figure 9.17 shows scanning of a set of pipes buried under silica sand. Initially, the pipes were buried under the sand-gravel mixture used for the court, but that mixture was found to be opaque to the millimeter waves due to the high ferrite and aggregate contents in the soil



**Figure 9.17.** Scanning Buried Pipes in Volleyball Court. The silica sand used to bury the pipes can be seen as a light-colored square. A canopy used for shade to prevent overheating of the laboratory electronics is seen at right. The silver tarpaulin on the laboratory cart contains more silica sand.

The following figures show the pipe set and Stokes Parameters images of scans under various conditions. Figures 9.19, 9.21, and 9.23 are shown in false color, with Q, U, and V mapped to red, green, and blue, respectively, and the I channel shown as brightness modulation. Figures 9.24 and 9.25 show the I values in gray scale, overlaid with data derived from the Q or V values.



**Figure 9.18.** Pipe Set Mounted to a Polystyrene Foam Block

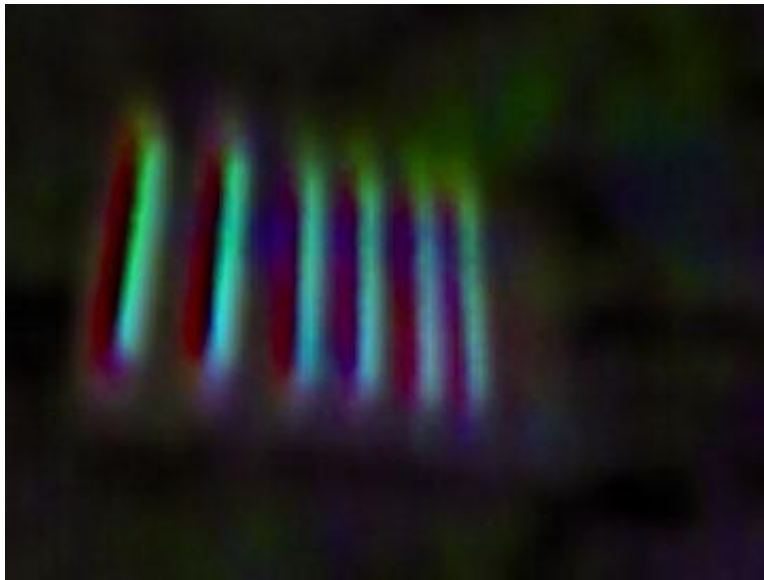


**Figure 9.19.** Millimeter-Wave Image of Pipe Set Mounted to Polystyrene Foam Block



**Figure 9.20.** Pipe Set, Laid in Trench, Partially Covered with Quartz (Silica) Sand

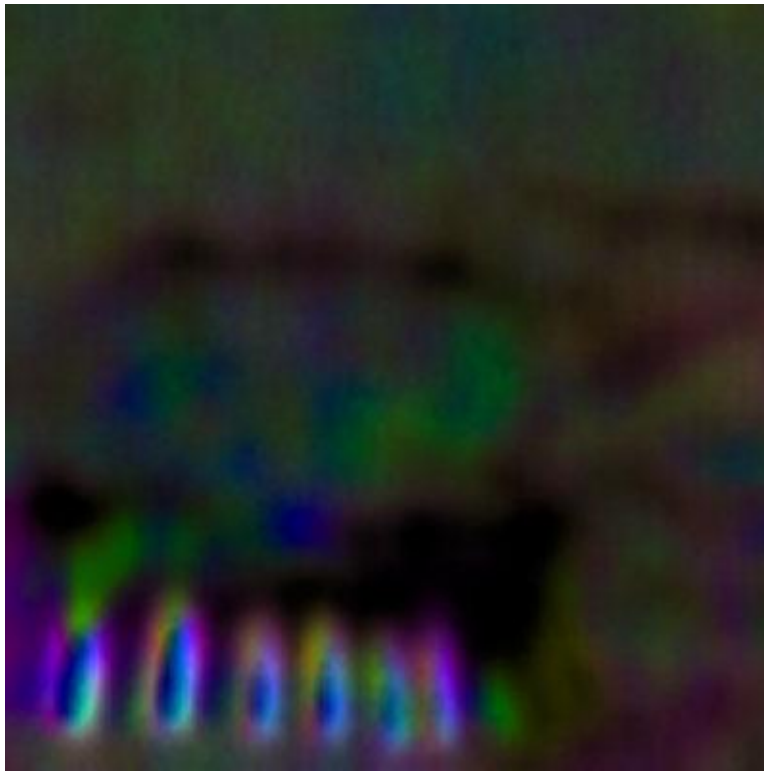


**Figure 9.21.** Millimeter-Wave Scan of Pipe Set, Laid in Trench, Partially Covered with Quartz (Silica) Sand



**Figure 9.22.** Pipe Set, Fully Buried Under Quartz Sand, with Markers on Surface to Aid in Locating Boundaries of Trench

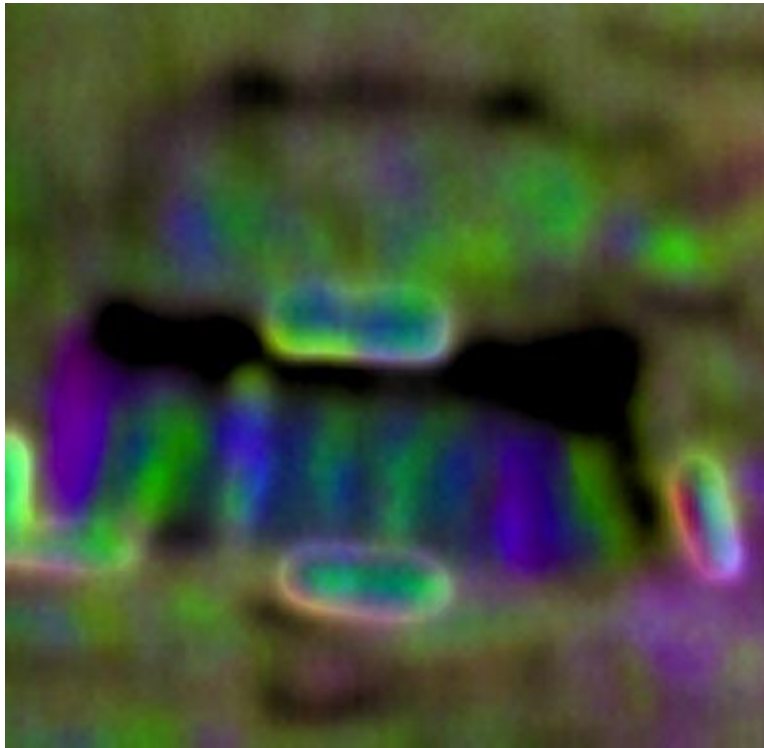


**Figure 9.23.** Scan of Buried Pipes and Surrounding Markers. The sand thickness above the pipes ranges from 2 mm for the largest pipe to 12 mm for the smallest pipe. The trench is readily visible by its black outline. The six pipes are visible, but are hard to distinguish from the edges of the hole.

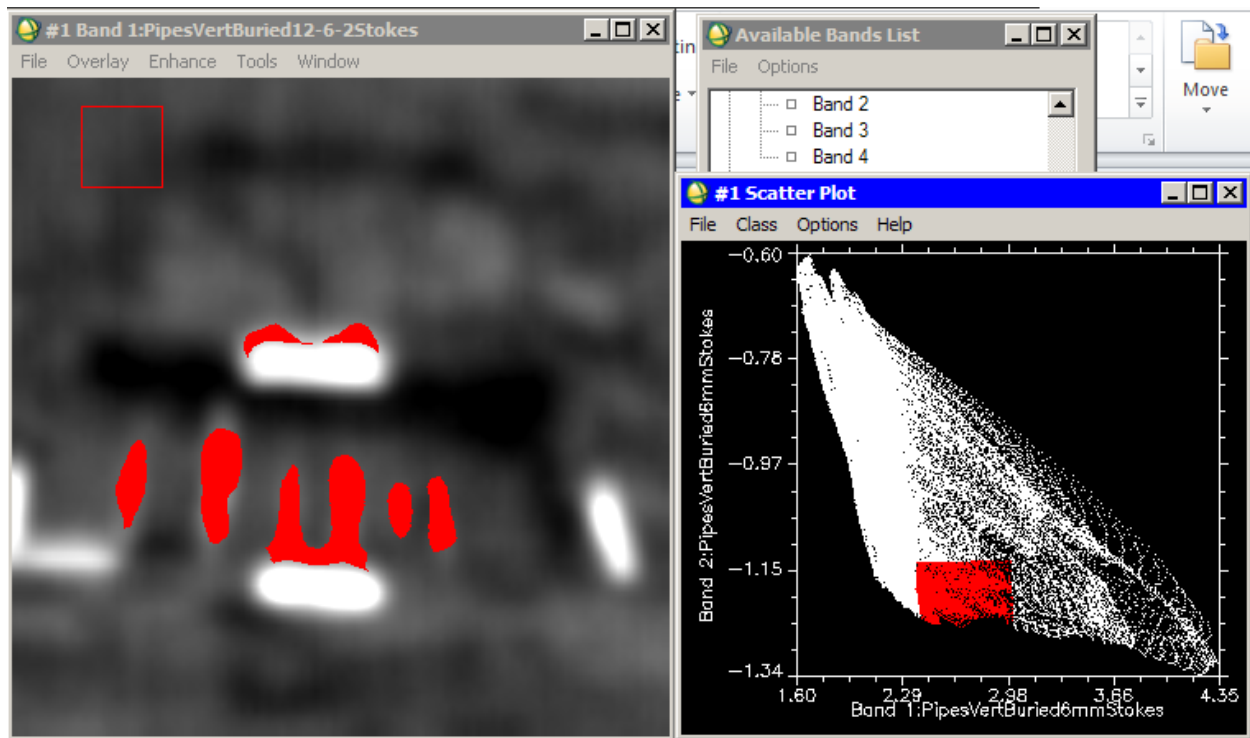


**Figure 9.24.** Scan of Buried Pipes (left). Same data as the preceding figure, but presented as the I image overlaid with red markings derived from a region of interest on a scatter plot (right) of I versus Q. The markings accurately show the positions of the pipes, plus the edge of one of the markers.

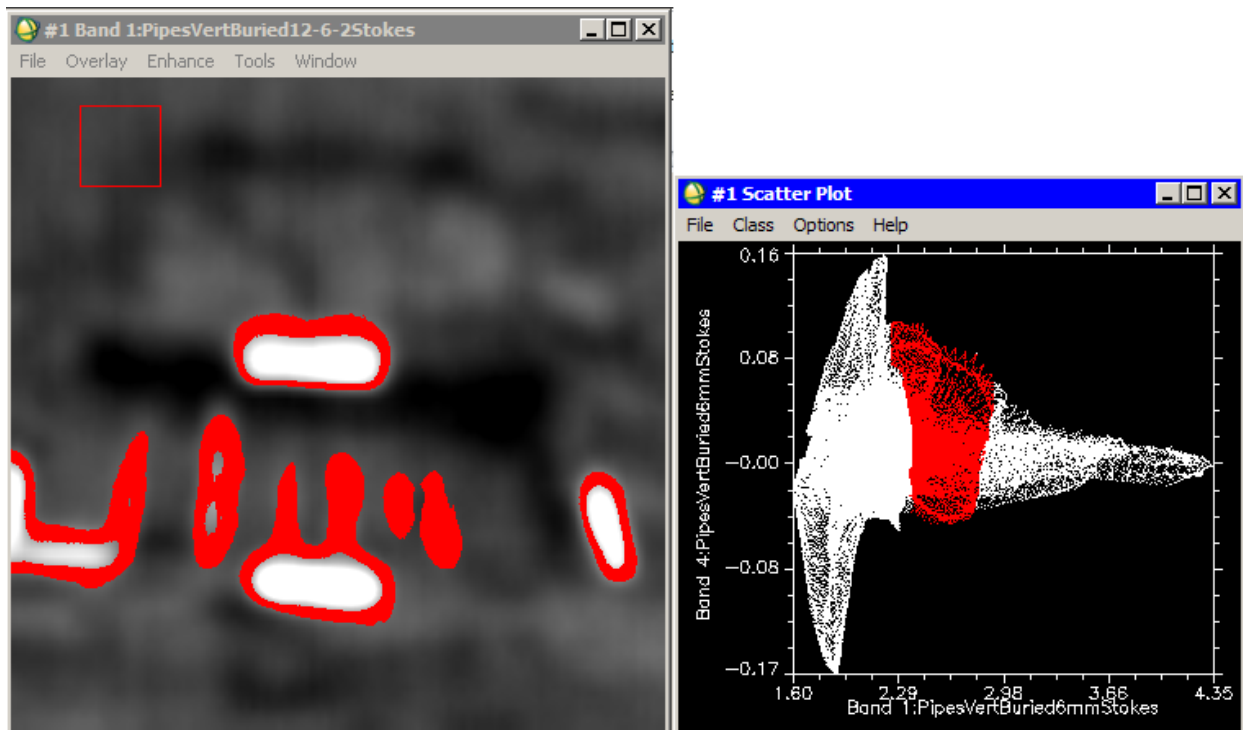


**Figure 9.25.** Scan of Buried Pipes (left). Same data as the preceding figure, but presented as the I image overlaid with red markings derived from a region of interest on a scatter plot (right) of I versus V. The markings accurately show the positions of the pipes, plus the edges of the markers.

Images of complex objects in simple scenes can also enhance understanding of the behavior of passive mm-wave imaging. The following images show a motorcycle in an asphalt parking area with an intermodal container in the background. Figure 9.26 shows the scanner in the foreground, inside a large building, and the motorcycle in the background, with an intermodal container behind it.



**Figure 9.26.** Motorcycle and Scanner

Figure 9.27 shows the motorcycle as seen in the visible (upper) and as an intensity plot of the reflected sky-shine in the 93-GHz mm-wave band. Examining these two images in detail provides a great deal of insight into the nature of passive mm-wave images. Further information is gleaned from the other mm-wave channels, as will be discussed below. The first aspect that is noticed in the mm-wave image is that it looks like an out-of-focus version of the visible image. However, closer inspection reveals many significant and interesting differences.

- Both images seem to have a shadow. However, the shadows are very different. In fact, the “shadow” in the mm-wave image is actually the dark silhouette of the motorcycle, reflected in the pavement, against the bright sky. At these wavelengths, the asphalt is a mirror.
- Similarly, both images show reflective highlights. However, the highlights in the visible image are mainly reflections of the sun, whereas the highlights in the mm-wave image are mainly reflections of the sky. The building blocks sky-shine from the side near the scanner, so there is little illumination of vertical surfaces. The sun is not a significant source of brightness in the mm-wave region, because its

energy is concentrated at much higher wavelengths, and only a negligible tail is present at mm wavelengths.

- The intermodal container is light-colored in the visible image, but mostly dark, with some very bright highlights at the top, in the mm-wave image. The darkness is because the vertical walls have no sky-shine to reflect; what little there might be is blocked by the building. The highlights at the top are reflected sky-shine from the angled panels in the doors.
- The intermodal container has a shadow in the visible image, but a reflection in the mm-wave image. And the reflection is brighter than the container itself, because the sky-shine from above the building is reflected down from the vertical wall and back up from the asphalt.
- The vertical dark streak near the upper left of the mm-wave image is a scanning artifact: a truck passed by between the motorcycle and the container, briefly interrupting the beam, and leaving a hole in the image.

Figure 9.28 shows three channels of the motorcycle scan in false color, with the Q, U, and V channels mapped to red, green, and blue, respectively. Since this is an additive color scheme, pale, whitish regions represent all three channels strong and nearly equal, yellow represents Q and U strong and equal, magenta represents Q and V strong and equal, and light blue represents U and V strong and equal. Black represents low intensity in all three channels.

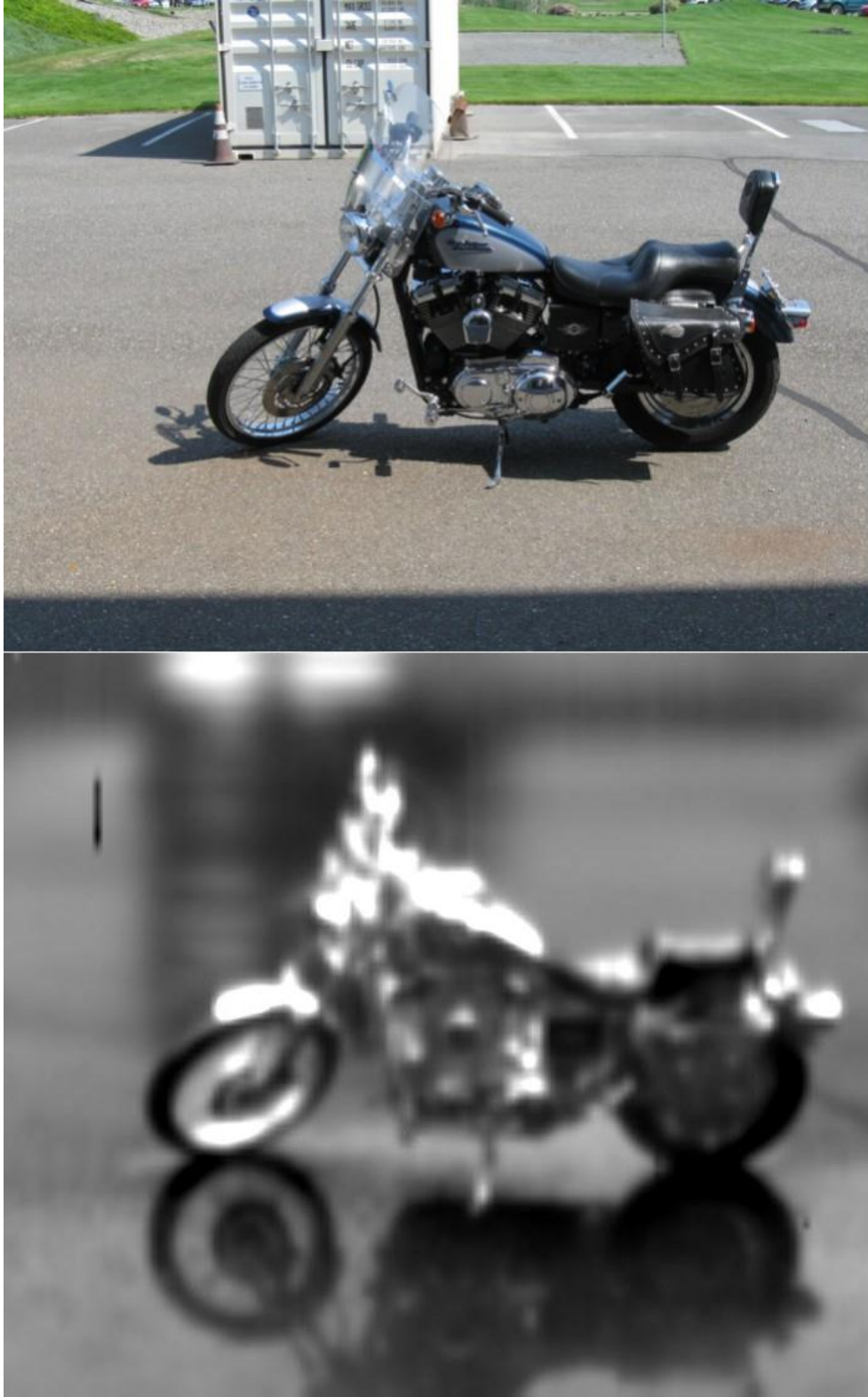


**Figure 9.27.** Motorcycle: Visible (top) and mm-wave Intensity (bottom)



**Figure 9.28.** Motorcycle in False Color Non-Intensity mm-wave Channels: QUV -> RGB, Respectively



## 10.0 Binocular Differential System

### 10.1 Overview

The binocular differential system consists of a two focusing mirrors and two mm-wave horns and receivers. The output of one is subtracted from the output of the other, creating a differential measurement. It would be possible to reconfigure the data acquisition electronics and add extra channels to create a fully binocular output, which could be post-processed for the differential measurement, but building both configurations was outside the scope of the project.

The fundamental design concept of the binocular differential system is as follows:

- Two off-axis parabolic mirrors reflect the object rays onto two “turning mirrors” (planar mirrors that redirect the optical axis).
- Each turning mirror reflects onto the respective receiving horn.
- Both off-axis parabolic mirrors are pointed at the object; consequently the angle between them is varied according to the object distance.
- The turning mirrors are kept fixed after initial alignment.
- The dual radiometer is translated to ensure that the output of both turning mirrors is coupled into the horns.

The ray-trace diagrams below show the optical architecture. Figure 10.1 shows rays from an object at a distance of 20 meters as they arrive, are focused by the parabolic sections, are reflected from the turning mirrors, and are detected at the horns. Figure 10.2 shows the turning mirrors and horns in detail. Figure 10.3 and Figure 10.4 show the beam footprint on one of the turning mirrors (i.e., an intensity cross-section of the beam in the plane of the mirror). Figure 10.3 shows the footprint at 20 m, while Figure 10.4 shows the position of the beam for different object distances, as the angle between the two parabolic mirrors is changed to converge at the specified distances. The receiver horns have to be translated correspondingly in order to remain at the focal point for different object distances.

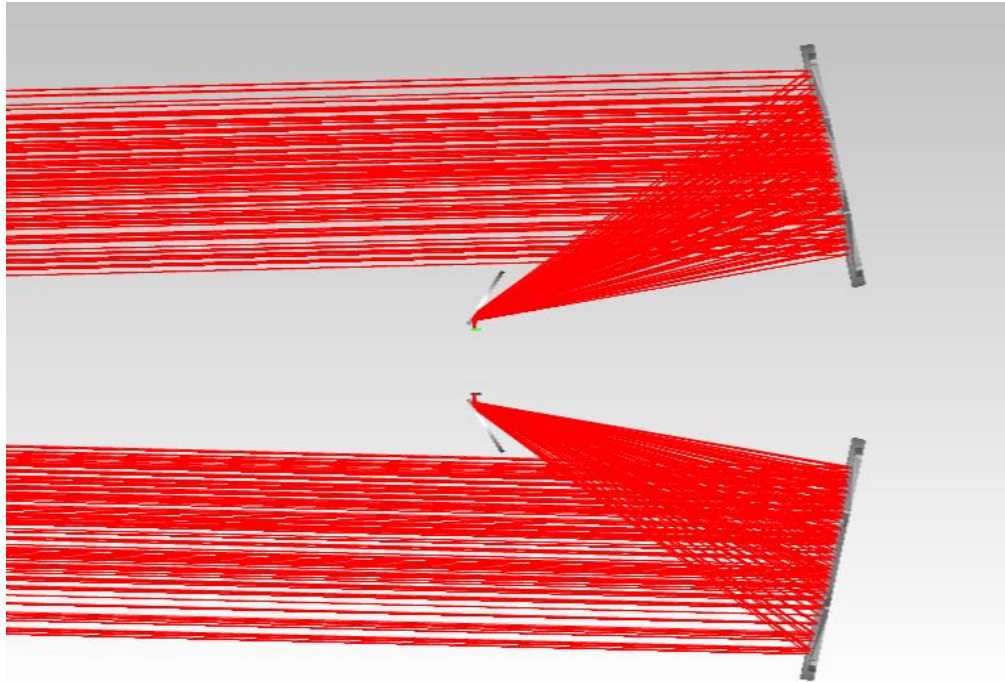


**Figure 10.1.** Ray-Trace for Object at a Distance of 20 m and Mirror Separation of 1 m

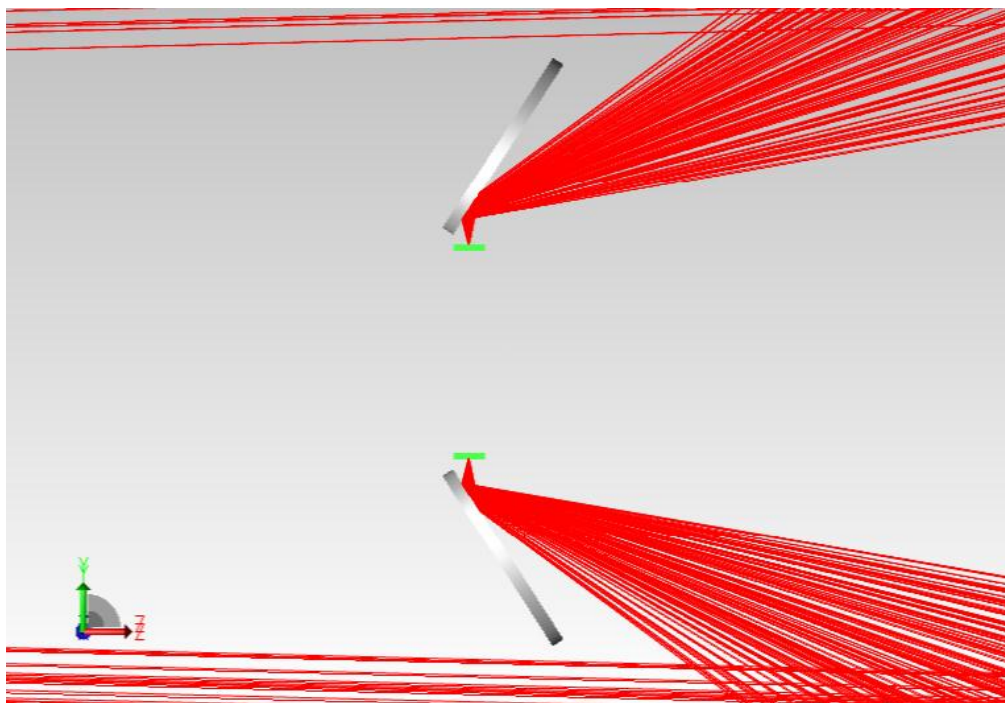


**Figure 10.2.** Close-up View of Ray Trace Near the Turning Mirrors (gray) and Horns (green), for Object at a Distance of 20 m and Mirror Separation of 1 m

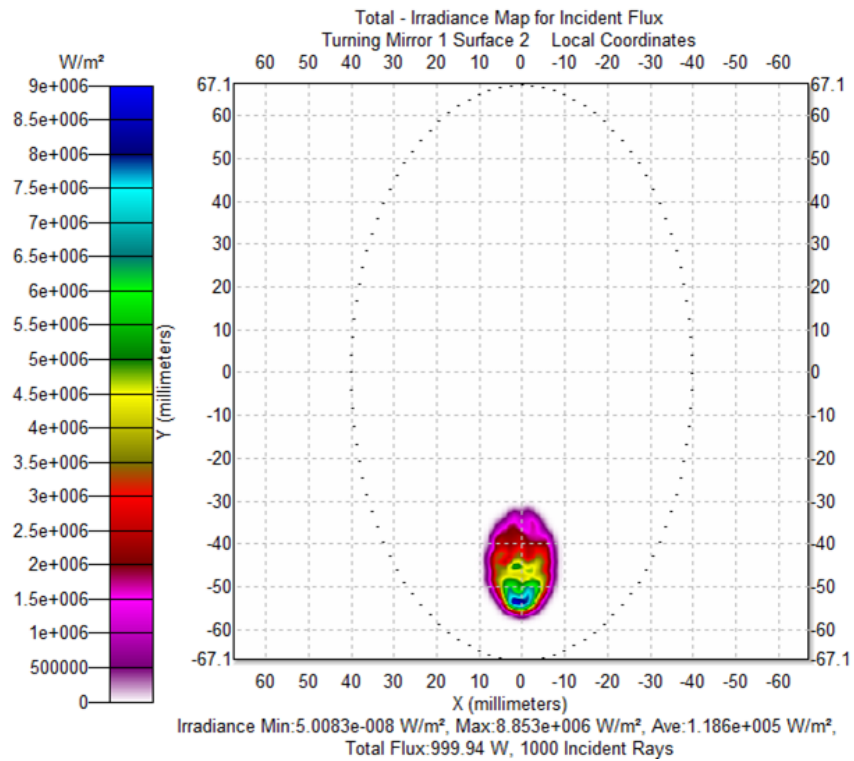


**Figure 10.3.** Beam Footprint on Turning Mirror, for Object at a Distance of 20 m and Mirror Separation of 1 m

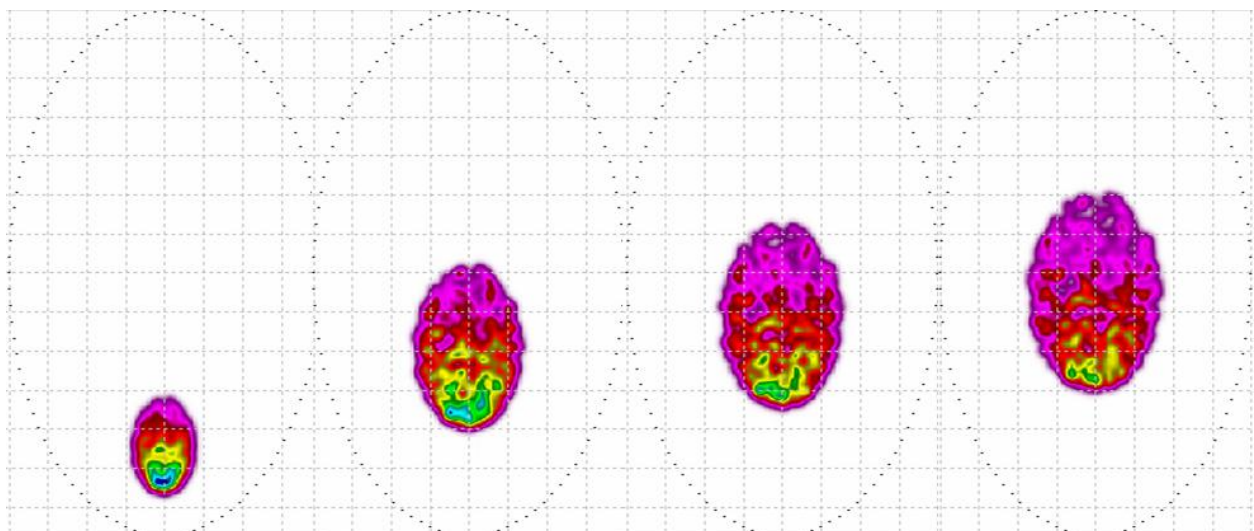


**Figure 10.4.** Beam footprint on Turning Mirror for Convergence (object) Distances of 20, 50, 100, and 500 Meters (left to right)

## 10.2 Development of the Binocular System

Initially, a monocular OAP system (Figure 4.17) was designed and fabricated to perform proof-of-concept work and phenomenology studies of samples. A Dragone-Mizuguchi type telescope pair was also designed consisting of four mirrors (see Figure 10.5). It was fabricated by Custom Microwave to initiate the development and testing of the Bracewell nulling concept detailed in the project SOW. This was a major focus of the development work in the second phase. The mechanical structure and platform that uses alt-azimuth scanning was designed to work with both the single mirror OAP and the Dragone-Mizuguchi design.

The team created and evaluated designs for both front-fed and side-fed Dragone-Mizuguchi offset dual reflector antennas.

- Both designs have nearly equal-sized primary and secondary mirrors that are approximately 0.5 m in diameter.
- The side-fed version is less flexible than the front-fed variant with respect to feed horn choice as only a limited range of horn divergences can be accommodated that do not result in beam obscuration.
- It appears that more compact mechanical designs can result from the side-fed variant which may give a slight edge from an instrument design standpoint.
- The front-fed design has  $-50$  dB cross-polarization performance, which is  $-3$  dB lower than the side-fed design, and would be the clear choice if the best cross-polarization performance is desired.
- To implement the Bracewell nulling technique, use of the side feed design was planned, as illustrated in Figure 10.5. It makes most sense for side scanning and/or whiskbroom scanning from aircraft.

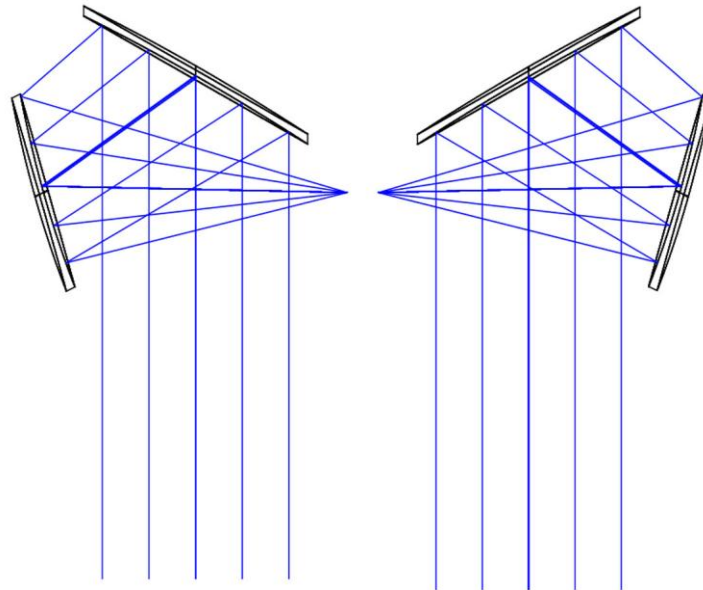


**Figure 10.5.** Side-fed Dragone-Mizuguchi Offset Dual Reflector Antennas Configured for Bracewell Nulling Imaging Experiments

An initial mechanical support structure design to hold and mount the Dragonian Offset Dual Reflector Antennas was created; a Solid Works depiction of it is shown in Figure 10.6. This would have used a commercial lightweight truss system that involved cutting out some of the space frame components that will be replaced with light weight braces that will also serve as thermal baffles and shields (not shown). Later, a second support structure design to hold and mount the Dragone-Mizuguchi Offset Dual Reflector Antennas and a scanner was created, as shown in Figure 10.7. The overall length of this system would be 5 meters. After further technical evaluation, it was determined that building components and a functional subsystem of the structure in Figure 10.7 to reduce technical risk was a prudent first step. This allowed laboratory and field evaluations of both the interferometric (Bracewell nulling) and differential radiometer designs to effectively remove common mode signals and highlight differences between the two radiometers without fabricating a 5-meter-long, high-mechanical-tolerance mounting structure. To this end, a two-telescope arrangement was initially envisaged (Figure 10.8), and then later an intermediate integrated design was considered (Figure 10.9), and finally the polarimetric radiometer was reconfigured with a dual antenna system, per the design shown in Figure 10.10. The constructed system is shown in Figure 10.11. This system was developed to understand how well partially coherent sources can be discovered using a coherent differential receiver. It was used to conduct differential measurements as discussed below.

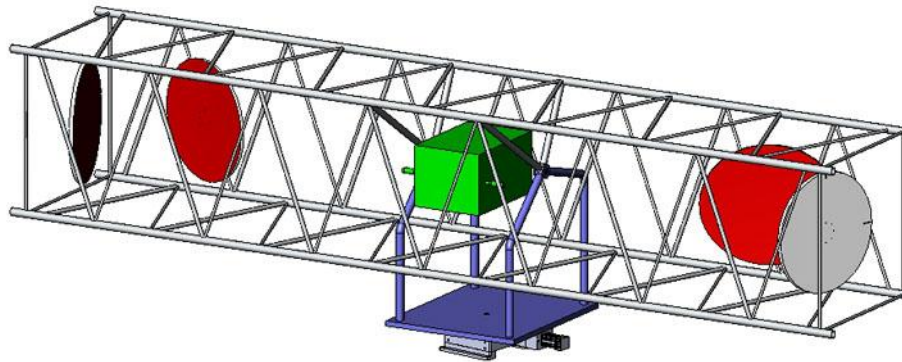


**Figure 10.6.** Initial Structure Support Design for Mounting the Dragone-Mizuguchi Offset Dual Reflector Antennas

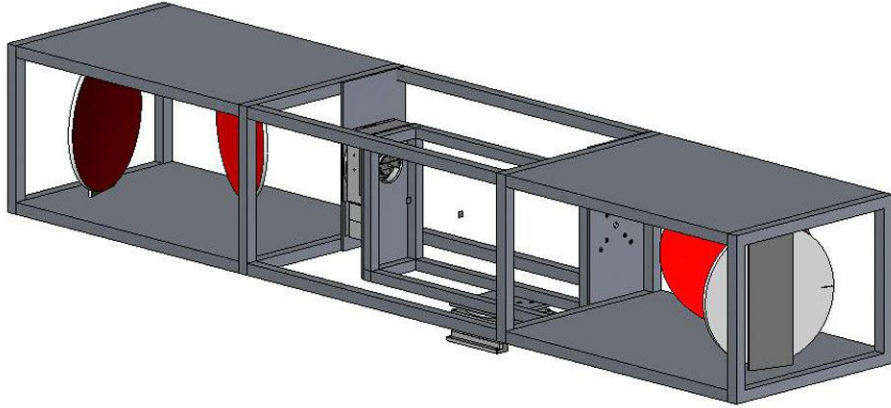


**Figure 10.7.** Second Structure Support Design for Mounting the Dragone-Mizuguchi Offset Dual Reflector Antennas

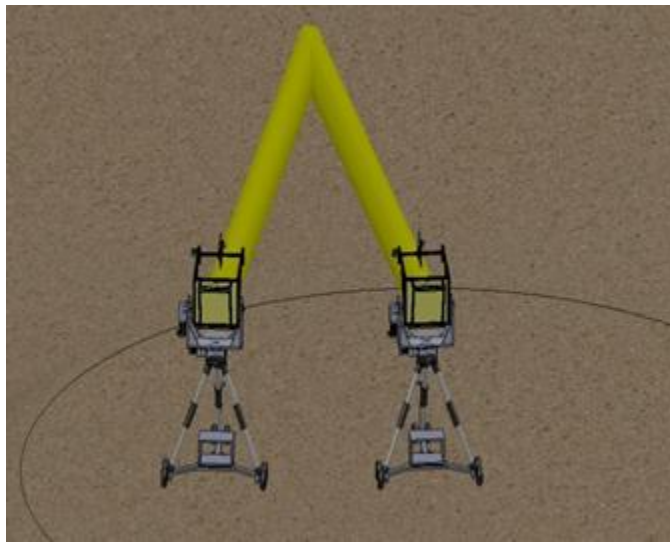


**Figure 10.8.** Initial Concept for Dual Pseudo-Differential System

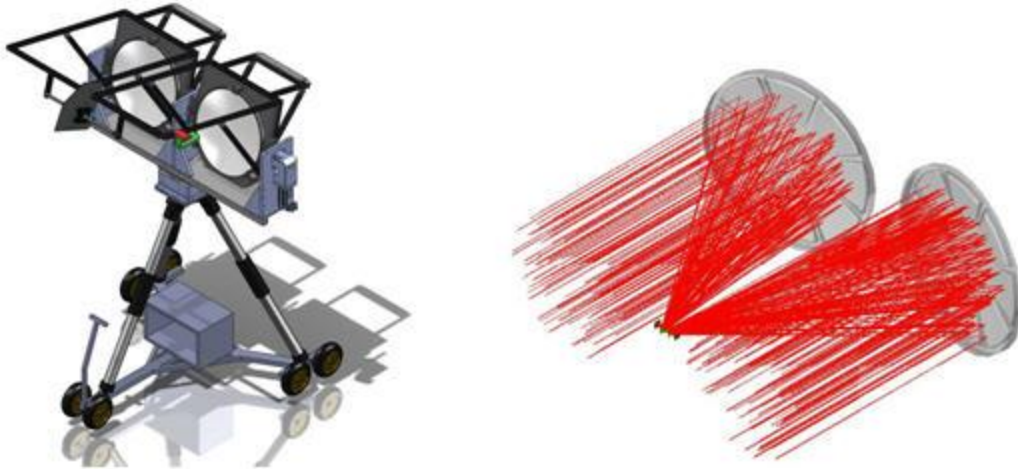


**Figure 10.9.** Intermediate Conceptual Design of the Dual Reflector Scanning Telescope and the Reflector Ray Trace Patterns of the Dual Off-Axis Reflector Parabolas Design



**Figure 10.10.** Final Design Depiction of the Dual Reflector Scanning Telescope Using Dual Off-Axis Reflector Parabolas (front and back views)

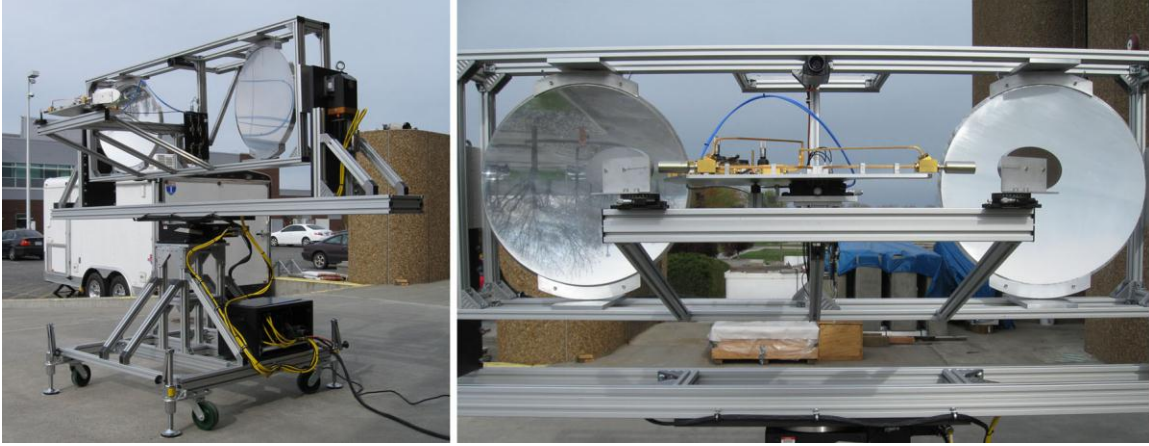


**Figure 10.11.** Assembled Binocular Differential Radiometer Dual Reflector Scanning Telescope (side and front views)

A dual-feed polarimetric radiometer receiver, shown in Figure 3.3, supports the evaluation of the Bracewell nulling concept.

The first experiment was to modify the single-channel polarimetric radiometer and configure it with a dual antenna system shown in Figure 10.12. This radiometer was combined with the single mirror OAP design shown in Figure 10.12 as well. The configuration allows for imaging two scenes with the same radiometer. The signals from this system will be processed to evaluate if common mode signals can be suppressed and structure artifacts can be enhanced. This is an alternative experiment, in addition to those done with the dual-telescope configuration, to determine whether the passive millimeter wave signals radiated from objects or reflected from sky shine are partially coherent.

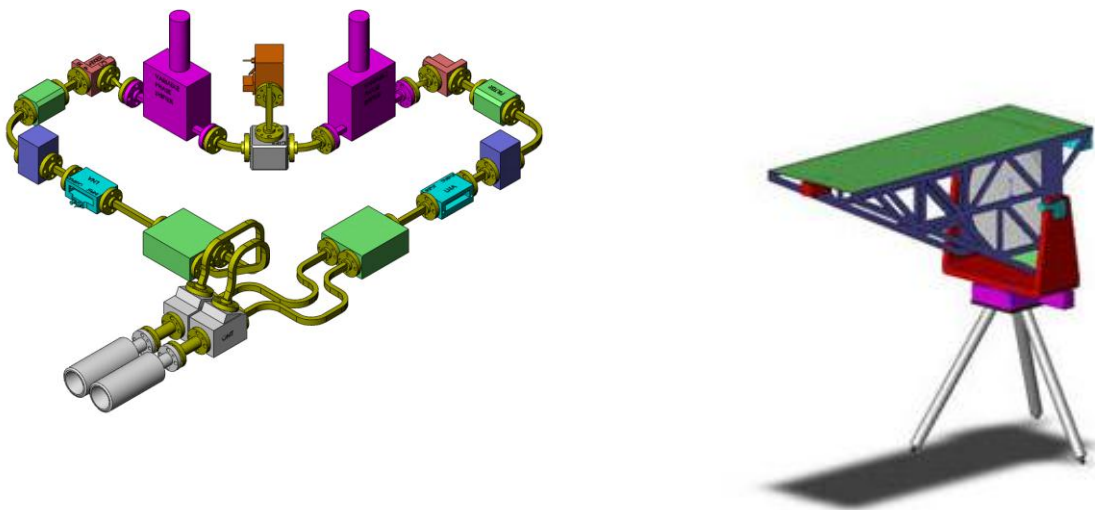


**Figure 10.12.** Modified Polarimeter Radiometer with Two Antenna Feeds and Single-Mirror OAP

The next development step is a true dual system either small scale with 750-mm separation on a single gimbal as shown in Figure 10.9 or the large scale 5m separation as shown in Figure 10.7 where we could set up a single common radiometer with two horns and combine them at the front end.

Polarimeter radiometric imaging results were analyzed using both Mathematica-based methods and ENVI, a commercial hyperspectral image processing software package. The image cube produced by the radiometer is analogous to a multispectral image cube and the additional processing necessary to form the Stokes images and image enhancement methods using the raw polarimeter outputs is easily accomplished using ENVI. Additionally, the Stokes images can be enhanced by manipulating the image histogram to bring out detail in regions of interest, as well as by other standard image enhancement methods such as filtering. Additional anomaly detection is provided by forming two-dimensional scatter plots of each of the Stokes Q, U, and V images versus the I or intensity image. The resulting plots highlight, by type, the location of polarimetric features that may be indicative of industrial activity. Figure 9.10 shows an example of this kind of analysis.

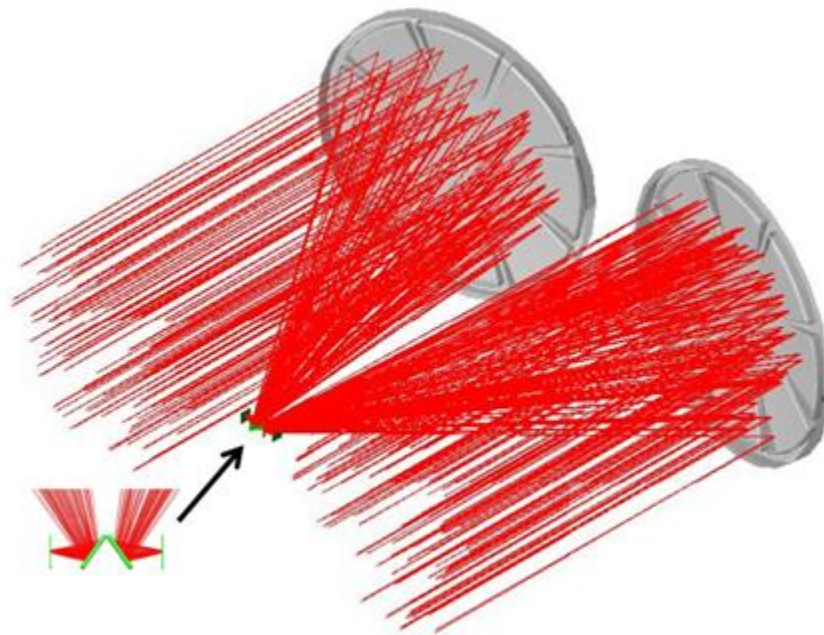


**Figure 10.13.** Dual System with 750-mm Separation

To initiate the testing of the side-fed Dragone-Mizuguchi offset dual reflector antennas, a laboratory test fixture was designed and built to test the high cross polarization isolation. The test fixture design is shown in Figure 10.14, and the as-built system in Figure 10.15. The object of this test fixture is to evaluate the benefit of the side-fed dual reflector design, especially with respect to off-axis imaging performance, which is essential for efficient use of MMW focal plane arrays. The plan, once the reflectors were mounted to this test fixture, was to use laboratory imaging to capture radiometric data using fixed telescope and by scanning calibration targets. Project resources were not sufficient to follow through with development of the Dragone-Mizuguchi system, and so this testing was not performed.

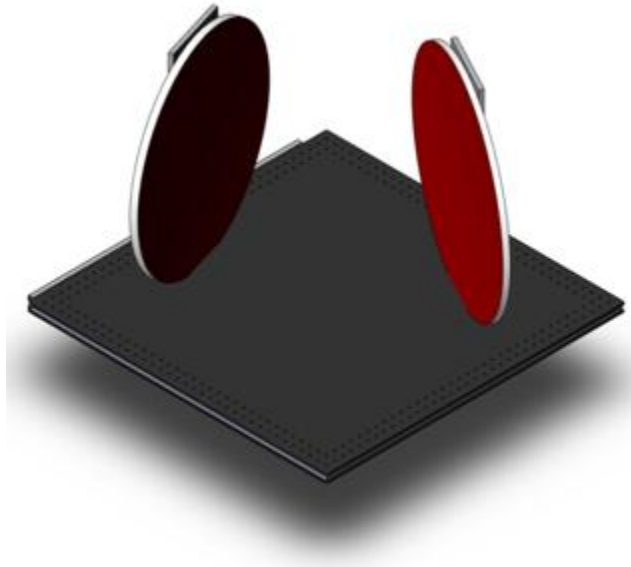


**Figure 10.14.** Side-Fed Dragone-Mizuguchi Offset Dual Reflector Antenna Test Fixture CAD Illustration

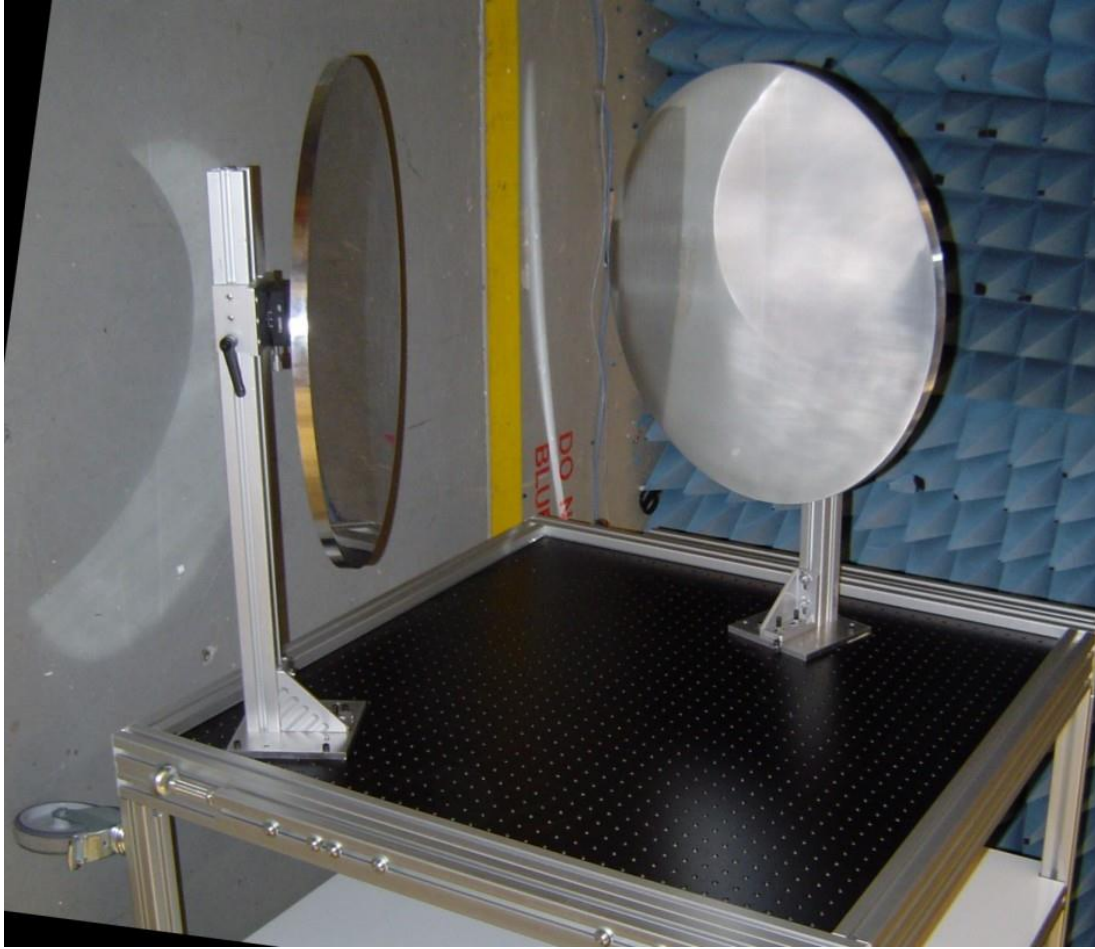


**Figure 10.15.** Dual Antenna Test Fixture, Showing Reflections from Flash and Reflections of Mirrors

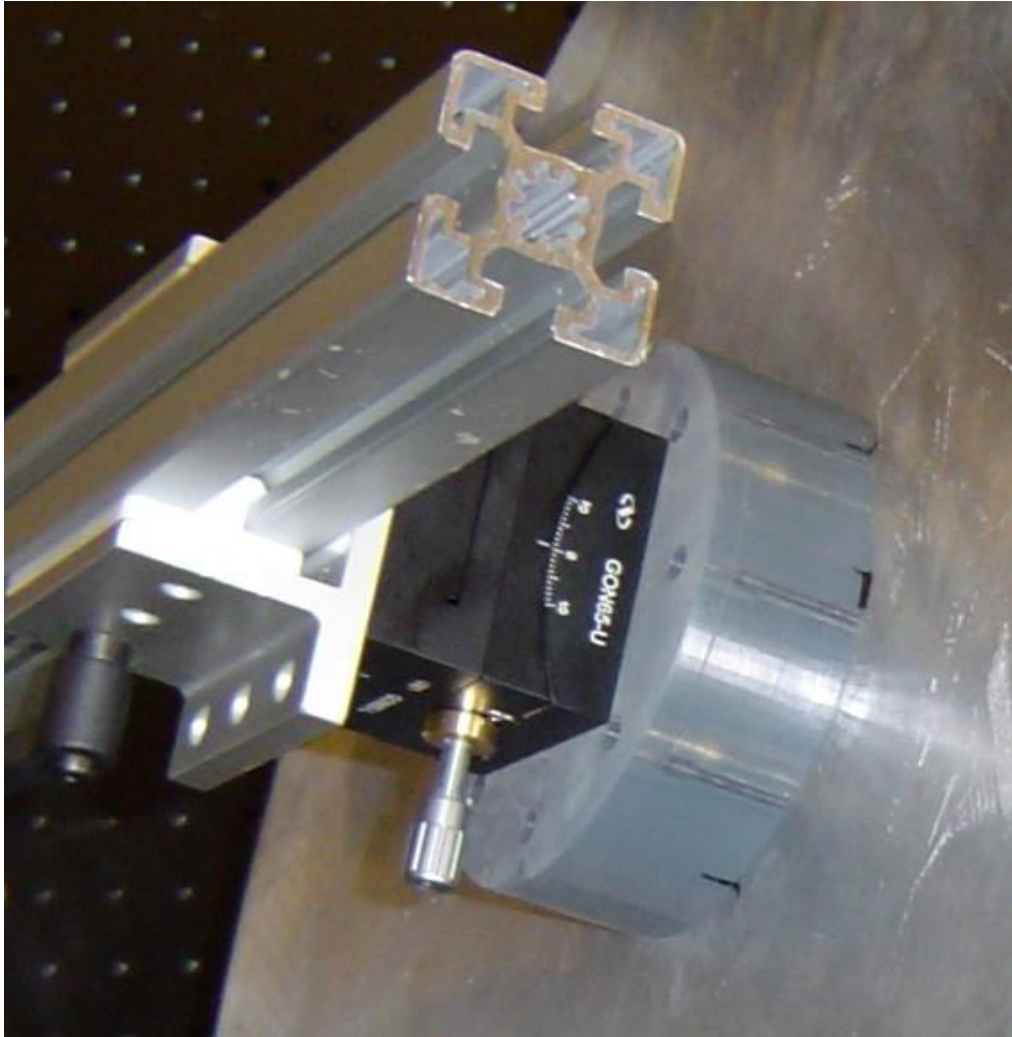


**Figure 10.16.** Dual Antenna Test Fixture Angular Adjustment Mechanism, Showing One of Its Two Axes

The initial structural tests of the system showed lack of rigidity in the mounting platform, which could potentially affect the measurements in an adverse way. A second design was completed and assembled for the mounting platform. Mounting of the off-axis parabolic mirrors (one of which is currently in use on the single reflector system), motor calibration for the binocular scanning apparatus, and checking the control gains of the motor drivers were completed. It was then necessary to align the reflectors and calibrate the dual radiometer. Then the system measurements could be made.

It was also necessary to redesign the front end of the radiometer. The redesign was due to issues obtaining either square or circular waveguide with a 90 degree bend with requisite cross-polarization isolation ratios. As shown in Figure 10.17, each OMT was moved to directly take the output from each horn. Then V and H channel rectangular waveguide return to the switches. A second set of custom waveguide was ordered to position the two receiving horns in opposite directions as is required from the mechanical design of the binocular system. The horizontal and vertical phase inputs from each OMT are matched using this new custom waveguide section of the differential radiometer, H1 to V1 and H2 to V2.

The waveguide section of the differential radiometer was assembled and completed. Final phase adjustments to the IF section were made, and the differential radiometer was installed on the binocular scanner.

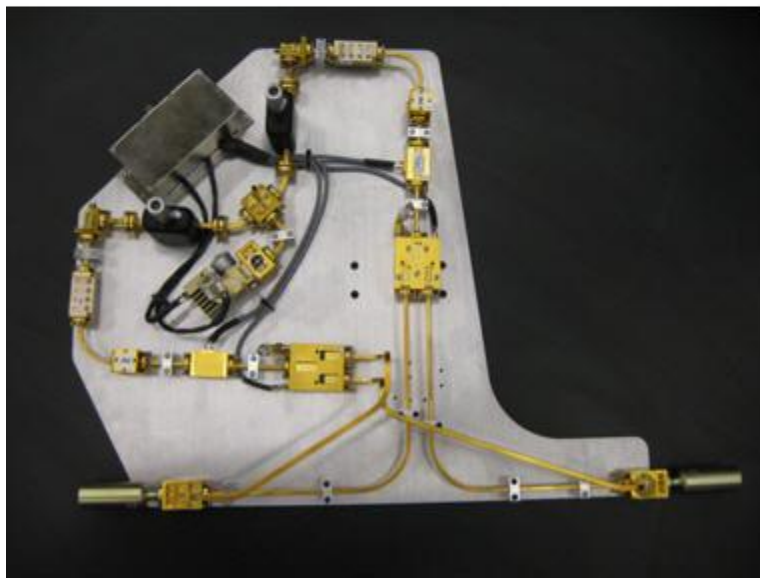
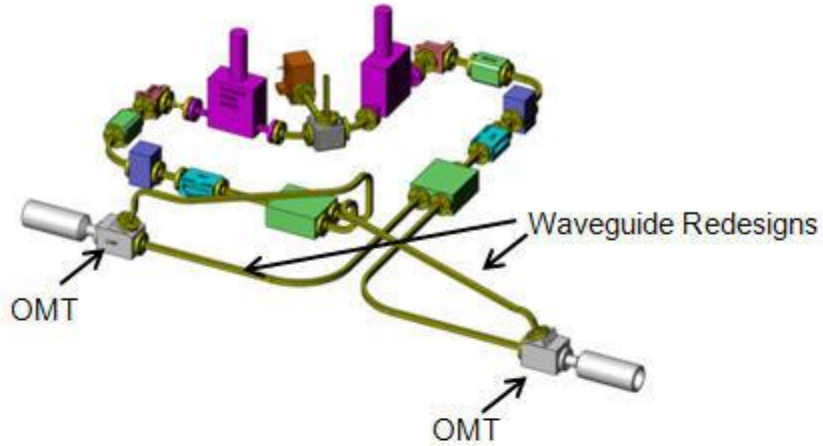


**Figure 10.17.** Reconfigured Differential Radiometer (design and system)

The binocular differential radiometer was assembled and tested. System performance continued to be improved as noise sources were identified and limited/filtered/isolated. The binocular system was aligned using two convergence distances ensuring that the beams were aligned in the vertical direction. To detect individual beams, the other input was blocked using w-band RAM. A cold source, ice pack, was used for detecting the beam in space by monitoring the signal response on an oscilloscope; the center of each beam was where peak responses were detected. Beams were aligned at the desired distance out in space to a laser centered and normal to horn antenna positions. Note that the convergence point distances are from 26m to infinity.

Preliminary imaging results showed a distinct increase (improvement) in system spatial resolution. Imaging studies will continue with the binocular differential radiometer post-processing systems optimization. Work continues to determine sources of error and how to calibrate the system. Numerical corrections to signal offsets and gain slope differences are needed in these highly sensitive polarimeters to achieve their ultimate polarization sensitivity. Figure 10.11 shows the side and front view of the completed binocular differential radiometer.

The Windows control software was updated to recognize the binocular (dual mirror) radiometer configuration and to be compatible with the Windows 7 operating system. Increased moment of inertia requires retuning the stepper servo gains first developed for single mirror test systems. The software was implemented and rigorously tested, but there was some evidence of minor image streaking, initially attributed to scanning irregularities, that required further study. These issues were fully resolved, as can be seen from the results in Section 10.3.

Imaging studies were performed using the 5-m ellipsoidal reflector in conjunction with the differential radiometer system. The differential radiometer system functioned as theorized: when two coherent signals are compared the result is a nulling of the signal, and where there is a difference in the signal received by either antenna this creates a very large differential response in the detected signal.

An alternative method of differential imaging was also explored using a single reflector and additional optical element with the differential radiometer. This exploration resulted in a patent disclosure of an invention entitled “Passive Millimeter Wave Differential Contrast Polarimetry.”

## **10.3 Measurements with the Binocular System**

### **10.3.1 CSF Scan at Ground Level**

The binocular system was set up at ground level near the PNNL CSF Building, as shown in the figures below. Photographs were taken to document the scanning. In particular, photographs from the viewpoint of the scanner were combined to allow overlay of the mm-wave data and the visible-wavelength optical data.

The scanner setup was as follows:

- Binocular system convergence set at 28.9 m
- Distance to front brick surface of CSF building: 29.8 m
- Horizontal samples: 140
- Vertical samples: 100
- Sampling: 0.486 deg/sample



**Figure 10.18.** Dual Radiometer Scanning the CSF Building. Radiometer is at left of light poles, between parked cars.



**Figure 10.19.** Dual Radiometer Scanner Aimed at CSF Building



**Figure 10.20.** CSF Building from Viewpoint of Scanner

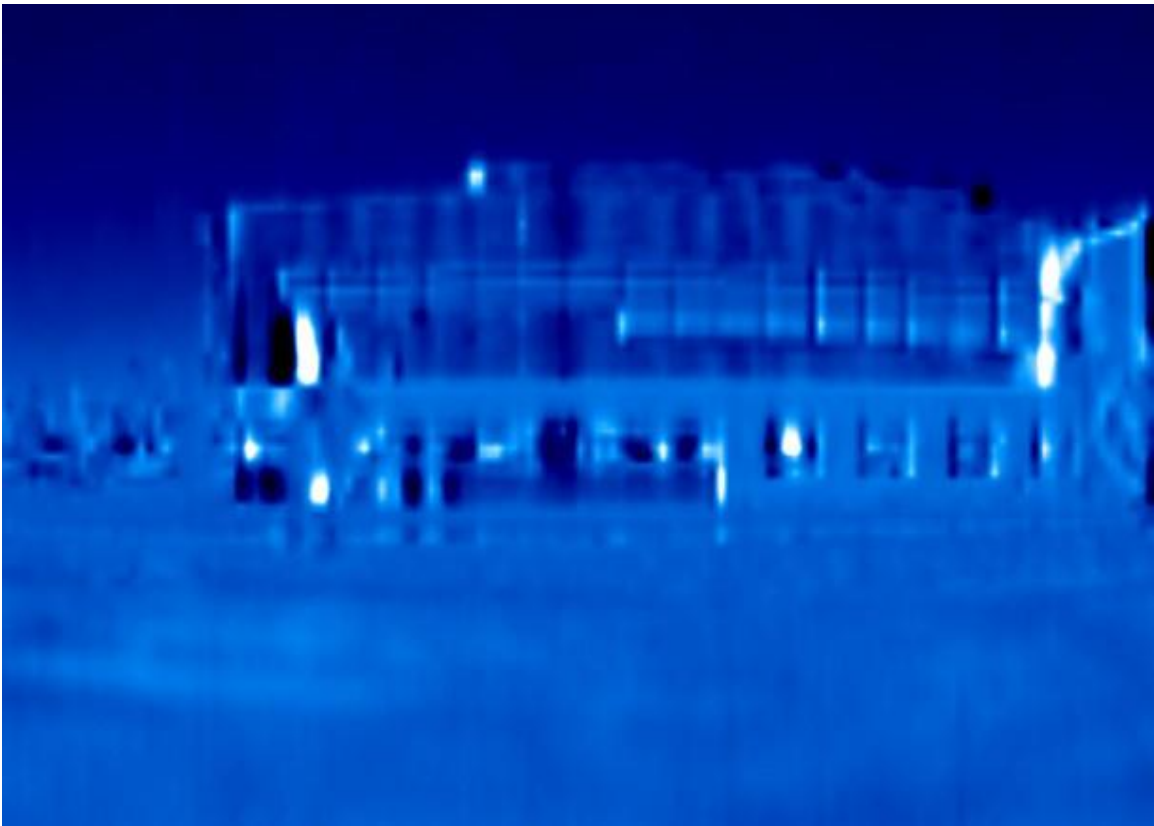


**Figure 10.21.** CSF Building, Differential Binocular Intensity (I) Plot

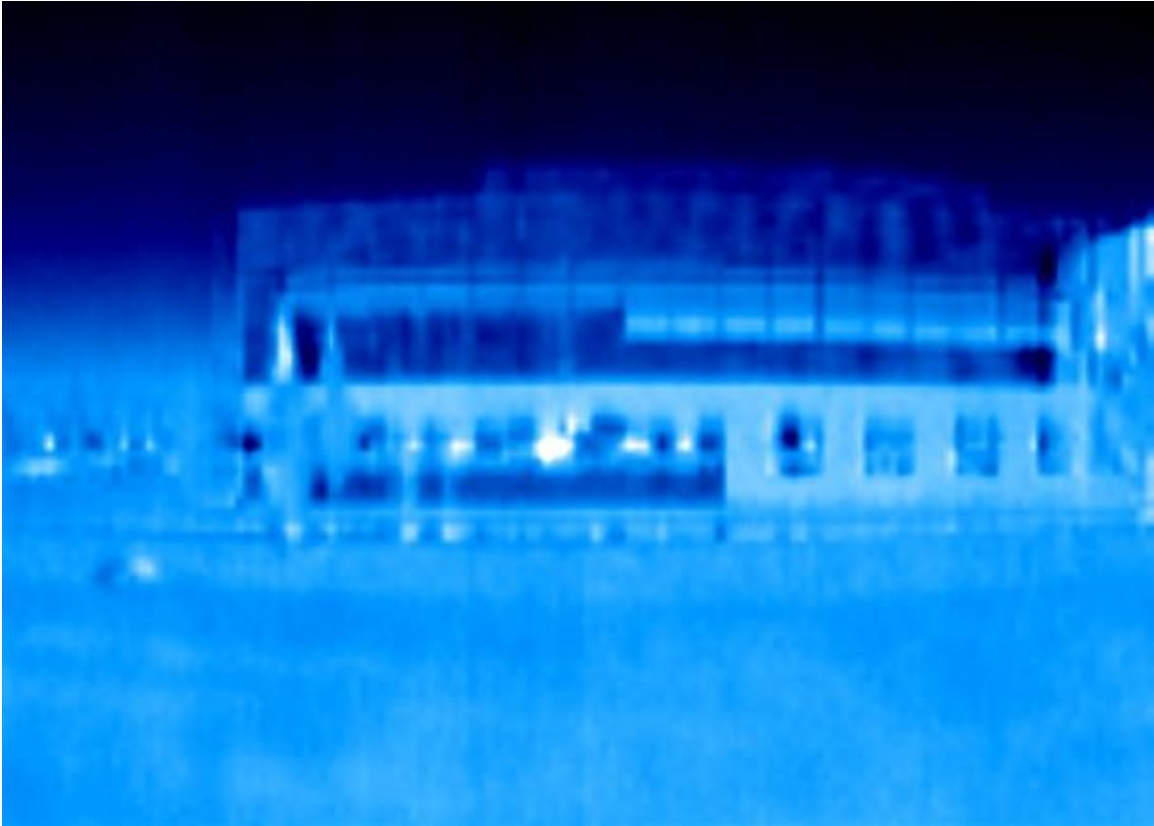


**Figure 10.22.** CSF Building, Differential Binocular Vertical/Horizontal Polarization (Q) Plot. Note the drain pipe at lower left, visible in the Q plot but not in the I plot.

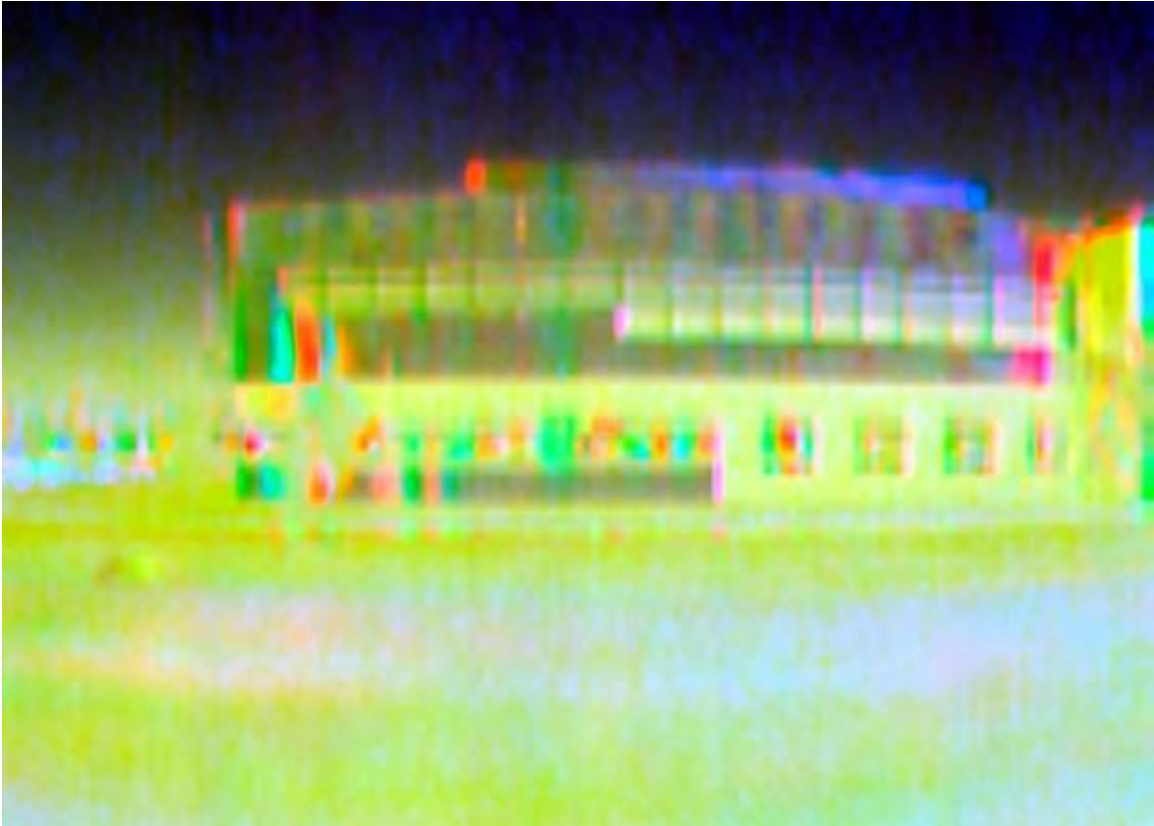


**Figure 10.23.** CSF Building, Differential Binocular Stokes IQU Parameters Mapped into RGB Channels, Respectively

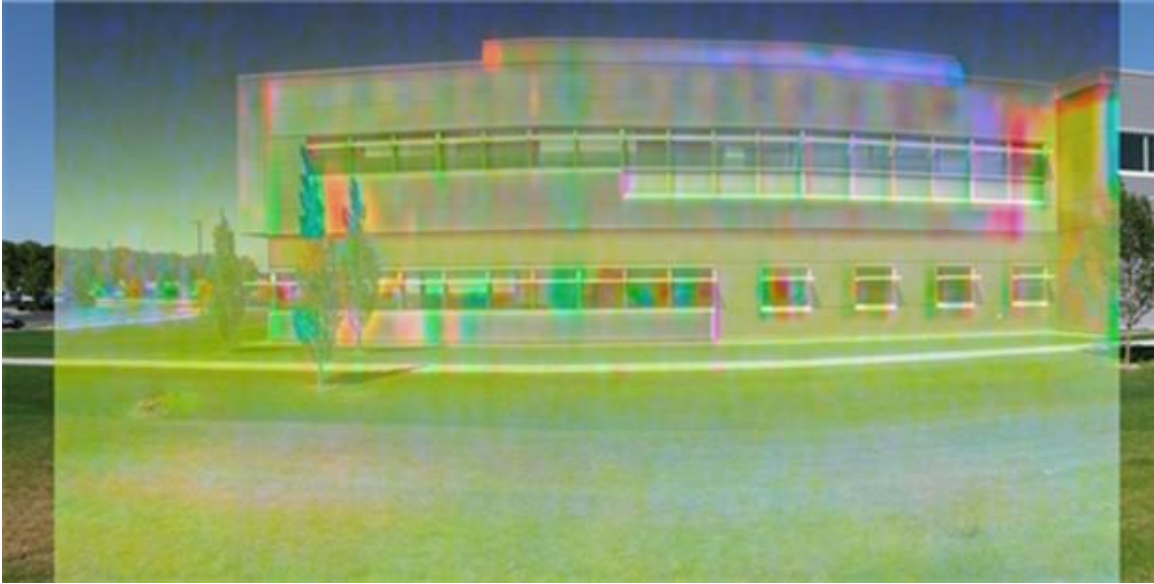


**Figure 10.24.** CSF Building, Differential Binocular IQU Plot Overlaid on Visible-Wavelength Optical Image

### 10.3.2 Elevated Scan of Grassy Area East of EDL, PNNL

The dual differential scanner was set up on a scissor lift looking down at a grassy area east of EDL at PNNL. The elevation of the radiometer was about 36 feet (11 meters). The photographs below show the radiometer from various perspectives as well as the view and data from the radiometer. A series of pipes has been laid end-to-end in the grass, nominally in a straight line.



**Figure 10.25.** Radiometer Viewed from the Northeast, with EDL at Right and PSL at Left



**Figure 10.26.** Radiometer Viewed from the East, Looking Across the Cooling Ponds



**Figure 10.27.** Radiometer Viewed from the South, with CSF in Background, and In-Line-Pipe Target in Foreground



**Figure 10.28.** View Looking South from the Radiometer Platform. This is a composite view from several video camera images. This is the approximate region covered in the single-pipe scan. Pipe target is seen in center foreground. EDL is at extreme right, PSL at back right, and Math Building at back left. Two cast-iron manhole covers are visible in the foreground.

Figure 10.29 shows differential mm-wave data. Because this is a differential binocular image at a small distance compared to the binocular spacing, features generally show up as a double image. This is evident in the image of the pipe, which shows up as an elongated “X”, with one stroke in white and the other in black. Only at the convergence distance of the two mirrors, describing an arc passing through the center of the “X”, is a single differential image produced. If the convergence were set at infinity (parallel optical axes), and the scene were far enough distant so that a pixel were smaller than the separation of the mirrors, then the entire scene would be gray except where an object exhibited a polarization anomaly detected differently by the two mirrors. In this near-distance test, bright objects show a light image on the left and a dark image on the right if they are closer than the convergence distance, and the reverse beyond that distance. Thus the two manholes show up as white on the left and black on the right, while the sidewalk section shows up as black on the left and white on the right.

Objects show polarization signatures only if they are able to reflect mm-wave sky-shine radiation from the sky into the radiometer mirrors, and have left-to-right variation. Diffuse objects such as grass and trees show up as mottled images. The sidewalks and roofs show a great variation in brightness. The east-west sidewalks are not expected to show up in a differential image, except at the ends. Most of the

north-south sidewalks appear to be reflecting trees, which block the sky-shine. The only one that shows up well is south-east of the end of the pipe. The walk to the west of the pipe shows up intermittently.

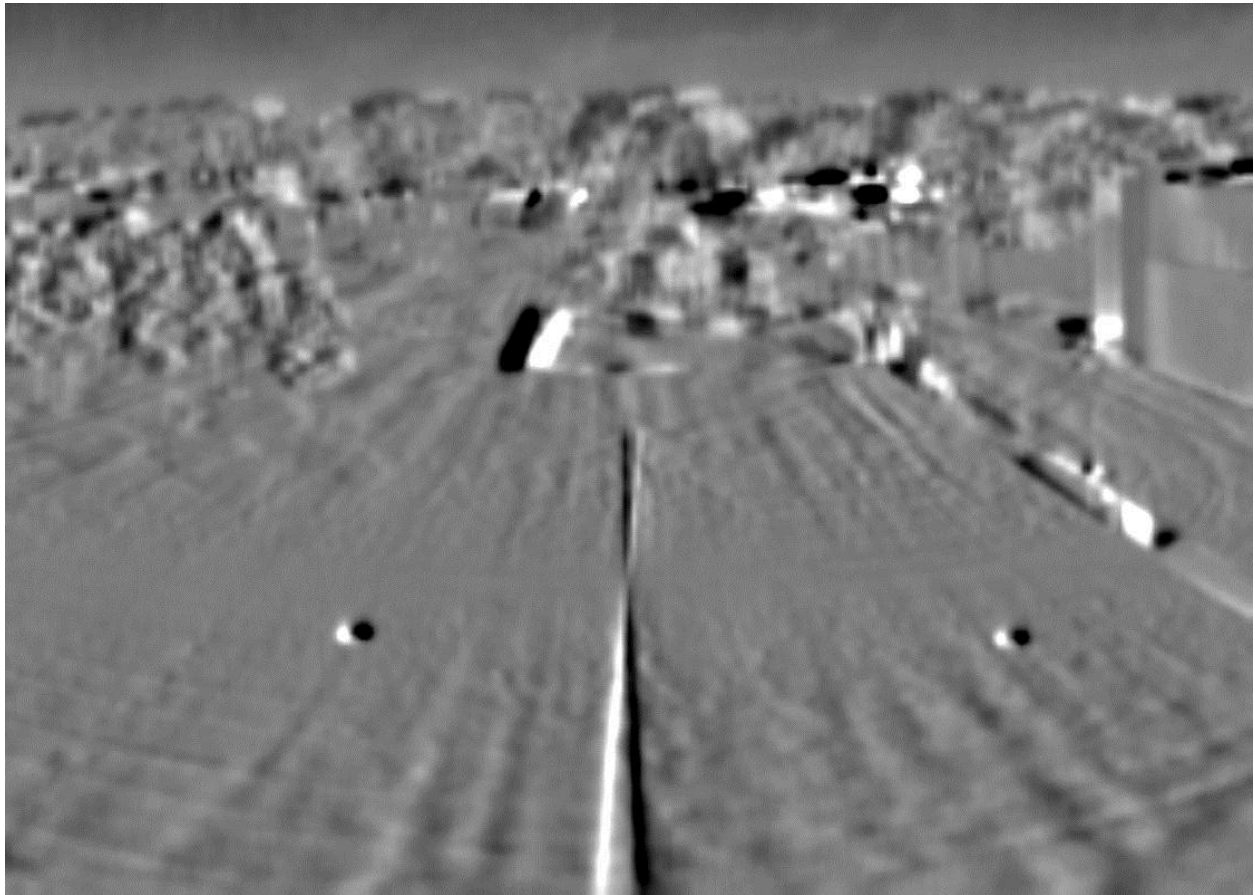


**Figure 10.29.** Differential mm-wave Scan of the Region Shown in the Previous Image. The convergence distance of the system's two mirrors is where the black and white images of the pipe cross. Closer than this distance, bright objects show a light image on the left and a dark image on the right. At this distance, a single differential image is produced, showing the difference in wave character as reflected by the two mirrors. Beyond this distance, bright objects show a dark image on the left and a light image on the right.

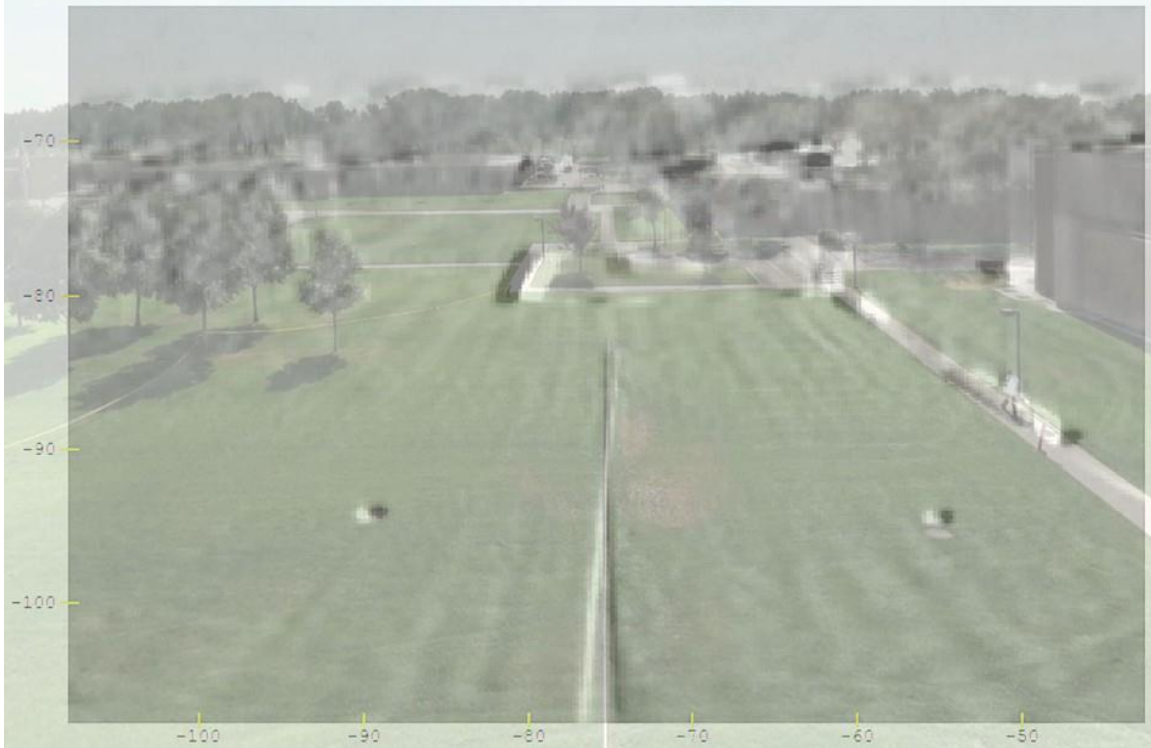


**Figure 10.30.** Overlay of the Optical Image and the mm-wave Image. Registration between the mm-wave image and the optical image is not exact, because of unequal image distortions in the composite optical image versus the tilt-swivel data collection image.

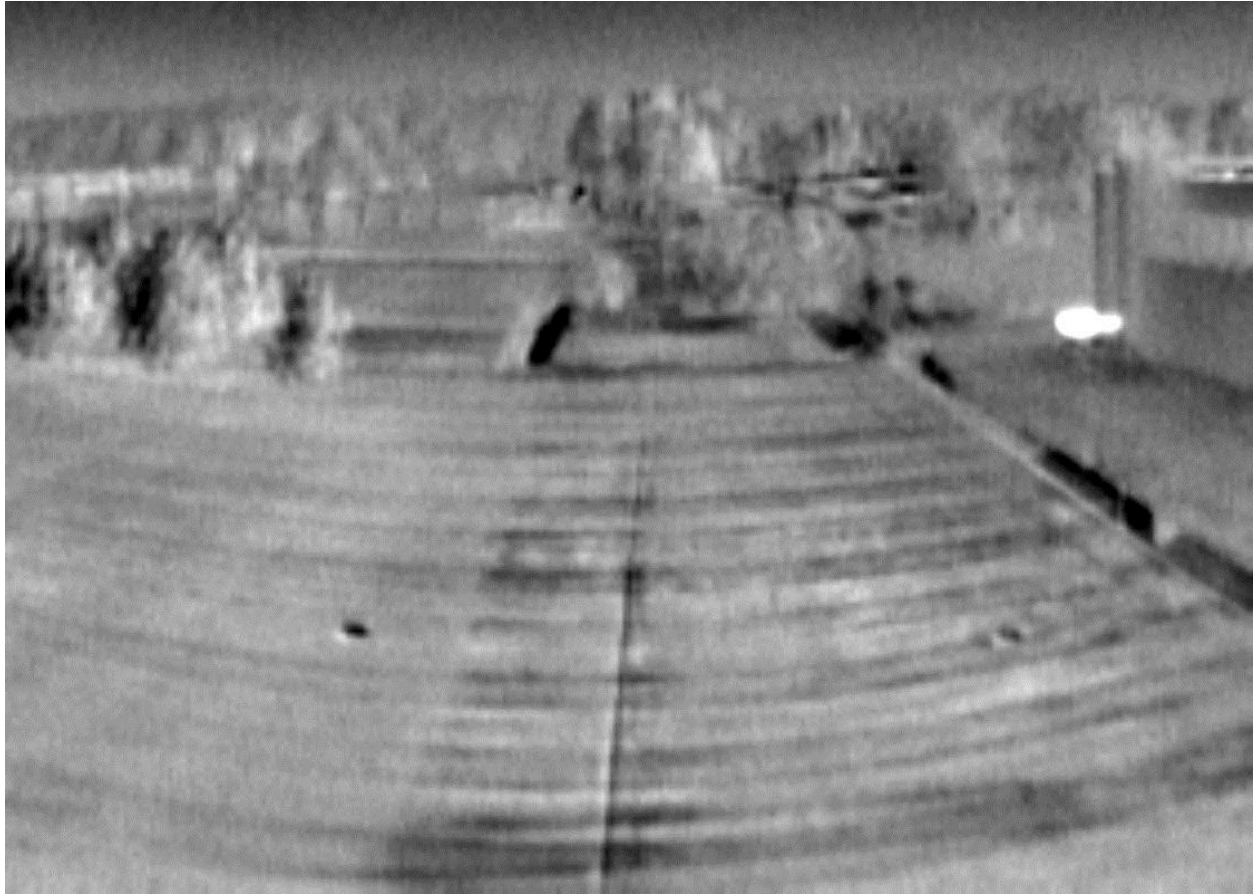


**Figure 10.31.** Stokes V Parameter Image of the Same Scan as Above. Lawnmower paths are clearly visible in the foreground. These paths are actually straight lines, transformed into curves by the coordinate system of the tilt-rotate scanner.

## 11.0 Real-Time System Concept

### 11.1 Introduction

The passive millimeter wave polarimeter was constructed as a point imager that builds up an image by scanning using a computer-controlled pan-and-tilt stage. This approach has its advantages:

1. The optical system needs only to be corrected for on-axis imaging, making single-surface conic reflectors ideal.
2. Only one radiometer needs to be constructed for cost savings.
3. The point spread function of a confocal system is the square of a non-confocal system, which slightly enhances its lateral resolution and reduces the depth of focus of the system.
4. Synchronous detection can be employed to increase signal-to-noise.

The disadvantages are, of course, relatively slow scanning speed due to the mechanical inertia of the pan-and-tilt positioner. Although the approach used in the PMMW system is to continuously scan in the vertical direction (in order to not work against the force of gravity), horizontal repositioning of the imager still requires waiting for the stages to settle for each line scan. A typical image of  $100 \times 100$  points takes longer than 1 hour to produce, even with 100-ms integration times. Although this was sufficient for the phenomenology studies and static scenes, it is too long for practical imaging of arbitrary scenes. Several approaches are possible to reduce scan time. Many of these are common to the optics community, since mm-wave imaging takes place in a quasi-optical regime where ray optics accurately predict system operation (so long as the aperture is much larger than the operational wavelength). These include mirror scanning, coarse arrays that are raster-scanned to form the image, integrated millimeter-wave 1D and 2D arrays, and lastly, synthetic aperture imaging. Some are more appropriate for exploiting polarimetric features, as will be evident.

### 11.2 Mirror Scanning

#### 11.2.1 Whisk Broom Scanning

To form a two-dimensional image using scan mirrors requires scanning in two orthogonal directions. In whisk broom scanning, a scan mirror rapidly sweeps out a line scan one point at a time. This can be achieved using a galvanometer-type scanner or, better still, a rotating polygonal scanner. To obtain the orthogonal scan direction, a slower scan or nodding mirror is employed. In airborne applications, the moving platform provides the second axis scan. The advantages of this approach are:

1. Only a single radiometer is needed.
2. Synchronous detection can be used to increase signal-to-noise.
3. It is faster than a single-point imager with pan-and-tilt scanner.
4. Only on-axis imaging is required of the input optic, simplifying optical fore-optic design for pre-objective scanning. Post-objective scanning samples different input patches of the receiving optic and thus must be corrected for off-axis performance.

The major drawback to this method is that due to the sequential nature of the scan, and if the dwell time on each pixel is limited to avoid smearing, the result is reduced temperature sensitivity. In the benefits listing above, two terms were introduced: pre- and post-objective scanning. We define pre-objective scanning as the use of a scanning element in the space between the object and the objective input. Post-objective scanning takes place in the space between the objective and the image plane. Pre-objective scanning is simple and is equivalent to the use of the pan-and-tilt stage scanning approach. However, for mm-wave imaging, the relatively large input objective required to enjoy acceptable resolution (usually greater than 0.5-m diameter) would require an equally large scanning mirror with its attendant mass and inertia, which would not appreciably decrease the image acquisition time.

### **11.2.2 Two-Dimensional Mirror Scanning**

Two-dimensional scanning typically combines one rapidly moving scanning element, be it a polygonal scanner, or wedged (nutating) mirror, along with a slowly changing nodding mirror. These functions can be arranged in either pre- or post-objective formats. As was true of the whisk brook method, the greatest speed gains come from post-objective scanning where the beam has converged to permit smaller-diameter elements having lower mass and inertia. However, the optical train must be capable of sufficiently good off-axis imaging to fully exploit this approach. Although the scanning process can proceed quite rapidly, each image point is still acquired serially with all of the processing overhead associated with it, which is mostly integration time.

## **11.3 Array Imagers**

### **11.3.1 Coarse Arrays of Receivers**

One transitional approach to fabricating a mm-wave equivalent focal plane array is the use of either linear or two-dimensional coarse arrays of receiver elements. In this way, an  $N \times 1$  linear array can be scanned like a pushbroom system or an  $M \times N$  coarse array can be scanned to cover the field of view. Suppose the system uses an  $M \times N$  array of receivers. This can image  $M \cdot N$  pixels. If the image size is  $Y \times Z$ , a single-receiver scanning imager requires  $Y \cdot Z \cdot t$  duration to form an image, where  $t$  includes per-pixel scanning and integration time. Using an  $M \times N$  coarse array, the scan duration will be  $(Y \cdot Z / M \cdot N) \cdot t$ , which makes faster image acquisition possible. A concrete example can help show the advantages of this approach. Suppose we plan to obtain an  $80 \times 80$ -pixel image of a scene, and that each pixel's acquisition time is, on average, 0.5 seconds. We can see in the example below in Figure 11.1 that the image acquisition time ranges from 53 minutes for the single pixel imager to 0.13 minutes (8 seconds) for a  $20 \times 20$  coarse receiver array, assuming the same 0.5-second figure for each pixel or pixel array.

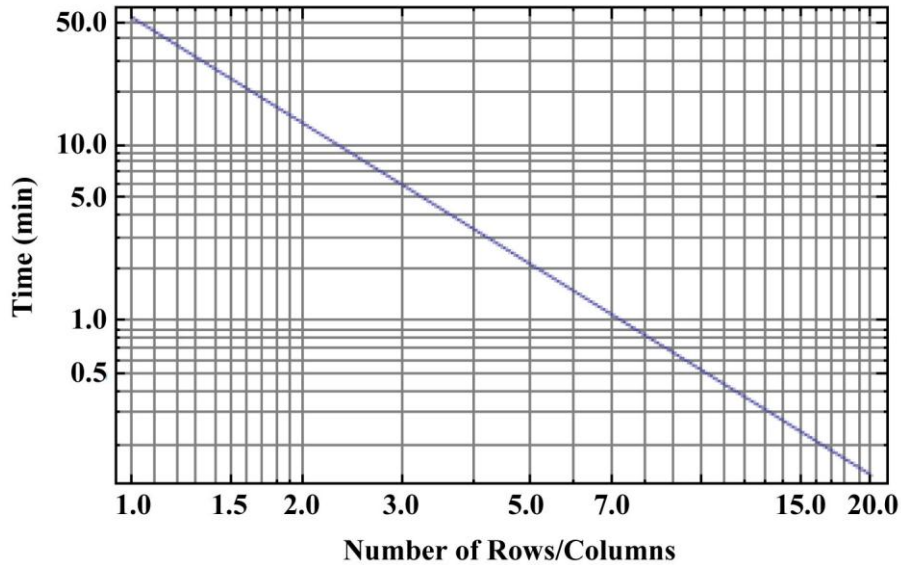


**Figure 11.1.** Log-Log Plot Showing the Time Duration Needed to Acquire an  $80 \times 80$  Pixel Image with 0.5-Second Overhead per Pixel Acquisition. The time to acquire an image slightly longer than 50 minutes in the single-pixel imager case to 8 seconds when a  $20 \times 20$  coarse receiver array is employed in place of the single pixel receiver.

The challenge with the coarse array of receiver approach is the packing density of the array, which is set by the physical size of the horns and orthomode transducer (OMT). In Roving Eye, the smallest center-to-center spacing between horns mounted to the OMT is 0.944 in. or 24 mm. The angular resolution of the off-axis parabolic telescope is shown below.

$$\text{resolution} = \frac{\lambda}{D} = \frac{3.2}{500} = 0.366^\circ \quad 11.1$$

This is manifested in a spatial offset at the focal plane of 6.3 mm of each imaged object point. The angular resolution corresponding to the 24-mm center-to-center horn spacing would be  $1.4^\circ$ , which is almost four times the diffraction limit of the system. Therefore, the coarse array must be sub-scanned roughly four 6-mm scan steps to take advantage of the maximum system resolution, and a  $20 \times 20$  array would result in an  $80 \times 80$  final image with full theoretical resolution. The concept of sub-scanning is shown in Figure 11.2. This is not a unique approach to enhanced resolution and has been used with visible-light cameras to increase the effective resolution of a focal-plane array. Since the minimum center-to-center distance is 24 mm, the array must be stepped in 6-mm increments to sample the image data between the fixed horn spacing.

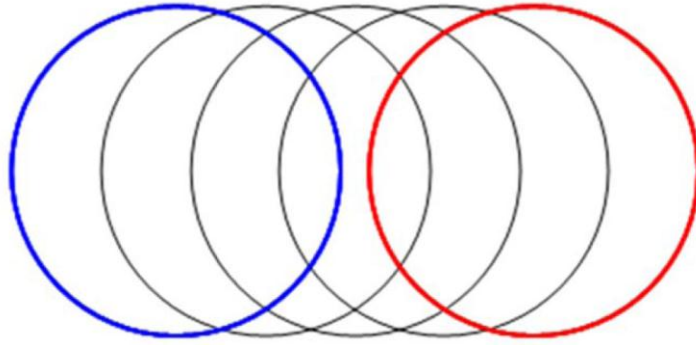


**Figure 11.2.** Unit Cell of Two Fixed Horns (blue and red circles) Showing How They Must Be Moved to Obtain the Maximum Imaging Resolution Offered by a 982.5-mm-Focal-Length Telescope Operating in the W Band. Each horn displacement step is 6 mm, providing approximately  $0.366^\circ$  angular resolution. The outer diameter of the horns is about 22 mm.

A more important issue is that a large coarse receiver array will have elements very far from the optical axis of the fore optic. Simple conic single reflectors like the off-axis parabola in Roving Eye demonstrate poor off-axis imaging. In the case of the  $20 \times 20$  array, the outermost element would be approximately 10 in. or 240 mm off axis (approximately the radius of the primary mirror). For coarse arrays, multi-element telescopes are necessary for the additional degrees of freedom provided by the second reflector surface to correct off-axis aberrations. Refractive corrector plates would also provide improved performance at the cost of insertion loss due to reflection from each surface of the refractive corrector. Figure 11.3 is a plot of the Strehl Ratio of the off-axis parabolic reflector as a function of field height at the image plane. The Strehl Ratio is a figure of merit of an imaging system, which describes the ratio of the point-spread function central-lobe magnitude of the system under consideration to that of a perfect imaging system. Its value ranges from zero to one, with diffraction-limited systems having a cutoff value of 0.8. The parabolic-reflector system ceases to be diffraction-limited at around 80-mm field height when the Strehl Ratio falls below 0.8, which would limit the system to perhaps an  $8 \times 8$  coarse array. An  $8 \times 8$  array would provide  $32 \times 32$  pixels at full system resolution in 50 seconds using the assumptions made earlier of 0.5-second data acquisition time per array scan step. If the design can tolerate a more complex fore optic, a two-element design, such as the f/4 Dragone design originally envisioned for the binocular system, will demonstrate better off-axis performance due to the additional degree of freedom in design optimization provided by the second mirror surface, position, and spacing. Figure 11.4 shows that the Dragone two-element telescope can tolerate off-axis field heights greater than 250 mm before the Strehl Ratio falls below the diffraction-limited value of 0.8.

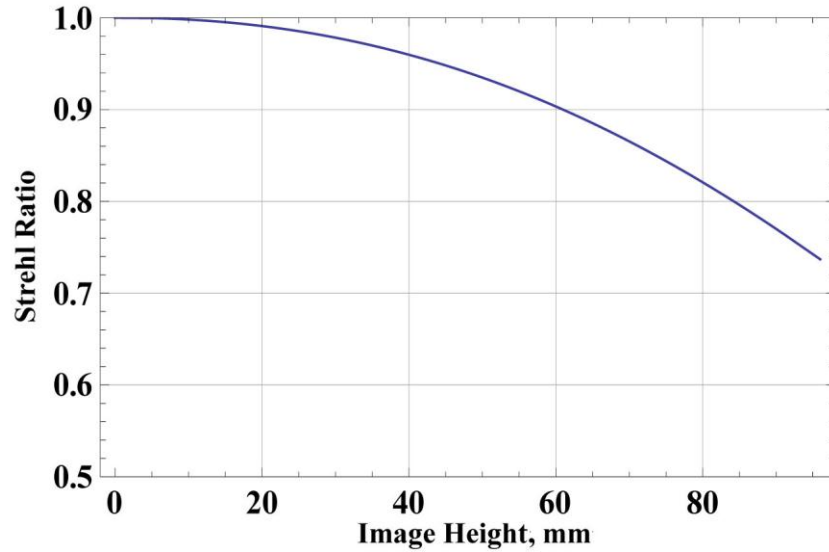


**Figure 11.3.** Plot Showing the Effect on Strehl Ratio as the Off-Axis Image or Field Height is Increased from Zero to 96 mm for the Off-Axis Parabola. The system ceases to be diffraction-limited at about 84 mm, which would only accommodate an  $8 \times 8$  coarse array.

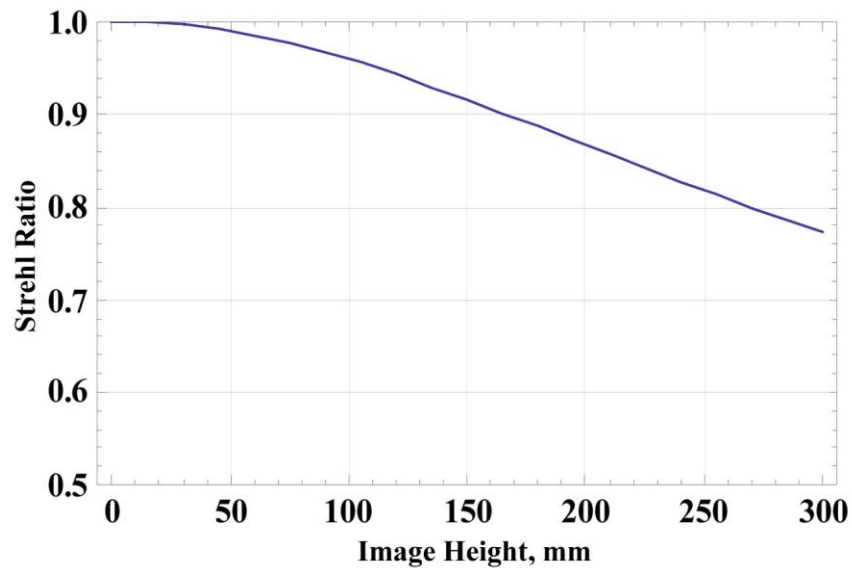


**Figure 11.4.** Plot Showing the Effect on Strehl Ratio as the Off-Axis Image or Field Height is Increased from zero for 300 mm for the Two-Element f/4 Dragone Design. A  $20 \times 20$  coarse array with 24-mm pitch could be readily accommodated by this two-element telescope.

### 11.3.2 Solid-State Arrays

Research is active in solid-state detectors for mm-wave imaging. These approaches include transition edge sensors (TES), those exploiting high-electron mobility transistors (HEMT), as well as antimonide-based backward tunnel diodes (Lynch et al. 2006). The first two approaches require cryogenic cooling,

while the antimonide detectors are room-temperature devices (Wikner and Grossman 2009). In Wikner and Grossman (2009), the pitch of each detector element of a 32-element array is 6 mm, which results in a 192-mm detector size, with an off-axis height of 96 mm. The authors decided on using a two-element air-spaced doublet to improve off-axis imaging but the aperture was only 300 mm, which would limit angular resolution at 94 GHz to  $0.61^\circ$ . For the focal length of the author's optical design, this maps into the detector array pitch. If the authors had selected a larger aperture for greater angular resolution, the linear array would have to be sub-scanned to map each resolution element into each detector element.

## 12.0 Conclusions

As noted in our proposal, persistent broad area search for cueing requires extremely high dynamic range for textural and thermal contrast analysis under adverse seeing conditions. The enormous scope to remotely observe large areas needs to be offset by filtering for sub-pixel anomalies of odd signal contrast. The concepts tested may be especially effective in detecting and tracking man-induced changes in natural clutter, including areas of full, taller vegetation, which may present weak or no returns to synthetic aperture radar imagers. This project set out to build a passive mm-wave imaging polarimeter for identifying jarring discontinuities in thermal scene clutter. By using balanced methods of differential polarimetry, abrupt yet small changes of scene thermal noise and/or polarization irregularities were clearly shown to be detectable at a sub-pixel level. In processing the data of a full Stokes analysis, we found that dimensional reduction techniques from spectral imaging analysis were also quite effective to harness the complicated multilayer scene data recovered with our polarimeters. These imagers developed and deployed at PNNL, when used in conjunction with the polar-to-spectral image reductions, can provide the means to greatly enhance contrast for man-made or induced novelties of changing scene radiance.

### 12.1 Notable Technical Accomplishments

We began by wanting to see if sub-Rayleigh limit spatial resolution is possible with PMMW imaging, in particular using additive beam combining techniques such as Bracewell-Fizeau fringe imaging. It strongly appears that the Airy disk of point resolution, given as  $2.44 \cdot \lambda \cdot F\text{-\#}$  in the focal plane of the two-aperture differential imagers can be improved fruitfully with large baseline offsets of two (or more) apertures.

In acquiring multiple look data of complex scenes, we found that contrast enhancements of sub-pixel changes can also be exposed by analyzing subsets of the four independent measurands (I, Q, U, V) afforded by full radiometric polarimeters. The contrast depends upon the viewing angle that the sensor makes, and especially strong contrast enhancements are often recovered with steeper down-looking depression angles. This is because reflected skylshine often undergoes large differences in polarization for horizontally and vertically aligned polarizations when the depression angle become greater than approximately 10 degrees. Thermal emission may also change polarization states when transmitted through dielectric coverings once the viewing angles become comparable to the Brewster angle at which materials scatter or re-radiate the two polarization vectors quite differently.

Approximately four useful generalizations have been observed to aid in using these effects:

1. The I component of the Stokes parameters highlights highly reflective materials well so can be used to assess building materials, especially painted metals, and would be excellent to detect the presence of sloped metal roofs, even under camouflage. This channel would be excellent as well in measuring relatively smooth fractures in rock faces or that might also be heaved at steep angles atypical of natural occurring weathered rocks.
2. The I component of the Stokes parameters would be excellent for heat flow studies to find areas of high/low heat capacity (water has both a high heat capacity and high reflectivity in the mm-wave). These effects could be studied with time-lapsed imaging, and the thermal mm-wave signatures are indeed complementary to that of IR images which only show surface-equilibrated temperatures. For

example, gypsum walls are highly transparent to the mm-wave, so thermal lapse effects from an externally heated or cooled building can transmit through the inner building and highlight hidden structures behind the walls in a manner complementary and often more effective than IR thermography. We saw effects of this early in our first systems development when the direct imaging radiometer-polarimeter scanned the walls of our building in the winter. Searches for polar liquid spills or partially buried wiring, cables, etc., may similarly benefit from simple thermal lapse studies of the ground performed by fly-overs at steeper depression angles close to the Brewster angle of soils' dielectric constants.

3. Q – U channels tend to be quite sensitive to the rake angles of surfaces. Subsidence effects and fresh changes to the rake angle of grasses or tufted vegetation seem to be easy to spot with changing viewing angles. These effects are anticipated to be strongest at viewing angles of less than  $-30$  degrees depression from horizontal and would be maximal for approximately  $-60$  degree depression angles for many soils and natural vegetation. Hence, side-looking or forward-looking aerial imaging from a prescribed stand-off slant range may actually benefit observation of disturbances to soils or vegetated areas. Linear subsidence features due to buried pipes or worn depressions in paths are highlighted well when the properties of vertical and horizontal brightness temperature ( $T_V$  and  $T_H$ ) are compared. The effects of correlated surface disturbances show up as interesting clustered correlations of the Q and U Stokes parameters when pixels are presented as 2D projections or histograms. The oddly outlying spurs of these correlation graphs were consistently identified as useful anomalies, and appear to be an excellent novelty tracking algorithm for scene disturbances.
4. Curvature and warping effects, such as bowed out car windshields or subsidence create their own unique clusters of correlations between the U and V Stokes components. We speculate such mappings would be useful for detecting and possibly quantifying the incurvations of spallation upliftings of forested areas or subsidence craters from weapons testing. The depth and angle of subsidence may be quantifiable by doing detailed tipping angle studies. Our current results show compelling methods of correlated mappings to at least rapidly detect anomalies in surface profiles.

## 12.2 Future Plans

In the near term, it would be quite interesting to restudy areas of historical weapons tests to gather new relevant signatures of partially buried or twisted metal remnants. Likewise, the study of subduction or curved spallation structures, fracturing of rock and other effects of man-made disturbance to natural scenes, would help to validate if these effects could be detected and quantified at more propitious viewing angles at great ranges. Our systems were designed to be robust and polarimetrically stable, so their application to surveys of NTS or other DOE sites of relevance would be a near-term objective for follow-on funding.

In the long term, passive mm-wave imaging seems to be a potentially powerful complementary technology to IR thermal imaging. It offers advantages for persistent and sensitive quantification of thermal maps and anomaly detection unlike that of the IR, and its polarimetric signal recovery is more straightforward and stable than IR-based polarimeters. Stereo or differential viewing is excellent for highlighting man-made disturbances. The systems we developed were made to be reliable and relatively low cost for implementation in less than three years from scratch! Their receiver temperature, which is a measure of their own self-emission and losses, is quite high compared to mm-wave polarimeters being developed by astrophysicists. Speed of imaging of a large field-of-regard is characterized in terms of a

radiometer's receiver temperature  $T_R$ .  $T_R \approx T_{\text{scene}}$  results in adequate speed of imaging and this can be improved nearly quadratically with the ratio of  $T_{\text{scene}}/T_R$ . By extension,  $T_R > T_{\text{scene}}$  will lead to much lower speed of 2D radiometric imaging as described in Griffin et al. (2002) and Bock et al. (2005). Our  $T_R$  for single spatial channel imagers were about 1500 to 1800 K compared to the ambient scenes with  $T_{\text{scene}}$  approximately 300 K. New developments in both RF-to-optical transfer of the mm-wave energy onto optical heterodyne receivers or low noise InP-based MMICs can potentially push  $T_R$  to approximately 300 K with ambient radiometer and polarimeter systems. These newer PMMW technologies would allow unprecedented speed of imaging improvements that should be considered, especially if new signatures from DOE sites of interest prove strong and/or compelling in their novelty.



## 13.0 References

- Angel R. 2000. *The Large Binocular Telescope - An Interferometer for Wide-Field Fizeau Imaging and Bracewell Nulling*. Presented at Interferometry Workshop, UCSC, on October 15, 2000. Available at [http://lbtwww.arcetri.astro.it/tech/angel\\_sc.ppt](http://lbtwww.arcetri.astro.it/tech/angel_sc.ppt).
- Bettenhausen MH, CK Smith, RM Bevilacqua, N-Y Wang, PW Gaiser and S Cox. 2006. "A Nonlinear Optimization Algorithm for WindSat Wind Vector Retrievals." *IEEE Transactions on Geoscience and Remote Sensing* 44(3):597-610.
- Bock JJ, S Church, M Devlin, G Hinshaw, A Lange, A Lee, L Page, B Partridge, J Ruhl, M Tegmark, PT Timbie, R Weiss, B Winstein and M Zaldarriaga. 2005. *Task Force on Cosmic Microwave Background Research, Final Report*. Available at [www.nsf.gov/mps/ast/tfcr\\_final\\_report.pdf](http://www.nsf.gov/mps/ast/tfcr_final_report.pdf), or <http://arxiv.org/abs/astro-ph/0604101>.
- Brooker GM. 2008. "Chapter 4, Millimetre Wave Radiometers." In *Introduction to Sensors for Ranging and Imaging*, pp. 77-110. SciTech Publishing, Inc., Rayleigh, North Carolina.
- Chang S and A Prata, Jr. 2004. "The Design of Classical Offset Dragonian Reflector Antennas with Circular Apertures." *IEEE Transactions on Antennas and Propagation* 52(1):12-19.
- Daniels DJ. 2009. "Chapter 6, Passive Systems." In *EM Detection of Concealed Targets*, pp. 214-228. Wiley, Hoboken, New Jersey.
- Dial G, H Bowen, F Gerlach, J Grodecki and R Oleszczuk. 2003. "IKONOS Satellite, Imagery, and Products." *Remote Sensing of Environment* 88(1-2):23-36.
- Dragone C. 1978. "Offset Multireflector Antennas with Perfect Pattern Symmetry and Polarization Discrimination." *Bell System Technical Journal* 57:2663-2684.
- Gaiser PW, KM St Germain, EM Twarog, GA Poe, W Purdy, D Richardson, W Grossman, WL Jones, D Spencer, G Golba, J Cleveland, L Choy, RM Bevilacqua and PS Chang. 2004. "The WindSat Spaceborne Polarimetric Microwave Radiometer: Sensor Description and Early Orbit Performance." *IEEE Transactions on Geoscience and Remote Sensing* 42(11):2347-2361.
- Granet C. 2001. "Designing Classical Dragonian Offset Dual-Reflector Antennas from Combinations of Prescribed Geometric Parameter." *IEEE Antennas and Propagation Magazine* 43:100-107.
- Griffin MJ, JJ Bock and WK Gear. 2002. "Relative Performance of Filled and Feedhorn-Coupled Focal-Plane Architectures." *Applied Optics* 41(31):6543-6544.
- Kendrick RL, J-N Aubrun, R Bell, R Benson, L Benson, D Brace, J Breakwell, L Burriesci, E Byler, J Camp, G Cross, P Cuneo, P Dean, R Digumerthi, A Duncan, J Farley, A Green, HH Hamilton, B Herman, K Lauraitis, E de Leon, K Lorell, R Martin, K Matosian, T Muench, M Ni, A Palmer, D Roseman, S Russell, P Schweiger, R Sigler, J Smith, R Stone, D Stubbs, G Swietek, J Thatcher, C Tischhauser, H Wong, V Zarifis, K Gleichman and R Paxman. 2006. "Wide-Field Fizeau Imaging Telescope: Experimental Results." *Applied Optics* 45(18):4235-4240.
- Korotkov AL, J Kim, GS Tucker, A Gault, P Hyland, S Malu, PT Timbie, EF Bunn, E Bierman, B Keating, A Murphy, C O'Sullivan, PAR Ade, C Calderson and L Piccirillo. 2006. "The Millimeter-

- Wave Bolometric Interferometer.” In *Proceedings of the SPIE: Millimeter and Submillimeter Detectors and Instrumentation for Astronomy III*, p. 62750X. May 2006, Orlando, Florida. DOI 10.1117/12.672246. The International Society for Optical Engineering (SPIE), Bellingham, Washington.
- Lahtinen J and MT Hallikainen. 2003. “HUT Fully Polarimetric Calibration Standard for Microwave Radiometry.” *IEEE Transactions on Geoscience and Remote Sensing* 41(3):603-611.
- Lettington AH, D Dunn, M Attia and IM Blankson. 2003. “Passive Millimetre-Wave Imaging Architectures.” *Journal of Optics A Pure and Applied Optics* 5(4):S103-S110.
- Lynch J, H Moyer, J Schulman, P Lawyer, R Bowen, J Schaffner, D Choudury, J Forschaar and D Chow. 2006. “Unamplified Direct Detection Sensor for Passive Millimeter Wave Imaging.” In *Proceedings of the SPIE: Passive Millimeter-Wave Imaging Technology IX*, pp. 621101-1 - 621101-7. May 5, 2006, Orlando (Kissimmee), Florida. The International Society for Optical Engineering (SPIE), Bellingham, Washington.
- Mizuguchi Y, M Akagawa and H Yokoi. 1978. “Offset Gregorian Antenna.” *Transactions of the Institute of Electronics and Communication Engineers of Japan* J61-B(3):166-173.
- Peichl M, S Dill, M Jirousek and H Sus. 2007. “Microwave Radiometry - Imaging Technologies and Applications.” In *Proceedings of Wave Propagation in Communication, Microwave Systems and Navigation (WFMN07)*, pp. 75-83. July 4-5, 2007, Chemnitz, Germany.
- Siegel PH. 2002. “Terahertz Technology.” *IEEE Transactions on Microwave Theory and Tech.* 50(3):910-928.
- Skou N, B Laursen and S Sobjaeg. 1999. “Polarimetric Radiometer Configurations: Potential Accuracy and Sensitivity.” *IEEE Transactions on Geoscience and Remote Sensing* 37:2165-2171.
- Tucker GS, AL Korotkov, A Gault, P Hyland, S Malu, PT Timbie, EF Bunn, B Keating, E Bierman, C O’Sullivan, PAR Ade and L Piccirillo. 2008. “The Millimeter-Wave Bolometric Interferometer (MBI).” In *Proceedings of the SPIE: Millimeter and Submillimeter Detectors and Instrumentation for Astronomy IV*, p. 7020M. June 28, 2008, Marseille, France. DOI 10.1117/12.788463. The International Society for Optical Engineering (SPIE), Bellingham, Washington.
- Ulaby F, R Moore and A Fung. 1981. *Microwave Remote Sensing: Active and Passive, Vol. I -- Microwave Remote Sensing Fundamentals and Radiometry*. Addison-Wesley, Advanced Book Program, Reading, Massachusetts.
- van Vliet AHF and T de Graauw. 1981. “Quarter Wave Plates for Submillimeter Wavelengths.” *International Journal of Infrared and Millimeter Waves* 2(3):465-477.
- Webber JC and MW Pospieszalski. 2002. “Microwave Instrumentation for Radio Astronomy.” *IEEE Transactions on Microwave Theory and Techniques* 50(3):986-995.
- Wikner D and E Grossman. 2009. “Demonstration of a Passive, Low Noise, Millimeter-Wave Detector for Array Imaging.” In *Passive Millimeter-Wave Imaging Technology XII, Proceedings of SPIE, Vol. 7309*, pp. 730909-1 - 730909-6. April 16, 2009, Orlando, Florida. The International Society for Optical Engineering (SPIE), Bellingham, Washington.

Wolfe WL, Ed. 1965. *Handbook of Military Infrared Technology*. U.S. Government Printing Office, Washington, D.C.

Yujiri L, M Shoucri and P Moffa. 2003. "Passive Millimeter Wave Imaging." *IEEE Microwave Magazine* 4(3):39-50.

Collet E. 2011. "Field Guide to Polarization." SPIE Press.

McClaning K, and Vito T. 1959. *Radio Receiver Design*. Noble Publishing Corp. Atlanta GA.



# **Appendix A**

## **Definitions**



# Appendix A

## Definitions

co-polarized	Polarized in the same sense (same linear direction or same rotational handedness)
cross-polarized	Polarized oppositely or differently (usually right versus left or horizontal versus vertical)
Dicke switch	A single-pole double-throw (electronic) switch at the receiver input, the common terminal being on the receiver and the two switched poles alternating between a source and a reference. The purpose of this arrangement is to minimize effects of amplifier drift.
Dragone-Mizuguchi	An offset dual reflector design providing a parabolic equivalent with low cross-polarization and low astigmatism. In the present report it means specifically the crossed Dragone-Mizuguchi design, using a large secondary and a right-angle feed.
Gregorian	A type of Dragone-Mizuguchi design with a smaller secondary, providing an on-axis feed.
millimeter wave	Electromagnetic energy with wavelengths from 1 mm to 10 mm in vacuo, also known as extremely high frequency (EHF) and having a frequency range of 30 GHz to 300 GHz.
noise equivalent differential temperature (NEDT)	The difference in temperature needed to give a signal equal to the noise figure; in effect, the temperature resolution capability.
off-axis parabola	A disk-shaped paraboloidal reflector in which the center of symmetry of the paraboloid is not at the center of the disk. This allows for a telescope design in which the receiver or secondary does not interrupt the field of view.
orthomode transducer	A microwave component that separates the signal into orthogonally polarized signals (or in other applications, combines two such signals into one).
skyshine	Generally, radiation incident from the sky. In this context, isotropic mm-wave radiation incident from the sky.
Stokes parameters	A set of four parameters, often denoted I, Q, U, and V, that fully describe the intensity and polarization of an electromagnetic signal. They are often more convenient and significant than the vector components of the signal. In general terms, I is the intensity, Q is the degree of vertical or horizontal polarization, U is the degree of diagonal polarization, and V is the degree of circular polarization. These parameters are closely related to the difference in light reflected from random natural surfaces versus light reflected from man-made structures.



**Appendix B**  
**Presentations**



- NA-22 all-lab, annual program review for Remote Sensing at Eglin Air Force Base on May 19 & 20, 2009 (Figure B.1).
- Presented a paper entitled “Phenomenology Studies Using a Scanning Fully Polarimetric Passive W-Band Millimeter Wave Imager” at SPIE Defense, Security and Sensing Conference, April, 2011.
- NA-22 Remote Sensing Program Review Meeting (RS2010) held at Sandia National Laboratory, on May 18 and 19, 2010. Dr. Bruce Bernacki gave the presentation “Passive MM-Wave Imaging Polarimeter.”
- Conducted an independent managed by Steve Schubert (Glen Sjoden) review 28 June 2010. Here are some of the highlights from the review:
  - “The Review Team concluded that the Researchers had indeed accomplished a great deal of work in the first year. Moreover, the utility of the project with regard to NA-22 goals and objectives was also readily apparent; it was clear to the team that the project was complimentary to other NA-22 programs, and had been carried out in a very high quality manner.”
  - “The Review Team noted that if the proposed project was successful, the impact of the work would be truly substantial with regard to application of passive imaging in support of the NA-22 mission.”
  - “...Finally, the Review Team was very impressed with the progress achieved, and specifically commended the Researchers on their efforts in the project, specifically noting the high value of this research and potential in national security/national technical means applications.”
- Conducted a program review with Dr. Victoria Franques and Dr. Robert Shirey on the 14<sup>th</sup> of September, 2010, and toured the EDL laboratory and demonstrated the passive millimeter-wave imager to them.
- Submitted a patent disclosure of invention entitled “Passive Millimeter Wave Differential Contrast Polarimetry.” We are now in the process of integrating a quasi-optical element to demonstrate enhanced spatial overlap performance with the single mirror differential radiometer for inclusion into the patent application.
- Dr. Bruce Bernacki and Doug McMakin attended RS2011 at Eglin Air Force Base. Dr. Bernacki presented a technical review on the Novel Passive Millimeter Imager for Broad-Area Search.

# Passive MM-Wave Imaging Polarimeter

Doug McMakin, Bruce Bernacki, Dave Sheen, Tom Hall, Jonathan Tedeschi and Jim Kelly



Proudly Operated by **Battelle** Since 1965

## Goals and Objectives

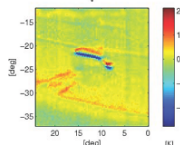
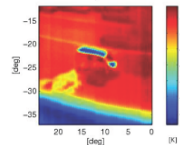
**Develop a W-band (3-mm) passive imaging radiometer for wide area search, capable of sub-pixel mapping of man-made surface textural changes via differential polarimetry**

- Support the Office of Nuclear Nonproliferation (NA-22) in their mission to locate, detect and "identify" nuclear proliferation activities using remote, passive imaging that can see through clouds and most obscurants.
- Support the USG in efforts to persistently detect sub-pixel changes of emitted mm-wave radiation from small WMD operations and/or spills of polar chemicals on surfaces.
- Verify that accurate temperature brightness and precision polarimetry can be done against small facilities using wide area search techniques (ie., whiskbroom / pushbroom scanning).
- Validate that modest concentration polar chemical spills or coatings can be classified on surfaces.
- Develop coherent beam combining techniques to achieve sub-pixel resolution using dual aperture telescopes.
- Show that these techniques are configuration independent and scalable.

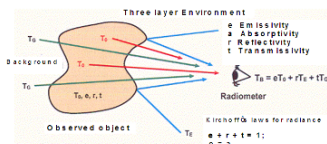
## Applications

**Passive Wide-Area-Search methodology with potential for persistent coherent change detection of surface disturbances via high SNR polarimetric signatures**

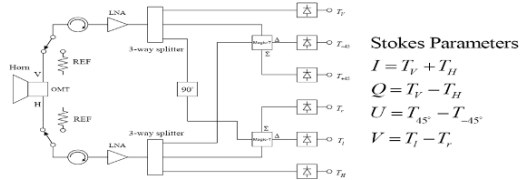
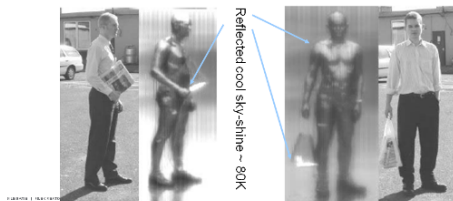
- Offers wide area searching using configuration-independent scanning.
- Suitable for 45° from-nadir front or side-angle mapping from UAVs (e.g. whisk-/push-broom)
- Delivers multiple modalities from larger airborne platforms
- Wholly passive imaging and mapping of thermal profiles and sub-pixel surface changes.
- Reveals important surface orientation change information, such as road tracks, or other striated disturbances that cannot be seen with high spatial resolution in the mm-wave.



Stokes V-parameter highlights polarization changes



Measured temperature < actual temperature due to cool sky-shine



## Scientific Basis

- Passive mm-wave radiometry penetrates non-conducting materials and obscurants deeper than thermal IR radiometry – uses cool reflected sky-shine to better highlight presence of painted or covered metals; polar-liquid / -solids spills under dust; etc.
- Reflected sky-shine from near nadir angles gives wider dynamic range for brightness temperature changes than LWIR.
- MM-wave polarimetry is quite stable against drift and effects of environmental humidity/dust/etc.: calibrations remain stable over > 8 hours, even several days.

## Challenges

- Can we avoid whiskbroom scanning and go to a pushbroom configuration?
- How can we overlay a full Stokes polarimeter into the system without sacrificing sensitivity?
- Should we cryo-cool the front end to achieve ultimate contrast performance below 0.1 mK/°s?
- How well can we do a pseudo-correlation (Bracewell) nulling of the background from diffuse emission sources?



Conceptual design showing a dual aperture mm-wave polarimeter configured for coherent change detection using Bracewell nulling.

## Planned Efforts

- FY2009 – Study phenomenology of polarimetric surface effects and clutter suppression ideas.
- Build and test full Stokes imaging polarimeter (mech. scanned) against Hanford site features.
- Initiate design and fabrication of dual aperture telescope to understand "coherent" signal combining.
- FY2010 – Test Bracewell clutter suppression with a pseudo-correlation polarimeter.
- Validate sub-aperture spatial resolution limit.
- Understand tolerance limits to build a dual aperture polarimeter.
- FY2011 – Design, fabricate & test a dual aperture linear focal plane array polarimeter.
- Evaluate whether pseudo-correlation or full Stokes polarimeter offers best performance.
- Develop field calibration techniques and verify stability of the system against drift and changing environmental factors.

**Figure B.1.** NA-22 All-Lab, Annual Program Review for Remote Sensing at Eglin Air Force Base on May 19 & 20, 2009

## **Appendix C**

### **Administrative Information**



## Appendix C

### Administrative Information

#### C.1 Final Report for the Period October 1, 2008 Through September 30, 2011

Project Title: A Novel Passive Millimeter Imager for Broad-Area Search  
Project Numbers: PNNL-09-098, PL09-NPMI-PD07  
Lab/Contractor: PNNL  
PNNL Project number: 55180  
B&R Code: NN2001-07/Proliferation Detection/Nuclear Fuel Cycle Remote Sensing  
Principal Investigator(S): Doug McMakin – PNNL (PM) 509-375-2206  
Jim Kelly – PNNL (PI) 509-375-2699  
Dave Sheen – PNNL (Co-PI) 509- 375-6412  
Bruce Bernacki – PNNL (Co-PI) 509-375-2135  
HQ Program Manager: Dr Victoria Franques 202-586-2560

#### C.2 Tasks

- FY2009 Task 1 – Development of a polarimeter bench test system
- FY2009 Task 2 - Evaluate test system with imaging 2-D scanners and establish calibration protocols
- FY2010 Task 1 – Develop dual-element nulling interferometric polarimetric receiver
- FY2010 Task 2 – Evaluate Bracewell nulling imaging polarimeter system and establish calibration protocols.

#### C.3 Financial Summary

- FY2009: \$847.2K
- FY2010: \$1,082.3K
- FY2011: \$782.8K (through July 22, 2011)

Initial baseline funding as requested by PNNL and budgeted by DOE

Fiscal Year	PNNL Requested	DOE Budgeted	Difference
FY09	\$1,130K	\$1,000K	\$130K
FY10	\$1,500K	\$1,100K	\$400K
FY11	\$1,750K	\$1,200K	\$500K

Program re-baseline documentation was generated to reflect the DOE funding profile changes from the original project LCP for FY10 and FY11. The development emphasis in FY10 will be prove out the Bracewell nulling technique for polarization analysis. In FY11 the emphasis will be development of

compact array(s) that can be used for rapid imaging and polarimetry tests for future field deployable systems. This re-baseline documentation was sent to DOE NA-22 for review and concurrence.

## **Appendix D**

### **Radiometer Components**



# Appendix D

## Radiometer Components

### D.1 Millimeter Wave Components

#### D.1.1 Ortho-Mode Transducer (OMT)

Notes:

Converts circular waveguide input to H and V polarized rectangular waveguide outputs

Quantity: 1

Specs:

Center frequency: 93 GHz

Frequency Range: 91–95 GHz

Operating bandwidth (>5%)

Isolation: > 30 dB desired (25 dB min)

Insertion loss < 1.5 dB

VSWR: better than 1.4: 1

Circular waveguide diameter: 0.094 inches

Suggested vendors/part numbers:

Quinstar: QWO-93AMW0 (Preferred, specifications meet requirements)

Millitech: OMT-10-094RR

#### D.1.2 SPDT Waveguide Switches

Notes:

Used for Dicke-switching. Critical component – want the lowest insertion loss possible.

Quantity: 2

Specs:

SPDT design

Waveguide: WR-10

Center frequency: 93 GHz

Frequency Range: 91–95 GHz

Bandwidth: (> 5%)

Integrated drivers with TTL inputs

Insertion loss: < 3 dB (critical specification as low as possible)

Isolation: at least 18 dB

Suggested vendors/part numbers:

Millitech: PDT-10-R1100, center frequency 93 GHz, 4 GHz Bandwidth, Frequency Range 91-95 GHz.  
(Preferred Vendor, lowest insertion loss, lower pricing, item *must* be ordered with specifications)

Hxi: HSW21001-174

### **D.1.3 Reference Loads – Use Normal Waveguide Termination**

Notes:

Standard waveguide terminations. Needed for the reference loads and for the unused port on the magic-T.

Quantity: 3

Specs:

Waveguide: WR-10

VSWR: < 1.1 : 1

Power handling: 0.5 Watts

Suggested vendors/part numbers:

Quinstar: QWN-W00000 (Preferred Vendor, lower pricing)

Mi-Wave: 580

Millitech: WTR-10-R0000

### **D.1.4 Low Noise Amplifier (LNA)**

Notes:

Critical component – want the lowest noise figure possible.

Quantity: 2

Specs:

Frequency range: 91 – 95 GHz

Noise figure: < 4.5 dB

Gain: > 30 dB

Suggested vendors/part numbers:

Farran Technologies: FLNA-10-30, Frequency Range 91-95 GHz (preferred, model has high gain and lowest noise, also see if there is anyway to reduce lead time <60 days.)

hxi HLNAW-277

Millitech: LNA-10-02140

Quinstar: QLW-92986014-II

Spacek: SLW-15-5 (looks very good, but gain is somewhat low ~18dB may need more gain)

### **D.1.5 Isolators**

Notes:

Prefer the smaller internally-terminated circulator-style isolators over the longer Faraday rotation isolators. Smaller isolators are limited to 2GHz bandwidth. Larger Faraday isolators are full-band. Lower insertion loss is also available with the smaller isolators.

Quantity: 2

Specs:

Waveguide: WR-10

Center frequency: 93 GHz

Bandwidth: 4 GHz (5%)

Isolation: > 18 dB  
Insertion loss: < .8 dB  
VSWR: < 1.4 : 1

Suggested vendors/part numbers:

HXI: HMI10-387-93.0-4.0 (preferred vendor, lowest cost, meets specifications)

Quinstar: QJI-93041W

Millitech: FBI-10-RSES0

Farran Technologies: ISFB-10

### D.1.6 High-Pass Filter

Notes:

Quantity: 2

Specs:

Waveguide: WR-10

Must reject <= 83 GHz

Passband: 91 – 95 GHz

Rejection: at least 35 dB (ideally >= 40 dB)

Insertion loss: < 1.2 dB (low as possible)

Suggested vendors/part numbers:

Quinstar QFH-90SW00 (Preferred Vendor, meets specifications)

Millitech FHP-10-08740

### D.1.7 Mixers

Notes:

Quantity: 2

Specs:

Balanced mixer design

Waveguide: WR-10

RF: 91 – 95 GHz

LO: 87 GHz

IF: 4 – 8 GHz

LO power required: 10-13 dBm

Conversion loss: < 8.5 dB

Suggested vendors/part numbers:

Millitech MXP-10-RSSXL, RF frequency range 91-95 GHz, RF Bandwidth 4 GHz, LO frequency 87 GHz, IF frequency Range 4-8 GHz, IF Bandwidth 4 GHz. (Preferred vendor, lower cost and meets specifications, NOTE: *must* give RF, LO and IF values in order)

Quinstar QMB-9387WS

hxi HBM10C- 196

### **D.1.8 Phase Shifters**

Notes:

Quantity: 2

Specs:

Waveguide: WR-10

Total phase shift range: 0 – 180 degrees

Mechanical tuning

Suggested vendors/part numbers:

Quinstar: QAS-W00000 (preferred vendor, low cost and meets specifications)

Millitech: VPS-10-R0000

### **D.1.9 Magic-T splitter**

Notes:

Used to perform an even phase power divide, needs a matched term on the unused port

Use compact design if possible (machined, split-block construction)

Quantity: 1

Specs:

Waveguide: WR-10

Center frequency: 87 GHz

Insertion loss: 1.0 dB (or less)

VSWR: < 1.6: 1

Isolation (E-H arms): 30 dB

Isolation (Colinear arms): 20 dB

Suggested vendors/part numbers:

Quinstar QJH-W N 87 00 (preferred vendor, low cost, meets all the spec requirements)

Millitech CMT-10-R6000

### **D.1.10 Gunn Oscillator (LO)**

Notes:

Quantity: 1

Specs:

Center frequency: 87 GHz

Mechanical tuning range: +/- 100 MHz

Waveguide: WR-10

Output power: 50 mW or 17dBm (min)

Frequency stability (MHz/deg C): +/- 4 (or better)

Integrated isolator

Integrated heater

Integrated voltage regulator

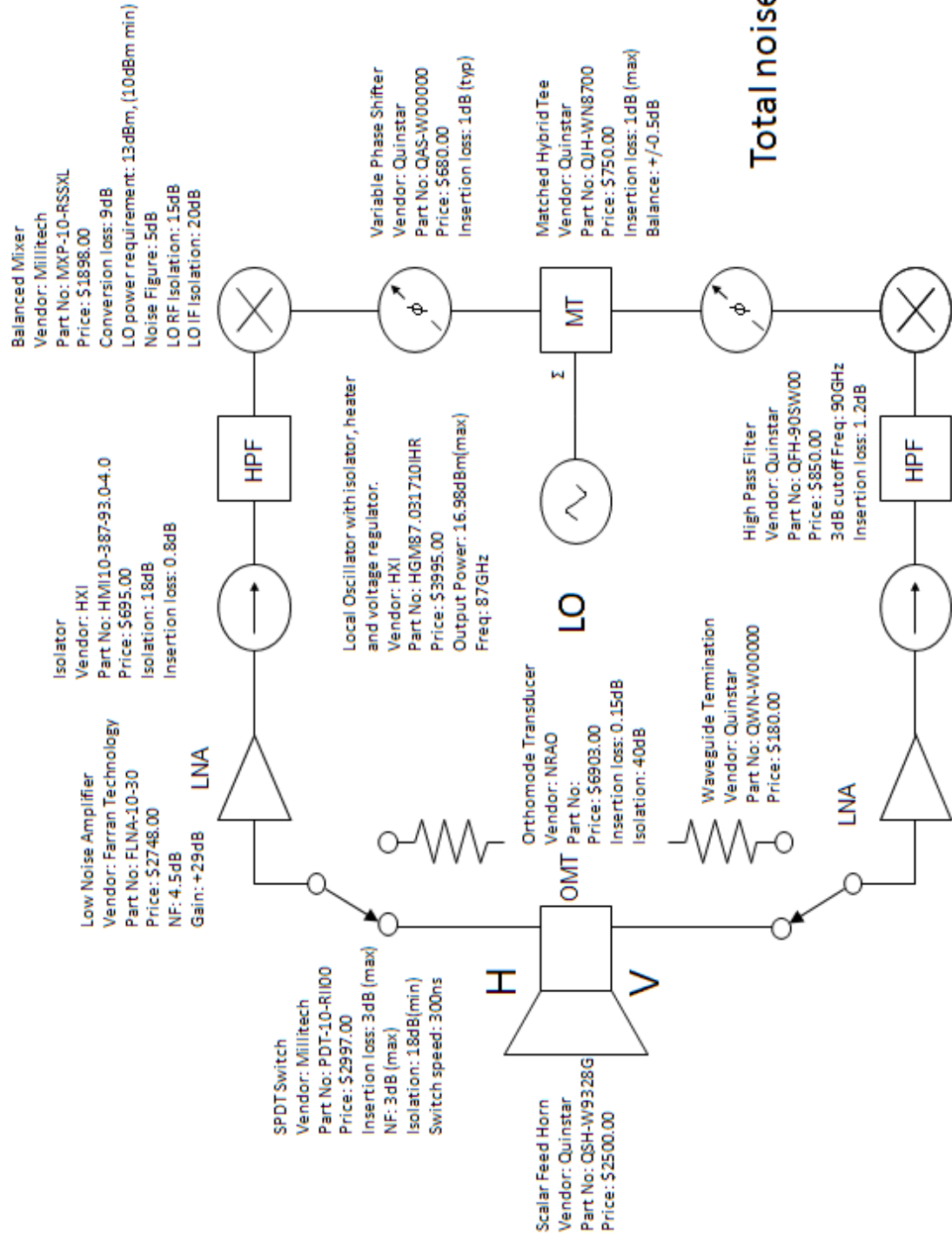
Suggested vendors/part numbers:

Hxi: HGM87.031710IHR (preferred vendor, meets specs and has high stability)

Millitech: GDM-10-3010HR

Quinstar: QTM -8718CW

# MM Wave Components

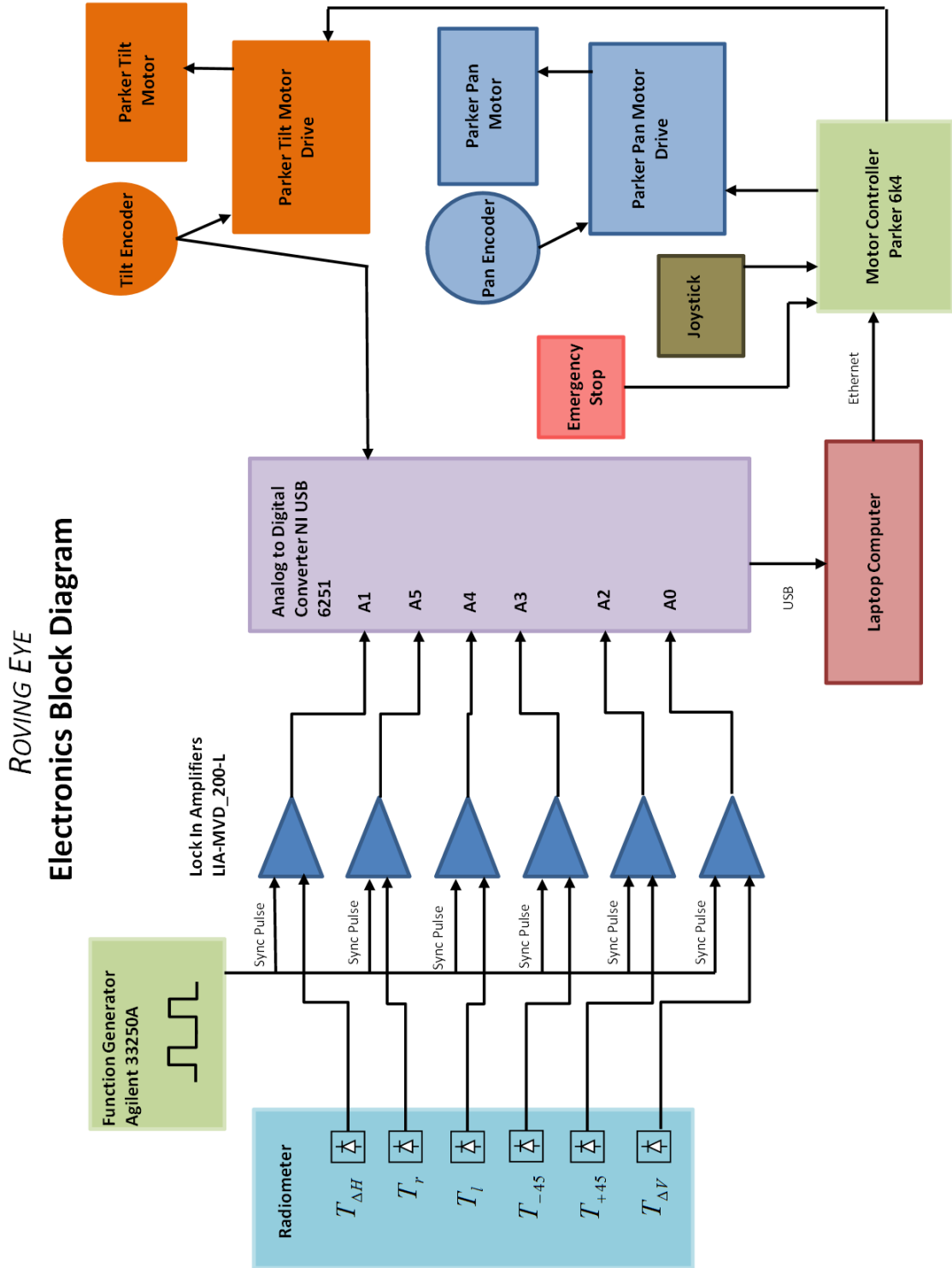


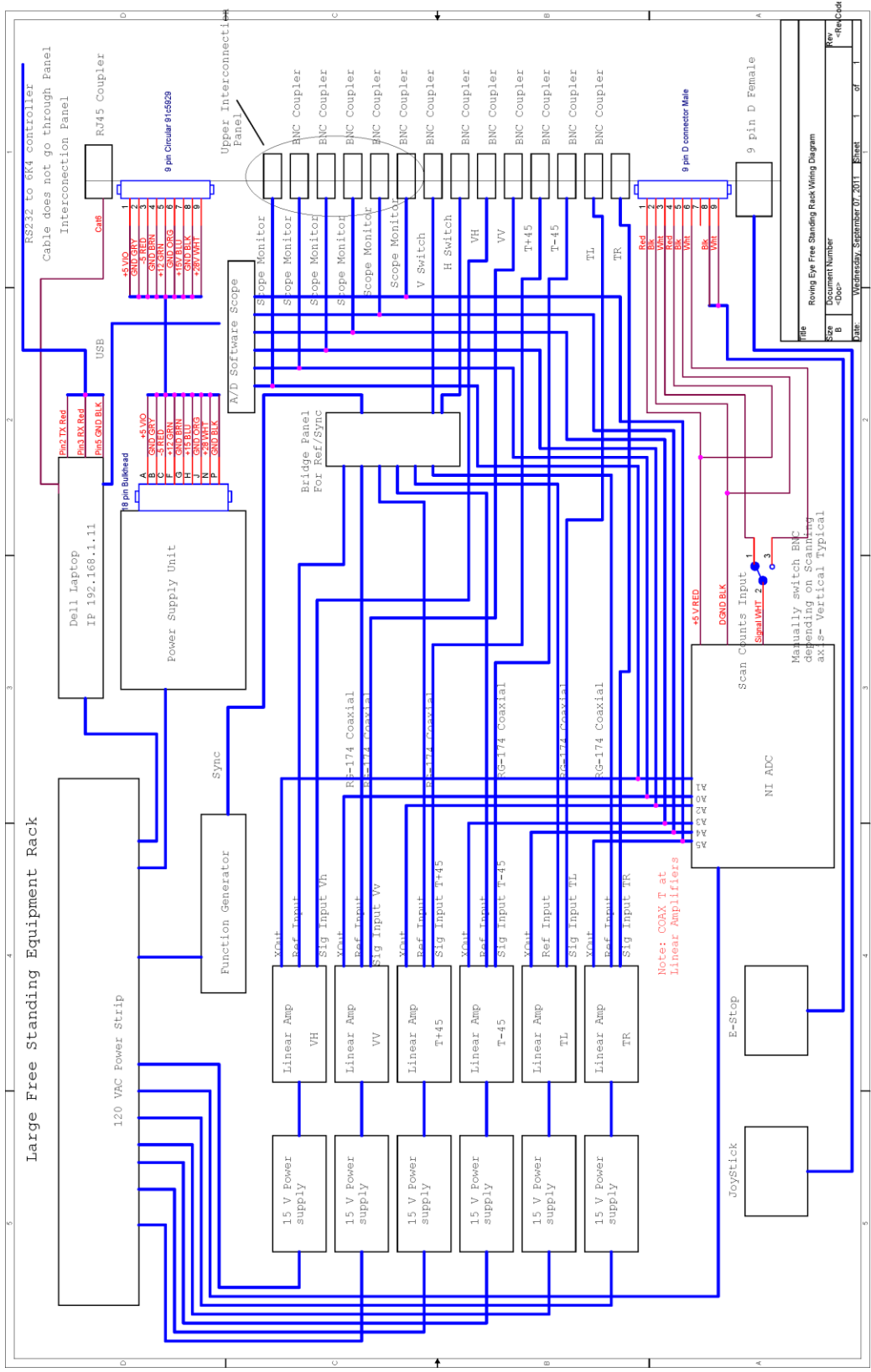
**Appendix E**  
**Electronic Diagrams**

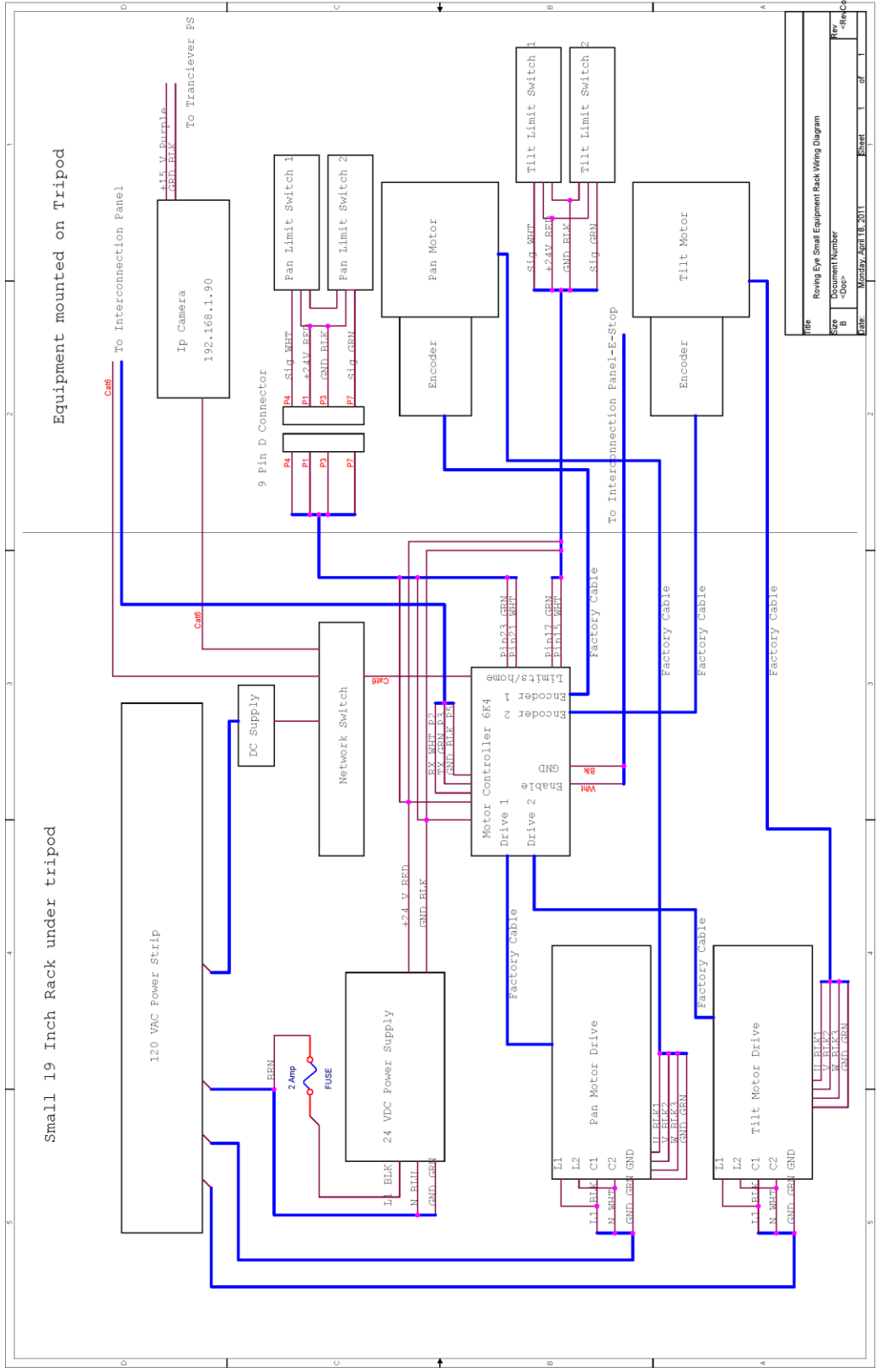


# Appendix E

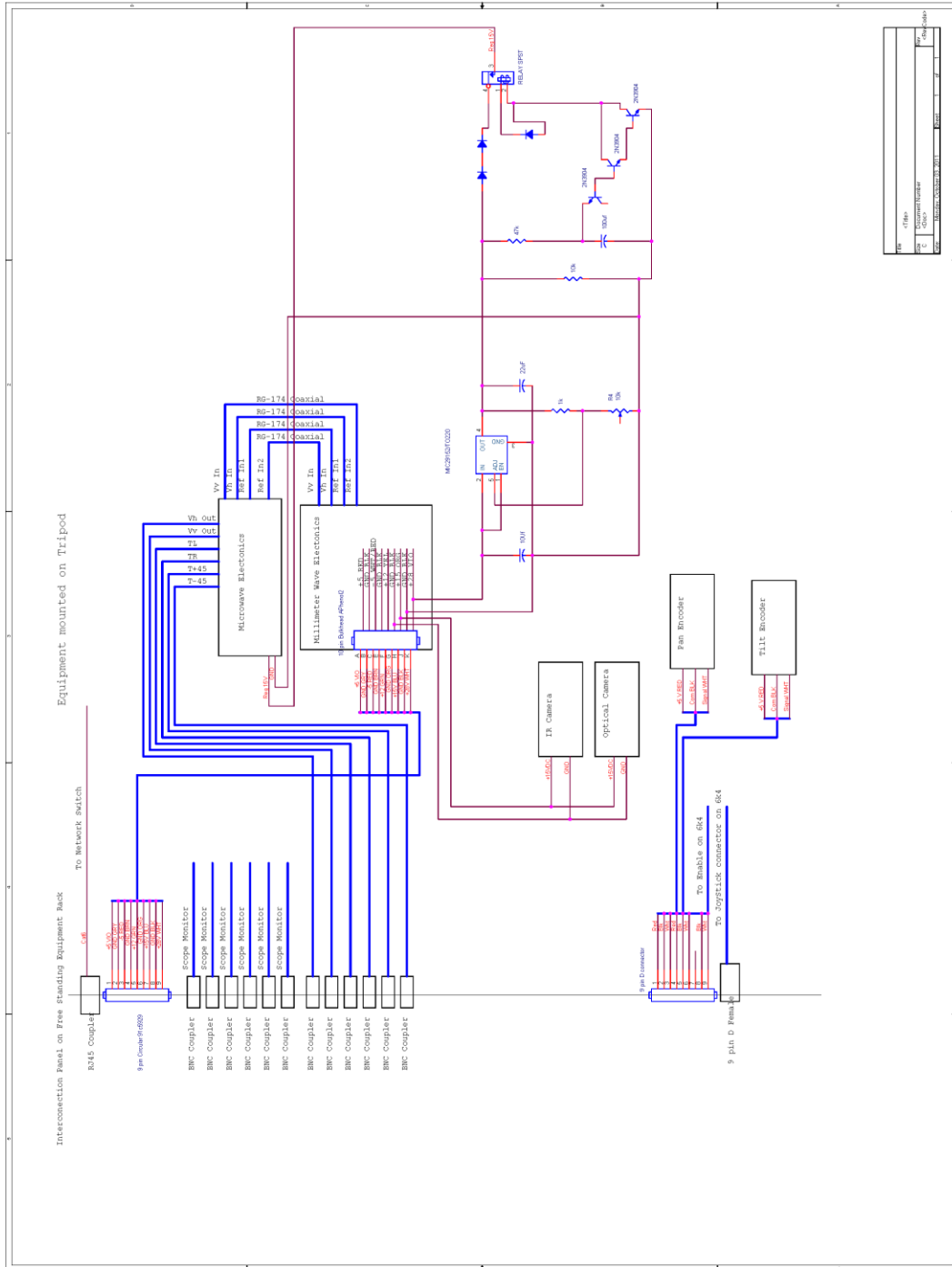
## Electronic Diagrams

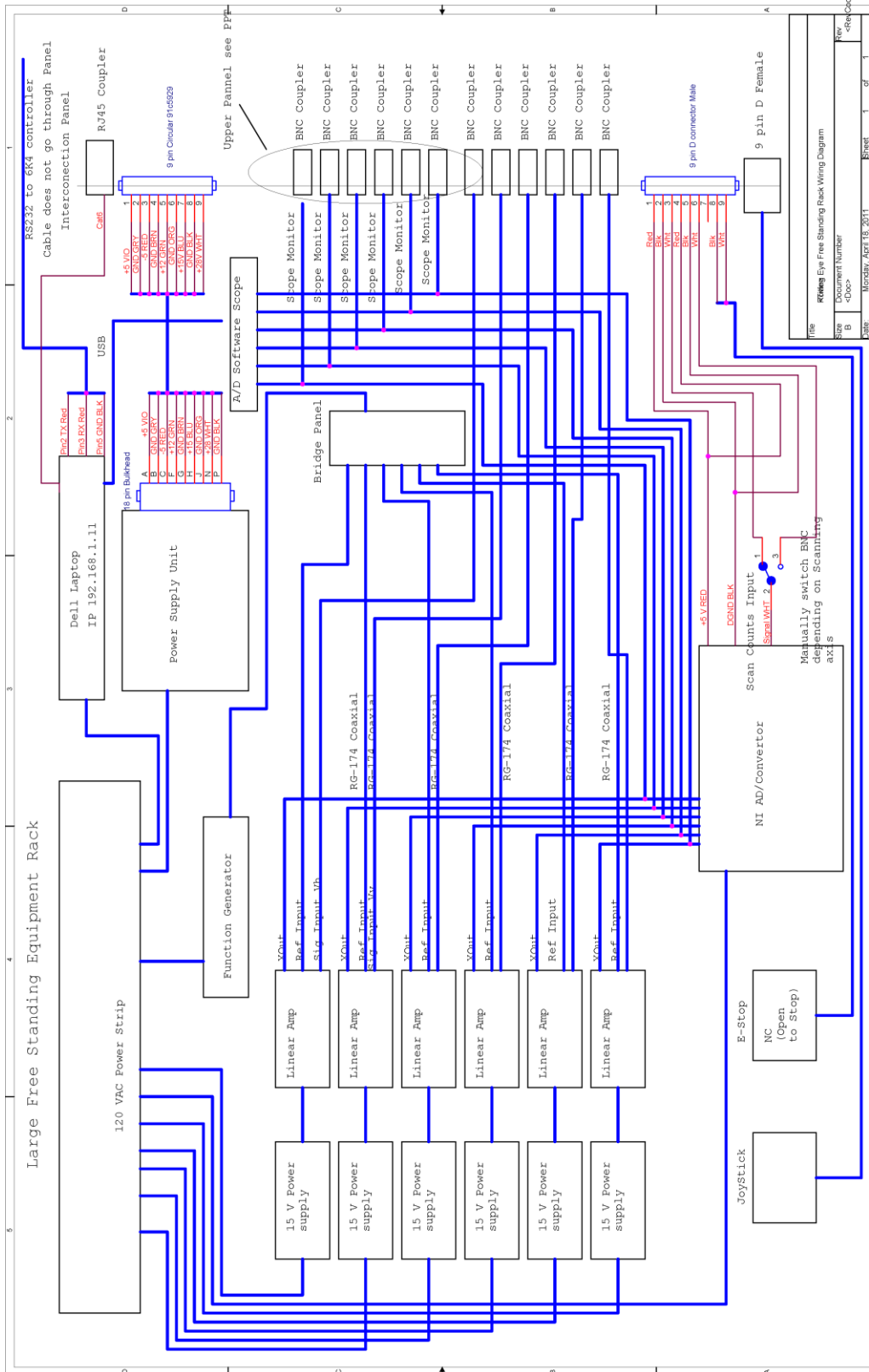




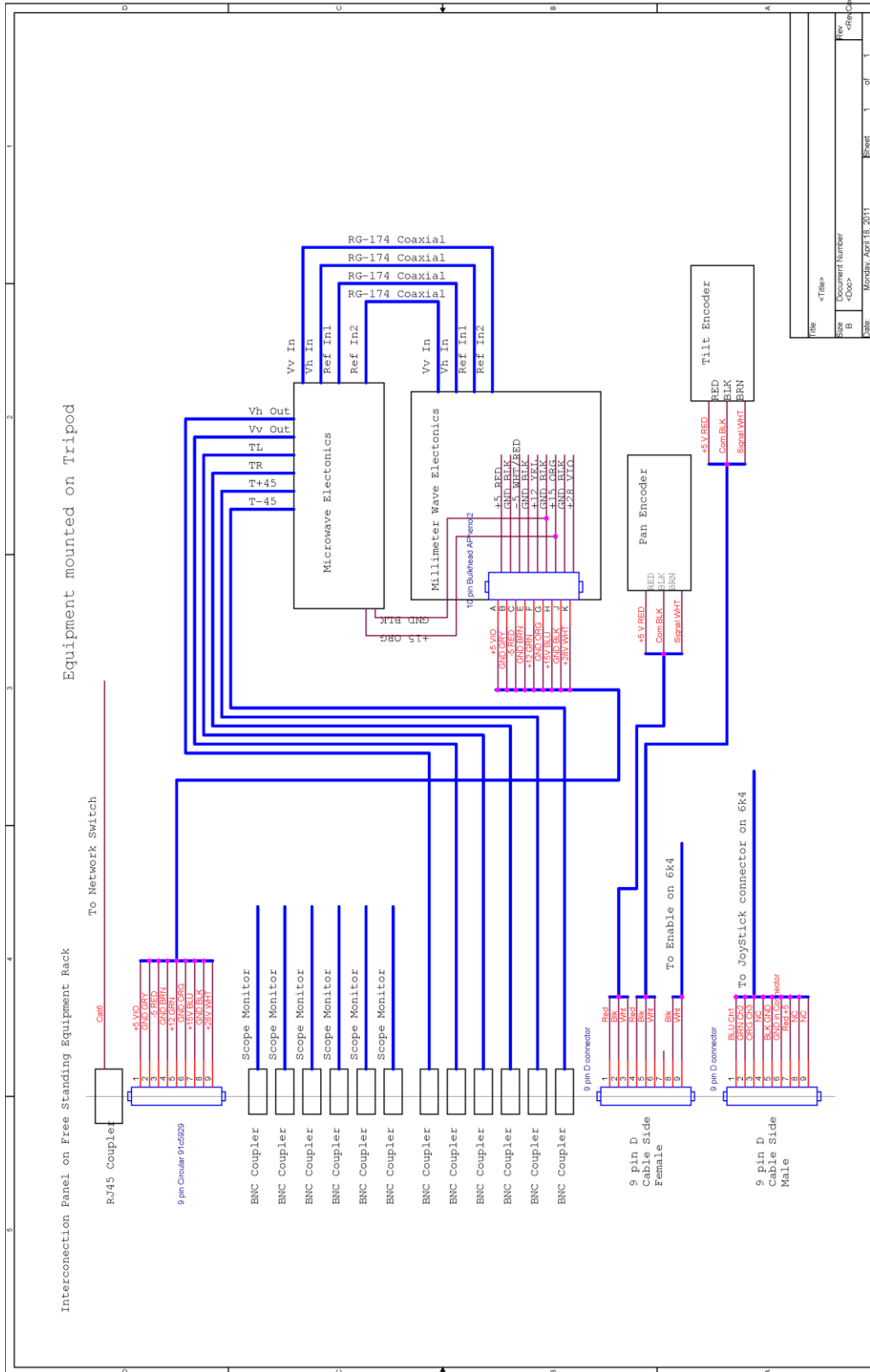


File	Roving Eye Small Equipment Rack Wiring Diagram
Size	Document Number
Rev	B
Doc	-Doc
Tab	Monday, April 18, 2011
Sheet	1 of 1











## **Appendix F**

### **Fully Polarimetric Radiometer Imaging Sets**



# Appendix F

## Fully Polarimetric Radiometer Imaging Sets

### F.1 Fully Polarimetric Infinite Conjugate Imaging Sets

#### F.1.1 Image Set #1

**Scene Description.** Circular polarized signal generator at base of loading dock ramp. Computational Sciences Facility across the parking lot. Cloudy conditions reducing contrast between targets with high reflectivity. The purpose of this image set is to verify the unique signature of a circular polarized signal.



**Figure F.1.** Panoramic Optical Image

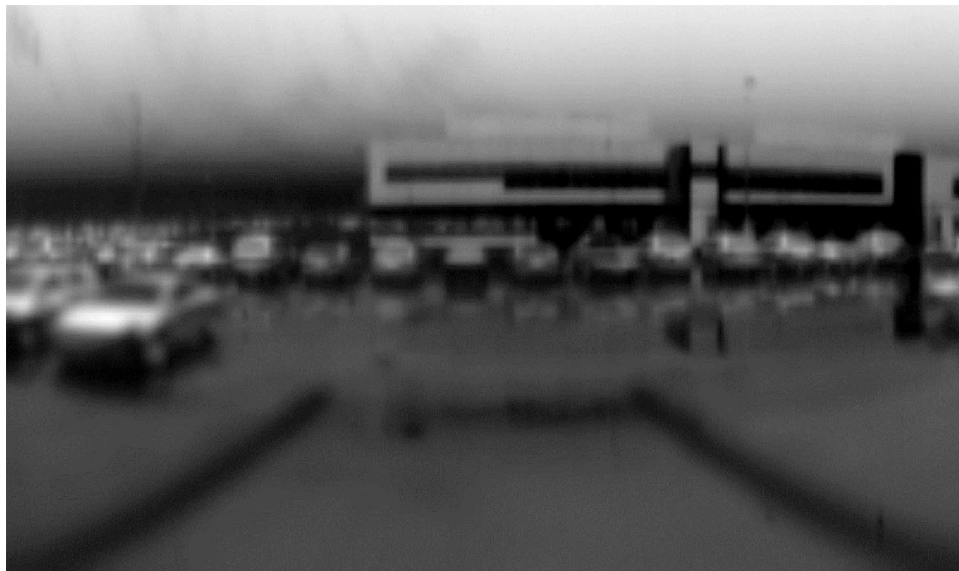


**Figure F.2.** Intensity Image (V + H)

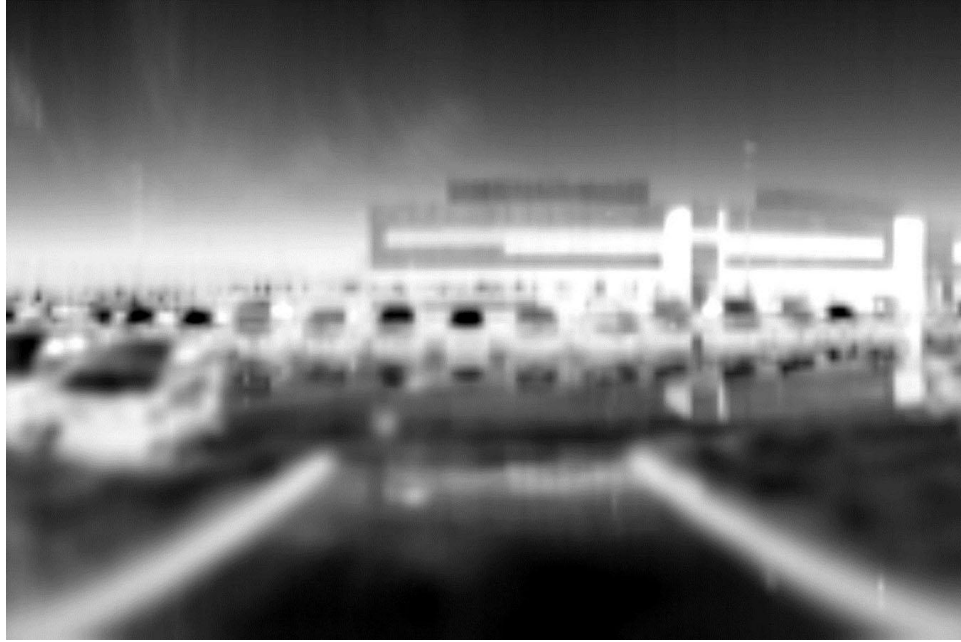


**Figure F.3.** Q Image (V – H)

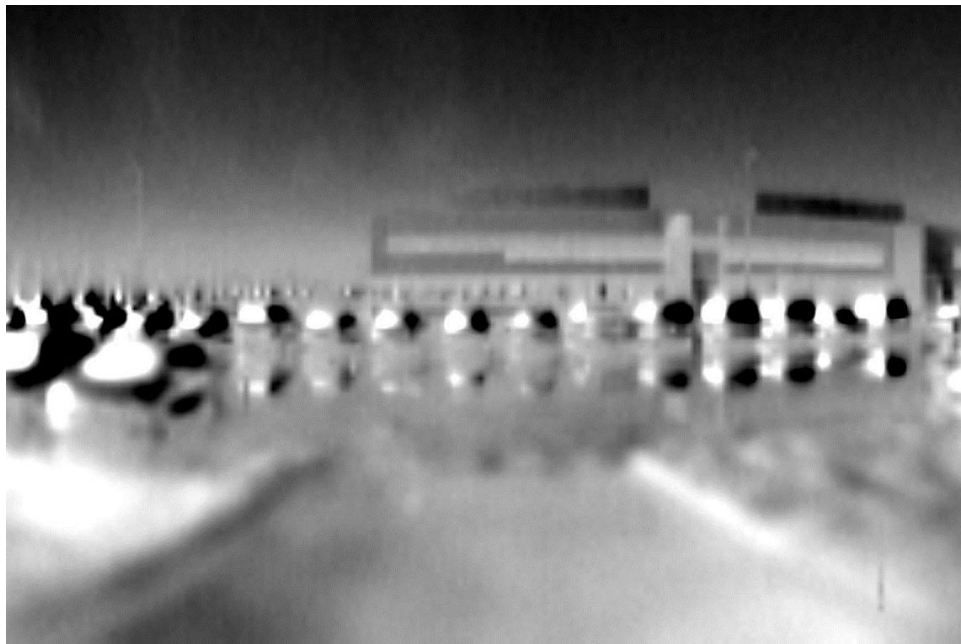


**Figure F.4.** U Image ( $T_{+45} - T_{-45}$ )

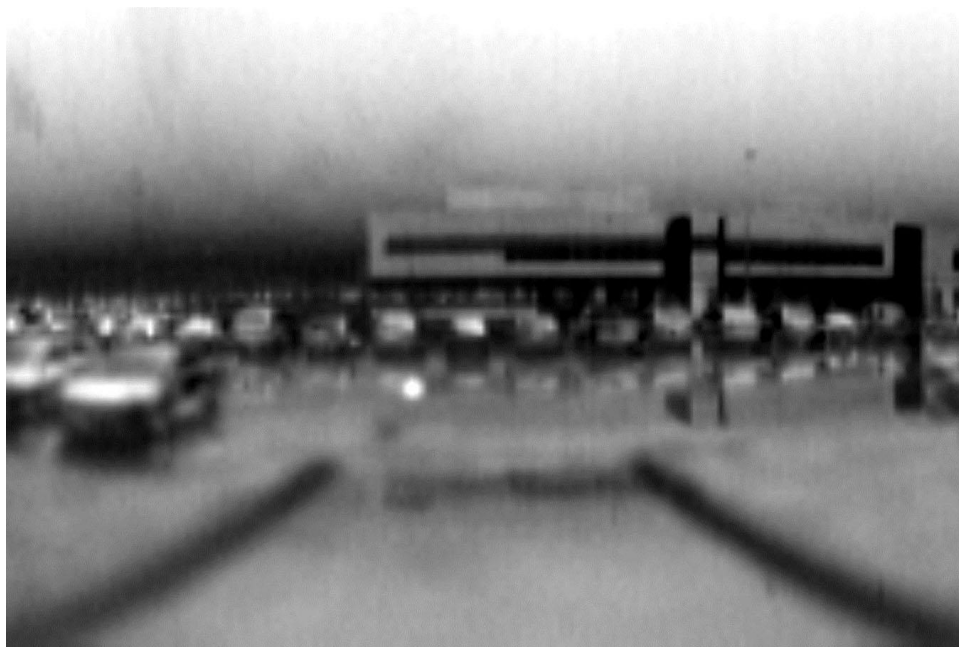


**Figure F.5.** V Image ( $T_1 - T_r$ )

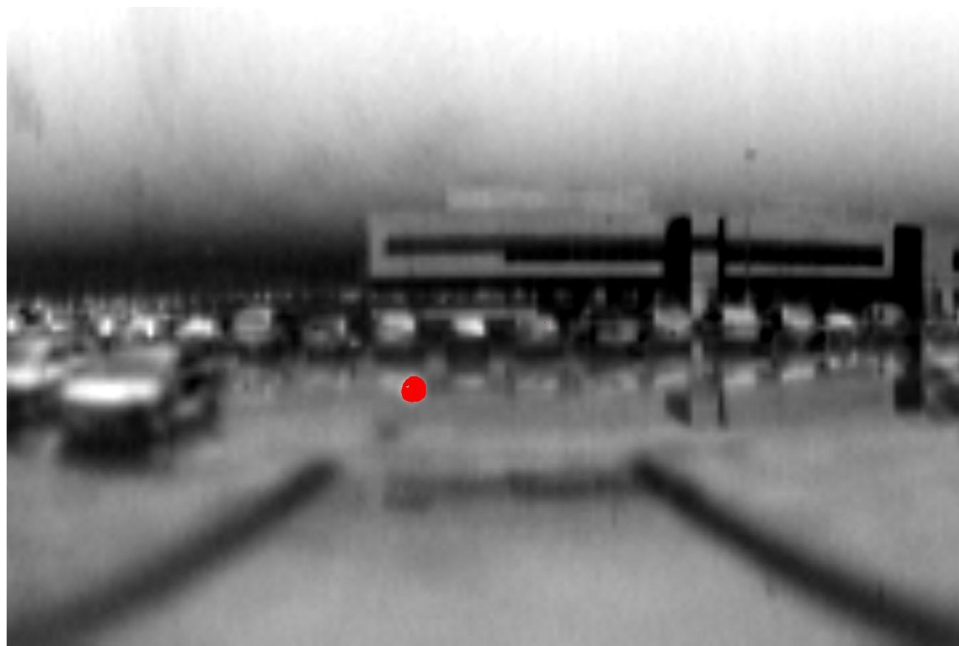


**Figure F.6.** V Image Highlighting Response from Circular Polarized Generator

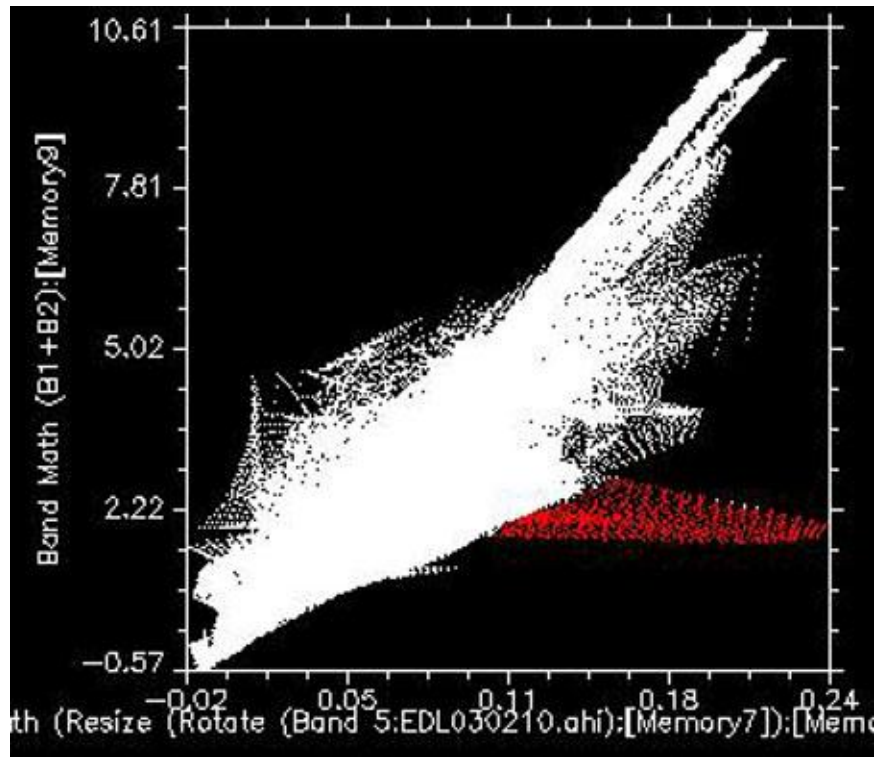


**Figure F.7.** V Verses Intensity Image with 2D Scatter Plot Highlighting Circular Polarized Outlier

### F.1.2 Image Set #2

**Scene Description.** Computational Science Facility on clear day (no optical image available). Notice reflection of vehicles on pavement and detection of their license plates.



**Figure F.8.** Intensity Image (V + H)



**Figure F.9.** Q Image (V - H)

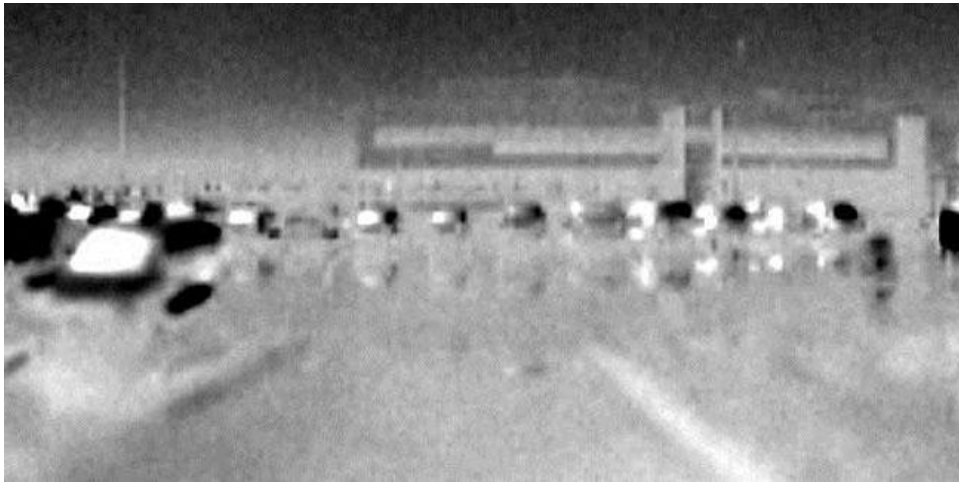


**Figure F.10.** U Image ( $T_{+45} - T_{-45}$ )

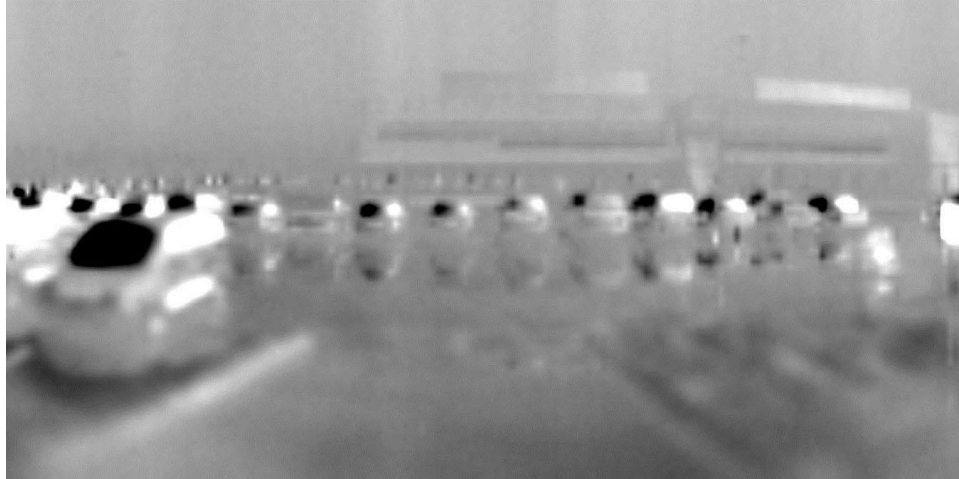


**Figure F.11.** V Image ( $T_1 - T_r$ )

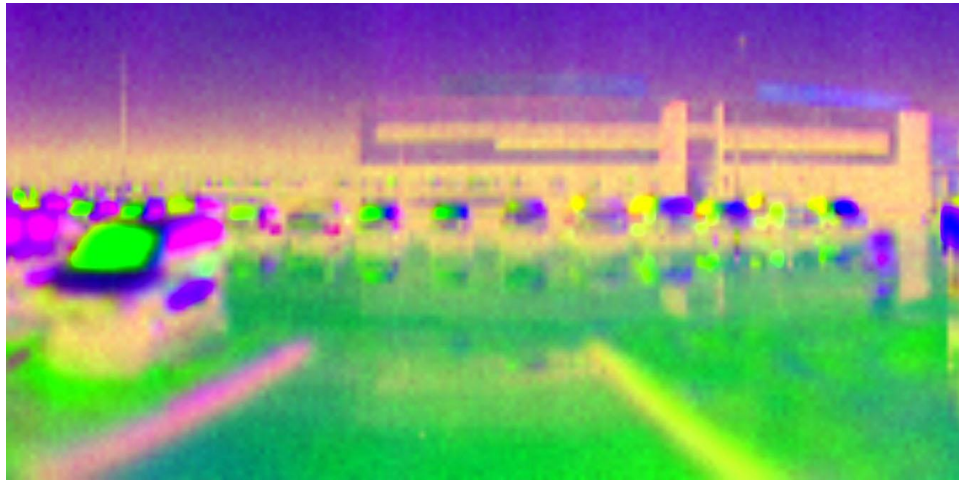


**Figure F.12.** QUV RGB Image (Q image assigned to red, U image assigned to green, V image assigned to blue)

### **F.1.3 Image Set #3**

**Scene Description.** Imaging Benton City from Mac Bee mountain. Approximately 1000 feet elevation and 6000 ft in the horizontal from the river, and 7000–12000 ft in the horizontal from the city. Clear day with high wind speeds contributing to system vibration/blurring.



**Figure F.13.** Scene



**Figure F.14.** Radiometer System Placed in Truck Bed Overlooking Benton City

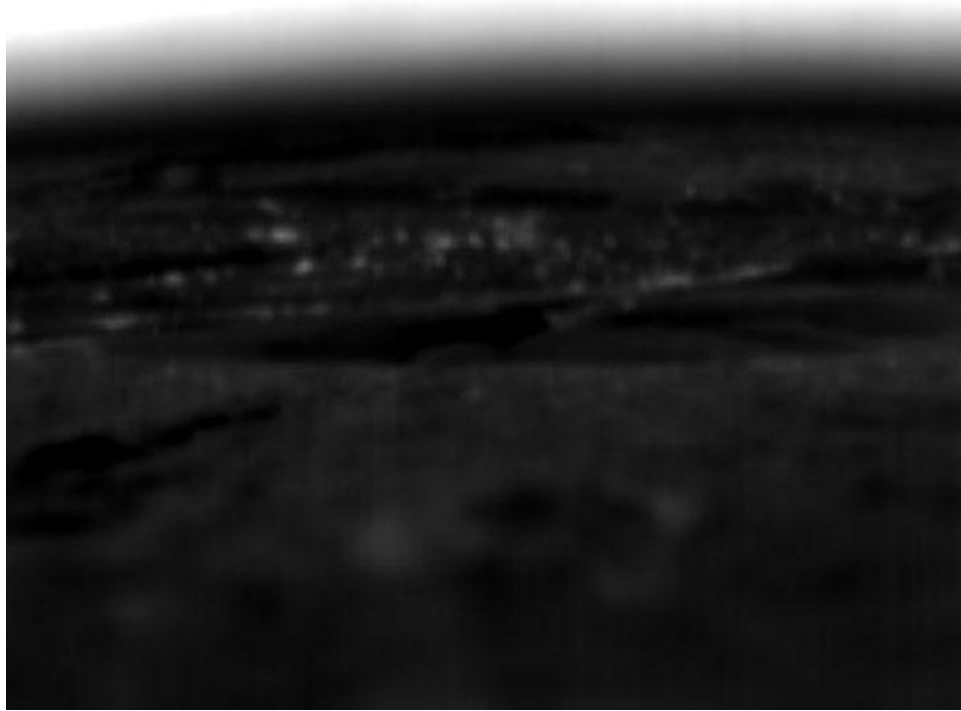


**Figure F.15.** Intensity Image (V + H)

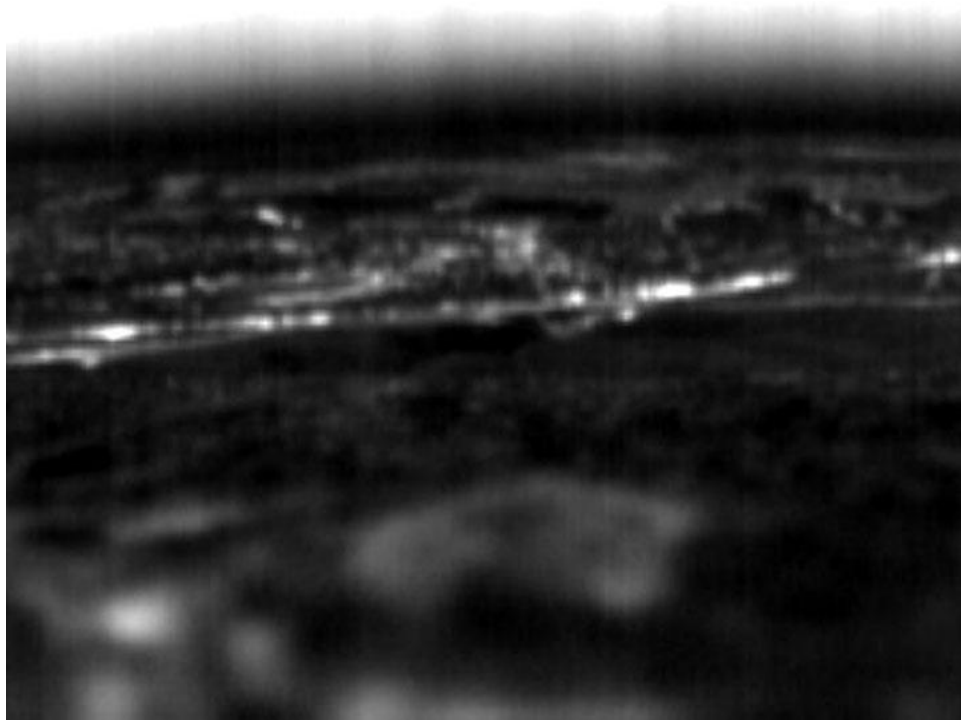


**Figure F.16.** Q Image (V - H)

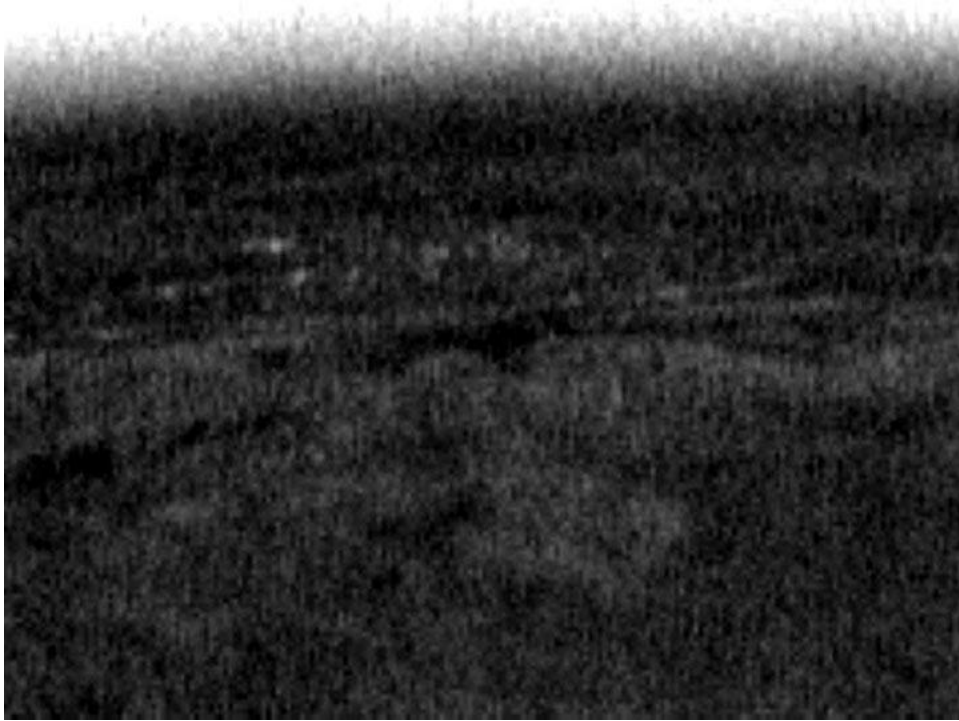


**Figure F.17.** U Image ( $T_{+45} - T_{-45}$ )



**Figure F.18.** V Image ( $T_1 - T_r$ )

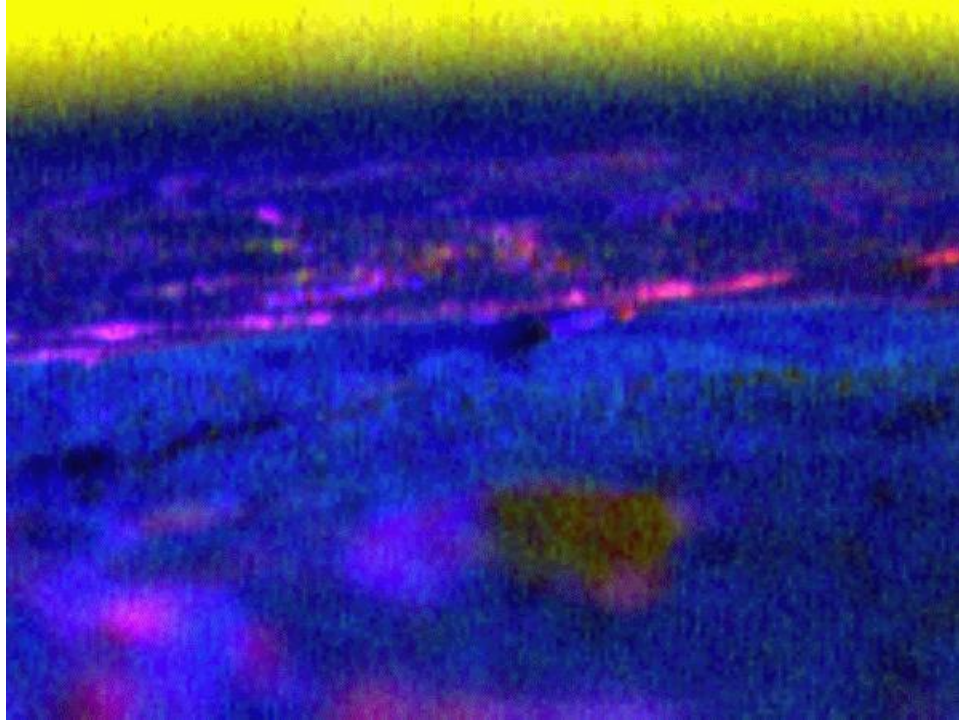


**Figure F.19.** QUV RGB Image (Q image assigned to red, U image assigned to green, V image assigned to blue)

#### **F.1.4 Image Set #4**

**Scene Description.** Radiometer mounted on a 30-ft vertical scissor lift overlooking grass lawn on Battelle campus. Targets placed below are metal pipes spaced at system angular resolution in a 4-ft  $\times$  4-ft sandbox. Radiometer achieved depression angles up to 40 degrees.



**Figure F.20.**



**Figure F.21.** Scene

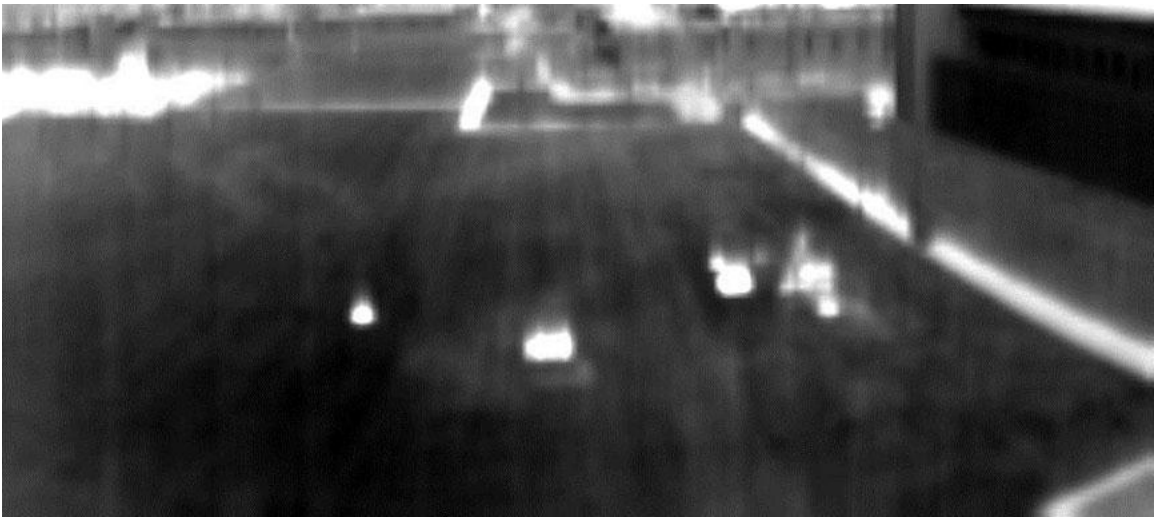


**Figure F.22.** Intensity Image (V + H)



**Figure F.23.** Q Image (V - H)



**Figure F.24.** U Image ( $T_{+45} - T_{-45}$ )



**Figure F.25.** V Image ( $T_1 - T_r$ )

Notice the distinctive foot paths shown in the grass area below. Pipes and windows are resolved.

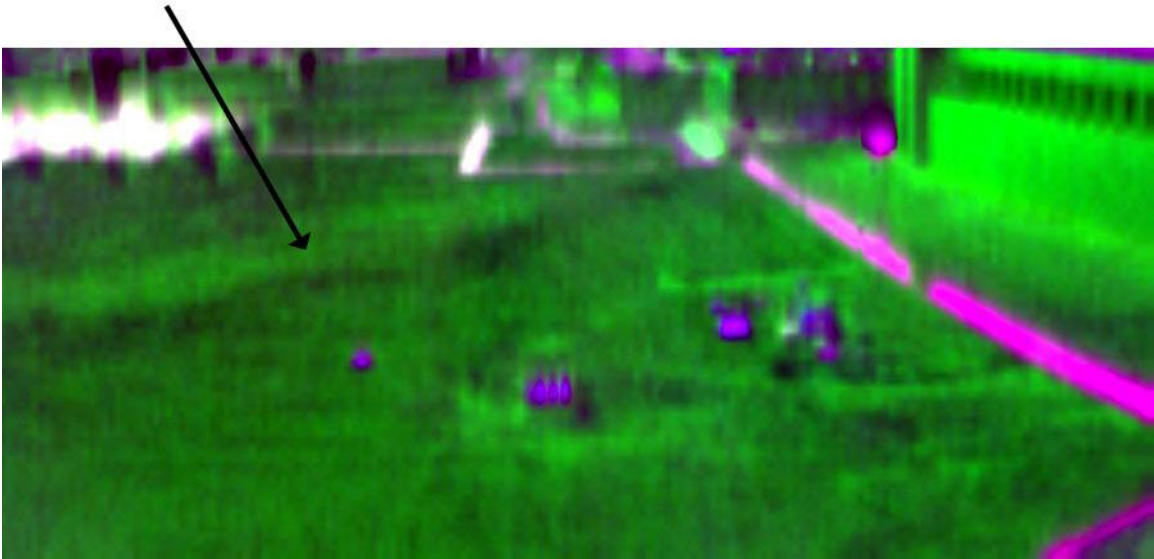


**Figure F.26.** QUV RGB Image (Q image assigned to red, U image assigned to green, V image assigned to blue)

## F.2 Fully Polarimetric Finite Conjugate Imaging Sets

### F.2.1 Image Set #5

**Target Description.** Steel pipe resolution target, with target sized and spaced at system resolution and greater.

Pipe OD and spacing dimensions:

X1 = 1.17 in. (2.97 cm)

X2 = 1.55 in. (3.94 cm)

X3 = 2.19 in. (5.56 cm)

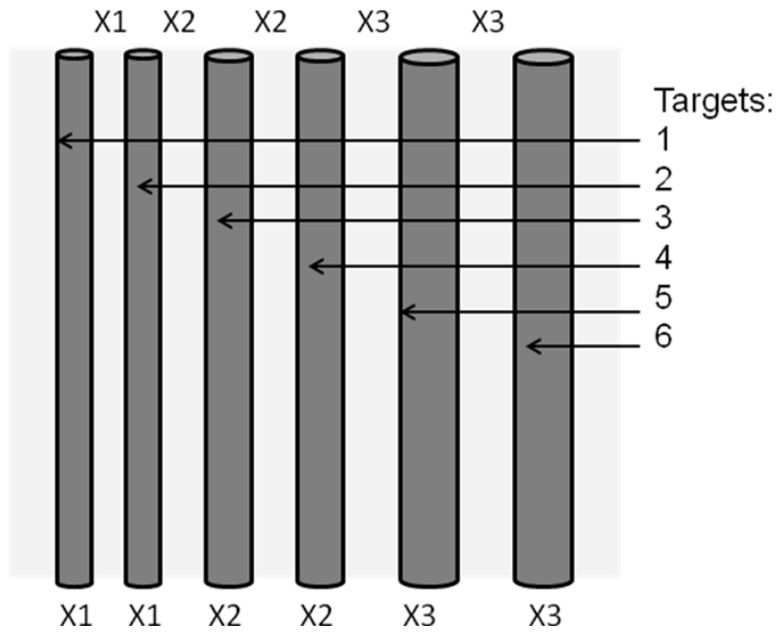


**Figure F.27.**

**Scene Description.** Vertically oriented steel conduit separated by systems spatial resolution and larger at a distance of 5 m.

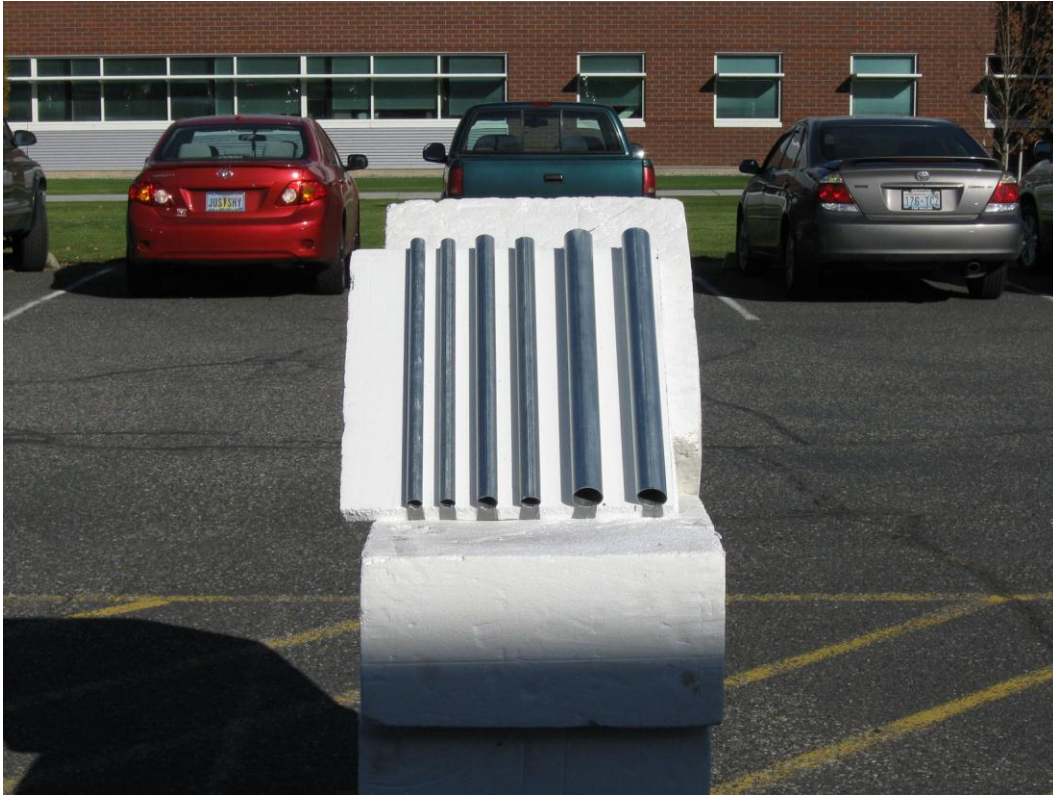


**Figure F.28.** Scene

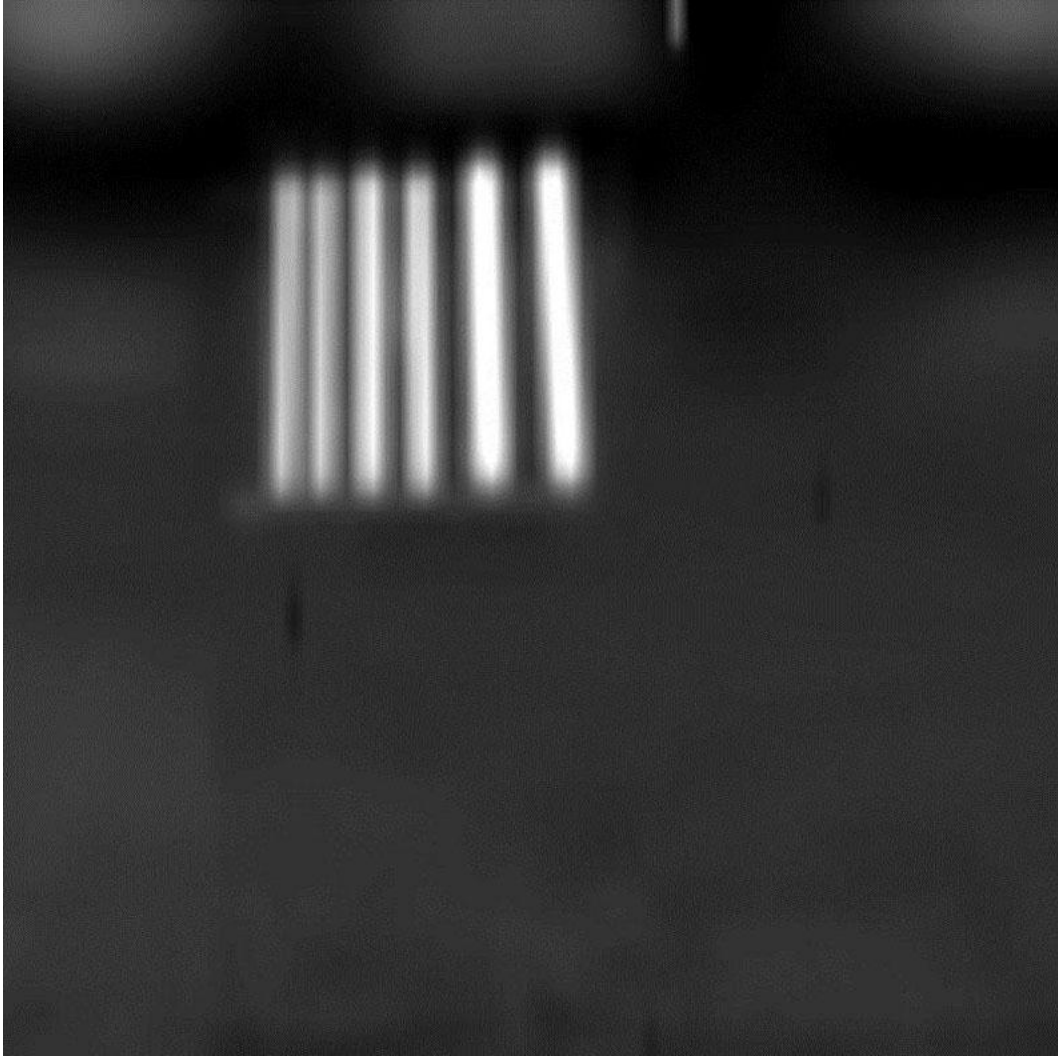


**Figure F.29.** Intensity Image (V + H)

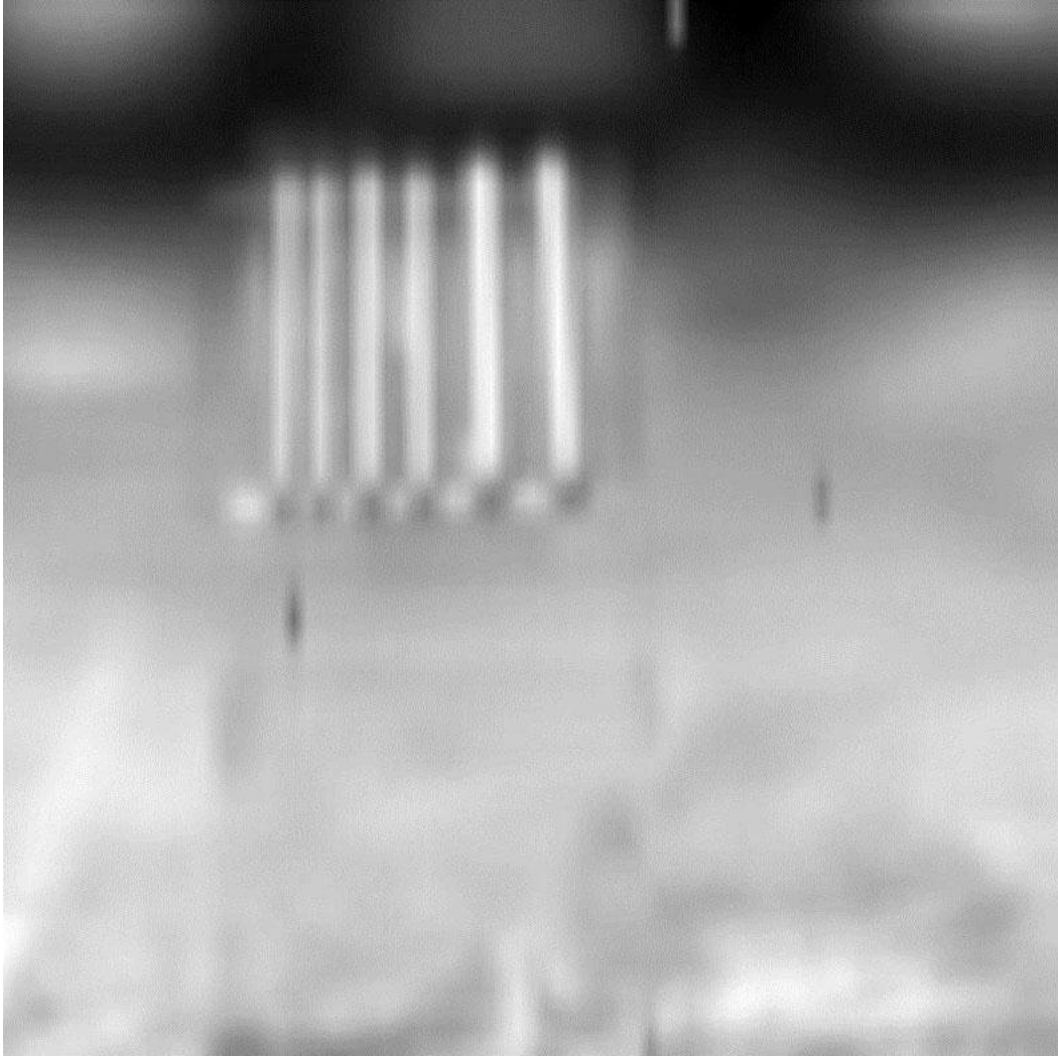


**Figure F.30.** Q Image (V - H)

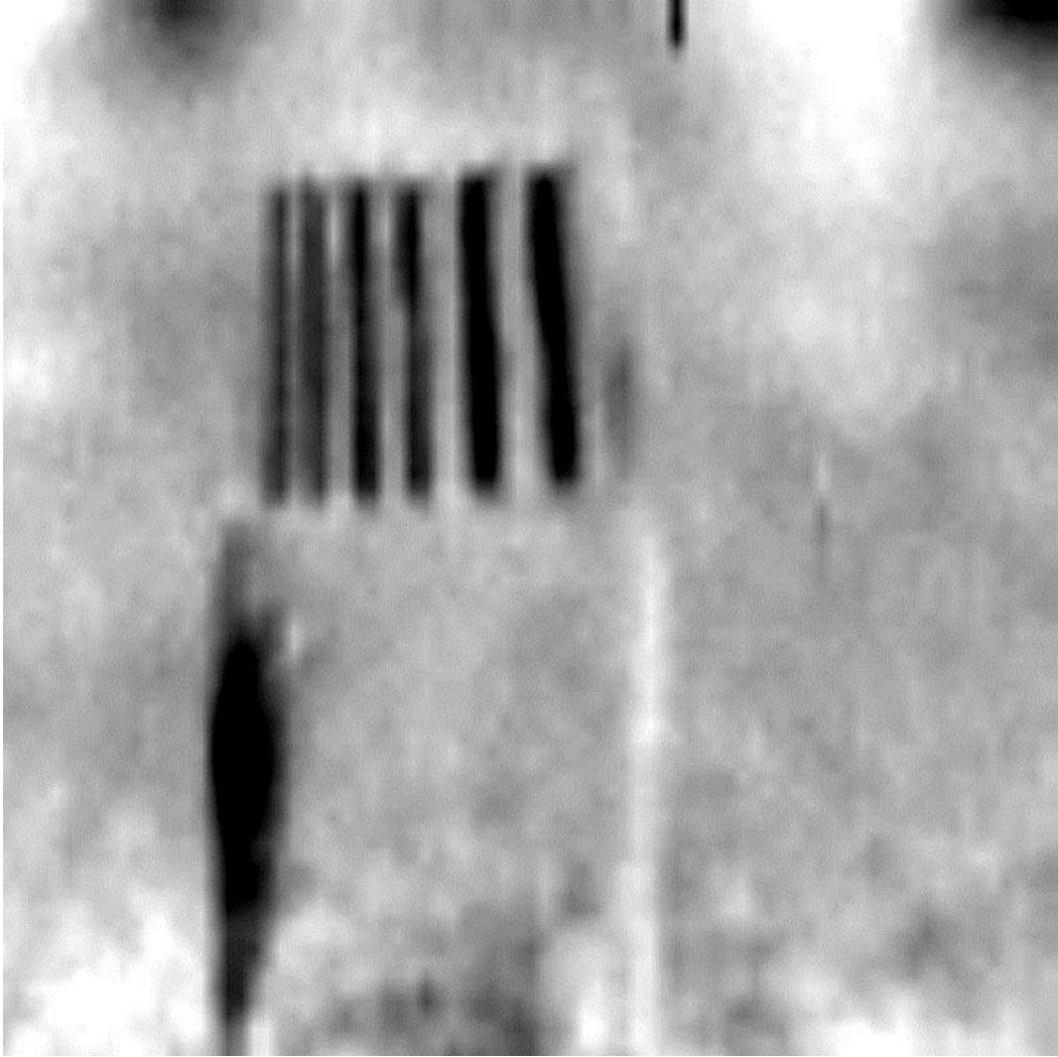


**Figure F.31.** U Image ( $T_{+45} - T_{-45}$ )

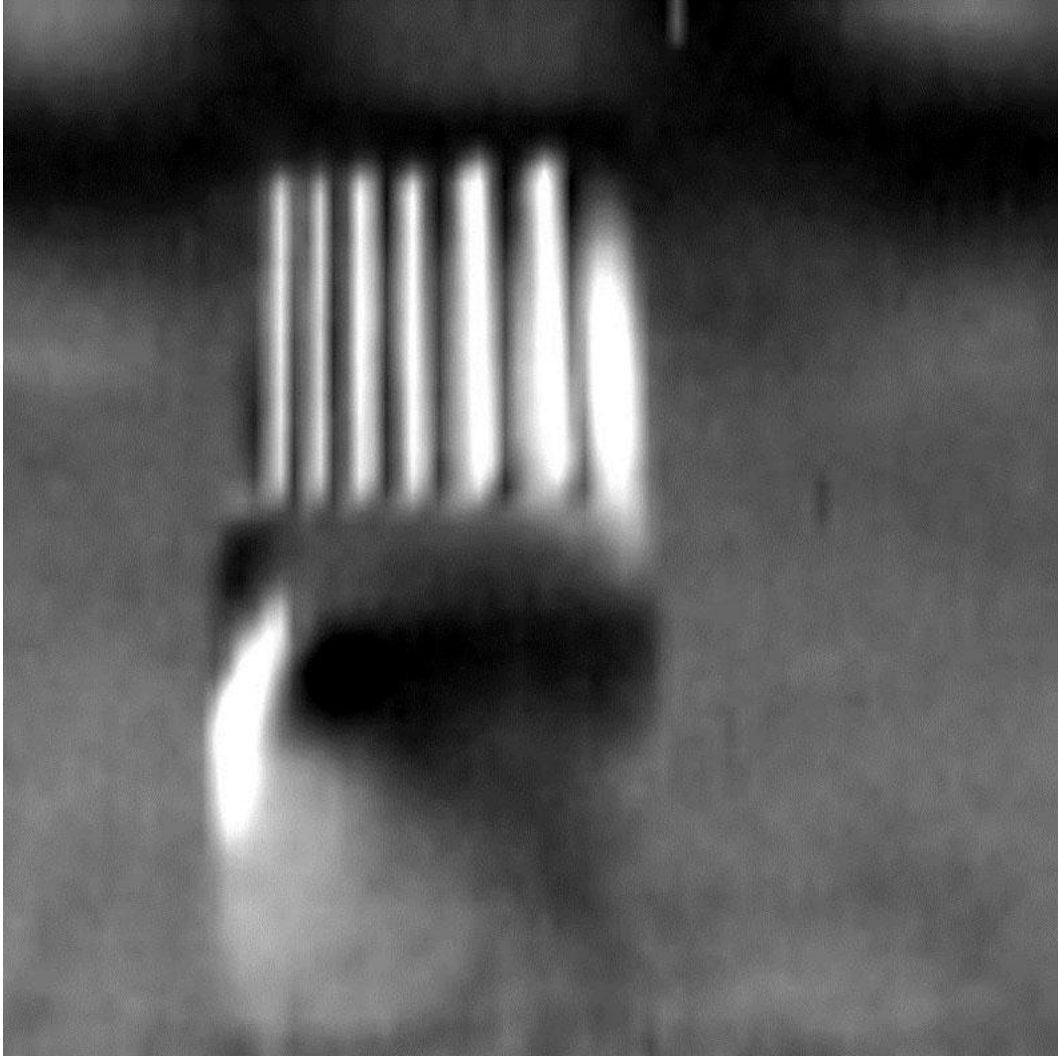


**Figure F.32.** V Image ( $T_1 - T_r$ )

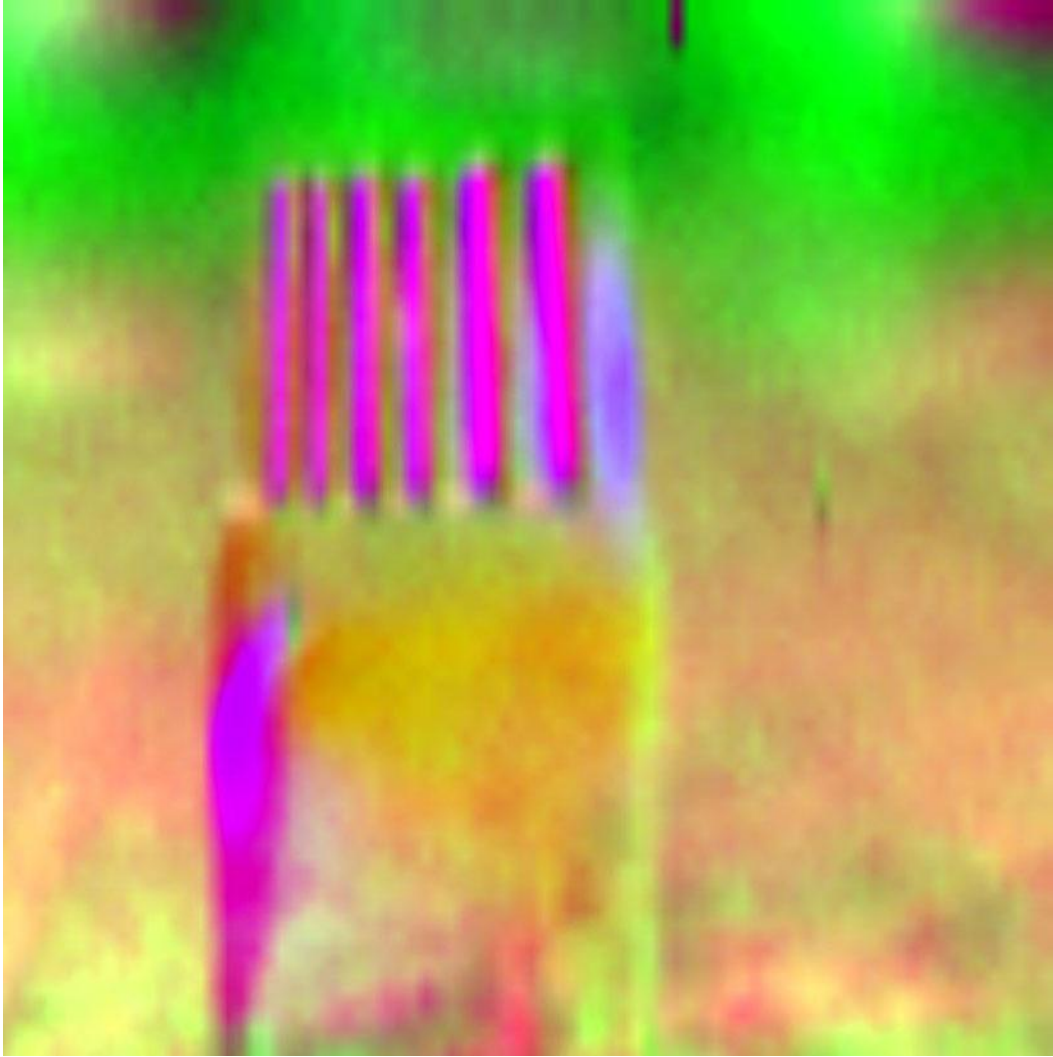


**Figure F.33.** QUV RGB Image (Q image assigned to red, U image assigned to green, V image assigned to blue)

## F.2.2 Image Set #6

**Scene Description.** Horizontally oriented copper tape resolution target at 5 m hidden by navy blue lab jacket.



**Figure F.34.** Scene

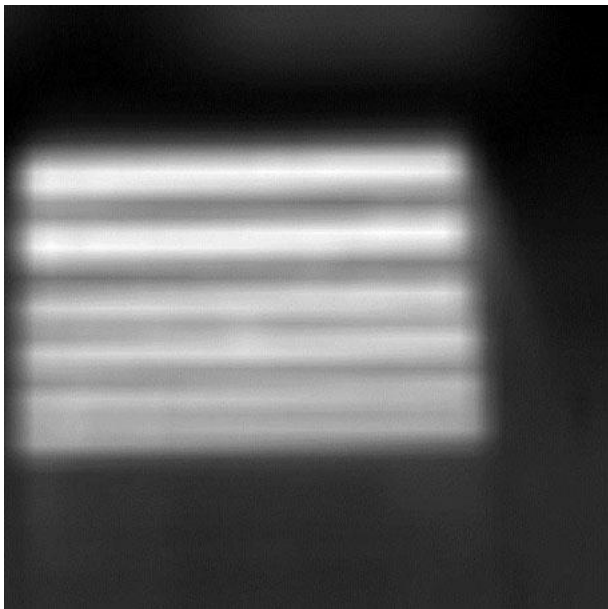


**Figure F.35.** Intensity Image (V + H)

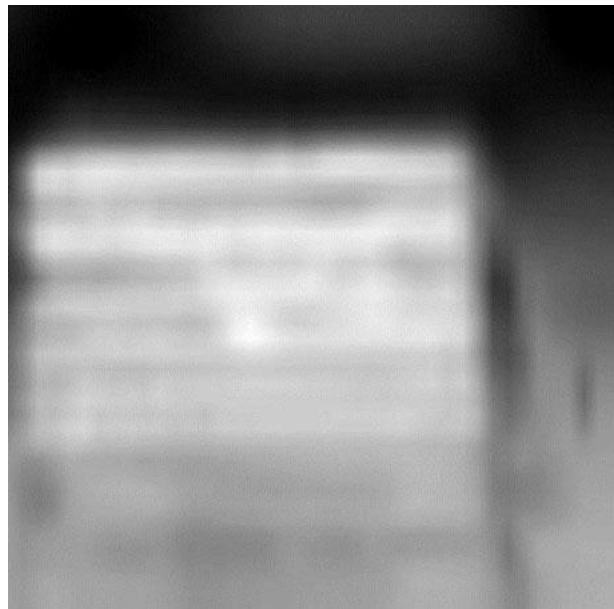


**Figure F.36.** Q Image (V - H)

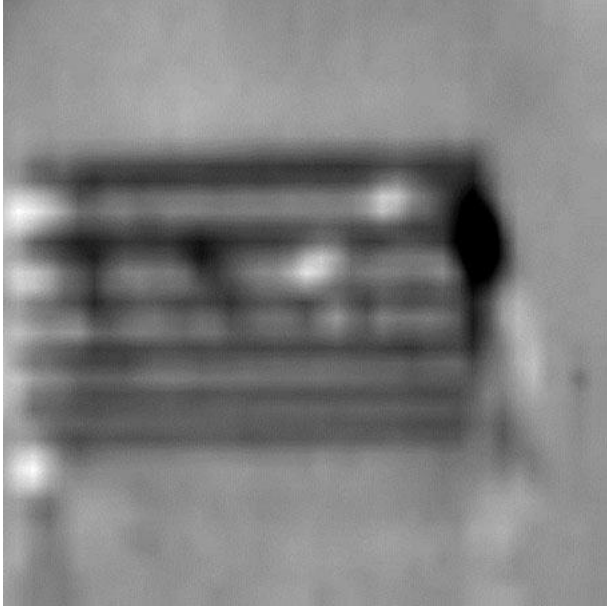


**Figure F.37.** U Image ( $T_{+45} - T_{-45}$ )

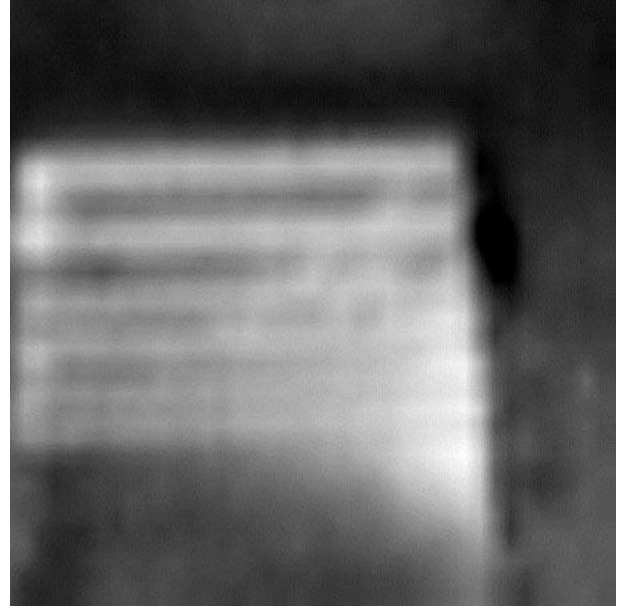


**Figure F.38.** V Image ( $T_1 - T_r$ )

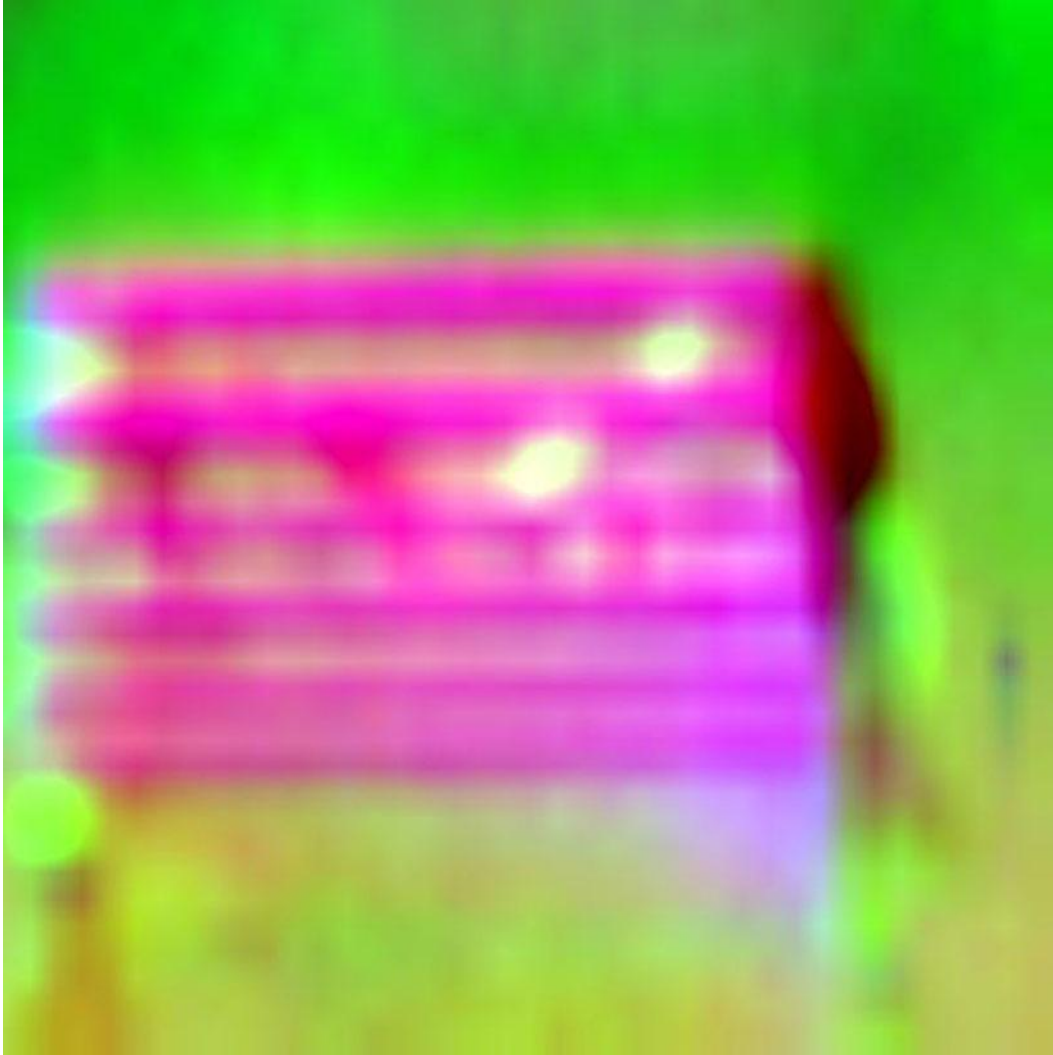


**Figure F.39.** QUV RGB Image (Q image assigned to red, U image assigned to green, V image assigned to blue)

### **F.2.3 Image Set #7**

**Scene Description.** Motorcycle placed at 5-m focal point distance in order to determine functionality of system. Note anomaly in upper left section of image is due to a vehicle traveling by during the scanning process.



**Figure F.40.**



**Figure F.41.** Intensity Image (V + H)



**Figure F.42.** Q Image (V - H)

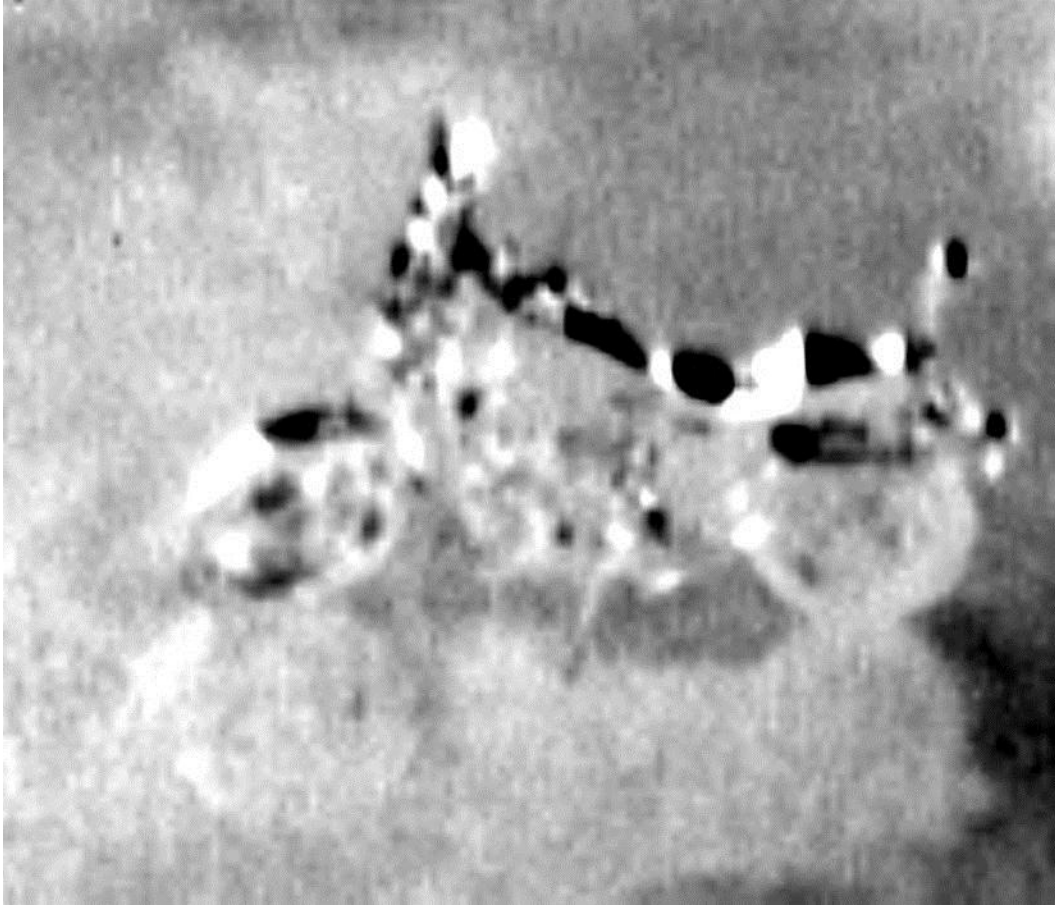


**Figure F.43.** U Image ( $T_{+45} - T_{-45}$ ). One can see the curvature of the fender, seat, and handle bars producing unique polarization signatures.

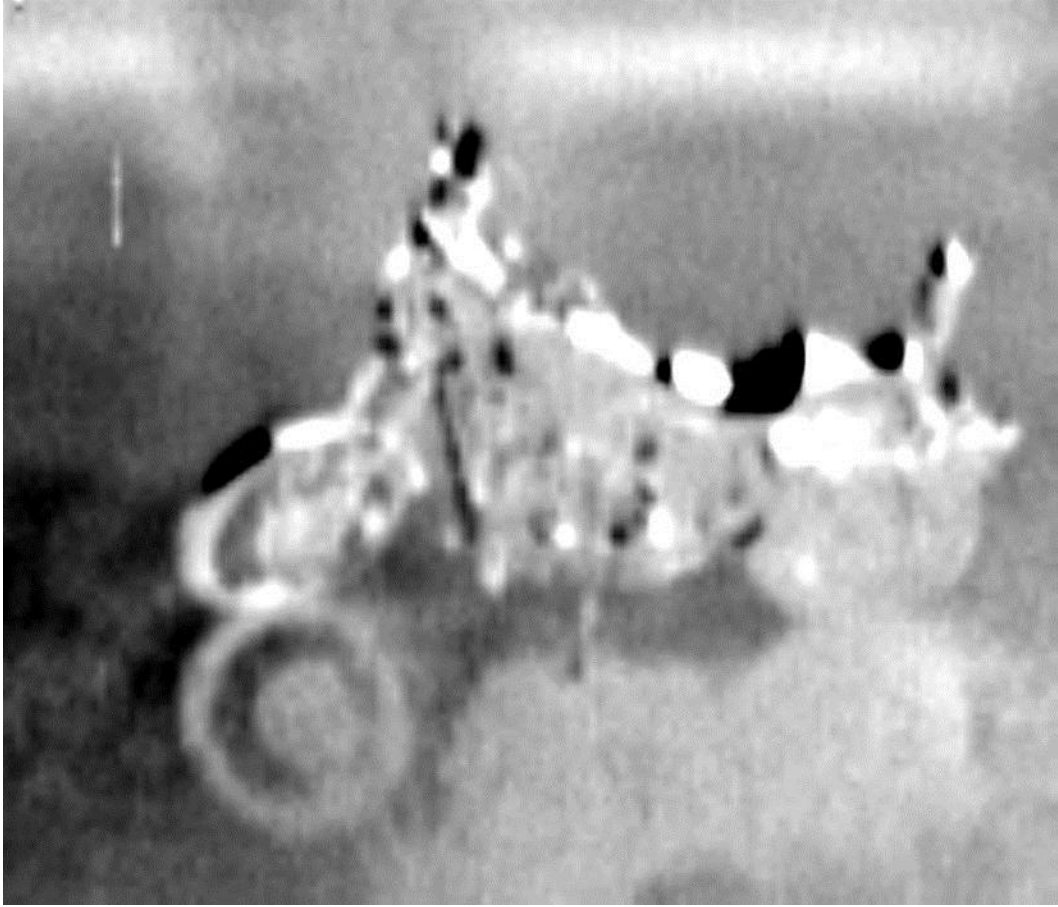


**Figure F.44.** V Image ( $T_1 - T_r$ )



**Figure F.45.** QUV RGB Image (Q image assigned to red, U image assigned to green, V image assigned to blue)

#### **F.2.4 Image Set #8**

**Scene Description.** Three vertically oriented twisted pairs of wire—10, 16, and 22 gauge. The widths of the twisted pairs are 3.79 mm, 2.45 mm, and 1.76 mm, respectively. Note that system resolution at this distance is 3.47 cm.



**Figure F.46.**

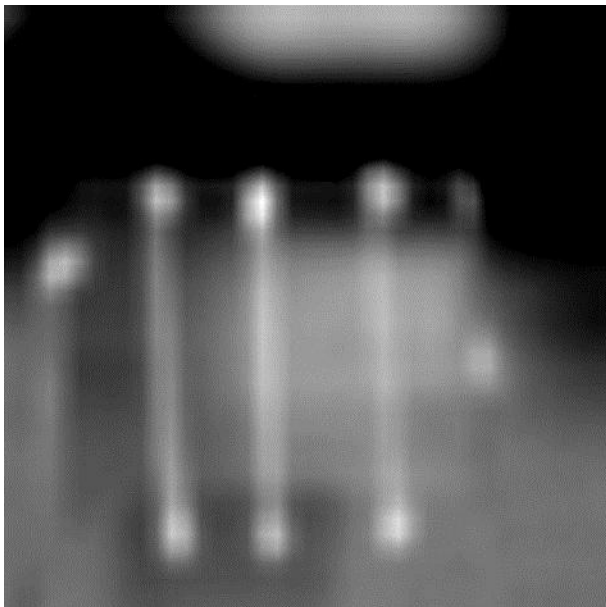


**Figure F.47.**



**Figure F.48.**

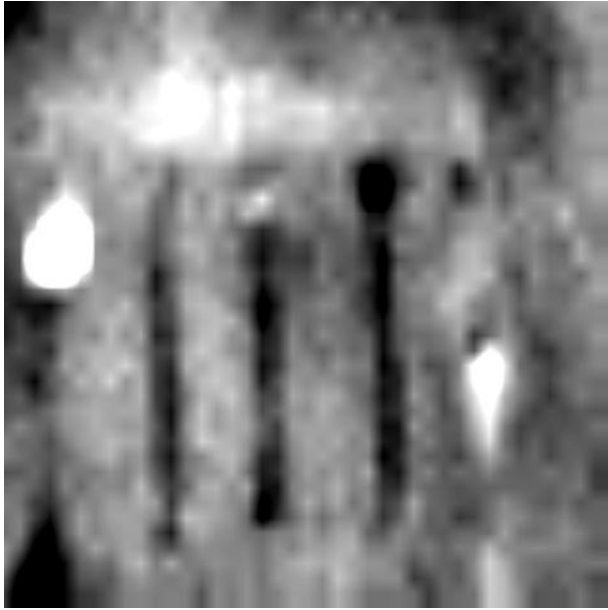


**Figure F.49.**

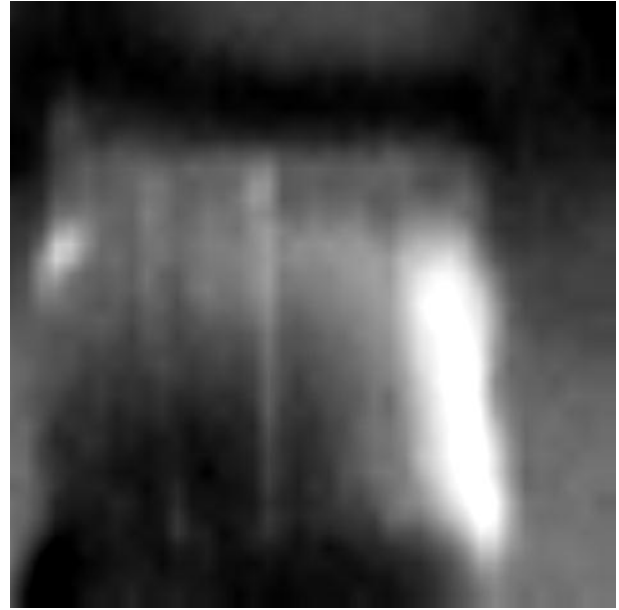


**Figure F.50.**

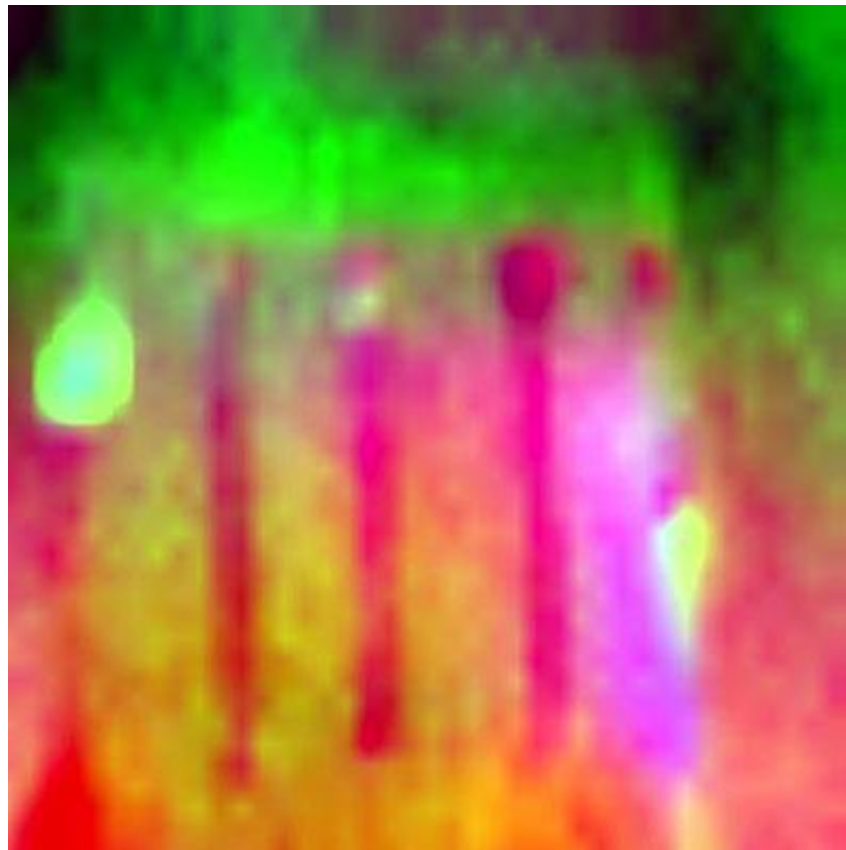


**Figure F.51.** QUV RGB Image (Q image assigned to red, U image assigned to green, V image assigned to blue)

## F.2.5 Image Set #9

**Scene Description.** Pipe resolution target scanned using very high sampling rates:  $0.05 \text{ deg} \times 0.1 \text{ deg}$  pixels. Pipes vertically oriented at a distance of 5 m from the radiometer.

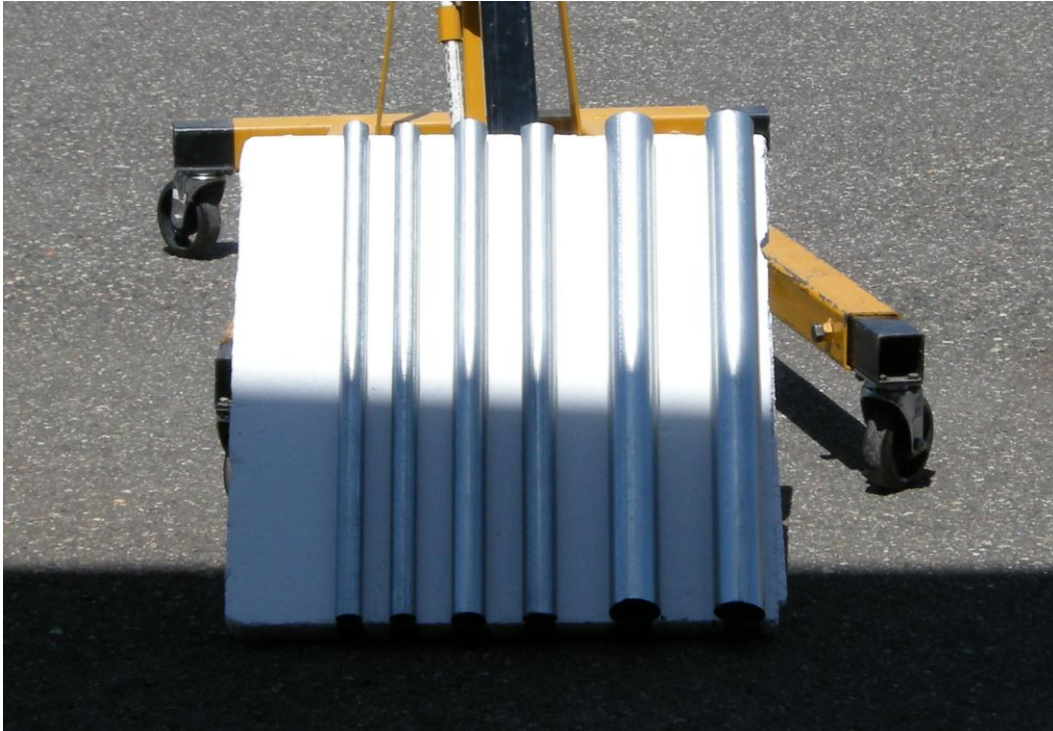


**Figure F.52.**



**Figure F.53.** Intensity Image (V + H)



**Figure F.54.** Q Image (V - H)



**Figure F.55.** U Image ( $T_{+45} - T_{-45}$ )



**Figure F.56.** V Image ( $T_1 - T_r$ )

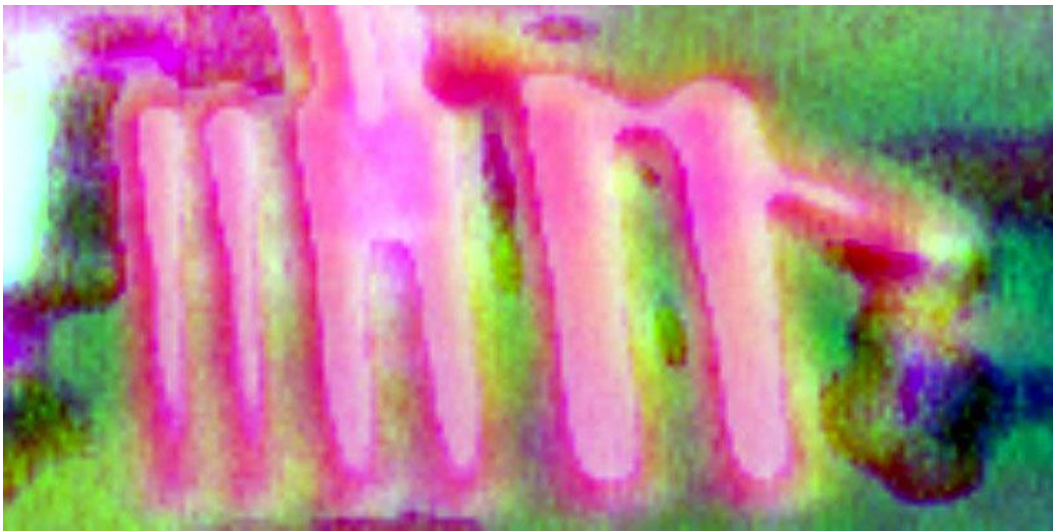


**Figure F.57.** QUV RGB Image (Q image assigned to red, U image assigned to green, V image assigned to blue)

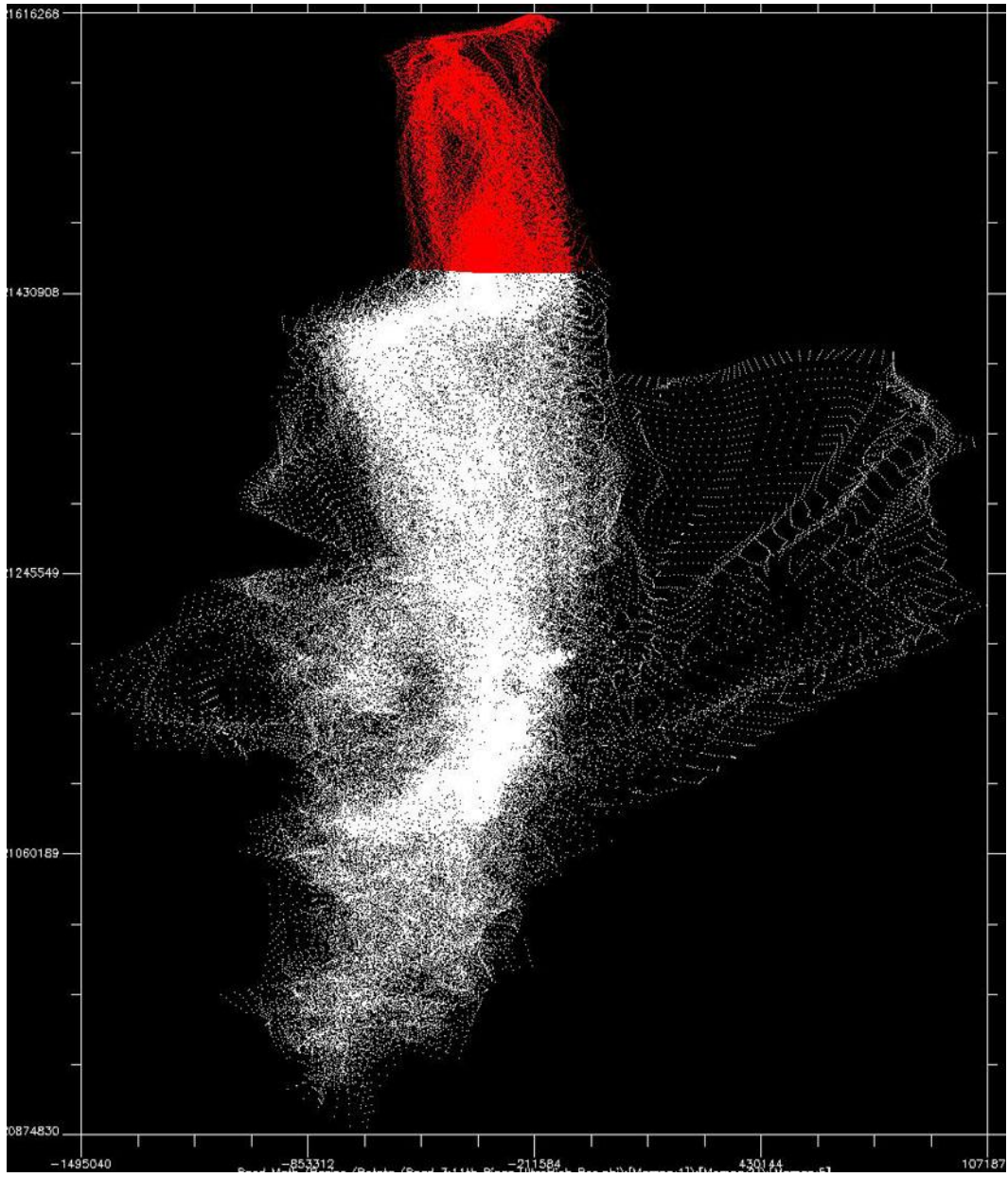


**Figure F.58.** U vs. I 2D Scatter Plot, Red Structure Highlighted in Following U Image

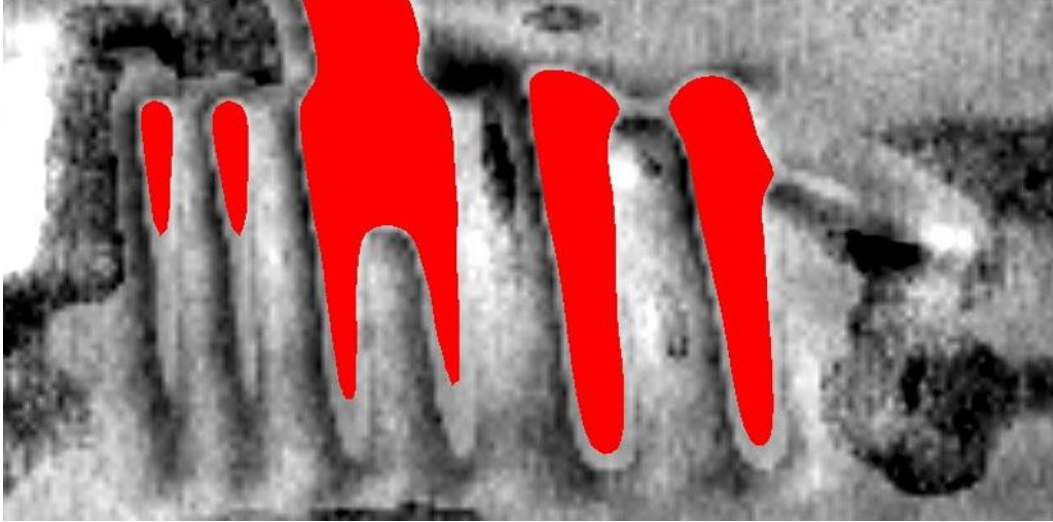


**Figure F.59.** U Image ( $T_{+45} - T_{-45}$ ). Red highlighting the selected pixels in the 2d scatter plot. These pixel values are unique to the U polarization, showing that specific geometries like these curved pipes produce unique polarization signatures.

### F.2.6 Image Set #10

**Scene Description.** Copper tape resolution target buried 18 mm. The purpose of this test was to determine the ability of mm-wave energy to penetrate the sand, return a distinguishable brightness temperature in a multilayer thermal environment, and the sand's resolution impairment effects. Note that the sand used to bury the target is finer than the surrounding terrain. Its composition is similar to beach sand, salts aggregates, and some ferrite materials.



**Figure F.60.** Scene Showing Copper Resolution Target on Sands Surface, and Copper Resolution Target Buried



**Figure F.61.** Intensity Image (V + H)

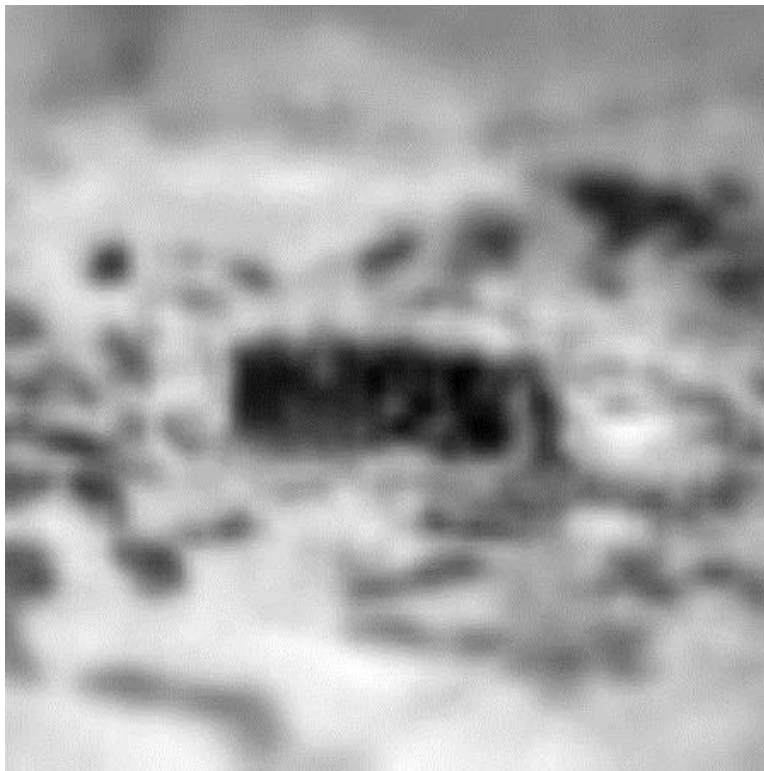


**Figure F.62.** Q Image (V - H)

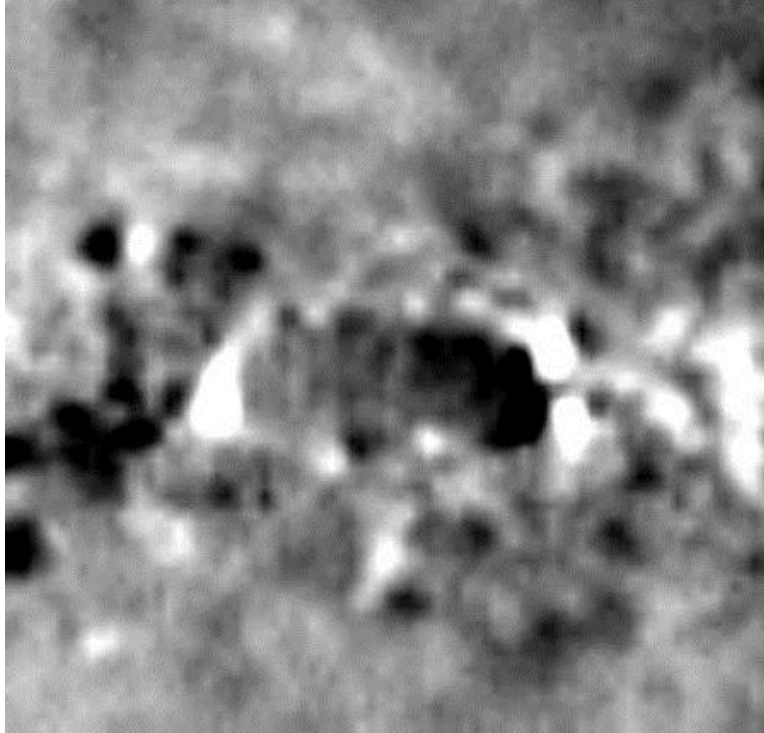


**Figure F.63.** U Image ( $T_{+45} - T_{-45}$ )

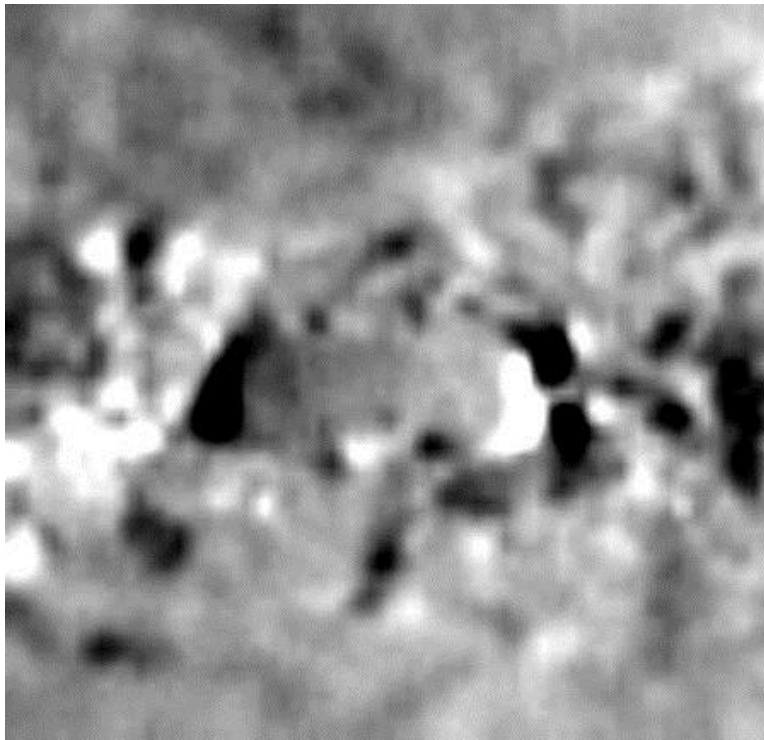


**Figure F.64.** V Image ( $T_1 - T_r$ ). Notice the V channel is picking up the curvature of the sand deformation, around the buried target.

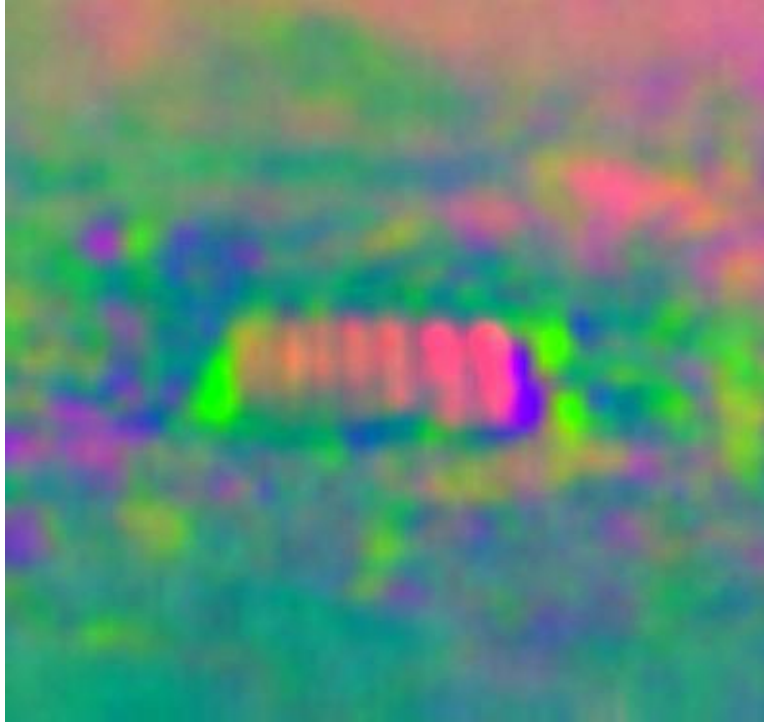


**Figure F.65.** IUV RGB Image (I image assigned to red, U image assigned to green, V image assigned to blue)

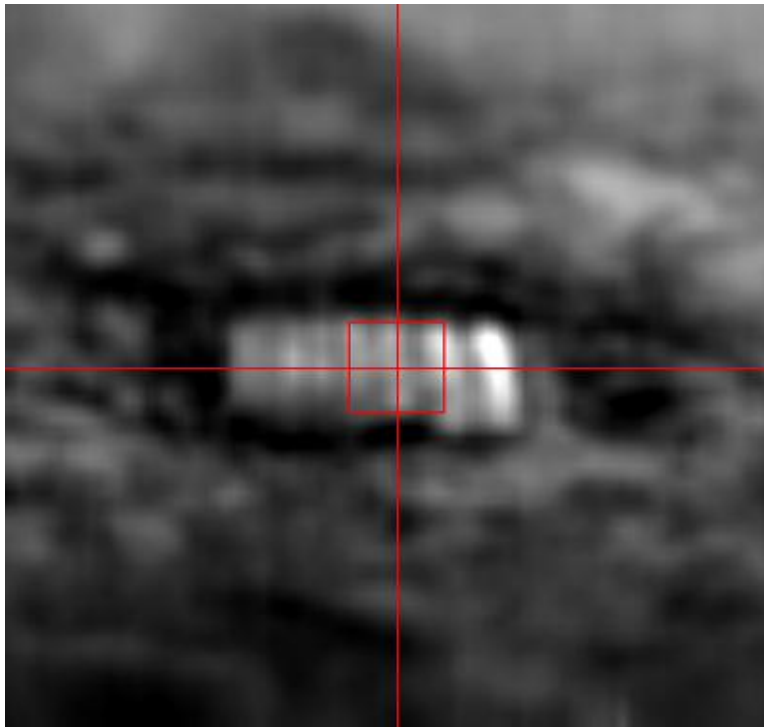


**Figure F.66.** Further Investigation of Intensity, Plotting Horizontal Pixel Profile (amplitude only)

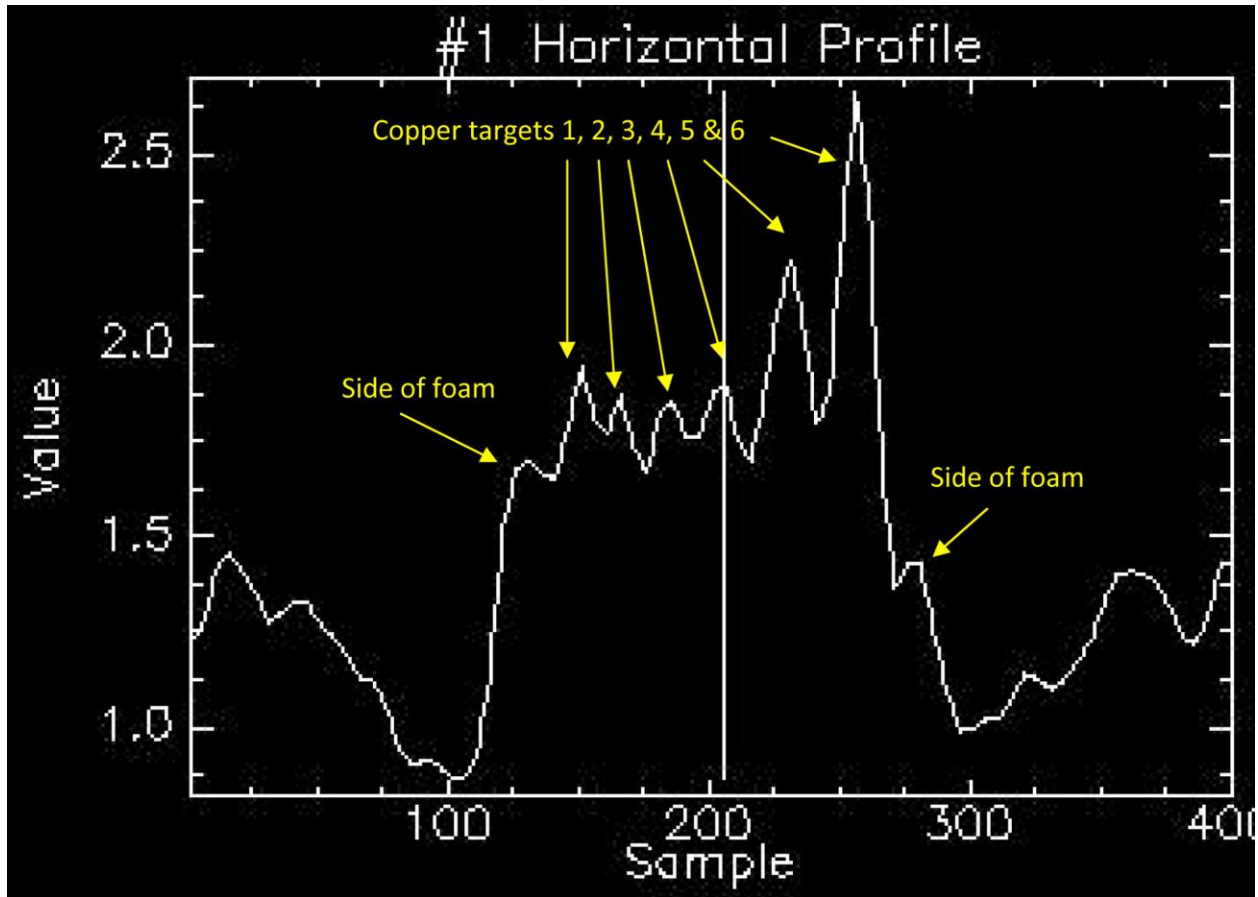


**Figure F.67.** Intensity Horizontal Profile Amplitude Plot Showing the Resolving of All Copper Targets Buried at a Depth of 18 mm

### F.3 Fully Polarimetric Differential Images

#### F.3.1 Image Set #11

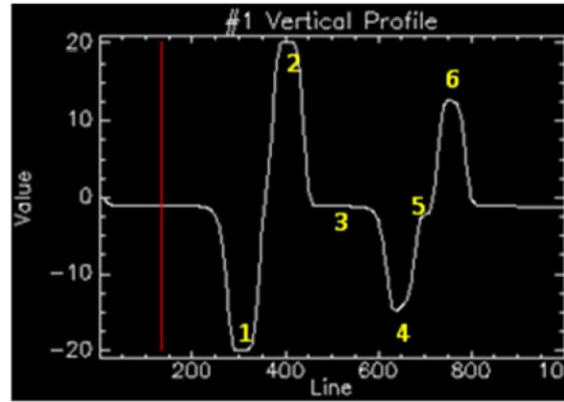
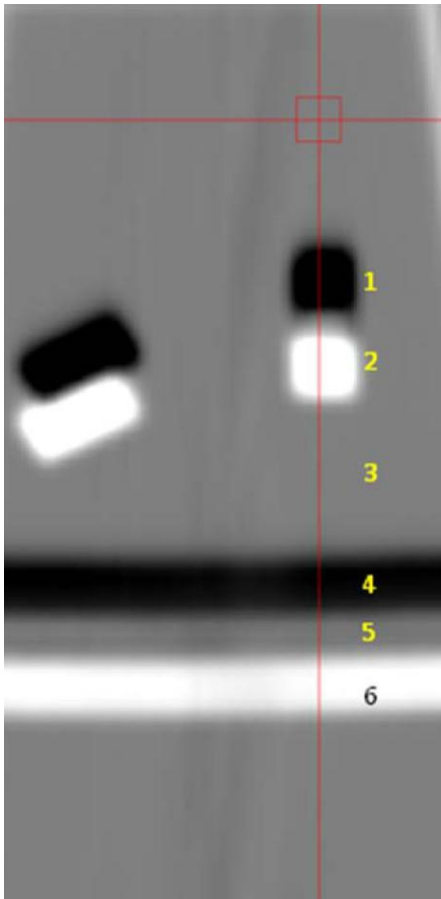
**Scene Description.** W-band RAM and a plastic PVC pipe placed on an aluminum background at a  $45^\circ$  angle. The Al plate presents the radiometer with a common background signal in order to verify the nulling of common signals and change detection. The two beams that are being compared are offset in the vertical direction.



**Figure F.68.** Scene



**Figure F.69.** Intensity Image (V + H)



1. R2 passing over RAM, R1 on Al plate.
2. R1 passive over RAM, R2 on Al plate
3. Both R1 and R2 on Al plate.
4. R2 passing over PVC pipe, R1 on Al plate.
5. Both R1 and R2 on PVC pipe
6. R1 passing over PVC pipe, R2 on Al plate.

**Figure F.70.** Explanation of Results



**Figure F.71.** Q Image (V – H)

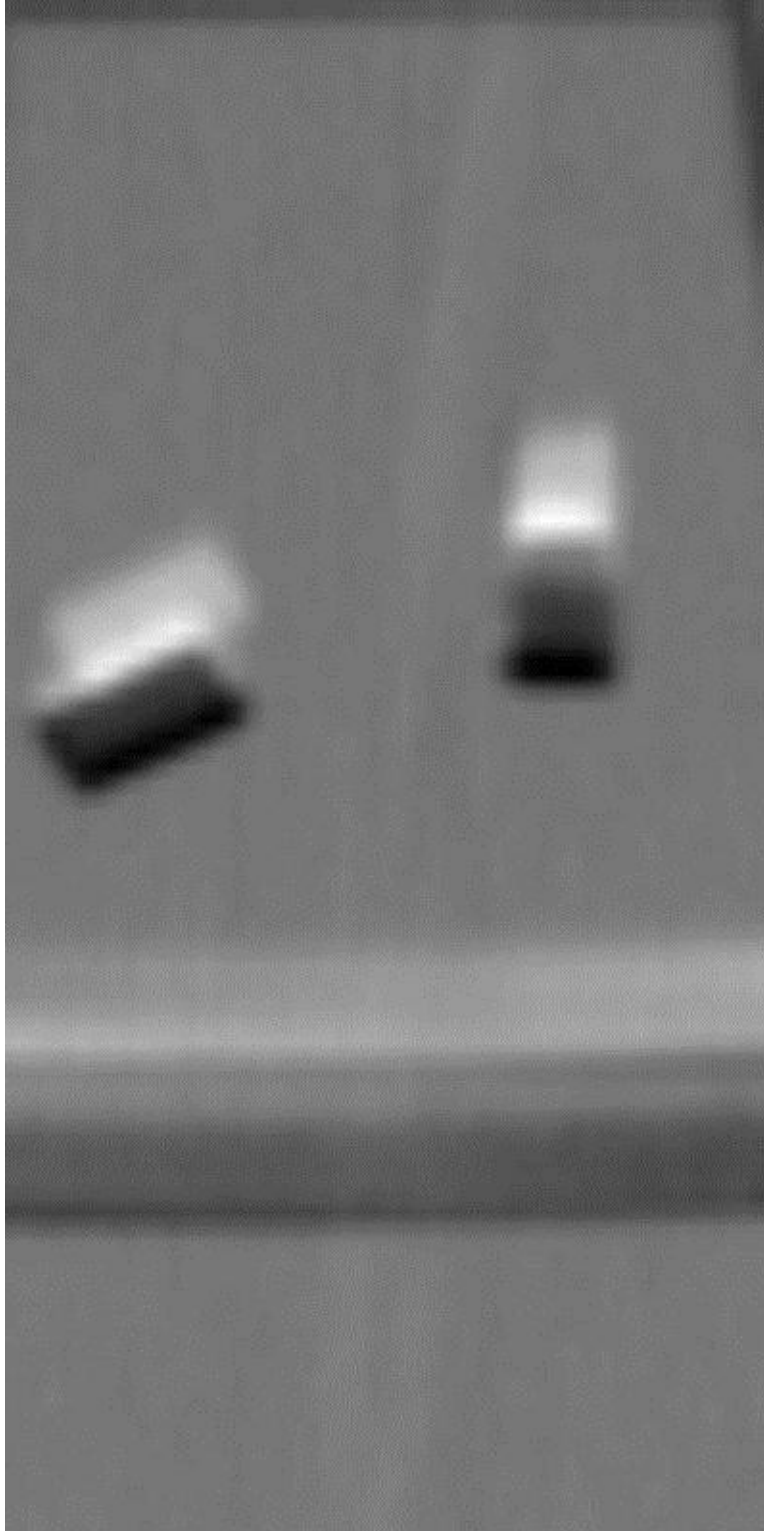


**Figure F.72.** U Image ( $T_{+45} - T_{-45}$ )

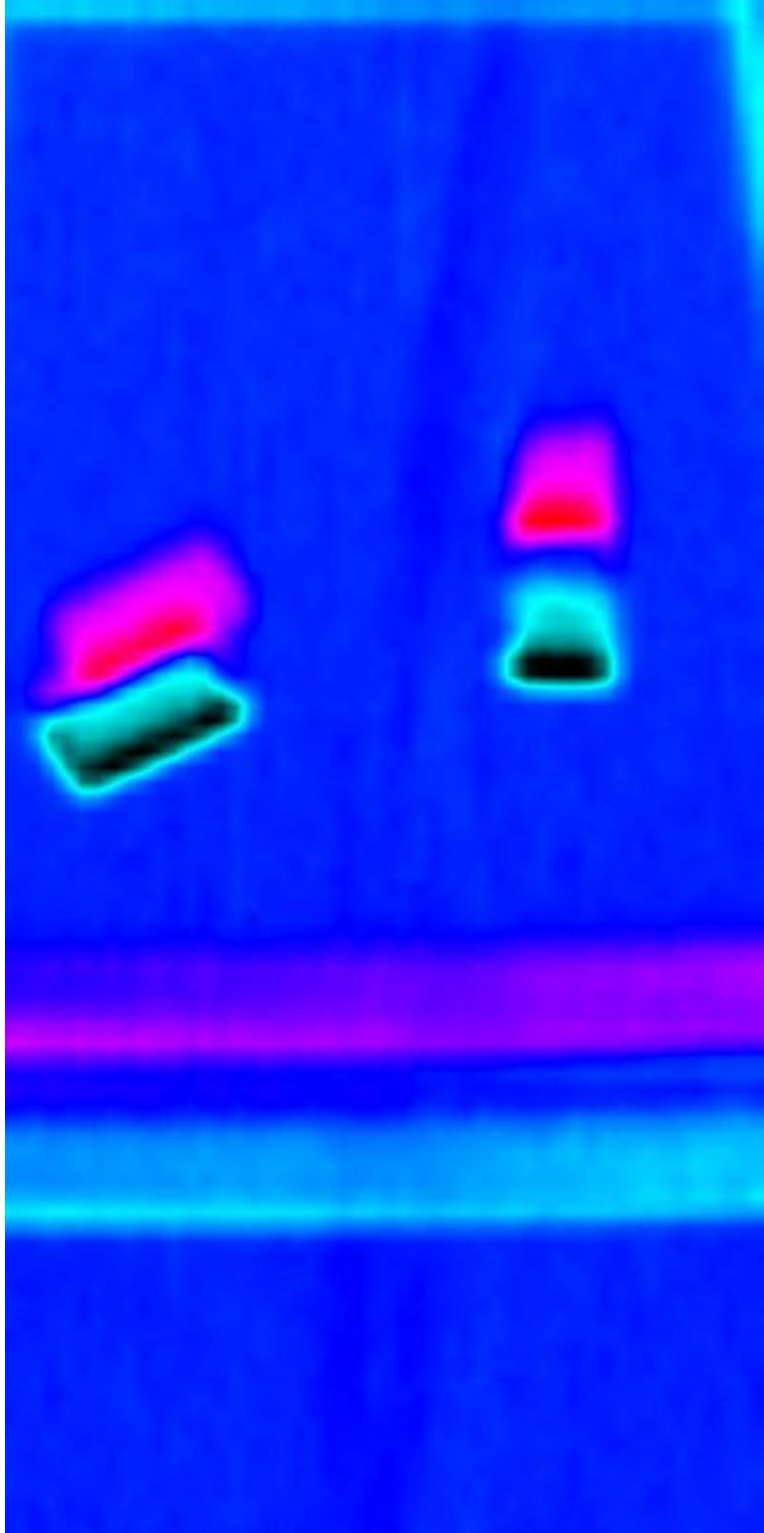


**Figure F.73.** U Image ( $T_{+45} - T_{-45}$ ) (blue-red color scheme)

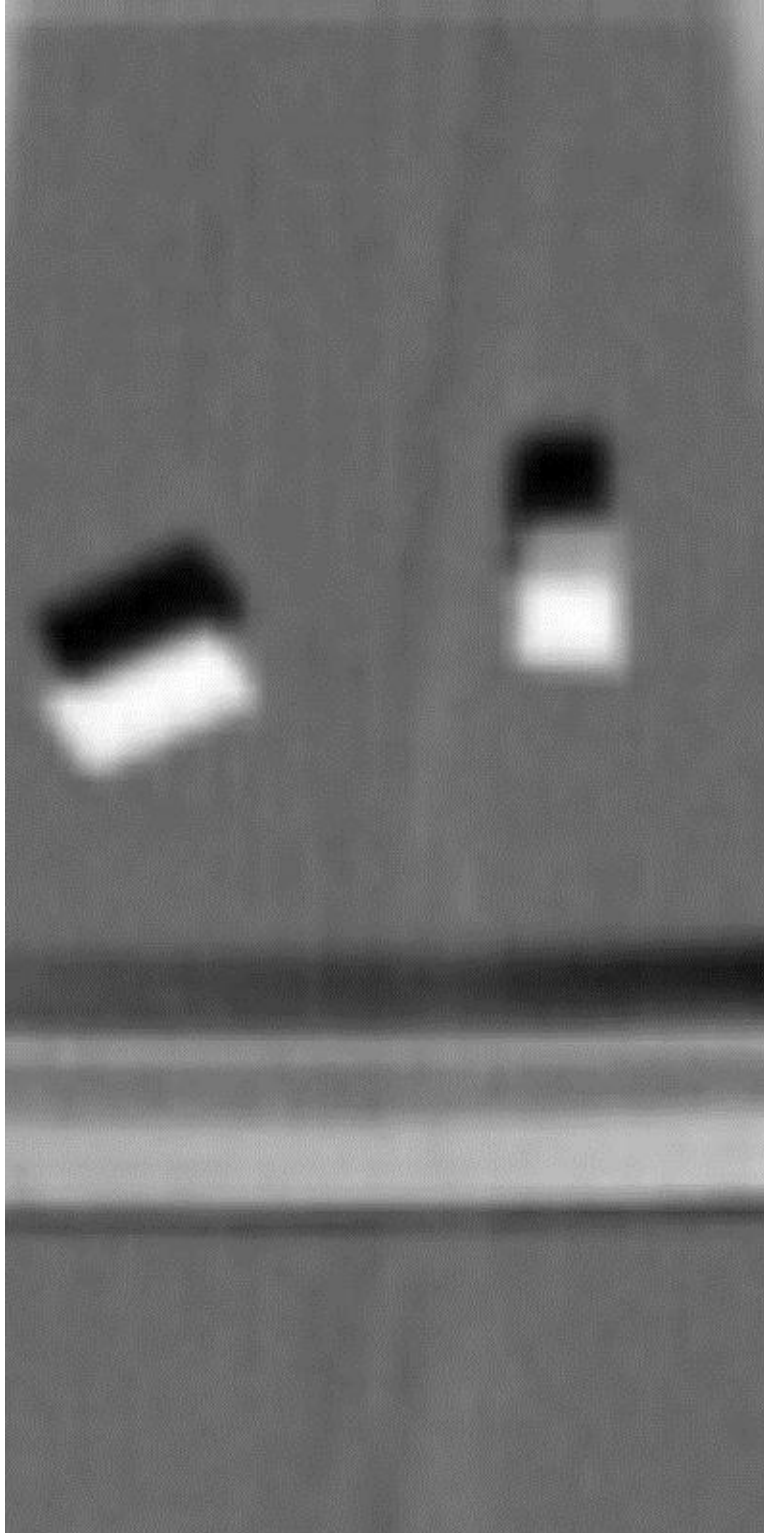


**Figure F.74.** V Image ( $T_1 - T_2$ )

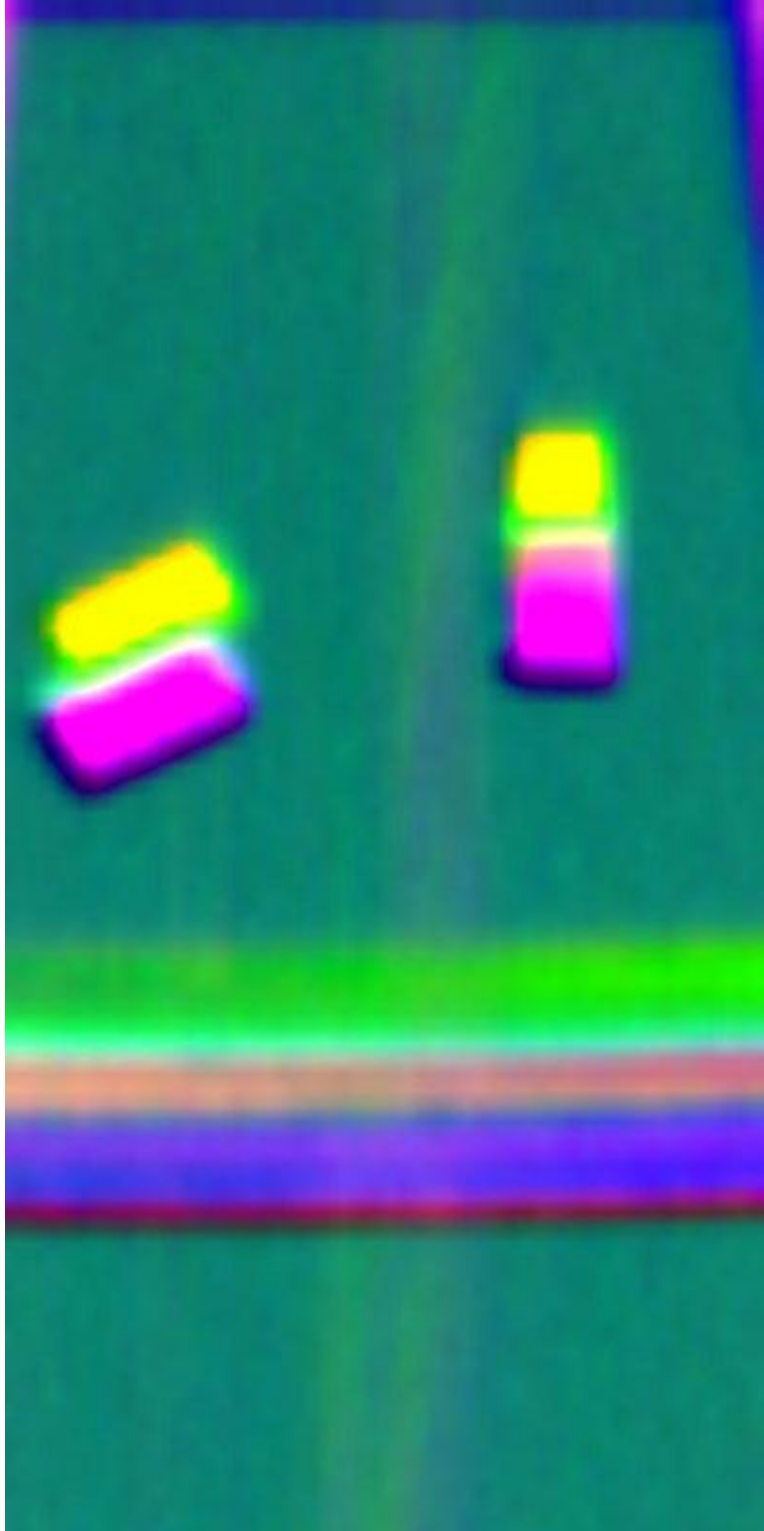


**Figure F.75.** QUV RGB Image (Q image assigned to red, U image assigned to green, V image assigned to blue)

### F.3.2 Image Set #12

**Scene Description.** Microwave RAM placed on an aluminum sheet oriented at a 45° angle. Atop the RAM is a twisted pair of 18AWG wire. Again, in this image, the two beams are offset in the vertical direction.

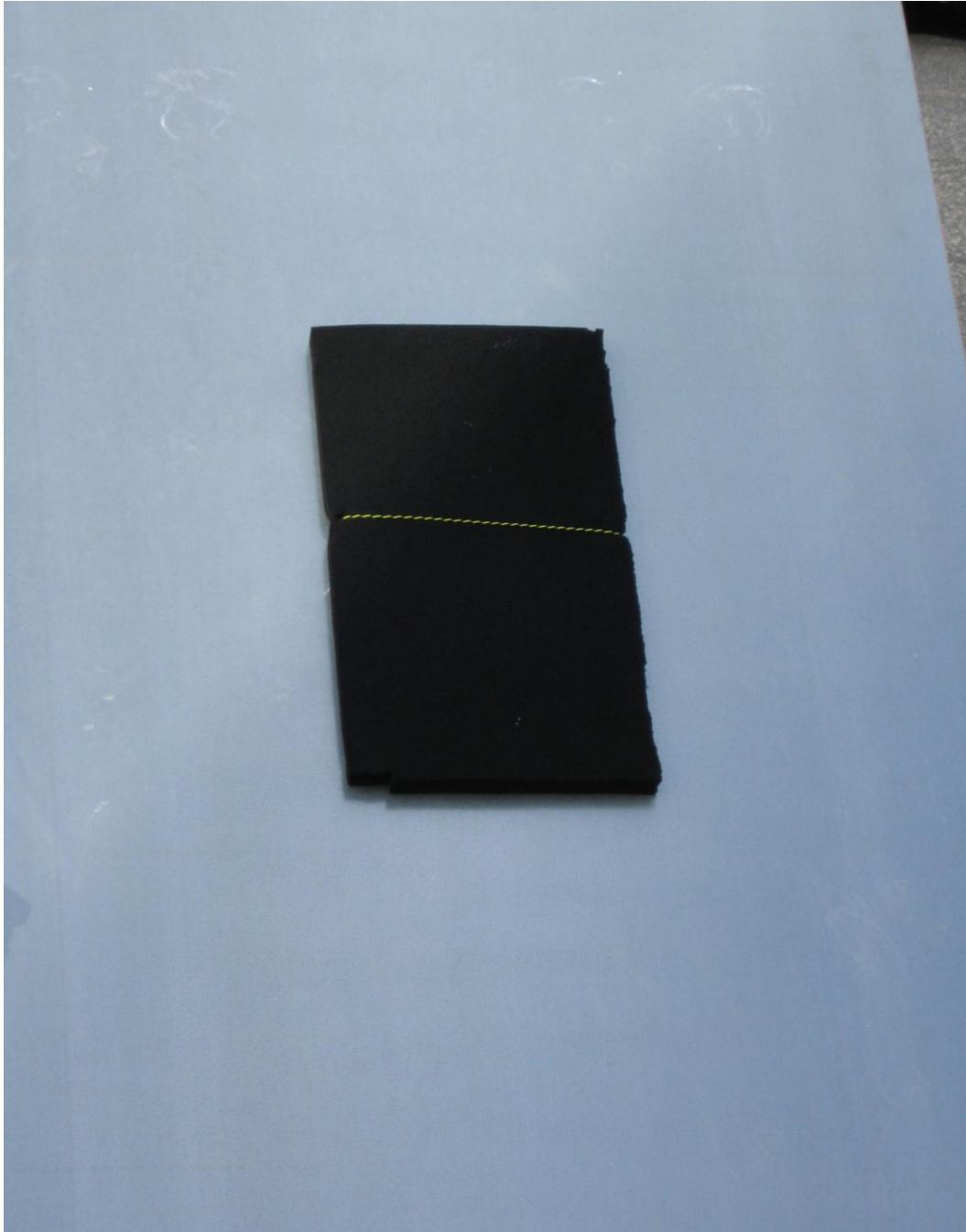


**Figure F.76.** Scene

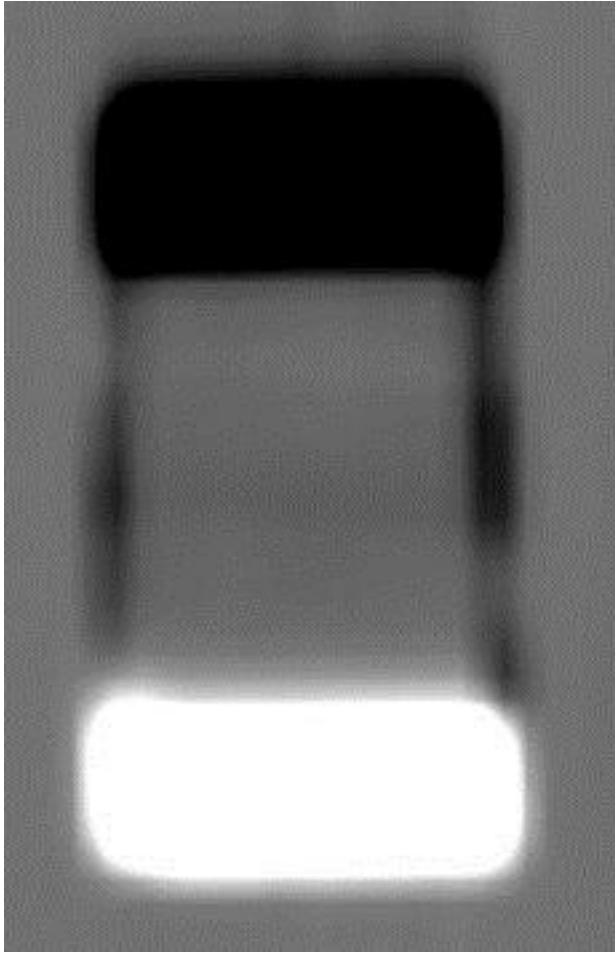


**Figure F.77.** Intensity Image (V + H)

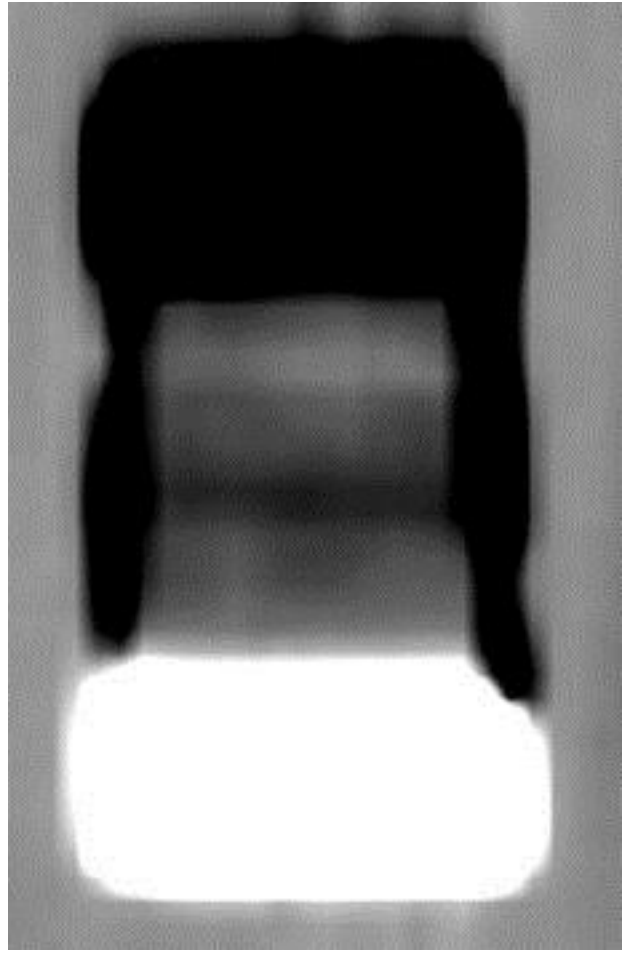


**Figure F.78.** Intensity Image (V + H) Histogram Stretched

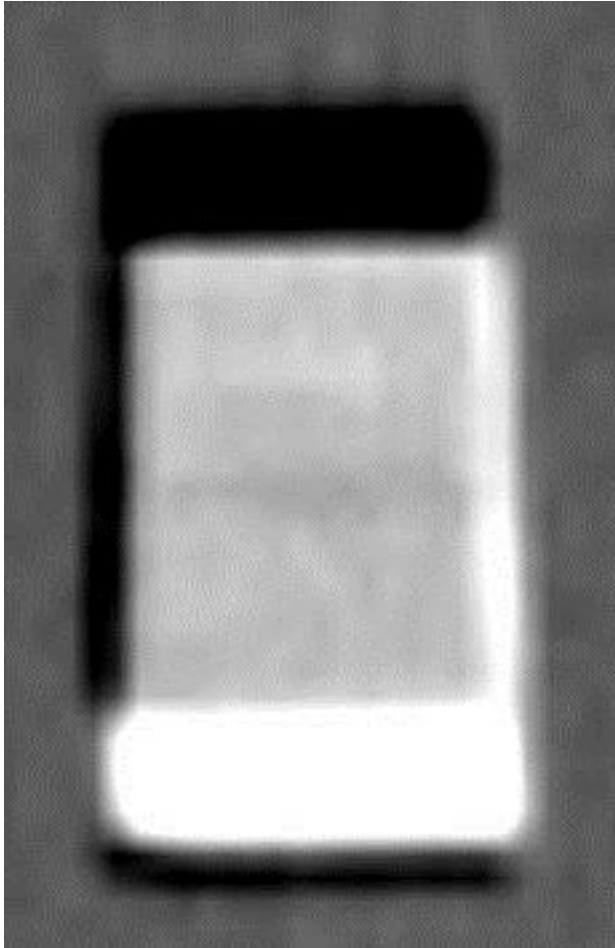


**Figure F.79.** V Image ( $T_1 - T_r$ )

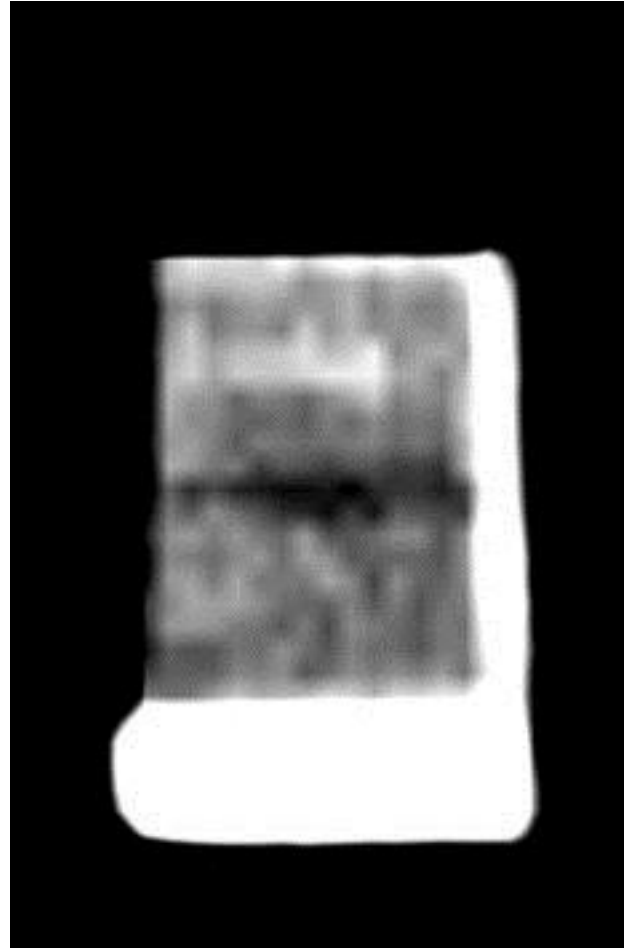


**Figure F.80.** V Image ( $T_1 - T_r$ ) Histogram Stretched

### F.3.3 Image Set #13

**Scene Description.** Binocular differential radiometer positioned on a 30-ft vertical scissor lift overlooking a steel pipe laid in the grass area below. Grass presenting a semi-common background for nulling the differential signal, while the pipe presents a strong change in brightness temperature.



**Figure F.81.** Scene

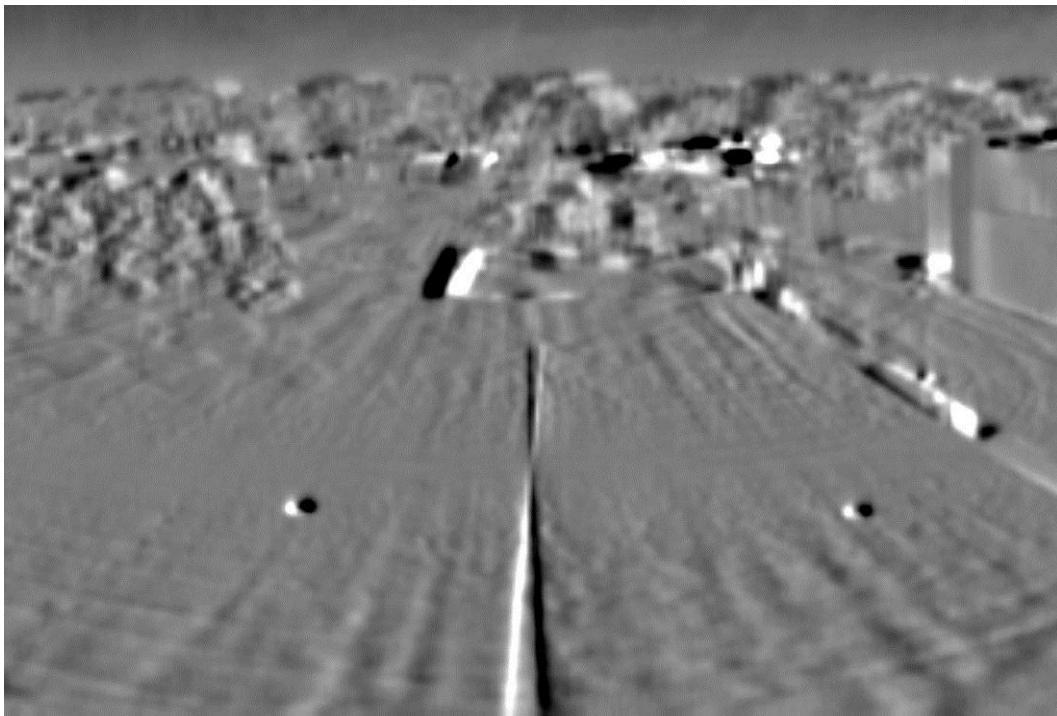


**Figure F.82.** Intensity Image (V + H). Note the distinct X shape of the pipe; this is due to the binocular system configuration, and the center point of the X is the convergence distance of the 2 beams.

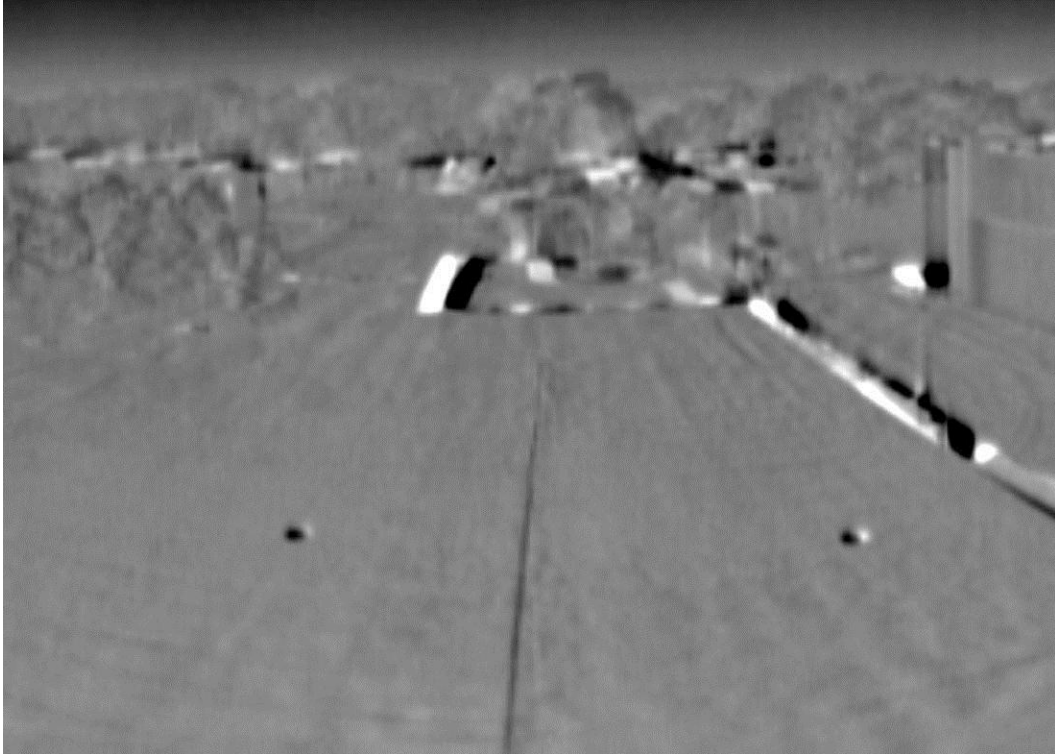


**Figure F.83.** Q Image (V – H)

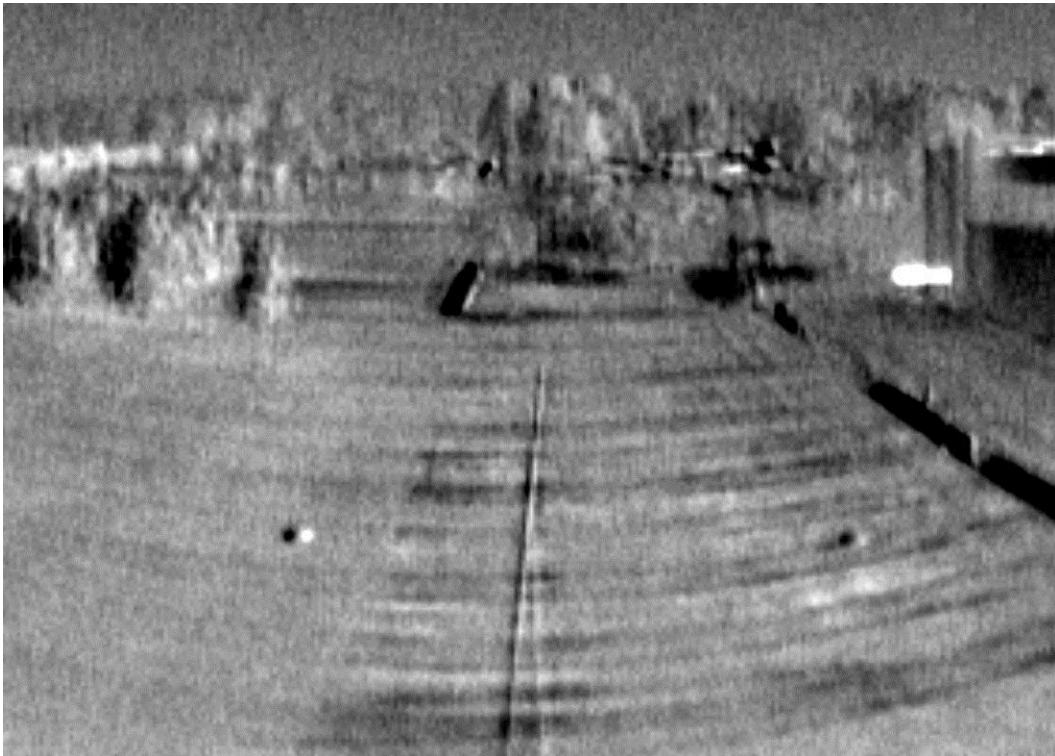


**Figure F.84.** U Image ( $T_{+45} - T_{-45}$ )

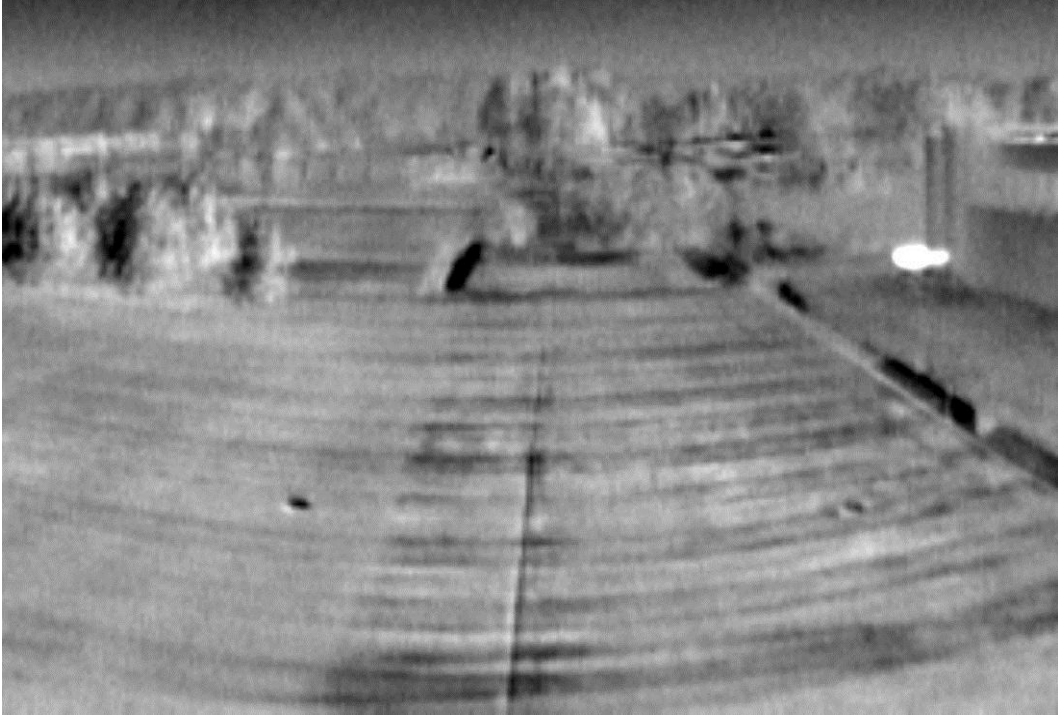


**Figure F.85.** V Image ( $T_1 - T_r$ )

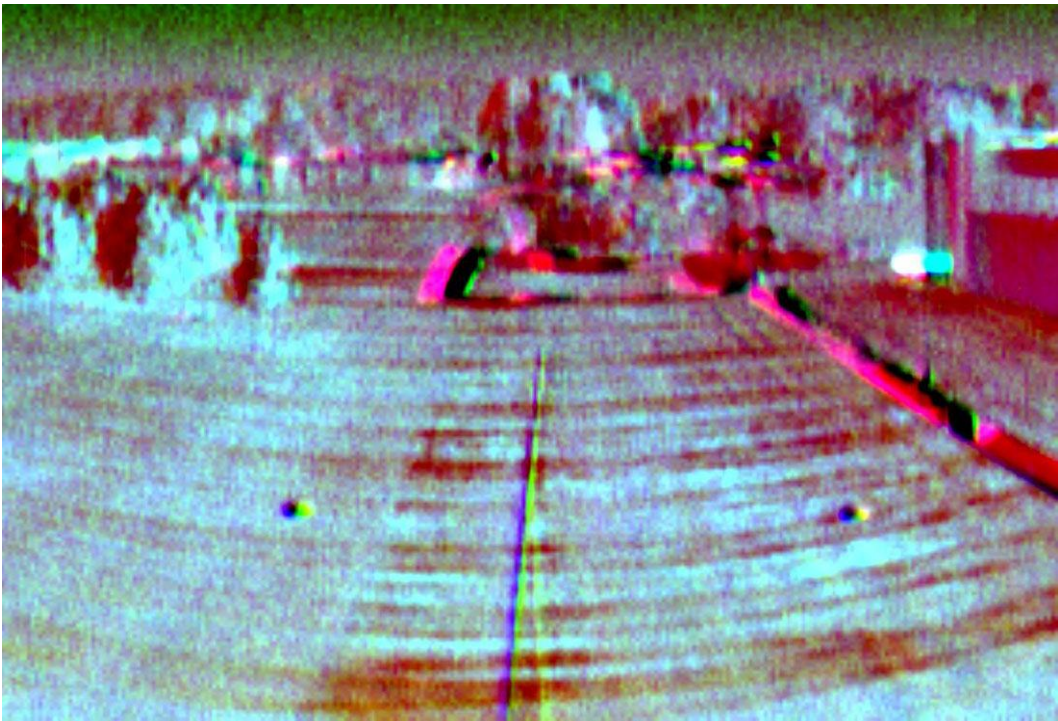


**Figure F.86.** QUV RGB Image (Q image assigned to red, U image assigned to green, V image assigned to blue)

### F.3.4 Image Set #14

**Scene Description.** Binocular differential radiometer positioned on a 30-ft vertical scissor lift overlooking two hidden targets and their associated control targets. The first target is a corrugated roof hidden under desert camouflage cloth material with its control being a piece of desert camouflage over bare grass. The second target is a small cylinder inside a cardboard box; its control is an empty cardboard box of the same size.



**Figure F.87.** Binocular Radiometer



**Figure F.88.** Scene

#### F.3.4.1 Results from 6 Channel Measurements



**Figure F.89.** Vertical Channel

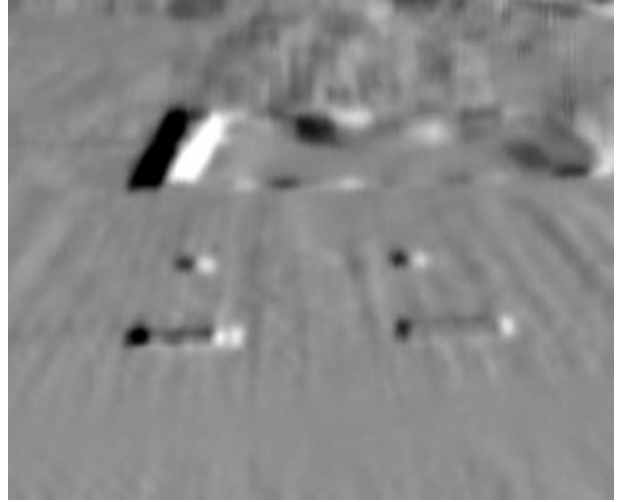


**Figure F.90.** Horizontal Channel

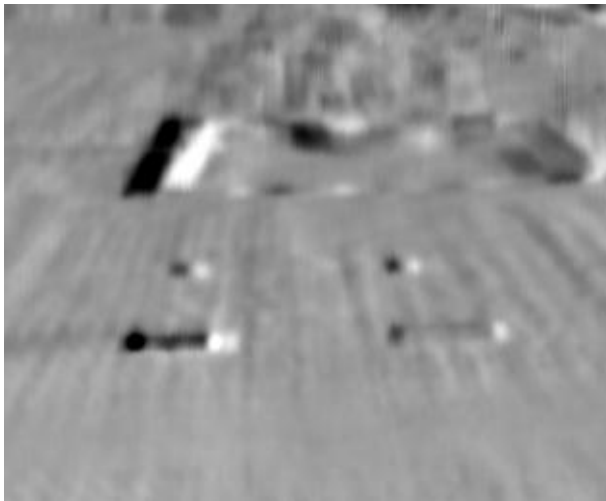


**Figure F.91.**  $T_{+45}$

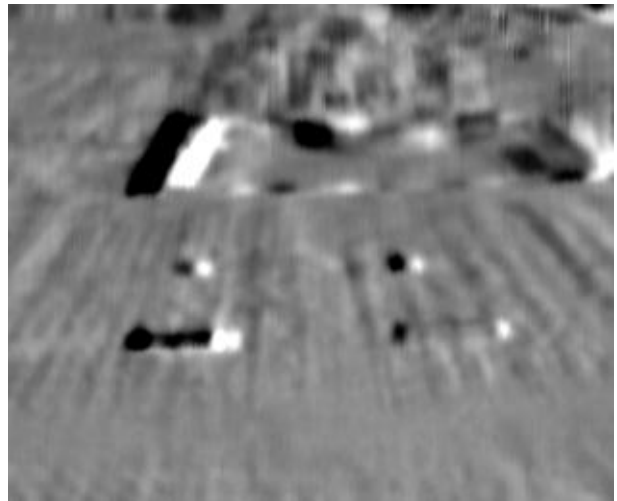


**Figure F.92.**  $T_{-45}$

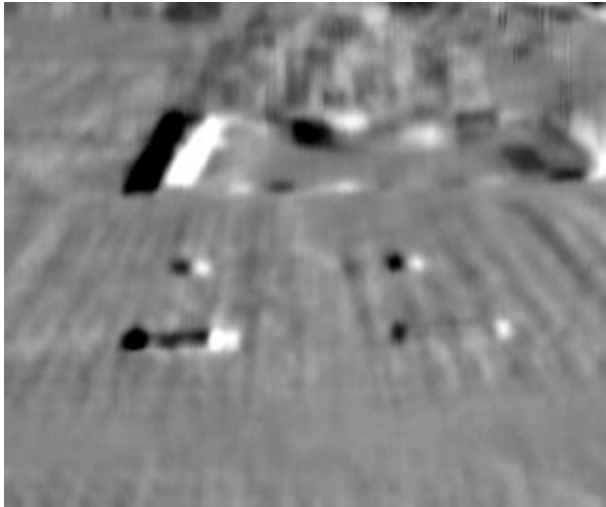


Figure F.93. T<sub>L</sub>

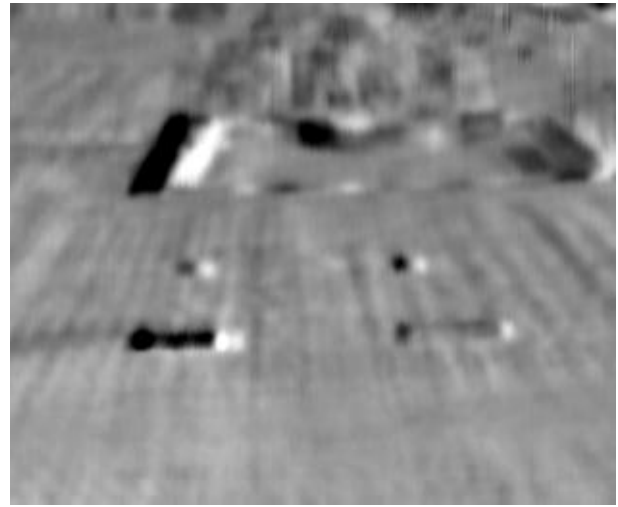


Figure F.94. T<sub>R</sub>

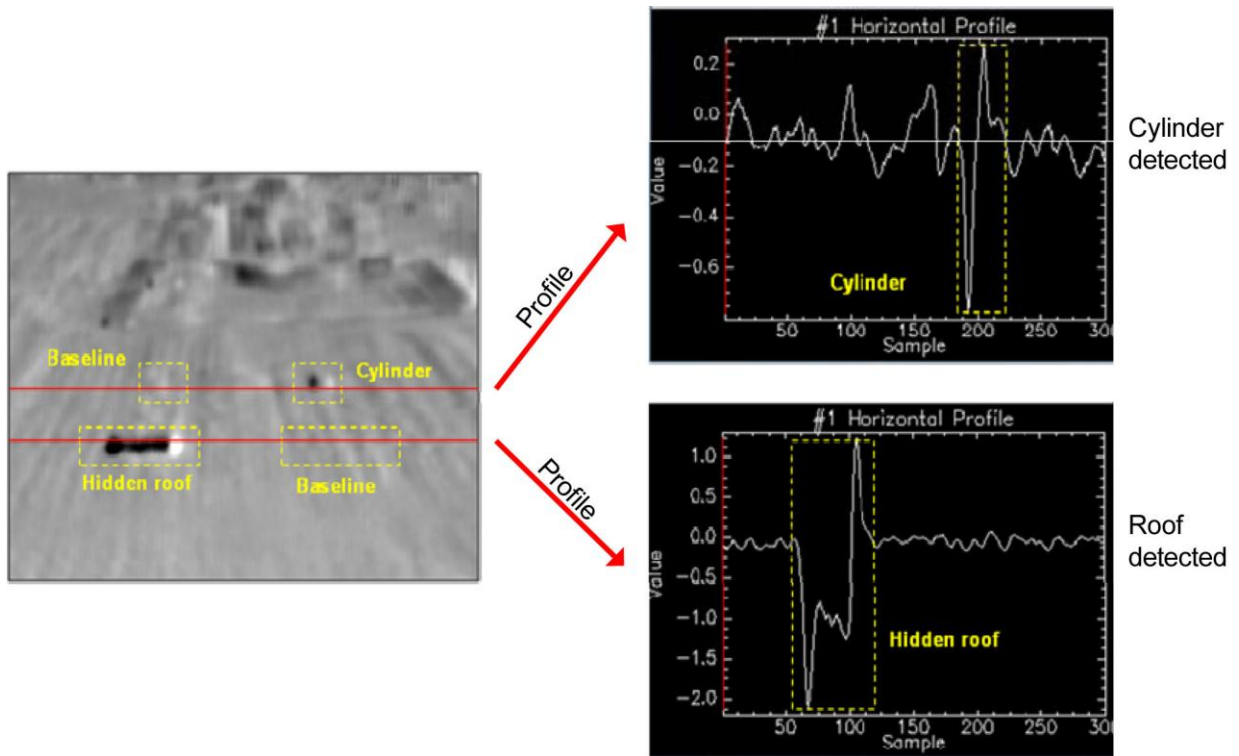
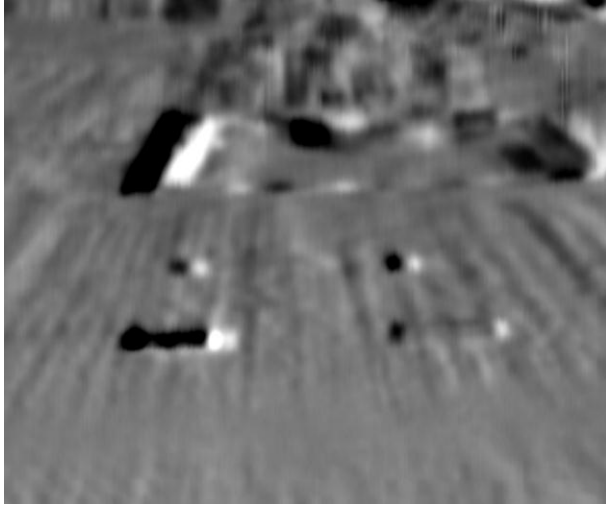
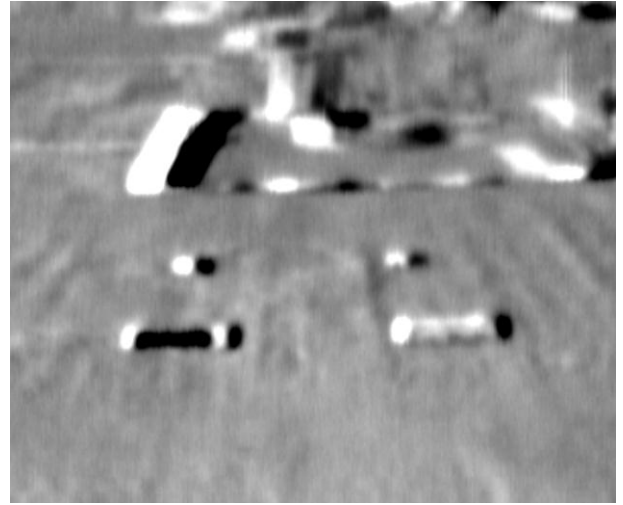


Figure F.95. Further Investigation of Vertical Channel



**Figure F.96.** Intensity Image ( $V + H$ )



**Figure F.97.** Q Image ( $V - H$ )



**Figure F.98.** U Image ( $T_{+45} - T_{-45}$ )

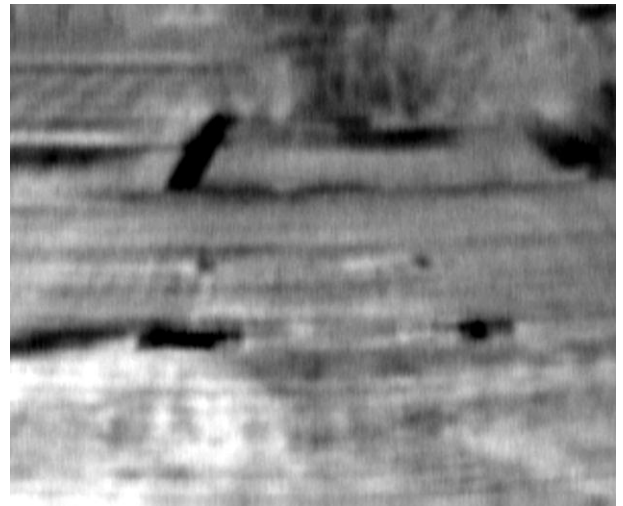


**Figure F.99.** V Image ( $T_1 - T_r$ )



## **Appendix G**

### **Binocular Imaging Trade-Offs for Aircraft**



## Appendix G

### Binocular Imaging Trade-Offs for Aircraft

This appendix outlines the developmental requirements to build a Fizeau combining “fringe” imager for high-altitude, long-endurance (HALE) aircraft. Figure G.1 shows a cartoon of the concept first considered in our proposal. The goal is to identify a binocular system with differential comparators for all four Stokes components of the passively emitted mm-wave radiation in the nominal W-band that extends from ~ 85 to 105 GHz. The concept being proposed should give instantaneous field-of-view (IFOV) spatial resolutions using fringe imaging of better than 30 m at operational altitudes ~ 65,000 feet (19.8 km). The other goal is to identify whether large swaths of territory can be scanned with a whiskbroom method so that near nadir or side-looking flight paths can be entertained past large proliferation sites. Ideally the use of any mechanical scanner should be reduced or eliminated if the system is meant for rapid, single-pass scene characterization. This way the system will become a simpler, lower power and low vibration pushbroom imager.<sup>(a)</sup> In the discussion below we illustrate that an ~ 3.3-km wide swath could be achieved now with no moving scanner system parts and, that if needed the side look angle can be adjusted for different types of flyovers, including side looking scans with about 6.6 to 9.9 km of offset per each 10-degree obliquity from nadir (perhaps useful in support of treaties where the flyover must be at fenceline). At present, the SAR side-looking radar developed for the Global Hawk (RQ-4A) gives ~ 6-m resolution with a swath 37 km (23 miles) wide at that UAV’s operational altitude of 19.8 km and cruise speed of 181 m/s (404 mph). We don’t expect any prototype PMMW-imaging system to match this immediately, but the PMMW-imaging systems would also offer reliable temperature profiling in spite of cloud or fog coverage and the potentially considerable advantage of preserving stealthy operation if necessary.

Like the Large Binocular Telescope used in IR astronomy, we are proposing a larger baseline separation  $L$  between reasonable sized collector apertures  $D$  ( $D \leq 2.5 L$ ) to achieve additive “fringe” resolutions given as  $\sim \lambda/2L$  much better than the single collector aperture Rayleigh resolution of  $1.22 \lambda/D$ . The DOE has access to a surrogate of the Global Hawk RQ-4 systems, the Proteus, which can carry fairly large instruments in a “superboom” center line pod. The superboom was developed by NASA Langley as a science pod for the Proteus, and it provides an 8-ft-long internal bay that can support instrumental systems with diameters up to 40-in. in that entire length. This pod was used by the Sandia AURA Airborne Remote Sensing System to test their UV fluorometer at typical altitudes of 1 to 5 km.<sup>(b)</sup> If simple “multiplicative” synthetic aperture imaging was implemented with the superboom layout (which assumes two or more fixed cutouts can be made), this would give an effective fringe resolution along the flight path of  $\lambda/2.44$  m, or worst case about  $\approx 1.3$  mR at 94 GHz. At nadir viewing from 19.8 km this would yield an in-track fringe GSD of  $\approx 26$  m, satisfying the original proposition of our proposal.

- 
- (a) Elimination of mechanical scanning to resort to push-broom data collection also reduces the computational burden to work out inertial pointing controls and feedback issues, and scene reconstruction could probably be done with extant software devised for hyper-spectral imaging.
  - (b) These parameters were derived from the Sand Report (SAND2004-0413), entitled “Laser Hazard Analysis for Airborne AURA (Big Sky Variant) Proteus Platform,” by A. L. Augustoni, available from OSTI as an unlimited release.



**Figure G.1.** Artistic Conception of a Bracewell, or Fizeau “Additive” Beam Combiner within a Centerline Pod of the Model 281 Proteus / Northrop-Grumman Model 395 UAV. As drawn (for ease of illustration), two co-rotated optical apertures would side-feed a series of beam combining feedhorns. Actual telescope layout would use dual side-fed Mizuguchi-Dragone crossed dual reflectors, as shown in Figure 10.5 of this report. Actual array layout would ideally be 4 by 16 feedhorns arranged with their long axis in the cross-track direction for nearly 10 degree of field-of-regard coverage, and the 4 rows would allow spatial summing strategies to improve SNR about 2-fold through statistical summing.

As described in Section 4.2.4.2, a side fed Mizuguchi-Dragone crossed offset telescope was proposed for this application. This particular crossed Dragone design has been extensively reviewed in the literature of the CMBR community as a means to effect a large field-of-regard for astronomical viewing with quite low cross polarization; simulated fidelity typically exceeding  $< -45$  dB for cross polarization at  $\pm 4$  degrees is expected off the center axis and, much better ( $< -50$  dB) closer to the central axis (Tran et al. 2008). Interestingly, this same design also gives an excellent Strehl-ratio across such a large focal plane as well. A design is considered close to diffraction limit if the Strehl-ratio is above 0.8, and the side fed design of Figure 4.11 can achieve a Strehl ratio  $> 0.76$  out to  $\pm 4$  degree from the central axis (ibid). This is considerably better than any standard side-fed microwave telescopes commonly employed including the crossed Gregorians used in telecommunications. It is also better than an equivalent Ritchey-Cretien Cassegrain style optical or IR telescope as well (Tran 2003).

While considering the GSD resolution for imaging, it is important to maintain a good radiometric sensitivity for the imaging if we want to do thermal profiling as suggested in Appendix H. Given that the cruise speed for the Global Hawk at operational altitude of 19.8 km (181 m/s) probably cannot be significantly adjusted, then the line imaging speed of any linear or multiple line focal plane array must be  $\geq 181$  (m/s)/GSD, or about 70 Hz for a nominal 26 m fringe GSD. We have three types of radiometer designs we can consider for early development with slightly different performance depending on whether  $T_R < T_{\text{ambient}}$ . For the case of a total power system the performance will be precisely 2-fold better than that of our balanced Dicke radiometer described in the report with noise injection at  $\sim 300$  K (Ulaby, Moore, and Fung 1981; Table 6.4 for exact comparisons). The unbalanced Dicke radiometer designs used in “additive” pseudo-correlators will be about  $\sqrt{2}$  better than a balanced Dicke radiometer if the switching occurs differentially between two unknowns in the scene, and  $T_R$  is  $\ll T_{\text{ambient}}$  and the gain variations between switching cycles is quite low (implying high speed switching like in the WMAP radiometer at  $\geq 4$  kHz). This asymptote of performance has also been achieved with cryogenically cooled pseudo-correlators developed by JPL (Bock et al. 2005), but for the purposes of comparison, we will use the radiometric sensitivity of a fully polarimetric based radiometer using balanced Dicke switching ( $2 \cdot [T_R + T_A]/\sqrt{B \cdot \tau}$ ). However, we will assume that the receiver can be developed around cooled and advanced InP based semiconductor preamps with a  $T_R = T_{\text{ambient}} \sim 300$  K. We also assume that this radiometer’s IF bandwidth will be  $\geq 10$  GHz; current InP electronics has demonstrated gain flat stability and low noise performance over 20 GHz in the W-band, but for simple scaling we assume 10 GHz IF bandwidth for these comparisons. The radiometric sensitivity of such a balanced Dicke radiometer with front end  $T_{\text{sys}} \approx 600$  K and a 14.3 mS post-detection dwell time is 0.100 K.

As noted in Griffin, Bock, and Gear (2002), feedhorn-coupled focal plane architectures with  $2 \cdot F \cdot \lambda$  spacing of the feedhorns (actually optimal for systems with  $T_R \geq T_A$ , using an edge tapered horn of about 12 dB) will need some level of dithering or “jiggle” to achieve comparable resolution as a Nyquist limited filled bolometer focal plane array. Typically, the jiggle pattern to achieve an effective projected beamwidth (GSD) of  $\lambda/D$  on the ground with a beam separation of horns ( $\approx 2\lambda/D$ ) would be 16 (4 steps in each axis), but because we are considering “fringe” addition techniques, this would reduce our scan dithering to 4 sub-steps along the cross track with a whiskbroom type architecture. Reducing the post-detection dwell time to 3.575 mS would thus degrade the radiometric sensitivity to  $\approx 0.201$  K, to accommodate optimal spatial dithering, which would still be a satisfactory radiometric sensitivity, since scene clutter and platform motions will probably degrade this some more. The baseline goal is to achieve radiometric sensitivities approaching 0.3 K consistent with space-borne platforms like WindSat.

The final issue is how large and ‘optically fast’ the binocular system’s apertures should be. According to Tran et al. (2008), it is hard to build a Mizuguchi-Dragone crossed-offset wide field telescope with  $F\#$  faster than about 1.5. Since this system has been extensively modeled by academics for CMBR studies at ultimate low receiver temperatures (i.e., very low telescope self-emissions), and for near diffraction limited resolution over wide fields ( $\pm 4$  degrees), we will use this concept as our ultimate objective. Our own Dragone-based system was designed and built for  $F\# = 2.05$  set up. In principle, this slightly ‘slower’ optical system should give cross polarization fidelity  $< -40$  dB over an even wider field of regard (perhaps  $\pm 5$  degrees or slightly more). Our own radiometers have high quality, low loss orthomode transducers (OMTs serve as front-end polarization separators) with  $\approx -40$  dB of cross polarization-isolation, so we hope to check this conjecture. (At the time of this report, this is one of two milestones that remain uncompleted.) For much of the field work presented, we tested our systems’ cross polarization fidelity as better than  $-30$  dB, but we did not take heroic measures to calibrate or balance the

systems regularly at the OMTs' limits of  $\approx -40$  dB isolation. Thus, if our results showing a contrast enhanced Rayleigh resolution limit somewhat better than about 0.5 to 1 times  $1.22 \lambda / D$  is general, then we expect that the field-of-regard for an operational binocular system may be softly delimited to about  $\pm 6$  degrees or more, allowing a wider swath to be studied without mechanical scanning. Table G.1 shows a number of plausible scaled systems up to a primary aperture of 1 m, which could be fitted into the NASA-Langley devised "superboom" pod for the Proteus aircraft. The Proteus is used as a manned surrogate for the Global Hawk, but can itself be used as a drone. Accounts of the Global Hawk radar pod that was tested with the Proteus on April 27, 2006, suggest it may be possible to consider even larger pods (30 ft/9.1 m in full length) with potential baselines approaching 7 to 8 m, but for this trade study we assume that a maximum baseline between aperture far edges is  $\approx 2.44$  m. According to press information, the NASA-Langley superboom does not delimit the Proteus' cruise speed of 181 m/S nor, its operational cruising altitude of  $\sim 19$  km, but the MP-RTIP (SAR) radar pod of 30 ft length and  $> 1$  m diameter was apparently only tested to altitudes of 6.7 km, and slower cruise speeds of 100 knots ( $\approx 51.5$  m/S or 185 km/h) (Paone 2006).

Table G.1 gives estimates for the instantaneous field-of-view for each feedhorn (under  $2 \cdot F \cdot \# \cdot \lambda$  optimal spacing for feedhorns with  $T_R \approx T_A$ ) projected to the ground assuming a 19.8 km air-to-ground altitude, and a slant range 10-degree off of nadir (20 km). This would correspond to approximately a 3.3 km lateral offset, presuming sanctioned flyovers will require a modest fenceline separation from presumptive proliferation facilities. Other GSD estimates for the Rayleigh resolution (GRD) of a single aperture and the fringe 'GSD' follow et. sequentially.

Parameters	Dragone as Designed	Fast Dragone	Larger, Fast Dragone
Primary D	0.500 m (19.7 in.)	0.680 m (26.8 in.)	0.750 m (29.5 in.)
F-#	2.05	1.5	1.5
Focal length	1198.5 mm	989.1 mm	1,091 mm
Resolution of aperture (Rayleigh $\approx 1.22 \lambda/D$ ) [mRad]	7.8 mR	5.74 mR	5.20 mR
GRD at 20 km slant range (10-degree off nadir)	156 m	114.8 m	104 m
IFOV for $2 \cdot F \cdot \# \cdot \lambda$ feedhorn beamwidth	10.95 mR	8.01 mR	8.01 mR
GSD at 20 km	219 m	160 m	160 m
Angular resolution of beam combiner ( $\lambda/L$ - widest separation 2.44 m)	1.3 mR	1.3 mR	1.3 mR
GSD for fringes at 20 km	26 m	26 m	26 m

Implicit in these calculation is the fact that we are not proposing to use a filled focal plane line array near Nyquist spatial sampling limit, given as  $0.5\lambda$ , nor even as  $1\lambda$ . Bock et al. (2005) and Griffin, Bock, and Gear (2002) discuss the fact that when the internal brightness radiance of the instrument becomes comparable or larger than that from the scene brightness radiance, filled arrays suffer greatly due to pick up of the instrumental radiance. This is when a feedhorn array is preferred, and one with a spacing of  $2 \cdot F \cdot \# \cdot \lambda$  with  $\sim 12$  dB edge tapering is considered nearly ideal to see point-like radiance sources in the larger scene clutter. As any proposed line imaging array will need to have a feedhorn separation of  $2 \cdot F \cdot \# \cdot \lambda$  to work well as described in Griffin, Bock, and Gear (2002), we are technically required to dither the array to achieve Nyquist sampling. In the in-track direction, this can be done by sampling at faster read-out rates above 70 Hz. In the cross track direction, the combined Dragone-Mizuguchi offset binocular

could be scanned around the center line of the secondary mirrors shown in Figure 10.5 of this report. This would project a zig-zag (sawtooth) pattern at the ground, as discussed in Ulaby, Moore, and Fung (1981; Section 6.17 and Figure 6.39), so some aspect of any ground imaging would be incomplete unless the scan rates could be greatly increased. We have not found a good simple solution to expand the angular field-of-regard beyond about  $\pm 5$  or 6 degrees, unless more advanced wide angle, unobscured reflective telescopes are used. Hughes holds a number of patents on IR reflective systems that will have well baffled, low emissivity characteristics for the thermal IR, so this is an avenue of possible future work. An alternative to double the swath of coverage would be to build two side-fed binocular systems, each counter-rotating to null primary inertial loads along the longitudinal axis of any pod, and thus keep pod vibrations to a minimum. Such a counter balanced system would allow more rapid and larger angular scan rates to be applied without inducing significant mechanical stresses to the pod or bay structure, and could be considered for implementation on P3 aircraft that have sizable bay openings.

During the mid-point of this work, it was discovered that Prof. Prather at the University of Delaware has developed a low insertion loss optical up-converter that might allow “multiplicative” forms of synthetic aperture imaging to be carried out with a considerable increase of smaller, more widely separated antennas. As these upconverters appear to offer nominal 3.5 to 4 dB conversion losses, they would lead to system temperatures of  $< 400$  K. They also have unprecedented bandwidths, in excess of 20 GHz in some cases (Ku band currently), which would benefit ultimate radiometric sensitivity. Interim results for the W-band also look like a large bandwidth conversion in excess of 25 GHz is possible. Moreover, since fiber optics are used to plump the various array antennas together with negligible transmission or mode coupling losses ( $< 0.2$  dB in total typically) compared to mm-wave waveguide losses ( $\sim 0.5$  to 1 dB/ft), it is possible to make both optically fast and well separated sparse aperture arrays that could also give much greater interferometric resolution. However, this great advantage comes with the penalty that nearly  $N^2$  cross correlations must be performed, albeit by doing up-conversion to optical frequencies this can be done very practicably with Fourier lens optical correlators (much better than with electronic correlators or multipliers devised for the W-band). With the likelihood that these upconverters may augur a better paradigm of interferometric “fringe” imaging, it is prudent to pause at this juncture to verify the Prather technology. However, there may still be benefit to the originally proposed methods of “additive” beam combining with optical telescopes, and that is that the intermediate results are vastly more interpretable as images by humans in the loop. When properly scanned, long, thin aspect man-made objects and disturbances can be observed quickly as ac disturbances that become manifest above scene clutter, so “additive” imaging may have a benefit for ‘novelty’ filtering the environment for such features.

## G.1 References

Bock JJ, S Church, M Devlin, G Hinshaw, A Lange, A Lee, L Page, B Partridge, J Ruhl, M Tegmark, PT Timbie, R Weiss, B Winstein and M Zaldarriaga. 2005. *Task Force on Cosmic Microwave Background Research, Final Report*. Available at [www.nsf.gov/mps/ast/tfcr\\_final\\_report.pdf](http://www.nsf.gov/mps/ast/tfcr_final_report.pdf) , or <http://arxiv.org/abs/astro-ph/0604101>.

Griffin MJ, JJ Bock and WK Gear. 2002. “Relative Performance of Filled and Feedhorn-Coupled Focal-Plane Architectures.” *Applied Optics* 41(31):6543-6544.

Paone C. 2006. “New Radar Flying High as Crucial Testing Begins.” *Air Force Print News Today*. 10/5/2006. Available at [http://www.afmc.af.mil/news/story\\_print.asp?id=123028466](http://www.afmc.af.mil/news/story_print.asp?id=123028466).

Tran H, A Lee, S Hanany, M Milligan and T Renbarger. 2008. "Comparison of the Crossed and the Gregorian Mizuguchi-Dragone for Wide-Field Millimeter-Wave Astronomy." *Applied Optics* 47(2):103-109.

Tran HT. 2003. "Polarization Comparison Between On-Axis and Off-Axis Dual Reflector Telescopes: Zemax and Grasp\* Simulations." *New Astronomy Reviews* 47:1091-1096.

Ulaby F, R Moore and A Fung. 1981. *Microwave Remote Sensing: Active and Passive, Vol. I -- Microwave Remote Sensing Fundamentals and Radiometry*. Addison-Wesley, Advanced Book Program, Reading, Massachusetts. See Section 6 for comparisons of radiometers and imaging techniques.

## **Appendix H**

### **Possible NNSA Applications for PMMW Imaging**



## Appendix H

### Possible NNSA Applications for PMMW Imaging

The essential criticism of this work has been that wide area change detection with either commercial satellite imagery or commercial satellite SAR data does a pretty good job finding relatively small anomalies in scenes (~ 10 to 100 m GSD disturbances depending on data, view angle, illumination, etc.). This might appear to be a solid criticism given that PMMW imagery has much lower spatial resolution. Work done by the German academics in support of the IAEA or Comprehensive Nuclear-Test Ban Treaty organization (CTBO) is particularly compelling (Canty et al. 2002; Canty et al. 2005a; Canty et al. 2005b; Schlittenhardt et al. 2010). Understand, however, that the German academic publications came out well after the events they described had occurred, so one matter of unknown but considerable interest is how long it takes to do these detailed change detection case studies. These case studies also involved some of the most studied areas of the earth using satellite imaging, so had excellent time series imagery to form a baseline and follow-ups of nested images.

The German test case analysis of satellite earth observations of the North Korean October 9, 2006, seismic event, which used strictly open source archived and available commercial imagery, makes an especially impressive case study for finding small anomalies in remote, forested and quite rough terrain . (Schlittenhardt et al. 2010). Likewise, their analyses of archived Landsat and other imagery to review *ex post facto* historical underground tests at Nevada Test Site would seem to suggest it is not only possible to accurately locate the tests, but reasonable to evaluate yields of underground tests in desert areas of low vegetation cover (Canty et al. 2002; Canty et al. 2005a; Canty et al. 2005b). They did however note that detecting tunnel based weapons testing at NTS under mesas that had moderate overlay of vegetation were more difficult to analyze (e.g., Pahute Mesa at NTS). In these circumstances they largely could only verify that side drilling activities and road work in preparation of these sites could be detected. They were not able to observe and quantify any subsidence or other definitive effects of spallation that would be helpful in assessing the yields of tests that were bracketed with contemporaneous Landsat and other archived imagery nor, could they suggest the scaled depth of burial (SDOB - in units of  $\text{m/kiloton}^{1/3}$ ) for any of the tunnel tests as they had done for the well tests. In their later analysis of the presumed tunnel test in North Korea, they focused near the declared epicenter of the seismic event. That work seemed to also show that any apparent evidence of surface change just indicated surface preparations at the entrances to tunnels. It was unclear whether the adits and vents of the tunnels were definitively seen in the commercial imagery data. The Germans were able to use current best case, closely nested in time, before- and after-imagery for their study of the North Korean seismic event, as indicated by the Global Monitoring for Security and Stability (GMOSS) network of seismic stations.

In reviewing that work, as well as the earlier work done with contemporaneous best case footage of NTS, it appears that complementary satellite SAR and differential interferometric SAR (DInSAR) might benefit the panchromatic analyses. One big caveat is that a collection of baseline information in the various EM channels (visible, IR, SAR) should be collected as early as possible in areas where Under Ground Facilities (UGFs) activities are *expected* for best exploitation of change detection (Happer and Price 1999). It has been noted by the Mitre JASON study led by Happer on characterizing UGFs (ibid) that SAR techniques are not optimal for detecting UGF signatures (e.g., adits and vents), but that interferometric SAR data would be useful in the detection of openings such as ducts and vents. However,

unless there are validated man-made structures near the suspect areas, which can act like good retro returns, obtaining prior baseline SAR and even DInSAR data is problematic. Basically vegetated areas tend to give poor results of change detection over extended areas of natural surfaces because of their low radar return SNR. For the same reasons that vegetation makes good in-scene IR blackbody coverings, the vegetation also acts as an excellent absorber of microwave radars. Hence they are areas with very low quality radar returns to do quality differential change detection with most SAR techniques. This may present an advantage to multispectral imaging, as noted in Harper and Prince (1999), but rugged scenery tends to be affected greatly by scene clutter and emissivity-temperature uncertainties from shadowing that require careful and intensive signal processing.

In considering PMMW imaging as an alternative means to spot small non-natural scene anomalies (GSD ~ 30 m), we were primarily concerned with spotting transient scene changes *ex post facto* without any baseline information. Scenes with poor or very dated baseline imagery would not be suitable for simple panchromatic or hyper-spectral change detection. (We were also expecting that circumstances where no definitive seismic or other obvious triggers would be available to help time stamp the important baseline imaging and cue the acquisition of follow-up data in a timely manner). Also, hyper-spectral imaging can be spoofed in the case of smaller scenes that can be quickly dressed over. It seemed that in the matter of low yield weapons testing or much lower impulse hydrodynamic metal tests, there are a large number of vegetated hilly areas that may not be suitable for SAR or simple multispectral change analyses. There are also many other related matters of analyzing small redoubts, such as the discovery of small UGFs currently being adopted in the Middle East for many practical scales of proliferation. Examples are UGFs built into the sides of wadis (dried up ancient river basins) and supplied with water from underground springs or aquifers. These may not be surrounded with significant permanent radar friendly 'retro' devices (power-line towers, etc) that are found in urban or built up regions. Without strong vetted RF 'retros' it is much harder to do precision and sensitive detection of naturally vegetated, and amorously changing surroundings using interferometric SAR techniques.

Another matter of interest to us has been the quantification of Pu reprocessing, especially small scale operations. In the case of hydrometallurgical reprocessing at the Hanford reservation, it is well known that prodigious amounts of low-level contaminated water was released to soil trenches and cribs designed to act as simple sand filters or evaporative ponds nearer to the reprocessing canyons. (At least three types of hydrometallurgical separations were operated successfully with separate canyons at Hanford, and all of them used some variants of cribs and trenches to deal with large waste-water treatments). Typical releases of waste water with PUREX flow sheets were about 10 million gallons/MTU processed. We felt that the detection and monitoring of the reprocessing tanks, cribs and trenches might serve as viable cueing of operational activity with low spatial resolution PMMW-imaging. Many of the modern reprocessing structures can now be hidden effectively using smaller scale reprocessing flow-sheets supported in smaller facilities, but the water usage may always remain a barrier to complete anonymity if the less costly, reliable hydrometallurgical are exploited. As was noted in the Introduction, water presents a rather cold ambient radiance temperature to down-looking PMMW imagers, because at microwave and mm-wave frequencies, the water is fairly reflective. At thermal IR frequencies and the short-wave IR of many multispectral imagers, the water is quite absorptive and presents a spectral radiance close to the ambient brightness temperature.

In Figure H.1 we show the scale of the chemical tank operations at the Hanford PUREX canyon. These tanks were the often shaken 'beakers' for continual chemical processing, and when those operations were completed, they became waste tanks for high level liquid wastes and sludge. One feature

of any hydrometallurgical separations work is the necessary need for full and effective ventilation of the headspace of these tanks, since radiologically driven breakdown of the solvents is always occurring at a high pace. Without strong natural convective air flow, these tanks will become pressurized with explosive gases. In addition to head-space venting with multiple large aperture metal vent manifolds, it is also necessary to add water cooled heat exchanger towers and/or evaporators near the tanks to handle the waste heat of fission products released to the tanks' walls. The large chimney structure seen in the foreground of the exposed tank shown in the RHS panel of Figure H.1 is an example of this. After construction and installation of all these tanks, they were covered with sandy soil (mostly quartzite sand) to assure good rain drainage around the tanks. Protected piping and filter manifolds were added to the tank openings seen at the tops of the tanks to reduce the collection of rain water. The thermal and probably polarimetric signatures from the aboveground vents and vent covers would probably be an excellent repeating metallic scattering feature to study with PMMW imaging. No individual vents would probably be seen, unless 2-m class PMMW-imagers were positioned cooperatively at fence-line or Open Sky ranges (~10 km), but the collective quasi-periodic array of metal spikes and vent coverings may show a distinct Stokes signature at great stand-off ranges. (For scale purposes, note that a man is emerging from one of the many vent ports in the tank shown on the LHS lower panel.) The other matter about these 'waste' tanks that may bear repeating is that radiological decay can create intense heat in these tanks; wall temperatures have been known to exceed 100°C, even with substantial forced cooling with pressurized water through heat-exchange tubes placed in the concrete covered steel walls of the tanks. Thus, it is expected that there may be large donut shaped heat zones seen in the dry overlayer of soil covering such structures. It would be interesting to view these fields of mostly buried tanks to see what can be observed with a full polarimetry PMMW imaging system.

In like manner, it would be helpful to study the signatures of any released water borne waste streams. Years ago, the trenches at Hanford were available to study. The trenches were a public note of concern so photographs of their original implementation are now hard to find. Most if not all trenches at Hanford have probably been remediated at the time of this writing. One historical example of a trench photo can be easily viewed at: <http://www.nuclearfiles.org/menu/library/media-gallery/image/tredici/30.htm> . What is of interest to us would be the study of the polarimetric signature that such a long trench with side berms on either side would look like; would it present the strong U component of Stokes analysis that we have seen for shallow depressions in grass, and would the apparent temperature of the ditches be reduced due to the periodic accumulation of rain-fog water. As noted in the caption of the long ditch in question,<sup>(a)</sup> there is probably waste water reserves below the surface (note the overgrowth of opportunistic weeds like Russian thistle in the center of the ditch), but the catchment walls will also naturally recoup fog water in the early morning fogs that are prevalent in deserts near rivers. In essence, from the perspective of monitoring hydrometallurgical reprocessing operations, it would be helpful to follow the water. At or near the source, the water will be hot (no pun intended), but low level waste water is inevitable and copious, so its disposal should be observable under the right viewing conditions with PMMW observations.

---

(a) "This ditch is used to dispose of large quantities of contaminated water from plutonium production operations. The water contains radioactive and toxic chemical contaminants. Sand soil is meant to act as a natural filter for the water as it percolates down to the water table. 200 Area, Hanford Reservation, Richland, Washington. November 16, 1984."

## Tank vent plumbing and evaporative cooling essential

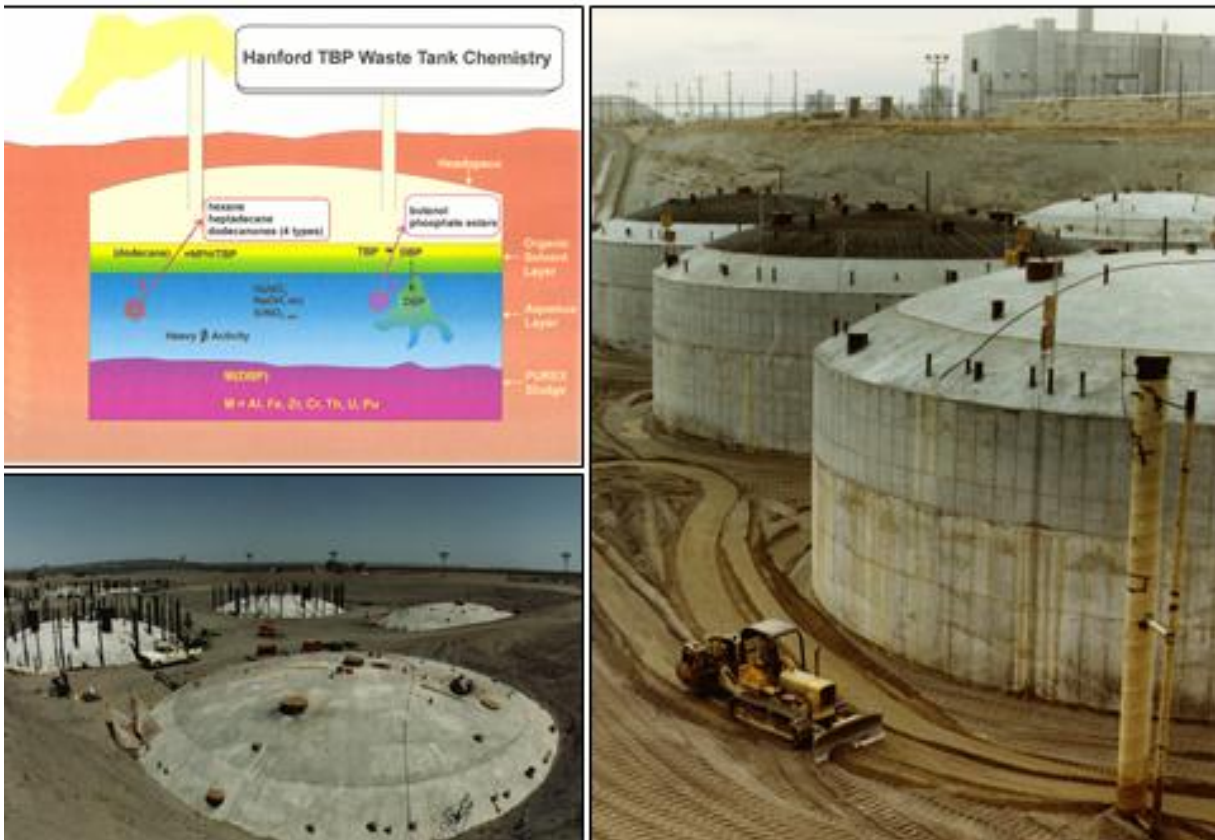


**Figure H.1.** Examples of Waste Tanks Used Originally as Process Chemical Tanks for PUREX Reprocessing

## H.1 References

Canty MJ, B Jasani and J Schlittenhardt. 2002. "Wide Area Change Detection with Satellite Imagery for Locating Underground Nuclear Testing." In *Symposium on International Safeguards - Verification and Nuclear Material Security*. October 29-November 2, 2001, Vienna. IAEA-SM-367/16/02. Available at <http://www-pub.iaea.org/MTCD/publications/PDF/ss-2001/PDF%20files/Session%2016/Paper%2016-02.pdf>.

Canty MJ, G Jahnke, AA Nielsen and J Schlittenhardt. 2005a. "Change Detection for Remote Monitoring of Underground Nuclear Testing: Comparison with Seismic and Associated Explosion Source Phenomenological Data." In *General Assembly of the European Geosciences Union*. April 24-29, 2005, Vienna.

Canty MJ, AA Nielsen and J Schlittenhardt. 2005b. "Sensitive Change Detection for Remote Monitoring of Nuclear Treaties." In *Proceedings of the 31st International Symposium on Remote Sensing of Environment, Global Monitoring for Sustainability and Security*. June 20-24, 2005, St. Petersburg, Russia.

Happer W and T Prince. 1999. *Characterization of Underground Facilities*. JSR-97-155, JASON, The MITRE Corporation, McLean, Virginia.

Schlittenhardt J, MJ Canty and I Gruenberg. 2010. "Satellite Earth Observations Support CTBT Monitoring: A Case Study of the Nuclear Test in North Korea of Oct. 9, 2006 and Comparison with Seismic Results." *Pure and Applied Geophysics* 167(4-5):601-618.











**Pacific Northwest**  
NATIONAL LABORATORY

*Proudly Operated by **Battelle** Since 1965*

902 Battelle Boulevard  
P.O. Box 999  
Richland, WA 99352  
1-888-375-PNNL (7665)

[www.pnl.gov](http://www.pnl.gov)



U.S. DEPARTMENT OF  
**ENERGY**